Advances in Electromagnetic Fields in Living Systems

Volume 4

Advances in Electromagnetic Fields in Living Systems

Volume 4

Edited by

James C. Lin

University of Illinois at Chicago
Chicago, Illinois

Springer

James C. Lin
Department of Electrical and Computer Engineering,
University of Illinois at Chicago
Chicago, IL 60707-7053 USA
lin@eecs.uic.edu.

ISBN-10: 0-387-23997-9 e-ISBN 0-387-24024-1 Printed on acid-free paper.
ISBN-13: 978-0387-23997-2

Printed in the United States of America. (TB/EB)

9 8 7 6 5 4 3 2 1

springeronline.com

Preface to Volume 1

Hardly any phenomenon in the modern environment is as ubiquitous as electromagnetic fields and waves. We have learned to understand the physical characteristics of these energy forms, and we have applied them in abundant ways to embellish our ways of life and our standards of living. Furthermore, we have come to depend on them for health, safety, information, comfort, and conveyance.

Apart from their intended roles, these electromagnetic fields and waves produce other effects that may influence the activities of living organisms. The effects produced depend on many physical, chemical, and biological factors. They may be grossly apparent and visible soon after exposure of the living organism or they may not appear to have influenced the organism at all upon casual examination. Even then, there may be subtle changes that are only detectable upon careful chemical or microscopic study, or which are apparent only after a considerable time delay.

Nevertheless, our understanding of the interaction of electromagnetic fields with living systems is advancing in a wide range of topical areas. This bi-annual series, with invited reviews by recognized leaders in their respective specialties, will present progress to date in key areas of research and scholarship. The guiding philosophy of this undertaking is the presentation of integrated, known, and confirmed phenomenological observations, basic mechanism of interactions, and applications in biology and medicine, as well as perspectives on current topics of interest.

A further intent of this series is to promote the interchange of ideas between biomedical, engineering, and physical science specialties, and thus the series is aimed at both practitioners and researchers. As the numbers of publications multiply, it becomes a challenge to locate and especially digest such a collection of papers, contradictions, and interpretations. It is hoped that volumes in this series will provide the catalyst in efforts to perfect our knowledge for health protection, and to develop new and better diagnostic, as well as therapeutic, procedures.

In the last two decades, research on the biological effects and health implications of electromagnetic fields not only has expanded, but also has become a subject of a public concern and private debate, worldwide. This series is aimed at bringing together contemporary advances in key areas of research and scholarship. Very seldom can advances be totally divorced from past accomplishments. Accordingly, this premier volume begins with

a chapter that discusses, briefly, contributions made by some of the early investigators on the interaction of electromagnetic fields with living systems. The interaction of radiofrequency (RF) electromagnetic fields with the central nervous system has been a subject of considerable contemporary interest, since the nervous system integrates and regulates an organism's response to its environment. The chapter that follows summarizes the known effects of RF radiation on the central nervous system and includes a review of interaction of RF exposure with psychoactive drugs on animals. The latter has become one of the most intriguing research subjects with profound implications for health effects and safety protection.

This volume presents basic, applied, and clinical information ranging from extremely low to super high frequencies. In general, the interaction of electromagnetic fields and waves with biological systems is frequency-dependent. Moreover, the mechanisms of interaction for fields at low frequencies are very different from those at high frequencies. While significant advances are being made on many fronts, a particular emphasis of this volume has been placed on the recent developments of our understanding in the very low and extremely low frequencies. They have led to some exciting new applications in the clinical management of tissue injury from exposure to extremely low frequency electric fields, and in the therapeutic treatment of the musculoskeletal systems, such as the repair of soft tissue wounds and bone fractures using low frequency fields (see chapters three and four). These low frequency fields also are emitted by circuitry within video display terminals (VDTs) and video display units (VDUs). Recently, considerable concern has been expressed by the public and some professionals about the possible health effects resulting from extended use of these devices. Chapter five examines, in detail, the possible effects of electric and magnetic fields from VDTs and VDUs on human health.

It is my pleasure to acknowledge the National Science Foundation, Office of Naval Research, and the National Institutes of Health, for their support of my research throughout the years. Some of the results are found in various parts of this volume. A portion of the writing and editorial activities was completed while on sabbatical leave of absence from the University of Illinois. I am grateful to the National Science Council of ROC on Taiwan, for the opportunity to serve as an NSC Chair Professor during the 1993–94 academic year. Many individuals have contributed to the realization of this volume. I want to thank especially, Mr. L. S. Marchand, the senior editor at Plenum, for his encouragement and patience through all phases of this work. I wish to express my appreciations to the authors for their friendship and willingness to share their intellectual accomplishments. And lastly, but importantly, to my family: my wife, Mei, and children, Janet, Theodore, and Erik. I am deeply indebted for their faith, love, patience, and ungrudging support.

James C. Lin
Chicago and Taiwan

Preface to Volume 2

This is the second volume in the series on **Advances in Electromagnetic Fields in Living Systems**. The objective of this volume is to add to the scientific and professional literature a number of significant pieces of research larger in scope than journal articles. We hope that this form of publication will make the information readily available to research organizations, libraries, government agencies, independent investigators, and interested persons.

The chapters in this volume are organized into two consecutive sets using two specific regions of the electromagnetic spectrum: extremely low frequency fields and radiofrequency radiation. While significant advances are being made on both fronts, greater emphasis of this volume is placed on recent developments at radio frequencies. Each chapter consists of a comprehensive review of a topic of current interest and growing importance. Much of the information is based on authors' own research and that of the contributions from investigators in the relevant scientific disciplines.

The first two chapters of the book review two of the most significant topics that have played pivotal roles in raising and addressing the question of whether extremely low frequency (ELF) electric and magnetic fields can affect the development of cancer. Chapter 1 scrutinizes the connection between exposure to ELF electric and magnetic fields and melatonin synthesis or utilization. It examines data that have been reported to indicate that exposure of animals to ELF fields reduces the ability of these animals to produce this hormone. And it discusses the significance of the findings relative to the incidence of cancer in humans exposed to ELF fields. The large number of epidemiological reports that focus on cancer and its potential association with ELF exposure are evaluated in Chapter 2. It provides a strength evaluation for the available evidence at this time and a discussion on the unique challenges that face epidemiological studies of ELF exposure.

An important task in assessing health risk from exposure to ELF and radiofrequency (RF) electromagnetic fields is the quantitative determination of ELF and RF fields within and without biological bodies. The emphasis of Chapter 3 is on computational methods for dosimetry and exposure assessment and their application in bioelectromagnetic investigations. It provides a general knowledge base for computational bioelectromagnetics. It also gives specific guides to computing ELF and RF coupling and field distributions inside homogeneous and nonhomogeneous phantom and animal bodies.

The biological effects of RF and microwave radiation have become a focal point of attention because of the accelerated use of RF radiation for wireless communication over the past few years. Wireless communication systems use low power modulated forms of RF and microwave radiation that were not investigated extensively in the past. Research addressing issues pertaining to the wireless communication spectra has begun only recently. Chapter 4 summarizes results from published studies using frequencies in the same spectral band and provides information on current research activity. It includes carcinogenesis and cancer promotion by RF and microwave exposure, and other *in vitro* and *in vivo* experimental studies that involve primarily the central nervous system and other tissues in the head. A brief description of epidemiological studies on RF and microwave exposure is also included. The material should be of use for preliminary risk assessment.

Chapter 5 examines, in detail, the reported experimental evidence for possible effects of RF fields on cancer initiation, promotion, and progression. It provides a necessary background for the direction of future laboratory research to help clarify whether RF and microwave radiation influences cancer initiation and development. It examines the critical parameters of the exposure that may account for any influence. An exciting new medical application, the clinical management of cardiac arrhythmia using catheter-delivered RF and microwave energy, is summarized in Chapter 6. RF cardiac ablation has become the most commonly used minimally invasive procedure for treatment of irregular heart rhythm. Microwave energy is a viable alternative energy source for percutaneous catheter ablation (additional references to this energy source are given at the end of Chapter 4).

While the health effects of RF and microwave radiation remain a concern to the general public and many professionals, the new ANSI/IEEE exposure standard represents a wealth of scientific understanding and significant improvement over its predecessor. However, its complexity has caused difficulties in the implementation of the standard in the real world exposure situation. Chapter 7 provides guidance on what is involved in assessing exposure and offers insights to applying the standard from a practical perspective

Lastly, I wish to thank the authors for their important contributions. I also want to pay a special tribute to the investigators in this field, whose published works and personal communications greatly helped us in writing the chapters. As always, I owe a huge dose of gratitude to my family for their faith and support.

James C. Lin
Chicago

Preface to Volume 3

The past few years have been exceptionally active periods for research on the interaction of electromagnetic fields with living systems. The subject has become a focus of attention because of the expansion of electric power use and distribution at 50 and 60 Hz in the extremely low frequency (ELF) spectrum between 3 Hz and 3 kHz and because of the accelerated use of radio frequency (RF) radiation (300 MHz to 6 GHz) for wireless devices over the past decade. In addition to the primary intended roles, electromagnetic energy may produce effects that could influence the vital activities of living organisms. A major research effort related to possible adverse health effects of environmental electric and magnetic fields (EMF) was completed in the United States. A report, summarizing the research, was issued by the administering agency, the National Institute of Environmental Health Sciences [NIEHS, 1999] Another report, appraising the research, was issued by the National Academy of Sciences [NAS/NRC, 1999].

In the summary report, NIEHS concluded that "the scientific evidence suggesting that ELF-EMF exposures pose any health risk is weak. The strongest evidence for health effects comes from associations observed in human populations with two forms of cancer: childhood leukemia and chronic lymphocytic leukemia in occupationally exposed adults. While the support from individual studies is weak, the epidemiological studies demonstrate, for some methods of measuring exposure, a fairly consistent pattern of a small, increased risk with increasing exposure that is somewhat weaker for chronic lymphocytic leukemia than for childhood leukemia. In contrast, the mechanistic studies and the animal toxicology literature fail to demonstrate any consistent pattern across studies although sporadic findings of biological effects (including increased cancers in animals) have been reported. No indication of increased leukemia in experimental animals has been observed."

The National Academy of Sciences' review and evaluation concluded that results, from the research that was authorized by Congress, "do not support the contention that the use of electricity poses a major unrecognized public health danger." Moreover, the report stated that, "The biologic research contributed little evidence to support the hypothesis that a link exists between MF (magnetic field) and cancer." However, the report went on to state that, "In contrast with laboratory research, some epidemiological studies have reported difference in incidences of cancer associated with MF exposure that differs by as little as

0.2 to 0.4 μT." It is interesting to note that these two reports reached a similar conclusion – there is a need for further research, especially at the basic science level.

This volume begins with a chapter describing the difference in coupling of ELF fields and RF radiation into biological systems and mechanisms of interaction disclosed through the Maxwellian formulation. While ELF fields and RF radiation occupy the same known electromagnetic spectrum, their mode of coupling into biological tissues and their mechanism of interaction can be very different. It is shown that electromagnetic energy at ELF and RF frequencies can be used to probe the body in different ways. These observations suggest that it is possible to deduce explanations for a broad range of biological interactions and reactions through an examination of the coupling mechanisms for ELF fields and RF radiation. The next four chapters present current and future biomedical applications of electromagnetic fields and RF radiation in diagnostic imaging and therapeutic treatment. The last two chapters are devoted to the biological effects of pulse RF radiation.

Clinical evaluation of magnetic resonance imaging (MRI), which relies on constant and RF magnetic fields for its operation, had begun in the 1980's. Continued developments in instrumentation and applications since then have allowed MRI to become the diagnostic imaging modality of choice in many medical practices. Moreover, the dramatically reduced scanning time has accelerated and diversified medical applications of MRI in recent years. Applications that are currently under investigation include magnetic resonance angiography, perfusion and diffusion imaging, temperature mapping, and functional imaging. Chapter **Two** reviews some of the techniques and applications of MRI, and introduces a novel tissue impedance MRI technique for the brain. Imaging electrical activity of the brain is a promising area of noninvasive biomedical application of low frequency electric field. Chapter **Three** provides a state-of-the-art review of imaging brain electrical activity using scalp electroencephalograms (EEG). The chapter discusses some of the inverse imaging algorithms used for EEG spatial deconvolution imaging. However, the focus of this review is on model-based spatial deconvolution imaging, namely cortical-potential imaging in a realistically shaped inhomogeneous head model.

The use of low frequency electric fields to improve and help maintain functions of the living system is a dazzling topic. External electric fields applied to biological materials interact directly on free electric charges and dipoles. They may cause intermolecular transitions and intermolecular processes that can lead to structural reorganization of the cell membrane through the technique of electroporation or electropermeabilization. The induced transient changes in membrane states have led to electric field pulse techniques to gain increasing importance in cellular and molecular biology, in gene technology, and in therapeutic medicine. Chapter **Four** gives a detailed account of the electric field pulse techniques and *in vivo* applications of electropermeabilization in combination with chemotherapy or as a tool for gene transfection. Likewise, a better understanding of the fundamental mechanisms of electric field induced tissue modification and injury could help to develop efficient therapeutic procedures and effective management tactics. Chapter **Five** discusses the theory and experimental evidence concerning the effect of intense electric field on cell membrane proteins and membrane active transporters.

The fact that pulsed RF radiation was used almost exclusively for radars meant that few people in the general population would have encountered exposure to pulsed RF radiation as a by-product of technological aids in their daily activity. The science and engineering of RF technology have expanded to the point that many types of devices have been developed

using pulse RF energy to embellish our lives. Indeed, we have come to depend on the pulse RF energy for health, security, information, and entertainment. Moreover, recent developments in high peak power pulsed microwave systems have renewed interest in exploring potential biological effects of high peak power RF pulses. Currently, there are systems capable of delivering 100 gigawatt (GW) pulses to a transmitting antenna and establishing hundreds of kV/m peak E-field intensity in the beam path. However, we know very little about the safety aspects of high peak power, ultra-short RF signals. Chapter Six presents an up-to-date review of the biological data available in the English language for pulsed RF fields.

It has been recognized for years that significant contributions to the field of bioelectromagnetics have been made by research performed in the former Soviet Union (FSU). Unfortunately, most of this research was published in the Russian language and was not readily available to scientists in the West. As a result, these publications have not been reviewed comprehensively in English until now. Chapter **Seven** gives a comprehensive review of the FSU research on biological effects and potential health hazards of pulse RF radiation. Most of the reported effects of low-intensity pulsed microwaves were subtle functional changes, which did not exceed the limits of normal physiological variation and could only be detected by sensitive physiological tests. However, some studies did report clearly pathogenic effects. Interestingly, such issues as RF-induced carcinogenesis apparently had not been a concern and were not studied at all. Nevertheless, some of the findings may have implications on the conceptual understanding of interaction mechanisms and on approaches to RF safety protection. Their replication by researchers in the West deserves consideration.

And, finally, to the authors who have generously contributed their expertise, kindly developed their chapters and patiently endured several stages of change, I am sincerely grateful. It is my earnest hope that the information presented in this volume will inspire scientific investigators to continue their efforts to expand our knowledge of the interaction between electromagnetic fields and living systems.

James C. Lin
Chicago

REFERENCES

NAS/NRC, 1999, *Research on Power Frequency Fields Completed under the Energy Policy Act of 1992,* National Academy Press, Washington, DC.

NIEHS, 1999, *Health Effects from Exposure to Power-Line Frequency Electric and Magnetic Fields*, Prepared in Response to the 1992 Energy Policy Act (PL 102-486, Section 2118) (NIH Publication 99-4493), Washington, DC.

Preface to Volume 4

The objective of the fourth volume in the series on **Advances in Electromagnetic Fields in Living Systems** remains the same as previous volumes. It is to add to the scientific and professional literature a number of significant advances in this area of research. These books are intended to serve the needs of graduate students and of researchers, as well as those of specialists in other fields who may desire an assessment of the advances in bioelectromagnetics and its capabilities as a strategy with the potential for solving specific problems. In general, the interaction of electromagnetic fields and waves with biological systems is a frequency dependent phenomenon. Moreover, the mechanisms of interaction for fields at low frequencies are very different from those at high frequencies. While significant advances are being made on many fronts, a special emphasis of this volume is on current and future biomedical applications of electromagnetic fields, ranging in frequency from quasi-static to the optical regime. The six chapters in this volume are partitioned into two groups: four chapters discussing the use of electromagnetic fields and waves for diagnostic imaging and two chapters dealing with mechanisms of interaction and therapeutic applications. Each chapter consists of a comprehensive treatment of a single topic of current interest and growing importance.

This volume begins with a chapter on fetal magnetocardiography (fMCG)—a noninvasive method of detecting components of the magnetic field produced by the electrical activity of the fetal heart as a function of time—which is experiencing a steady growth, and is expected to gain influence in diagnosis of certain congenital fetal heart defects and to provide the optimal care for these patients. Although fetal heart rate monitoring is the most widely used method of assessing fetal well-being, it suffers from a fairly high false-positive rate, since it relies on surface electrical recording. Fetal magnetocardiography overcomes this problem, and it offers an excellent technological approach for assessing fetal heart rate and rhythm. With suitable signal processing, it provides a distinct signal, free of maternal cardiac interference, which can be detected throughout the last half of pregnancy.

Nuclear magnetic resonance imaging (MRI) has become the diagnostic imaging modality of choice for many medical conditions. Its success—and that of X-ray computed tomography—has encouraged introduction of several novel tissue imaging techniques. The next two chapters examine respectively microwave thermoelastic tomography (MTT) and optical diffusion imaging—as promising areas—for noninvasive biomedical application of

electromagnetic energy. Microwave thermoelastic imaging uses microwave-pulse-induced thermoelastic pressure waves to form planar or tomographic images. Since the generation and detection of thermoelastic pressure waves depends on dielectric permittivity, specific heat, thermal expansion, and acoustic properties of tissue, microwave thermoelastic imaging possesses the characteristic features of a duel-modality imaging system. The unique attributes of the high contrast offered by microwave absorption and the fine spatial resolution furnished by ultrasound are being explored to provide an imaging modality for noninvasive imaging of tissues, especially for early detection of breast cancer.

Near-infrared light penetrates relatively easily into biological tissues due to the existence of an optical window in this wavelength region. The goal of diffuse optical imaging is to use diffuse near-infrared light to obtain quantitative information about changes in the optical properties inside the tissue, including changes in blood flow, blood volume or tissue oxygenation. Some of the most important applications of diffuse optical imaging are oxidative-metabolism in muscles, breast cancer detection, and optical tomography of the brain. This chapter describes the basic mechanisms of light–tissue interaction in the near infrared region, discusses different types of instruments used for diffuse optical imaging, reviews important applications of diffuse optical imaging, and presents some of the newest results.

The following chapter expands on the use of high-frequency electromagnetic energy and explores the use optical radiation for biotelemetry. Telemedicine aims to provide advanced medical care through modern telecommunication and information technologies, and to provide expert-based health care to understaffed remote sites. Radio-frequency electromagnetic radiation typically is tapped as the carrier wave for biotelemetry. With the advances in reliable laser diodes and photo diodes—as the infrastructure for a rapidly maturing optoelectronic technology—optical biotelemetry is gaining considerable renewed attention. The advantages of optical biotelemetry include, among others, the elimination of electromagnetic noise and interference, especially in the clinical environment and a wide-band transmission channel capable of supporting intelligent communication techniques. Optical biotelemetry is a new technique with abundant potential. This chapter outlines the basic technologies used to enable optical biotelemetry in practice, and gives examples of the optical biotelemetry systems which have been developed to date.

The last two chapters explore respectively the use of extremely low frequency (ELF) magnetic fields in pain therapy and the mechanisms of interaction for reported weak ELF effects in biological systems. The effects of ELF magnetic fields—between zero and 300Hz—on animal and human systems have been studied for more than a century. Many aspects of physiology and behavior have been examined in the pursuit of an explanation of how ELF fields could exert a systemic effect. One of the more sensitive systems in the body to ELF magnetic-field exposure appears to be the pain system, with effects that seem to be independent of phylogeny. Several laboratories have reported that ELF magnetic fields strongly influence opioid-like behavior in animals as diverse as rodents, pigeons, and snails. The first of these two chapters document pain therapy and magnetic fields. It reports on the effectiveness and efficacy of specific pulsed-magnetic field designed for the treatment of pain, including human subjects.

Weak electromagnetic field effects in biological systems have been reported since the 1980's. Some well-known examples include the so-called Ca^{++} efflux effect from chick brain tissue and ELF magnetic-field enhancement of DNA synthesis in cell cultures.

These results indicated a nonlinear frequency dependence, which did not scale with either frequency or strength of the applied field. The results were rather unexpected. The last chapter in this volume discusses the conjecture that cyclotron resonance may play a role in enhancing the sensitivity of biological systems to magnetic fields. Because the effect occurs specifically at the cyclotron resonance frequency and because the charge-to-mass ratios of certain ions are specifically implicated, these observations have been referred to as ICR interactions. Nevertheless, because of the lack of a reasonable explanation at the molecular level it is important to recognize that this designation is strictly empirical in nature.

Before signing off, I wish to thank the authors for their important contributions, and also for their cooperation and endurance throughout the publication process of this volume. I am grateful to several anonymous reviewers of parts of this volume, whose excellent advice has been graciously given and commonly taken. I also wish to thank especially, Mr. Aaron S. Johnson, Senior Editor, for his encouragement and patience through all phases of this work.

James C. Lin
Chicago

Contents

Chapter 1

Fetal Magnetocardiography

Maria J. Peters, Jeroen G. Stinstra, Siarhei Uzunbajakau, and Narayanan Srinivasan

ABSTRACT

Fetal magnetocardiography is a non-invasive method to study the fetal heart: the patient (i.e., the mother) is not even touched. A fetal magnetocardiogram (MCG) is the registration of a component of the magnetic field generated by the electrical activity of the fetal heart. Usually the component of the magnetic field that is perpendicular to the maternal abdomen is measured. Fetal MCGs show the typical features that are found in ECGs of adults (i.e. a P-wave, QRS-complex and T-wave). To enable the discrimination between pathological and healthy fetuses, values of the duration of these waveforms are collected in several research groups. These durations can be used as a reference. Measurements show that MCGs of fetuses with severe congenital heart disease have an abnormal shape. Hence, fetal MCGs may be of help in the early intra-uterine detection of congenital heart anomalies and the progress of the disease. Fetal magnetocardiography can also be used to classify fetal arrhythmias.

The fetal MCG is a very weak signal (about 10^{-13} tesla) compared with fields that are present in a hospital. The Earth's magnetic field, for example, is about 5×10^{-5} tesla. The only magnetic field sensor that is sensitive enough to measure fetal MCGs is a SQUID. This sensor has to be cooled in liquid helium. The vessel containing the helium and the sensor is positioned near the maternal abdomen. At present, fetal MCGs are measured within magnetically shielded rooms

Maria J. Peters, Jeroen G. Stinstra, Siarhei Uzunbajakau Faculty of Science and Engineering, University of Twente, 7500 AE Enschede, The Netherlands. **Narayanan Srinivasan** Biomedical Engineering Research Centre, Nanyang Technological University, 639 798 Singapore.

Advances in Electromagnetic Fields in Living Systems, Volume 4, edited by James C. Lin, Springer Science+Business Media, New York, 2005.

in order to avoid disturbing fields. Signal processing techniques, such as filtering and averaging, are used to enhance the signal–to-noise ratio. The electrical activity in the heart gives rise to currents in the fetus and maternal abdomen. These currents also contribute to the fetal MCG. In order to estimate this influence, simulations are carried out and discussed in the last section of this chapter on fetal MCG.

1. INTRODUCTION

Fetal magnetocardiography involves the acquisition and interpretation of the magnetic field near the maternal abdomen due to the electrical activity of the fetal heart. A fetal magnetocardiogram (MCG) can be recorded reliably from the 20^{th} week of gestation onward. Fetal magnetocardiography is a truly non-invasive technique in which the body is not even touched. It can be used to classify arrhythmias and to diagnose certain congenital heart defects. Hence, it may help to provide optimum care for the patient. However, until now, fetal MCGs have mainly been measured in research laboratories. Apparently, the application of fetal magnetocardiography in a clinical setting is hampered by the fact that the measuring instrument and its exploitation are still rather expensive and skilled personnel is needed to carry out the measurements. However, it is expected that these problems will be overcome in the near future.

A recording of a component of the magnetic field caused by the electrical activity of the fetal heart as a function of time is called a fetal MCG. This magnetic field is the result of the synchronous activity of many heart cells; the magnetic field of a single cell cannot be measured. At least 10^4 heart cells forming a dipole layer have to be active simultaneously. The first fetal MCG was measured in 1974 [Kariniemi et al. 1974]. The subsequent 25 years saw a slow and steady growth of interest in fetal magnetocardiography. During that period, the development of biomagnetometer systems was primarily dedicated to the study of the adult brain and heart. However at the beginning of the nineties, fetal MCG regained some popularity and instruments specially designed for measuring the fetal MCG became commercially available. An example of such a fetal magnetocardiograph is shown in Fig. 1. Currently, several groups in the world are developing systems for measuring fetal MCGs in an unshielded environment as well as collecting MCGs from healthy fetuses and of fetuses with a multitude of heart diseases.

Several aspects of fetal magnetocardiography will be considered in this chapter. In section 2, a short description of the electrical activity of the heart will be followed by a discussion on other methods for fetal surveillance and subsequently, fetal MCGs of healthy fetuses will be characterized. In section 3, the detection of fetal arrhythmias and congenital heart diseases by means of fetal MCG will be discussed. As fetal MCG signals are weak, an extremely sensitive sensor is needed. The most sensitive sensor for magnetic fields that fulfills the requirements is a SQUID. It has a sensitivity of some femtotesla ($1\ \text{fT} = 10^{-15}\ \text{T}$) and is discussed in section 4. Magnetic disturbances in urban surroundings are roughly $10^6 - 10^7\ \text{fT}/\sqrt{\text{Hz}}$ in the frequency range of fetal MCGs. The noise power spectrum shows also high peaks at specific frequency components, as for instance the frequency generated by power lines. A comparison with other magnetic field strengths is given in Fig. 2, making it clear that measures have to be taken to reduce the disturbances. In section 5, tools to

Figure 1. A multichannel fetal magnetocardiograph manufactured by CTF systems inc.

enhance the signal-to-noise ratio will be discussed, i.e., magnetically shielded rooms and flux transformers. The subject of section 6 is signal processing. In order to estimate the influence of the tissues surrounding the fetal heart on the fetal MCG, models are composed that describe the fetoabdominal volume conductor. These models are used in simulations discussed in the sections 7 and 8.

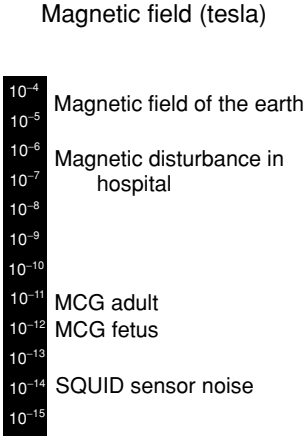

Figure 2. A comparison of magnetic field due to a fetal heart with magnetic fields of other sources.

2. THE FETAL HEART

Blood rich in oxygen and nutrients travels along the umbilical vein from the placenta to the fetal body. About half of the blood travels to the fetal liver; the rest goes via a vessel, called the ductus venosus, to the inferior vena cava. There the oxygenated blood from the placenta mixes with deoxygenated blood from the lower part of the fetal body. This mixture continues to the right atrium. In an adult heart, the blood from the right atrium enters the right ventricle and is pumped to the lungs. In the fetus, however, the lungs are nonfunctional and the blood largely bypasses them. A large part of the blood from the fetal right atrium is shunted directly to the left atrium through an opening in the atrial septum, called the foramen ovale. The rest passes into the right ventricle, where it enters the pulmonary circuit. The blood that enters the left atrium through the foramen ovale moves to the left ventricle and is pumped into the aorta. A part of the blood in the aorta reaches the myocardium, the brain, the lower regions of the body, and a part passes through the umbilical arteries to the placenta where it is reoxygenated. At the time of birth, important adjustments have to occur as the placenta ceases to function and the newborn starts to breathe.

The anatomy of the heart is sketched in Fig. 3. The heart muscle, like other tissues in the human body consists of cells surrounded by a membrane. The electrical behavior of a single cardiac cell has been recorded by measuring the potential difference between an intracellular and an extracellular microelectrode. At rest, the intracellular potential is about 90 mV lower than the extracellular potential. Any process that abruptly changes the res ting potential above a critical value (the threshold) results in an action potential. An action potential is a rapid change in the intracellular potential, called the depolarization of the cell, and is followed by a return to the resting potential, called the repolarization of the cell. Typical action potentials recorded from a cell in the ventricles and from a cell in the sinoatrial (SA) node are depicted in Fig. 4. The various phases of the cardiac action

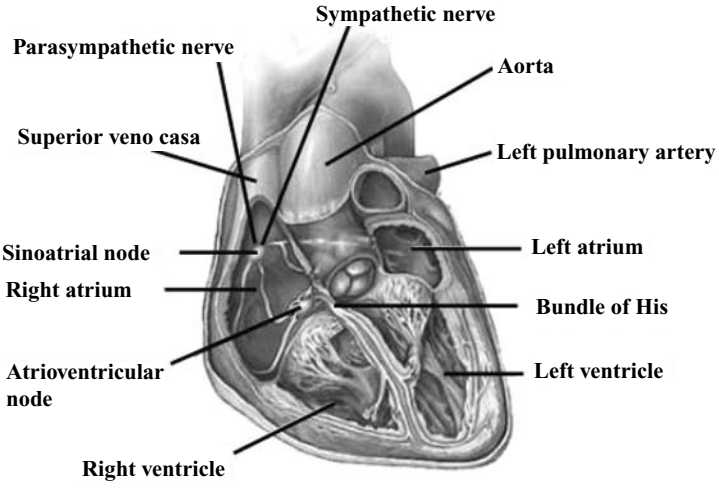

Figure 3. The conduction system of the heart.

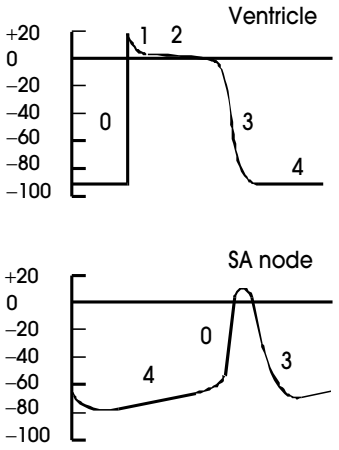

Figure 4. Typical action potentials r ecorded from a cell in the ventricles and from a cell in the sinoatrial (SA) node in an adult heart.

potential are associated with changes in the permeability of the cell membrane, mainly to sodium, potassium, and calcium ions. The five phases are:

1) Phase 0 indicates the rapid depolarization and is related almost exclusively to a rapid influx of Na^+ ions.
2) Phase 1 is a rapid partial repolarization achieved by the efflux of K^+ ions.
3) Phase 2 the plateau phase, achieved by a balance between the influx of Ca^{++} ions and an efflux of K^+ ions.
4) Phase 3 indicates the repolarization.
5) Phase 4 indicates the period between repolarization and the beginning of the ne xt action potential.

The SA node is called the natural pacemaker of the heart. An important distinguishing feature between the action potential of a cell in the SA node and that of a ventricular cell is phase 4. In the ventricular cell the potential remains constant during phase 4, whereas in a pacemaker cell there is a slow depolarization throughout phase 4. This depolarization proceeds at a steady rate until the threshold is attained, and then an action potential is triggered. Depolarization is transmitted to adjacent cells through the so-called "gap"-junctions between the cells. The atria and ventricles are separated by fibrous connective tissue that does not transmit the depolarization. The only structure capable of transmission of the depolarization is the atrioventricular (AV) node. An action potential that starts at the pacemaker cells in the SA node spreads over the entire heart following a well-defined pathway. From the SA node, the cardiac impulse spreads through the atrial walls at a velocity varying between 0.2 and 1 m/s. During its progress through the atria, the impulse reaches the AV node; here the conduction velocity is very low (0.05 m/s). From the AV node the impulse passes rapidly through the bundle of His and the Purkinje's fiber system and next it spreads through the ventricles.

In general, the pattern of an electrocardiogram (ECG) or MCG consists of a P, QRS, and T-wave (see Fig. 5). The P-wave reflects the spreading of the depolarization through

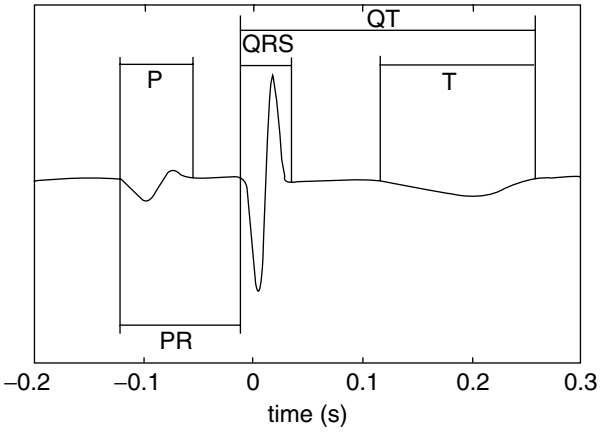

Figure 5. Identification of fetal cardiac time intervals from an averaged measured fetal MCG.

the atria. The PQ-interval is a measure of the time from the onset of atrial activation to the onset of ventricular activation. The depolarization of the ventricles is reflected in the QRS-complex, and the repolarization of the ventricles in the-T wave. The repolarization of the atria coincides with the depolarization of the ventricles. As the distances within the fetal heart are small in comparison to the distance between heart and the surface of the maternal abdomen, the activation sequence of the fetal heart may be described by a current dipole that rotates in time and is positioned at the center of the heart: the heart vector. The projection in the frontal plane of the locus of the tip of the heart vector during the cardiac cycle is represented in a vectorcardiogram.

The SA-node, which normally controls the heart rate, is under the influence of the autonomic nervous system. Heart rate variability is developed due to changes in stimuli that are exerted on the SA node from the autonomic nervous system. The autonomic nervous system includes two divisions, called the sympathetic and parasympathetic divisions. Changes in heart rate usually involve a reciprocal action of these two divisions. Thus, an increase in heart rate is produced by a diminution of parasympathetic activity and a concomitant increase in sympathetic activity; deceleration is usually achieved by the opposite mechanisms. In normal adults, the heart rate is approximately 70 beats per minute, but it is significantly greater in children. The fetal heart rate decreases from around 175 beats per minute at the ninth week to about 140 beats per minute at the end of normal pregnancy. Both fetal and maternal factors influence the fetal heart rate. Fetal factors include age, behavioral state, movements and pathological factors, such as congenital abnormalities, brain damage and hypoxia. Maternal factors include position, physical condition, such as fever, and the administration of certain drugs.

2.1. Methods to Monitor the Fetal Heart

Apart from using fetal MCGs, the condition of the fetal heart can be assessed using various methods that will be discussed shortly in this section. The oldest method to determine the fetal heart rate is listening to the sound produced by the fetal heart, since the French

physician Laennec invented in 1816 the acoustic stethoscope, by means of a stethoscope. Physicians and midwives are able to recognize certain sounds associated with a healthy heart as well as pathologies.

The action potential in the cardiac cells is accompanied by currents in the tissues that surround the fetal heart, the so-called volume currents. These currents produce potential differences that can be measured by means of electrodes attached at the surface of the maternal abdomen. The electrical conductivity of amniotic fluid is high in comparison with that of other tissues present in the maternal abdomen. As a consequence, volume currents flow primarily in the amniotic fluid. Only a small part of volume currents will reach the surface of the abdomen, giving rise to small potential differences at the abdominal surface that are often too small to be measurable. A recording as a function of time of the potential difference between two of these electrodes is called a fetal ECG. The first fetal ECG was obtained in 1906. During the remaining part of the 20th century numerous improvements have been made both in fetal ECG equipment as well as in the understanding of the propagation of the fetal heart signal. However, despite the advantage of being a cheap and non-invasive method, transabdominal fetal electrocardiography suffers from the fact that the acquisition of the fetal ECG cannot be guaranteed. Piéri et al. [2001] found an average success rate of about 60 percent during the last trimester of gestation and of about 30 percent around weeks 28 until 34. The success rate was defined as the percentage of the total recording time in which a reliable fetal heart rate could be obtained. Apart from the low overall success rate, large individual differences in success rate were found between recordings. Since the fetal heart traces are difficult to spot within the background noise of a fetal ECG recording, the analysis of these traces is customarily limited to the determination of the beat-to-beat fetal heart rate.

Currently, ultrasound is the most common technique used to study the fetal heart. Ultrasound became popular in the 1980s. It is the predominantly used technique for fetal surveillance. At present, the realm of ultrasound consists of a wide variety of techniques and devices ranging from a Doppler-ultrasound device for obtaining a cardiotocogram (CTG), displaying the fetal heart rate, to ultrasound imaging devices with color-Doppler imaging possibilities and options to reconstruct three-dimensional images. The latter reconstruct an image of the anatomy of the fetus within the womb and map movements of, for instance, blood flow on top of this image. In the "M-mode ultrasound scan", a two-dimensional image is created in which the structure along a line is depicted as a function of time. Hence, this mode is often used to study cardiac arrhythmia. A skilled operator is needed to detect arrhythmias using M-mode. Another way of studying fetal movements is using Doppler-ultrasound. In this technique, Doppler shifts are recorded in the reflected ultrasonic waves. These shifts occur when particles, such as blood cells, or structures, such as the heart wall, move towards or away from the transducer. This allows for monitoring the fetal heart as well as the detection of fetal arrhythmias. This technique is applied in two kinds of devices, one built for the sole purpose of obtaining the fetal heart rate lacking any imaging capabilities and another with imaging capabilities. The signal processing techniques to resolve the Doppler shifts are known to produce erroneous fetal heart rate data in some cases, like doubling or halving the fetal heart rate or making educated guesses during those short intervals in which noise inhibits the fetal heart rate detection [Dawes et al., 1990]. Problems can occur especially during episodes of high fetal heart rate variability. Furthermore, due to the signal-processing strategies employed, the beat-to-beat variability may not be observed at all.

2.2. Fetal Magnetocardiograms of Healthy Fetuses

Fetal MCGs can be reliably recorded from the beginning of the second trimester of pregnancy until term. A typical measured fetal MCG is displayed in Fig. 5 in which the definition of the various time intervals is indicated. The duration of a heart cycle is defined by the RR-interval and can be obtained from fetal MCGs with an accuracy of a few ms. The fetal heart rate is the inverse of the RR-interval.

Fetal MCG offers a precise method to study the heart rate variability, which is considered an important indicator for fetal well being [Cooley et al., 1998]. Van Leeuwen at al. [1999[a]] computed various parameters such as the standard deviation, the root mean square of successive differences, and the approximate entropy. High correlations were obtained between these values and gestational age that may provide an indication of changes in parasympathetic influence as the autonomic nervous system develops. The root mean square of successive differences shows a trend to lower values in growthretarded fetuses [Lange et al., 2002].

Traditionally, three frequency bands have been described in the heart rate power spectrum: a high-frequency band ($f > 0.2$ Hz), a low-frequency band ($0.05 < f < 0.2$ Hz and very-low-frequency band ($f < 0.05$ Hz). The signal in the high-frequency band corresponds to the respiratory rate and is mediated by the parasympathetic system. The signal in the band around 0.1 Hz is mediated by both the sympathetic and parasympathetic system. The signal in the very-low–frequency band ($f < 0.05$ Hz) can be influenced by a wide variety of factors. Zhuravlev et al. [2002] identified the three frequency components in the heart rate power spectrum obtained from fetal MCGs and extracted them using appropriate digital filtering. Comparing the integrated amplitude of the high-frequency curve within a moving 4-second time window with that of the lowfrequency curve showed a high degree of correlation for extended periods of time, although it depended on the fetal behavioral state. In addition, time delays of one to three seconds were observed. These time delays decreased as a function of gestational age. We may conclude that the heart rate power spectrum is a useful tool to study the balance between the sympathetic and parasympathetic division of the autonomic nervous system.

In order to discriminate between pathological and healthy fetuses, reference values of the parameters describing the cardiac waveforms were obtained from different centers involved in fetal MCG measurements [Stinstra et al., 2002]. The MCGs were recorded in uncomplicated pregnancies, i.e. no maternal or fetal complications were noticeable. The parameters collected include the duration of the P-wave, the PR-interval, the PQ-interval, the QRS-complex, the QT-interval and the T-wave. The P-wave and the QRS-complex can be easily identified in averaged fetal MCGs, whereas the detection of the T-wave is difficult. The beginning of the T-wave is often hardly definable, as its amplitude may be very small. The QT-interval is dependent on the fetal heart rate. Hence, QT_c is introduced defined as $QT_c = \text{QT-interval} \times (\text{RR-interval})^{-1/2}$. Scatter plots of the duration of the various intracardiac time intervals versus the gestational week are shown in Fig. 6.

Superimposed are the linear regression lines and the bounds marking the 90%-, 95%- and 98% prediction interval. The prediction interval can be used to define normal parameter values and abnormal parameter values. It can be seen that the duration of the T-wave and QT-interval have a wide spread, which can be explained by the difficulties in determining the onset and termination of the T-wave due to its poor visibility in the fetal MCGs. The duration

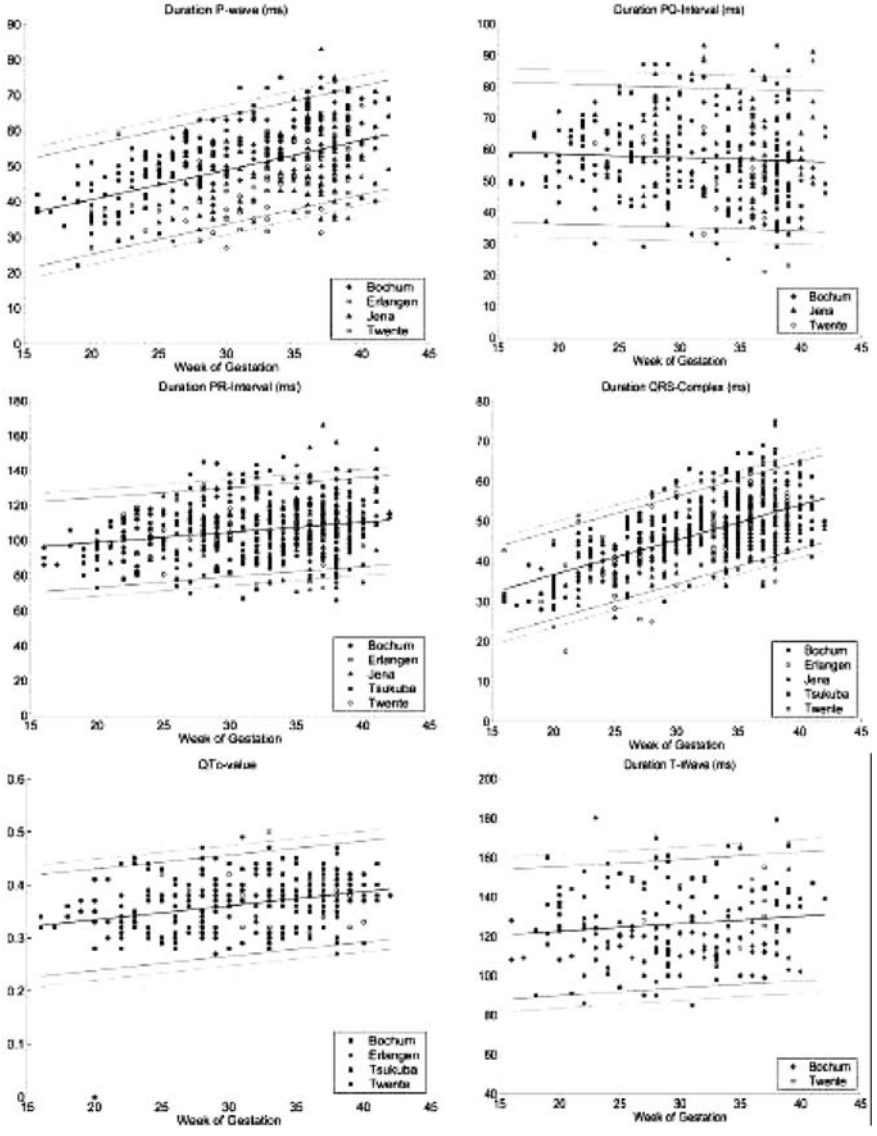

Figure 6. The duration of various cardiac time intervals against the week of gestation. The gray lines mark the 90%, 95%, and 98% prediction interval.

of the QRS-complex, the P-wave, and the PR-interval increases linearly with gestational age, as is the case during normal development after birth. Although the duration of the QT-interval increases slightly with fetal age, QT_c is not dependent on the fetal age.

Fetal MCG is not the only method for obtaining the intracardiac time intervals. Time intervals between atrial and ventricular contractions can be measured by Doppler techniques. Andelfinger et al. [2001] measured the Doppler AV time intervals in 264 fetuses with a

Table 1. Comparison between the Means of the Intracardiac Time Intervals Obtained from Fetal MCGs During the 38th Week Until the 41st Week of Gestation and Postnatal ECG

	Fetal MCG			Postnatal ECG*			Postnatal ECG**		
	mean	s. dev.	n	mean	s. dev.	n	mean	s. dev.	N
P-wave	56	10	84				59	10	126
PR-interval	109	16	110	113	13	13442	108	15	126
PQ-interval	57	16	73				49	12	126
QRS-complex	52	8	113	57	7	13442	62	9	126
QT-interval	243	27	100	274	28	13442	284	50	126
QTc	0.37	0.04	46	0.400	0.002	13442			
T-wave	131	20	21						

*Schwartz et al., 1998.
**DePasquale and Burch, 1963.

structurally normal heart. This time interval is on average 35 ms longer than PR-intervals due to the incorporation of the electromechanical delay and isovolumetric contraction time in the Doppler measurements. Their results for the AV time interval and confidence limits correspond with the MCG-based PR-intervals. So we may conclude that the observed wide spread in both types of measurements can be ascribed for a large part to physiological variations, such as the weight of the fetus or dimensions of the heart. In addition, ECGs of prematurely born children may provide values for comparison. In this case, the question remains whether these children can be considered healthy. Another source of values of the durations of the intracardiac time intervals are the ECGs obtained during labor and shortly after birth. During labor, the fetus experiences a lot of stress and may be for instance anemic: this may alter the durations of the various intracardiac time intervals. Schwartz et al. [1998] measured the postnatal ECG in the third or fourth day after birth, because they observed that the ECG is stable in this period.

In Table 1, a comparison is made between the intervals in the last weeks of gestation (week 38–41) obtained from fetal MCG and from postnatal ECG. Comparison of these results shows that they agree within one standard deviation, although the blood flow through the heart has altered from a system, where the pulmonary system is mainly bypassed and an additional pathway exists between both atria, to a normal double looped system.

As the fetal MCG data were gathered at different centers, the magnetometer systems varied considerably, from multi-channel magnetometer systems to a one -channel vectorgradiometer system. A multi-channel system usually measures the magnetic field component perpendicular to the maternal abdomen at several positions over the maternal abdomen, simultaneously. A one-channel vectorgradiometer measures all three components of the magnetic field at one position over the maternal abdomen. The drawback of the systems that cover only a small part of the abdomen is that the measurement position might not be ideal, resulting in a poor signal-to-noise ratio. In order to cope with this drawback, the system is repositioned to look for the optimal measuring position, which is in general the position where a prominent QRS-complex is seen in the time trace. In other words, this is not necessarily a position with a high signal to-noise ratio for the P-wave or T-wave. A question that arises when using a multichannel system is which channel to use for the determination of the various intracardiac time intervals. The duration of the P-wave may

differ for different channels. The more channels are included in the determination of the duration of the P-wave, the longer the P-wave interval [van Leeuwen et al., 2001[a]]. One way to reduce this problem is taking into account all the channels available and not relying on only one channel for the determination of the duration of the various waves.

Cardiac time intervals have also been studied in twins and growth retarded fetuses.The results show that fetal development is reflected in the duration of the P-wave and the QRS-complex [van Leeuwen and Schüszler, 2000; van Leeuwen et al., 2001[b]; Costa Monteiro et al., 2001].

3. CLINICAL IMPLICATIONS

For a reliable evaluation and full clinical acceptance of fetal magnetocardiography, a large number of patients' investigations is required. In order to get reliable data that can be compared and pooled between different groups an international standard protocol has been proposed [Grimm et al., 2002]. This protocol provides, for instance, guidelines for signal processing.

3.1. Detection and Classification of Arrhythmias

The fetal heart rate is considered normal when it is between 100 and 160 beats per minute. The rhythm is considered a bradycardi a when the fetal heart rate falls below 100 beats per minute and a tachycardia when it is higher than 160 beats per minute. Tachycardia are considered mild when the baseline rate is between 160 and 180 beats per minute and severe when it exceeds 180 beats per minute. Depending on the origin, tachycardia are divided into supraventricular and ventricular tachycardia. Ventricular tachycardia are rarely observed in the fetus, whereas supraventricular tachycardia are more common. About two-thirds of the fetal arrhythmias are found in the last trimester of pregnancy. Strasburger [2000] estimates the incidence of malignant arrhythmias to be one in 5000 pregnancies. As arrhythmias come in different forms, from innocent to life threatening, classification of arrhythmias may help to determine which drugs to use to restore the heart rate to normal sinus rhythm. Choosing a therapy appropriate to the arrhythmia reduces the chance of causing accelerations of the fetal heart rate or the chance of degeneration to a life-threatening arrhythmia. For this reason, it is important to know the origin and mechanism of a tachycardia. In case it is supraventricular, one may for example choose the drug digoxin to treat the arrhythmia. However, in case of a ventricular origin, this ther apy could potentially exacerbate the arrhythmia [Clark and Case, 1990].

In about half of 155 fetal magnetocardiography recordings arrhythmias were observed [van Leeuwen, 1999[a]]. These arrhythmias included supraventricular and ventricular ectopic beats as well as bradycardia and tachycardia. The most common fetal arrhythmia is an irregular rhythm due to isolated extrasystoles, in particular premature atrial contractions. Premature beats are beats that occur earlier than expected and briefly interrupt the normal sinus rhythm. These arrhythmias rarely cause hemodynamic problems and often disappear before term or within a few days after birth. However about one percent of the fetuses having premature atrial contractions, have a concomitant structural heart disease as well and about 0.5 percent are found to develop a reentrant tachycardia later on in the pregnancy.

Fetal MCG provides a reliable method to classify an atrioventricular (AV) block, a bradycardia due to a conduction delay or block at or near the AV node. Three types of AV-blocks can be distinguished; the first-degree AV-block refers to a slow conduction of the depolarization front through the AV-node. In a second-degree AV-block only one out of several depolarization fronts is conducted through the AV-node, thence the ventricles are stimulated only once for several atrial beats. A complete or third-degree AV-block refers to a condition of the heart, in which the depolarization front is not conducted through the AV-node and as a consequence the ventricles are not activated by the electrical impulse traveling down the atria. The heart compensates for this loss by triggering the depolarization of the ventricles using an independent pacemaker in the ventricles. Hence, this condition reveals itself by an independent pace of the atrial and ventricular contraction. Copel et al. [1995] found in one patient a progression from a second-degree AV-block into a complete AV-block. However, in two other cases they observed an improvement from a second-degree AV-block into normal sinus rhythm and an improvement from a third-degree AV-block to a second-degree AV-block. In both cases, the mothers were treated with 4 mg of dexamethasone in order to stop the inflammatory process in the fetal heart. Hence, a second-degree AV-block may still be reversed to normal sinus. Especially, those children showing a slow ventricular rate (50 beats per minute or less) are at risk and often require the implantation of a pacemaker shortly after birth. A congenital complete (AV) block is manifest in one of 20,000 live births, but probably twice as much in utero. Currently, the prenatal detection of a complete AV-block is obtained from ultrasound images. As the mechanical contraction of the heart can be monitored on a modern ultrasound machine, a complete AV-block shows up as a desynchronized contraction of the atria and ventricles. However, the detection of a fetal AV-block by means of ultrasound is difficult, especially the classification of the type of block. Therefore, fetal magnetocardiography provides an alternative to detect this condition, as it directly relates to the electrical phenomena taking place in the heart [Wakai et al., 2000[a]; Menéndez et al., 2001; Hosono et al., 2001; Quartero et al., 2002; Zhao et al., 2002]. An example of the measurement of a seconddegree AV-block that changes into a complete one is shown in Fig. 7.

Atrial flutter, a potentially lethal arrhythmia, is a supraventricular tachycardia constituting one to two percent of all fetal arrhythmias. It may occur in normal individuals; however, there is usually an underlying heart disease. The ventricular rhythm is most often regular and not as fast as the atrial rate with a varying degree of AV-block, usually 2:1. The ventricular rate is usually above 200 beats per minute. Postnatal, an electrocardiogram of an infant with atrial flutter shows typical waves with a saw toothlike pattern. Prenatal, an echocardiographic diagnosis of atrial flutter is usually based on an atrial contraction rate in the range of 300 to 500 beats per minute. This atrial rate is determined using M-mode echocardiography, while the ventricular rate is determined with the use of M-mode and echo Doppler. Recently, Oudijk et al. [2000] found a conversion rate of 80 percent for atrial flutter with sotalol and this may become the in utero treatment. Fetal MCG recordings can be used for the diagnosis of fetal atrial flutter [Ménendez et al., 2001; Quartero et al., 2002]. A fetal MCG of a fetus in the 36th week of gestation with atrial flutter is given in Fig. 8A. The MCG shown is averaged during an episode of tachycardia. It shows the typical saw-tooth pattern that is expected for atrial flutter. The diagnosis of 2:1 atrial flutter was made by means of M-mode ultrasound that showed an atrial rate of abo ut 400 and a ventricular rate of about 200 beats per minute. However, with M-mode ultrasound it is difficult to distinguish

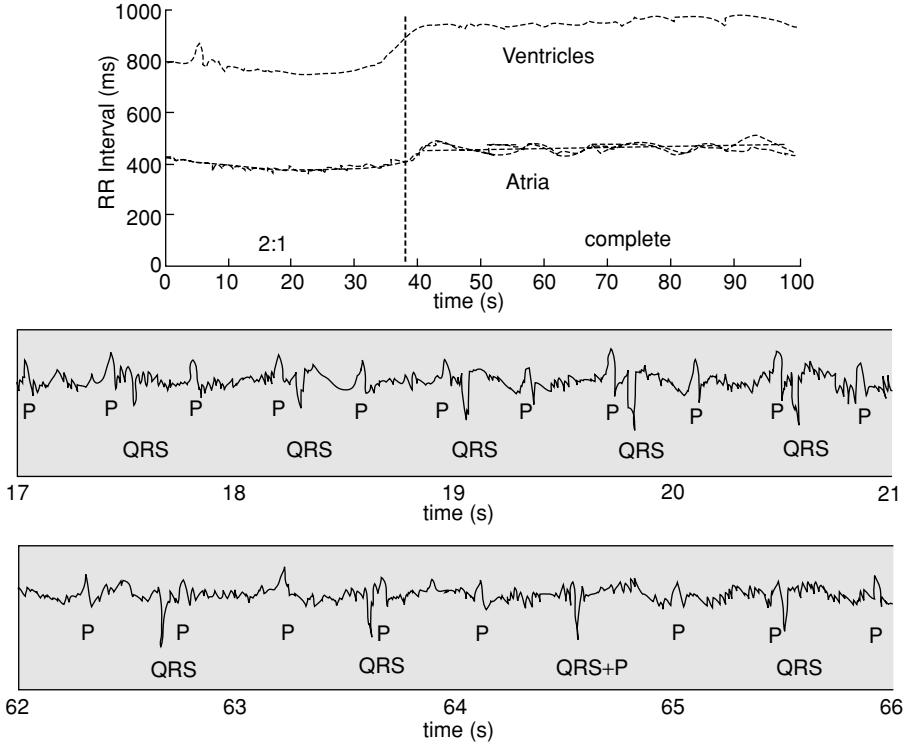

Figure 7. Fetal heart rate and time traces of a 35-week old fetus showing the progression of a second degree AV-block (second trace) into a complete AV-block (third trace).

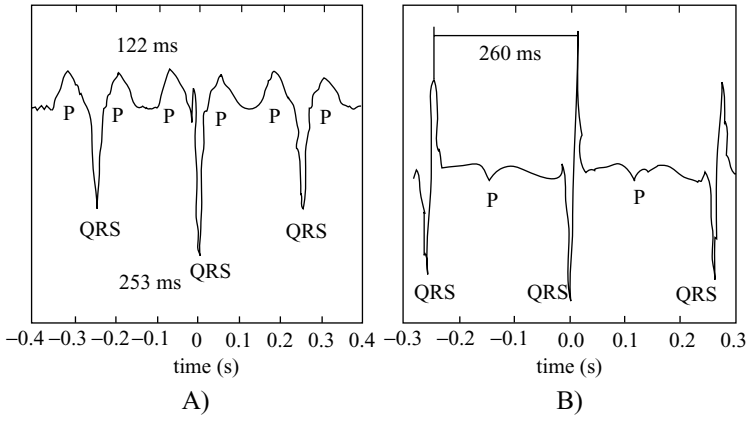

Figure 8. A) Averaged fetal MCG of a fetus in the 36th week of gestation with atrial flutter. B). Averaged fetal MCG of a fetus in the 30th week of gestation with PJRT.

between atrial flutter and persistent junctional reciprocating tachycardia (PJRT), an uncommon tachycardia, occurring in one percent of patients with supraventricular tachycardia. It is resistant to conventional antiarrhythmic therapy. In Fig. 8B, an averaged fetal MCG is shown of a fetus in the 30th week of gestation with PJRT. With M-mode ultrasound, it was found that the atrial rate was about 400 beats per minute and a diagnosis of 2:1 atrial flutter was made. The fetal MCG does not show the typical saw-tooth pattern and led to the diagnosis of PJRT. A proper diagnosis is important as it can help to decide if the administration of cardiac medicine is necessary. Intra-uterine pharmacological treatment exposes the mother to potential side effects.

3.2. The Long QT-Syndrome

The long QT-syndrome is an abnormality in the myocardiac cell membrane, which changes the electrical system of the heart. The syndrome may be inherited. Already six genes have been identified which cause long QT-syndrome. It appears to be a cause of sudden infant death syndrome (SIDS). The frequency of long QT-syndrome in the USA is approximated at one in 7000 children, and accounts for 3000–4000 childhood sudden deaths annually [Berul, 2000]. Schwartz et al. [1998] recorded 34,442 ECGs of newborns and analyzed the QT_c-values. The 97.5th percentile for the QT_c among the infants was 440. The data obtained from fetal MCG given in Fig. 6 are in agreement with these findings. Consequently, they considered a QT_c longer than 440 to be prolonged. During one year of follow-up, they found that 12 of the 24 infants who died suddenly had long QT-syndrome. A prenatal diagnosis of this syndrome can be obtained from fetal MCG [Hamada et al., 1999; Menéndez, 2000; Hosono et al., 2002]. An example of a fetal MCG measured at the University of Twente showing a QT prolongation in a fetus is given in Fig. 9. The value of QT_c is 490.

3.3. Congenital Heart Defects

Routine fetal ultrasonic examinations carried out in Europe in 709.030 pregnant women showed congenital heart defects in 8126 cases (the study period was from July 1996 to

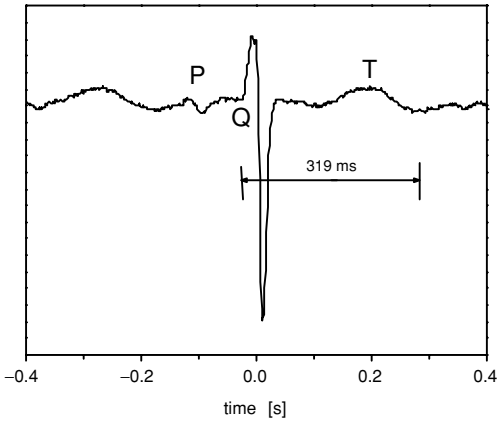

Figure 9. Averaged fetal MCG of a fetus in the 37th week of gestation with prolonged QT syndrome.

December 1998). The detection rate in countries where three ultrasound examinations were performed was 56 % [Stoll et al., 2001]. As many cases of fetal cardiac disease remain unrecognized, fetal MCG may be of help in the early intra-uterine detection of congenital heart anomalies and the progress of the disease [Wakai et al., 2000[b], Kähler et al., 2001, Quartero et al., 2002]. This may be of importance, as more knowledge allows a better planning of pregnancy, a better choice of the modality of delivery and an indication of the optimal therapy. The possibilities to diagnose congenital heart defects by means of fetal MCG is illustrated with the following case:

The patient, a 29-year-old woman in her third pregnancy was referred for nuchal translucency screening. Obvious edema was visible on the first ultrasound. Detailed evaluation in the 17^{th} and 20^{th} week of pregnancy showed a cleft lip and a cleft palate, a right dysplastic kidney and an underdevelopment of the left side of the heart. Aorta and pulmonary artery both originated from the right ventricle (double outlet right ventricle). Chorionic villus sampling showed a normal male karyotype (46 XY). The prenatal diagnosis was a fetus with multiple congenital anomalies without apparent syndromal diagnosis. Fetal MCG was performed in the 33^{rd} week of pregnancy. The averaged fetal signal showed a broad QRS-complex of about 70 ms. Compared to uncomplicated pregnancies the QRS-interval is larger than the 99 percentile, thus abnormal. After 38 weeks of pregnancy a boy was born. The prenatal diagnosis of functional monoventricle with a left hypoplastic ventricle, a ventricular septal defect, transposition of the great arteries and abnormal localized pulmonary veins was confirmed by means of cardiac ultrasound.

4. THE FETAL MAGNETOCARDIOGRAPH

4.1. The Sensor

The amplitude of the R-peak in the fetal MCG is about 10^3 fT. The amplitude of the P-wave in healthy fetuses is about a factor ten smaller. For the diagnosis of certain arrhythmias, it is important to recognize the P-wave in the raw data. Therefore, the required sensitivity of a fetal magnetocardiograph is about 100 fT or less. The only instruments that are sensitive enough are magnetometer systems that use as a sensor a SQUID (an acronym for Superconductive QUantum Interference Device). The sensitivity of a SQUID is determined by its intrinsic noise. Since the SQUID noise increases as the square root of the bandwidth, it is expressed in fT/$\sqrt{}$Hz. A typical noise figure is 10 fT/$\sqrt{}$Hz, so that in a 100 Hz bandwidth the SQUID can measure the magnetic field down to 100 fT. The SQUID has to be superconducting and therefore it has to be cooled to about 4 K (-269 °C). For this reason, it is immersed in boiling helium. The liquid helium is contained in a vessel, the so-called cryostat that is held near the maternal abdomen. SQUIDs made of materials that are superconductive when cooled by liquid nitrogen (boiling temperature 77 K), so-called high-T_c SQUIDs, have a higher noise level. Therefore, SQUIDs that have to be cooled by liquid helium are preferable; moreover, the techniques to fabricate high-T_c SQUIDs are still unreliable.

One of the properties of a superconductor is that the resistance to electric currents is zero. Another property of superconductivity is that in a ring the magnetic flux is conserved. Hence, if a flux is applied to a superconducting ring then currents will be induced that cancel the applied flux. A SQUID consists of a small (about 10^{-2} mm^2), thin, superconducting

ring. Often the SQUID ring is made of a thin film of niobium that is superconductive below 9.2 K. This ring is interrupted by one or two non-superconducting barriers, for instance, oxide layers of some nanometers. From quantum-mechanical theory, it follows that a small current can tunnel resistanceless through such a barrier. Whenever the current exceeds the amount of current that can pass through a barrier without any resistance, a potential difference arises across the barrier. When the magnetic flux in the ring is changed, a circulating current is induced in the SQUID. As the potential difference across a barrier depends on the current, it also depends on the change in magnetic flux and the relationship between these two quantities is used to determine a change in the applied magnetic flux. Because this relationship is non-linear, a feedback system is applied in which the change in flux is cancelled by an opposite change in flux that is fed into the SQUID. In this way, the system is used as zero-detector.

Strictly speaking, the SQUID is a sensor for a change in the magnetic flux, the latter being the magnetic field component perpendicular to the SQUID ring integrated over the area of the ring. A bare SQUID is fairly insensitive to magnetic fields, because in general the area of the SQUID loop is very small. Therefore, a superconducting input circuit is necessary. This consists of a pick-up coil, sensing the magnetic field, and an input coil that is closely coupled to the SQUID. A magnetic field has a strength and an orientation and can be represented by a vector. The Earth's field at the surface of the earth is about 5×10^{-5} T. Starting with our sensing coil in the direction of the Earth's magnetic field and then turning over an angle of 10^{-8} radians gives rise to a change of field of $5 \times 10^{-5} \times 10^{-8} = 5 \times 10^{-13}$ T. This change in field is of the order of the fetal MCG and should be avoided. However, it is impossible to avoid vibrations over 10^{-8} radian, therefore, a pickup coil is used that forms a gradiometer. A first-order gradiometer is insensitive to uniform magnetic field changes such as those due to vibrations in the Earth's magnetic field, as will be discussed in section 5.2. Usually, the measurements take place in a magnetically shielded room and the recorded signals are fed to a computer system located outside the shielded room. The measurement setup is pictured in Fig. 10.

4.2. Electronic Circuit

A SQUID can be considered as a flux-to-voltage transducer with a sine-like flux-voltage characteristic. The flux is expressed in flux quanta; one flux quantum is $\Phi_0 = 2.07 \times 10^{-15}$ Wb. An example of the flux-voltage characteristic is given in Fig. 11A. In order to linearize the relationship between the measured voltage and the applied magnetic flux, a zero-detector is commonly used (a so-called flux-locked loop). In Fig. 11B, a simplified scheme of a flux-locked loop is depicted. A change of flux in the SQUID ring causes a change in the output voltage that is amplified, filtered and converted into a flux in the feedback circuit consisting of a resistor and inductance. The feedback flux compensates the applied change of flux, ke eping the total flux in the SQUID ring constant. Therefore, the voltage across the feedback circuit is proportional to the applied change of magnetic flux. The point in the flux-voltage characteristic that is chosen as the point where the flux is kept constant is called the working point.

If the flux transformer is not connected, the output noise ($S_\Phi{}^{1/2}$) is defined by the noise of the SQUID ($S_{\Phi,\mathrm{SQUID}}{}^{1/2}$) and that of the first-stage amplifier ($S_{\mathrm{V,AMPL}}{}^{1/2}$). The two noise

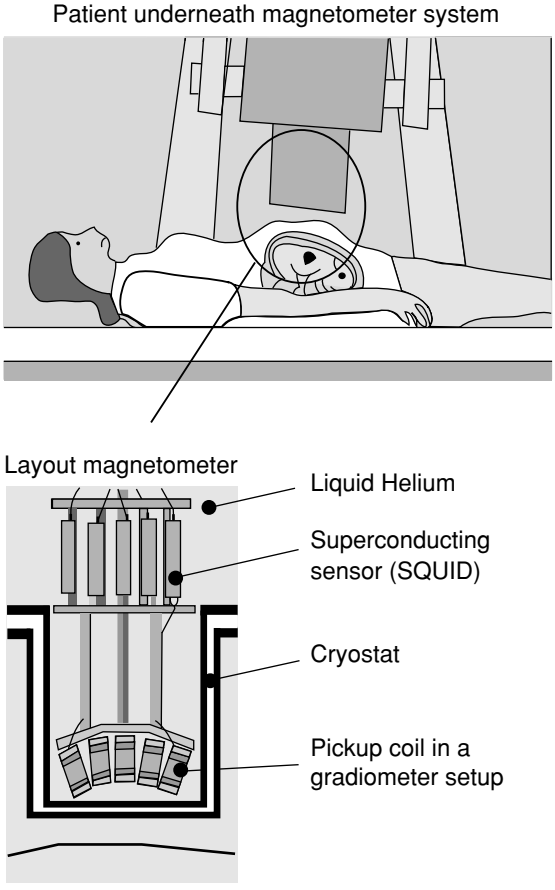

Figure 10. The measurement setup.

contributions can be expressed in terms of flux noise (i.e. the equivalent magnetic flux in the SQUID ring) using the following expression

$$S_{\Phi}^{1/2} = \sqrt{S_{\Phi,\mathrm{SQUID}} + \frac{1}{{V_{\Phi}}^2} S_{\mathrm{V,AMPL}}} \tag{1}$$

where $V_{\hat{\Phi}}$ is the derivative at the working point of the flux-voltage characteristic. The smaller the derivative is, the larger the influence of the noise of the amplifier. Typically, the noise level (in its flat part) of a room-temperature amplifier is about 0.8–1 nV/$\sqrt{\mathrm{Hz}}$ (AD797 for example). A typical value of $V_{\hat{\Phi}}$ (for a DC SQUID) is about 100 μV/Φ_0. Combining these values yields an equivalent flux noise of the amplifier of about 10 $\mu\Phi_0/\sqrt{\mathrm{Hz}}$, being close to the typical noise level of a DC SQUID (in its flat part). In other words, the noise of an amplifier at room temperature and that of a DC-SQUID are of the same order. In order to decrease the influence of the noise of the room-temperature amplifier, several modifications

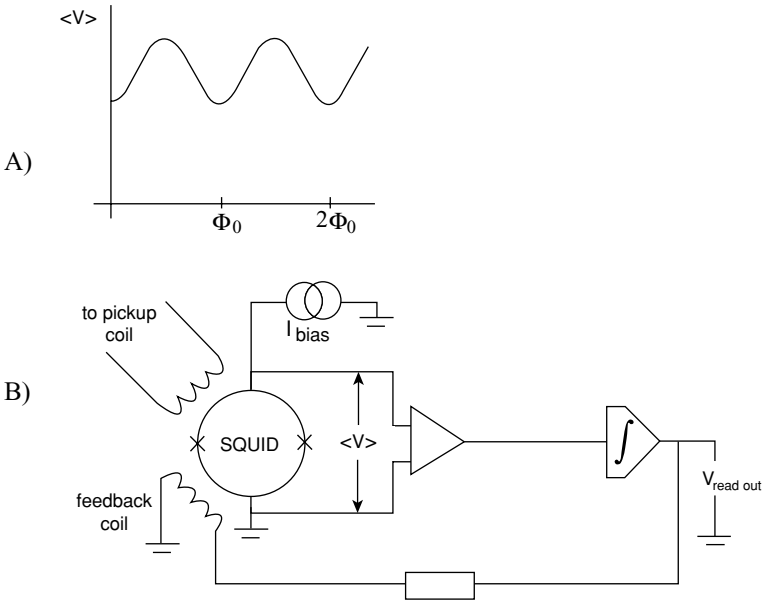

Figure 11. A) Typical flux – voltage transfer of a DC SQUID. B) Simplified scheme of a flux locked loop.

of the "basic" scheme of Fig. 11 can be used. Three of these modifications are:

1) Cooling the resonant transformer stage. This results in an amplification of the output voltage of the SQUID by about a factor of ten; thus increasing $V_{\hat{O}}$ in Eq. (1) by the same factor. To do so, the flux in the SQUID ring is modulated via a feedback circuit by a frequency in the range of 100−500 kHz. Apart from increasing $V_{\hat{O}}$, this modification provides another advantage. By means of the modulation, the spectral content of the signal shifts towards higher frequencies, thus escaping from the low-1/f noise of the preamplifier.
2) Using an additional positive feedback. The introduction of a positive feedback makes the flux-voltage characteristic asymmetric, i.e. the first slope of the flux voltage characteristic is increased while the second one is decreased.
3) Using SQUIDs that have a higher flux-to-voltage coefficient such as a DROS (1−3 mV/Φ_0), or using an extra SQUID as a cooled cryogenic preamplifier [Podt e t al., 1999].

In biomagnetic applications, the output voltage of the flux-locked loop is digitized and processed further by a computer. When operated in an unshielded environment, the measurement system is subjected to large magnetic disturbances, which require a relatively large dynamic range. The required dynamic range evaluated for power-line interference is equivalent to 21–22 bits precision. In order to achieve this dynamic range, a digital flux-locked loop is used in which the amplified output voltage of the SQUID is digitized instead of the output voltage of the flux-locked loop. The loop is closed digitally in a point of the flux-voltage characteristic where $V_{\hat{O}}$ is maximal. The digital flux-locked loop maintains its

locking while the change of flux at the working point is in the range $\pm\Phi_0$. As soon as the change of flux is out of this range, the electronics releases the locking and allows the working point to slip towards the adjacent zero crossing, which is one period away in the flux-to-voltage characteristic. The digital flux-locked loop counts all events of relocking and adds or subtracts (depending on the direction of the slipping of the working point) one flux quantum. The digital flux-locked loop provides a dynamic range of 32 bits with a linear ity of 10^{-7}.

5. NOISE SUPPRESSION TECHNIQUES

Three main sources of disturbances can be distinguished: the environment, the subject under study, and the measurement system.

1) The environmental noise is a combination of natural and man-made magnetic disturbances. For instance, vibrations of the measurement system within the Earth's magnetic field lead to disturbances. Moreover, the Earth's magnetic field varies in time due to, for instance, solar winds. Buildings distort the Earth's magnetic field, giving rise to gradients of about 2×10^8 fT/m. To supply power to electrical equipment, energy is transported via the cables generating noise with the power-line frequency. Typically, this has a level of $10^7 - 10^8$ fT. Besides noise at the power-line frequency, noise at frequencies that are harmonics of 50 or 60 Hz is frequently present. In addition, there are more periodic disturbances to consider, for instance, those from computer monitors, motors, vacuum pumps, ventilation systems or traffic. To appreciate the magnitude of environmental disturbances relative to the fetal MCG, see Fig. 2.
2) When measuring a fetal MCG, metallic objects worn by the mother give rise to disturbances. For instance, a watch generates a magnetic field of the order of 10^{-9} T. Also a hook o f a bra that moves due to breathing may lead to a magnetic field contribution. These disturbances are best dealt with by removing all metallic objects. Another disturbance is the magnetic field generated by the heart of the mother. Although the pick-up coil is closer to the heart of the fetus, the magnetic signal of the maternal heart is that much larger that it still is clearly visible in the fetal MCG traces measured over the maternal abdomen.
3) As mentioned before, the performance of a SQUID is limited by its intrinsic noise. In addition, the thermal shield used in the cryostat in order to keep the evaporation of helium low, the wires used in the electronics, and the metal used to shield the SQUID from rf-shielding give rise to eddy currents and thermal noise.

5.1. Flux Transformers

In order to couple the magnetic flux present above the maternal abdomen into the SQUID a flux transformer is used. A flux transformer consists of a pick-up coil and an input coil and is made of superconducting wire. Since the flux transformer forms a closed superconducting loop, each change in the applied magnetic flux induces a superconducting current that keeps the total flux in the flux transformer constant. In other words, a magnetic flux applied to the flux transformer will be compensated by a superconducting current, which

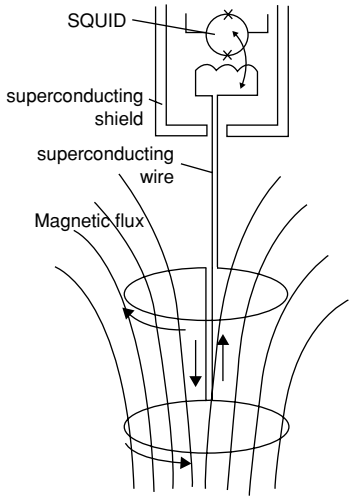

Figure 12. An example of a flux transformer, a first-order gradiometer.

generates a counterbalancing flux. The superconducting current is linear proportional to the applied magnetic flux. The input coil is a small coil that is positioned on top of the SQUID. The superconducting current in this coil generates a magnetic flux, which in turn is linear proportional to the superconducting current. This magnetic flux, being linearly proportional to the applied magnetic flux, is inductively coupled into the SQUID.

The configuration given in Fig. 12 is a first-order gradiometer. The pick-up coil consists of two coils at a certain distance wound in opposite directions. In case this gradiometer is exposed to a uniform magnetic field, the net flux coupled into both coils of the flux transformer is zero. Hence, the flux transformer is sensitive to sources close to the pick-up coil and insensitive to sources far away, as these will render almost uniform magnetic fields. In other words, gradiometers attenuate environmental noise generated by sour ces that are far from the pick-up coil. First-order gradiometers have been used in a large majority of SQUID magnetometers produced to date. For better rejection of environmental noise in order to perform measurements in an unshielded environment, a second-or third-order gradiometer is necessary [Vrba, 1996].

5.2. Shielded Rooms

Usually, a magnetically shielded room is made of one or more layers of material with a high electrical conductivity, such as pure aluminum, and one or more highpermeability magnetic layers, such as nickel-iron alloys. The aluminum layers are used to shield against the higher frequencies by means of eddy currents induced in these layers and the nickel-iron layers are used to shield against low-frequency magnetic fields. The latter layers have such a high magnetic permeability that the magnetic field lines prefer to flow through these layers instead of through the interior of the magnetically shielded room. The shielding performance depends on the construction of the room and on the number and thicknesses of

the various layers. The shielded room in Berlin is the best shielding room in the world with a shielding factor of about 80.000 at 0.010 Hz. Commonly, rooms are used with a shielding factor of about 70 at 0.1 Hz and of about 1000 at 100 Hz.

6. SIGNAL PROCESSING

A signal-processing procedure should be able to remove the noise present in a measured fetal MCG. Signal processing tools are also advisable for the automatic extraction of characteristic features from the fetal MCG, including the onset and offset of the P-wave, QRS-complex, and T-wave, amplitude of these waves, spectral plots and heart rate variability measures. An online processing system that can identify various arrhythmias would also be useful. A significant number of algorithms used for fetal MCG extraction are based on techniques developed for fetal ECG. Fetal ECGs and fetal MCGs have the same features, although the signal-to-noise ratio in the ECGs is usually much lower than in the MCGs. Presumably, signal processing techniques that are good for fetal ECG are good enough for fetal MCG. However, these techniques have to be used for the tasks for which they are designed. For instance, a non-linear technique based on state-space projection can be used to increase the accuracy of heart rate detection from fetal ECG [Richter et al., 1998]. Application of state-space projection to fetal MCG has shown that indeed the R-peaks are extracted very accurately. However, the effectiveness of this nonlinear filtering is limited; increasing the dimension leads to a loss of information about the P-and T-waves [Stinstra, 2001].

As most of the signal energy of the fetal MCG is concentrated in the bandwidth 2–120 Hz, the signal-processing scheme may start by filtering the signal by means of a band-pass filter in the range from 2 to 120 Hz. When the signals are obtained in a magnetically shielded room, the contribution of power-line interference is small and a special filter is not required to remove power-line interference. Only when a clear powerline frequency contribution is visible in the signal, a notch filter for this frequency should be used. Noise sources affecting the fetal MCG include the maternal MCG, low-frequency baseline wandering due to breathing, fetal movement and noise from the magnetometer system. Especially, in the early weeks of gestation the fetus is able to move freely within the uterus, thereby limiting the number of complexes that can be used in the averaging procedure. To suppress or eliminate the maternal influence in the fetal signal it turns out to be advantageous to measure the maternal ECG simultaneously with the fetal MCG.

Not all noise results from the body; the magnetometer system also produces noise. This noise consists of thermal noise of the cryostat and noise of the SQUID-system. The latter noise stems from the SQUID as well as from the amplifiers and other electronic components in the SQUID read-out electronics. Before the digital signal is obtained for analysis, the signal is already processed to a certain extent. The signal from the magnetometer system is amplified and an analog high-pass filter (RC network) with a cut-off frequency of about 0.01 Hz followed by an anti-aliasing filter is applied to the amplified signal.

As each research team involved in fetal magnetocardiography has a different measuring system at their disposal that is located in different surroundings, the optimal signal processing will be different too. In the next section, some signal-processing procedures will

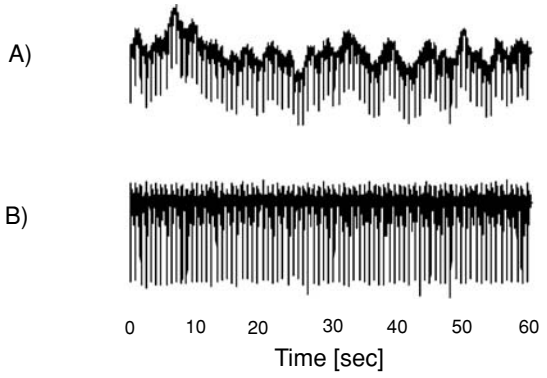

Figure 13. An example of the filtering procedure. A) The raw signal. B) The filtered signal.

be discussed that have proved to be adequate for measurements carried out inside a shielded room.

6.1. Filtering

The first step of the signal-processing procedure is the suppression of the baseline wandering. This may be performed by applying the following two band-pass filters. First, a pre-detection finite impulse response (FIR) filter with 50 coefficients and a bandwidth of 10–40 Hz is applied to the fetal MCG signal. This range is chosen because it excludes the power-line frequency of 50 Hz as well as the bandwidth in which the fetal cardiac complex has most of its signal energy. When the power-line frequency is 60 Hz, the bandwidth is of course chosen somewhat differently. The second filter is applied to the measured signal before the actual averaging procedure takes place. This pre-averaging filter consists of a high-pass filter and a low-pass filter, which together form a band-pass filter with bandwidth from 2 to 120 Hz. The low-pass filter is a FIR filter with 25 coefficients and cut-off frequency 120 Hz. Sinc e a high-pass filter requires many coefficients, the signal is resampled. It is then passed through a low-pass filter of 2 Hz, after which the baseline wandering remains. This signal is interpolated to the original sample frequency of 1 kHz and subsequently subtracted from the original signal. The manipulation with the sampling rate reduces the computational burden. Alternatively, a high-pass Butterworth filter with a cut-off frequency of 2 Hz is implemented for baseline correction. A result of this procedure is shown in Fig. 13.

Power-line interference may be tackled with FIR or IIR (infinite impulse response) notch filters. An alternative procedure is the following: First, the PQRST-complexes are removed from the signal by means of averaging and the resultant signal is passed through a band-pass filter with cut-offs at 40 and 60 Hz. The spectral content is estimated using FFT. The signal is then divided into 2-second segments and the phase and amplitude of the 50-Hz component is determined. The phase and amplitude information is used to reconstruct the 50-Hz interference, which is then subtracted from the measurement. This filter does not affect the amplitudes and intracardiac-time intervals.

For the subtraction of the contribution of the maternal heart from fetal MCG, adaptive filtering techniques can be used successfully [Zarsozo et al., 2000; Zarsozo et al., 2001]. An adaptive filter has two input channels, a primary channel and a reference channel. The input to the primary channel is the fetal MCG signal corrupted with noise and the input to the reference channel is the maternal ECG signal. The filter has a set of modifiable weights and the weights are updated using an adaptive filtering algorithm. The reference signal v(k) is processed by the adaptive filter to produce the output signal

$$y(k) = \sum_{i=0}^{K-1} w_i(k)v(k-i) \tag{2}$$

where the $wi(k)$ are the adjustable (real) weights of the adaptive filter. The LMS algorithm [Haykin, 2002] is used to modify the filter weights by

$$w_i(k+1) = w_i(k) + 2\eta e(k)v(k) \tag{3}$$

where e(k) is the error signal obtained by subtracting the fetal MCG signal corrupted with maternal ECG with y(k), the output of the adaptive filter. The filter will take some time for tracking the signal and hence the output obtained for the first few samples will be noisy. Once the adaptive filter starts tracking, the contribution of the maternal heart is significantly reduced. The advantage of adaptive noise cancellation is that no explicit processing is applied to the maternal ECG to compute any parameters.

Recently, independent component analysis has been proposed for the extraction of the fetal- MCG waveform. This method refers to a family of related algorithms [Bell and Sejnowski, 1995] that exploit independence to perform blind source separation. It was originally proposed to solve the blind source separation problem, i.e., to recover source signals, $\mathbf{s} = \{s_1(t), s_2(t), \ldots, s_P(t)\}$, from an unknown matrix $\mathbf{x} = \{x_1(t), x_2(t), \ldots x_P(t)\}$. The elements o f the vector **x** possess diffuse and complex patterns of correlations between them. Independent component analysis is a method to remove those correlations by multiplying **x** with a matrix as follows:

$$\mathrm{U} = \mathbf{W}\mathrm{x} \tag{4}$$

The goal is to find a matrix **W** such that the components of **U** maximally are independent. The infomax algorithm, which minimizes the joint entropy, is used for extracting the fetal signals. Results of independent component analysis applied to fetal MCG are shown in Fig. 14.

6.2. Signal Averaging

Commonly, signal averaging techniques are based on processing the fetal MCG signal in the time-domain since the spectral components of the maternal and the fetal signals overlap. The R-peak locations in time obtained from the maternal ECG indicate when a maternal R-peak is present in the fetal signal. A template of the maternal cardiac complex can be constructed by averaging the maternal complexes in the fetal signal. This template can be subsequently subtracted at all the time instants where a maternal complex is found in the fetal signal.

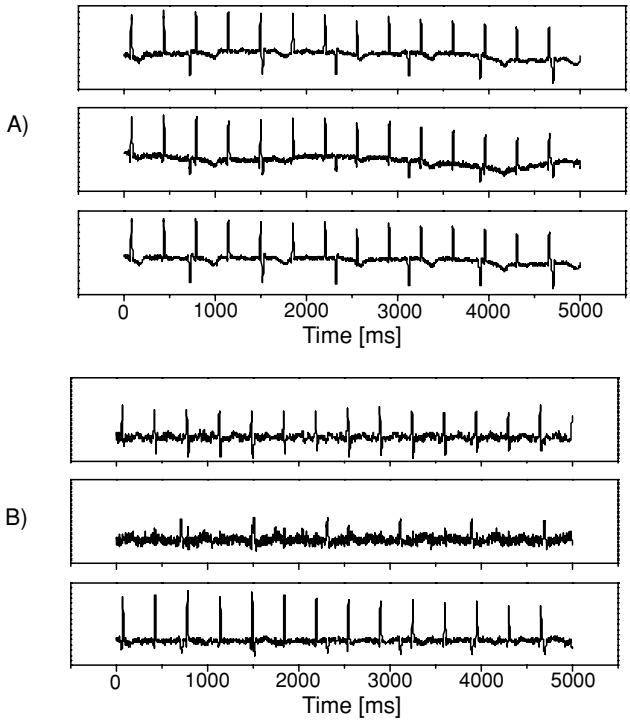

Figure 14. An example of application of ICA. A) Raw fMCG data. The maternal MCG and fetal MCG are present in all channels. B) Output of ICA. The maternal and fetal MCG are separated. The first channel shows the fMCG signal only. The last channel shows the maternal MCG. The middle channel is a combination of fMCG, mMCG and white noise.

The R-peaks in the fetal MCG can be detected using the following method. Segments of two seconds are used in this R-peak detection algorithm. First, the median value of the largest peaks in the interval is computed and 65% of this value is used as a threshold. In the next step, the cardiac complexes are extracted from the filtered signal. These complexes are used to construct a template of the cardiac complex. Using this template the signal is filtered again and the template serves here as a matched filter. Using the algorithm described above, the events are again detected and a threshold of 65% of the median value is used again. The last step in the detection process is checking the minimum time interval between two detected R-peaks. Whenever the interval is shorter than 200 ms, the R-peak with the lowest correlation in the matched filter is rejected. The assumption that R-peaks cannot follow each other within 200 ms is based on the fact that the refractory period of the ventricular pacemaker cells is such that they cannot sustain a faster contraction rate than 300 beats per minute [van Wezel-Meijler et al., 1997]. Complexes that have a small or large amplitude are rejected e.g., peaks in the range 0.8 to 1.2 times the median amplitude. A template of the PQRST-complex is created by averaging the individual PQRST-complexes. The template is then modified by flattening the baseline, which is done by fitting a linear function in the first and last 15 ms of the interval in which the PQRST-complex is located. The position of the

R-peak is then corrected by making a cross correlation of each complex with the template. After these corrections, baseline corrections are made in each complex. The complexes that do not resemble the template based on a residue measure are rejected. The residue measure R is given by

$$R = \sum_{i=1}^{n} \frac{(S_{i,complex} - S_{i,template})^2}{n} \tag{5}$$

where S_i is the i^{th} sample of the signal. After this, the final average is calculated and the intracardiac time intervals are manually calculated.

To compute the noise reduction achieved, the distribution of the noise has been estimated. In the lower-frequency range, the noise level is somewhat higher, possibly due to an incomplete removal of maternal or fetal complexes. When $S_i(t)$ is the individual cardiac complex retrieved from the fetal MCG recording and $f_{MCG}(t)$ is the fetal complex that is assumed not to change during the recording then

$$S_i(t) = f_{MCG}(t) + n_i(t) \tag{6}$$

The noise $n_i(t)$ is Gaussian [Stinstra et al., 2001[a]]. The signal-to-noise ratio improves by a factor $\sqrt{N}$, where N is the number of complexes used in the average. However, the effectiveness of including more complexes decreases because the fetal complexes change over time. The number of complexes available for averaging is constrained by the time elapsed between fetal movements.

7. THE FORWARD PROBLEM

In normal patients, the P-wave is about ten times smaller than the R-peak. In fetal arrhythmia patients the ratio between the P-wave and the R-peak is higher [Stinstra, 2001; Li et al., 2002]. The reason for this enhancement in fetuses with a complete heart block is probably atrial hypertrophy, as the atria often have to pump blood into a contracted ventricle. The same effect is observed for atrial flutter. Unfortunately, at this moment only information based on the duration of various time intervals obtained from fetal MCGs can be used for diagnostic purposes. The amplitudes of the various waves cannot be used, as they are dependent on parameters that are (still) unknown. For example, the strength of the magnetic field measured depends on the distance between the pick-up coil and the location of the electrical activity within the fetal heart. It depends also on the direction of the field component measured in relation with the generator within the fetal heart. Moreover, it depends on the currents that are present in the tissues surrounding the fetal heart. These currents are caused by the electrical activity within the heart. The currents are deflected at the interfaces between different tissues. The degree of deflection depends on the conductivities of the tissues involved. In order to have a trustworthy result for the solution of the forward problem, adequate models for both the generator and the volume conductor are required. The depolarization of the heart can be described by a current dipole layer that is moving as the activity spreads through the heart. At some distance, this current dipole layer can be approximated by a single moving current dipole or by one at a fixed position that rotates

during the cardiac cycle. The latter model is based on the fact that the dimension of the fetal heart is small in comparison to the distance between the dipole and the point of observation. The volume conductor model is very complicated. There are several reasons. First, many tissues which differ in conductivity are present. Second, their conductivities are not well known. Finally, the volume conductor depends on both the stage of pregnancy and position of the fetus.

For an adult heart the volume conductor is usually described by a model of the torso that consists of regions that are piecewise homogeneous and isotropic. Commonly, these compartments are the heart filled with blood, the lungs and the remaining part of the torso. The realistically shaped boundaries of the various compartments are obtained from magnetic resonance images. To compute the current distribution and the magnetic field numerically, the boundary element method is used. The boundaries are described by triangulated surfaces. The reconstruction of the electrical activity in the adult heart is so precise that it is used to localize non-invasively a Kent-bundle (i.e., an accessory pathway between the atria and ventricles) with a precision of about 1 cm in the adult heart [Moshage et al., 1996].

Models of the volume conductor describing the pregnant woman have to explain the following observations:

1) From week 20 until 28 of gestation, the amplitude of the fetal ECG is increasing.
2) In the period from the 28^{th} until the 34^{th} week, a considerable decrease in the amplitude is observed.
3) In the last period of gestation, the amplitude is increasing again.
4) During the period of the 34^{th} week to term, the vectorcardiogram based on fetal ECG measurements describes almost a straight line [Oldenburg and Macklin, 1977].
5) Fetal trunk movements are not apparent in fetal ECG.
6) In fetal MCG, no dramatic changes in the amplitude versus the stage of pregnancy are found. Moreover, the vectorcardiograms are not straight lines. When the fetus moves the MCG changes.

Phenomenon 2 is ascribed to the insulating effect of the layer of vernix caseosa; a fatty layer that surrounds the fetus and that is present from about week 28 onward. Vectorcardiograms of adults, children, and infants born at term and preterm all demonstrate a heart vector that is rotating during the heart cycle. Presumably, the fetal heart vector is also rotating. A vectorcardiogram displaying a straight line can only be explained by assuming that the volume conduction from the fetal heart to the skin of the maternal abdomen takes place through preferred pathways. The hypothesis is that the currents escape the fetus in areas that are not covered by the vernix caseosa. Kahn [1963] and Roche and Hohn [1965] suggested the oronasal cavity of the fetus as a preferred pathway. Kahn further suggested a preferred pathway through the umbilical cord to the placenta. These observations led to the conclusion that due to the presence of the layer vernix caseosa in the period from the 28^{th}–34^{th} week, the fetal ECG is in general impossible to measure. In the period from the 34^{th} week to term, the volume conduction is determined by preferred pathways. These conclusions are affirmed by measurements carried out by Wakai et al. [2000^{b}], who measured both the fetal ECG and MCG in a case that the layer of vernix could not play a role. They performed measurements in weeks 28 and 31 of gestation on a fetus diagnosed with ectopia

Table 2. Effective Conductivity of Tissues Surrounding the Fetal Heart at 37°C in the Frequency Range From 0–100 Hz as Taken From Literature

Tissue	Conductivity S/m	Tissue	Conductivity S/m
Placenta[d]	6×10^{-1} (25°C)	Bladder[a]	1×10^{-1}
Uterus[a]	5×10^{-1}	Liver[a]	2×10^{-2}
Kidney[c]	1×10^{-1}	Spleen[a]	1×10^{-1}
Muscle[a]	2×10^{-1}	Ovary[a]	3×10^{-2}
Bone (cortical)[a]	2×10^{-2}	Cartilage[c]	2×10^{-1}
Skin (dry)[a]	2×10^{-5}	Adipose tissue[a]	1.2×10^{-2}
Skin (wet)[a]	2×10^{-1}	Fetal membranes[b]	0.40
Vernix caseosa[b]	2×10^{-6}	Wharton's jelly[b]	1.4
Amniotic fluid[e]	1.54−1.74		

[a]Gabriel et al., 1996; [b]Oostendorp et al., 1989; [c]Geddes and Baker, 1967; [d]Stinstra et al., 1999[a]; [e]De Luca et al., 1996.

cordis, a rare condition in which the heart is situated outside the fetal body. They reported fetal ECGs with large amplitudes and a vectorcardiogram that was not a straight line.

7.1. The Electrical Conductivity in the Volume Conductor

The highest conductivity in the abdominal volume is found in the amniotic fluid and the lowest in the vernix caseosa. In the maternal abdomen, the skin and the subcutaneous fat are poorly conducting, the conductivity being about a factor 10 less than that of muscle tissue. Other tissues that are a factor 10 to 50 times less conducting include the bone in the spinal column. The volume of the placenta may be as large as the volume of the fetus it self. The conductivity of the placenta will be less than that of the amniotic fluid, but may be larger than that of the other tissues in the maternal abdomen due to its large blood content. Conductivities for the fetoabdominal volume conduction problem as found in the literature are given in Table 2.

The conductivity of the amniotic fluid measured by De Luca et al. [1996] at a temperature of 20°C was in the range from 1.25 to 1.30 S/m for the gestation period of week 15 to 32. After this period a decrease in conductivity was observed with values ranging between 1.15 and 1.30 S/m with an exceptional value as low as 1.10 S/m. This change in conductivity is ascribed to the maturing lungs of the fetus, which release phospholipids (lecithin) into the amniotic fluid from the 24th week onward. To obtain the conductivity at 37°C a correction of about 2 percent per °C has to be applied, leading to a conductivity in the range from 1.67 to 1.74 S/m for the period before the 32nd week and a range from 1.54 to 1.74 S/m after this week.

The conductivity in case no values or contradicting values are found in literature, the conductivities can be estimated. Human tissue consists of cells and fibers that are surrounded by an aqueous conducting medium. For low frequencies and low current densities, currents will circumvent the cells. Therefore, tissue can be modeled as a suspension of non-conducting particles surrounded by interstitial fluid. Although the cells are of microscopic size, they are much larger than the ions in the extracellular fluid, so that this fluid can be considered as a continuum. The applied electric field is assumed to be homogeneous.

Most cells can be described as spheroids. Thus a tissue can be modeled as a concentrated suspension of non-conducting spheroids with axes a and b. If the cells are oriented with their a-axis in parallel and when the field is applied parallel to one of the axes, an expression for the effective conductivity is obtained known as Archie's law, which reads

$$\sigma_{\text{eff}} = \sigma_{\text{solv}}(1 - \text{p})^{\text{m}} \tag{7}$$

where p is the volume fraction occupied by the particles, σ_{solv} the conductivity of the interstitial fluid, and m is the cementation factor that depends on the shape and orientation of the particles, but not on their size. If the field is applied parallel to the a-axes $\text{m} = 1/(1 - \text{L}_\text{a})$, where L_a is the depolarization factor. If the field is applied parallel to the b-axes, $\text{m} = 1/(1 - \text{L}_\text{b})$. For a needle-shaped ellipsoid or a cylinder with a << b, La = ½ and $\text{L}_\text{b} = 0$. For a sphere with a = b and $\text{L}_\text{a} = \text{L}_\text{b} = 1/3$ leading to $\text{m} = 3/2$. For a disk-shaped ellipsoid with a >> b, $\text{L}_\text{a} = 0$ and $\text{L}_\text{b} = 1$. Archie's law has also been found for a solution of several types of ellipsoidal non-conducting particles, which differ in shape (i.e. the ratio a : b : c is different for each group of particles in the suspension), which are randomly oriented. The cementation factor in that case is given by Peters et al. [2001].

In most cases, it is very difficult to calculate the effective conductivity of a composite material due to a lack of detailed information on the micro-geometric structure. However, lower and upper bounds for the effective conductivity can be given based on the information available. The range between these bounds decreases with increasing knowledge about the constituents of the composite medium. For elongated homogeneously-distributed and randomly-orientated nonconducting spheroids the effective conductivity is limited by the following bounds [Peters et al., 2001]

$$\sigma_{\text{solv}}(1 - \text{p})^{5/3} \leq \sigma_{\text{eff}} \leq \sigma_{\text{solv}}(1 - \text{p})^{3/2} \tag{8}$$

As no measured values for the conductivity of the human fetus are available, its conductivity is estimated. It is assumed that the cells in the fetus are randomly orientated and have a shape somewhere between a sphere and a cylinder. Looking at the histology of the fetus, most tissues consist of elongated spheroids. D isc-like cells are less commonly encountered. According to Rush et al. [1984], many tissues in the human body such as lung, liver and fat do not show a preferred direction. Hence, the assumption of randomly distributed and randomly orientated elongated spheroidal cells is reasonable. Brace [1998] and Costarino and Brans [1998] measured the average value of the volume fraction occupied by the extracellular fluid as function of gestational age. The volume fraction of the extracellular space at the end of gestation is around 40 percent of the total body volume. However at the end of second trimester Brace reports a value of 60 percent whereas Costarino and Brans state a value of 40 percent. In both cases, the extracellular space includes the fluids in the body cavities like the cerebrospinal fluid and the blood plasma besides the interstitial fluid. The blood plasma is about 18 percent of the total extracellular water content. As the fetus is considered as one single entity, it makes sense to take all the extracellular fluid into account in estimating the conductivity, as all fluids contribute to the conductivity. In comparison, the extracellular fluid fraction of an adult tissue is about 20 percent. Thence, the fetus is at least a factor two more conducting than the maternal abdomen. Assuming the conductivity of the extracellular volume in both fetus and adult to be comparable at a value of 1.9 S/m

the conductivity of the fetus is expected to be in the range

$$1.9 \times (0.4)^{5/3} \approx 0.41 \leq \sigma_{\text{fetus}} \leq 1.9 \times (0.6)^{3/2} \approx 0.88\,\text{S/m}. \tag{9}$$

Assuming that volume fraction will be somewhere between 40 and 60 percent and will approach 40 percent at the end of gestation a value of 0.5 S/m is a reasonable estimate for the conductivity of the fetus.

The average conductivity of the maternal abdomen can also be estimated. As the average interstitial volume is about 20 percent of the total volume [Shier et al., 1996], a volume fraction p of about 0.2 is estimated. Assuming most tissues consists of elongated particles or spherical like particles, the conductivity averaged over a large volume of the maternal abdomen would be in the order of

$$1.9 \times (0.2)^{5/3} \approx 0.13 \leq \sigma_{\text{abdomen}} \leq 1.9 \times (0.2)^{3/2} \approx 0.17\,\text{S/m}. \tag{10}$$

The estimated conductivity is of the same order as those of tissues like the kidney, the uterus, the bladder, the spleen and muscle tissue, with an average conductivity in the order of 0.1 to 0.2 S/m. Therefore, a value of 0.2 S/m will be a reasonable estimate for the average conductivity of the maternal abdomen.

7.2. Geometry of the Volume Conductor

The fetoabdominal anatomy is depicted in Fig. 15. The volume conductor changes throughout gestation, its electrical properties and geometry depend on gestational age. Since we are interested in the influence of the volume conductor on the fetal MCG, only the gestational period from the 20th week onward needs to be considered. In order to be able to use the boundary element method to study the influence of the volume conductor on fetal MCG, the volume conductor has to be described by compartments with a homogeneous conductivity.

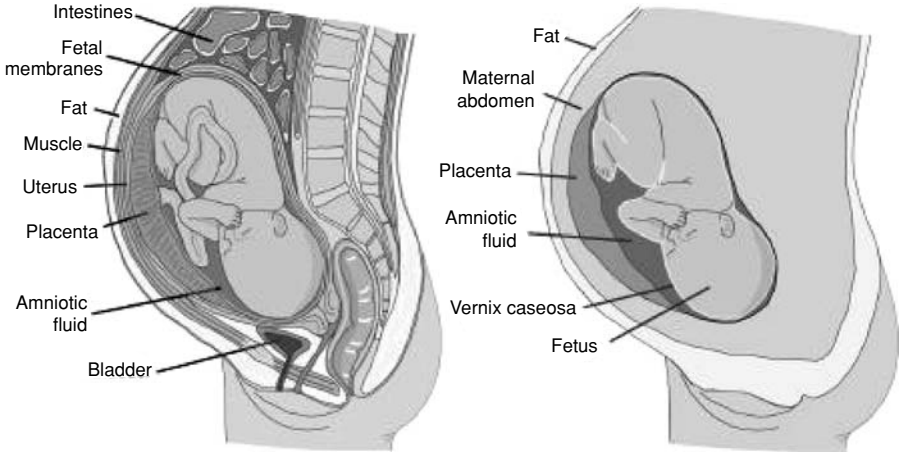

Figure 15. Fetoabdominal anatomy and how it is split up into compartments.

The layer of vernix caseosa does not form before the 28th week of gestation and thence does not have to be included in a model of the second trimester of gestation. The highest value reported for the volume of amniotic fluid in the period between the 26^{th} and 40^{th} week of gestation is about 4200 ml and the lowest value is about 150 ml [Brace and Wolf, 1989; Magann, 1997]. In the same period of gestation, the average fetus will grow from 630 g to a weight of 3400 g at the end of gestation [Baker et al., 1995]. The placental volume is about half of that of the fetus. Hence, it is the second largest volume within the uterus [Baker et al., 1995].

Whereas the fetus can move relatively easy within the uterus at 24 weeks, near the end of gestation the fetus is stuck within the uterus and cannot move that easily. In obstetrics, it is common to describe the fetal position and orientation by means of fetal lie, presentation and position. The fetal lie is the orientation of the fetus, defined by the axis from head to bottom, in relation to the longitudinal axis of the uterus. The presentation of the fetus reflects the part of the fetus that is orientated towards the birth channel. The fetal position refers to how the fetus is rotated in relation to the pelvic bone. About 96.8 percent of the fetuses are in the vertex position at the end of gestation. The fetal position that prevails is the left occiput transverse position in which the fetus is facing the right side of the mother with its spinal column at the left side of the uterus. About 40 percent of the fetuses have this position at the end of gestation.

7.3. Modeling the Fetal Heart Electrical Activity

As the heart of the newborn has not had any time to adapt to the different pressure distribution in the heart, the electrical activity in the heart of the newborn should resemble that of the fetus. Therefore, the current dipole may be obtained from vector ECGs measured shortly after birth. Vector ECGs were measured by Namin [1996] in 100 subjects 30 hours after birth and by DePasquale and Burch [1963] in 50 subjects within the first week of life. The dipole orientations differ with respect to those obtained in adults. The maximum amplitude of the QRS-complex is found when it points to the right-anterior-inferior octant, whereas for adults it is rotated over 90 degrees and points to the left. The reason behind this shift is the distribution of the mechanical load between the left and right ventricle [Namin and Miller, 1966]. After birth, the right ventricle pumps the blood to the lungs and the left ventricle pumps the blood through the body. The heart adapts by increasing the thickness of the wall of the left ventricle. As a consequence, the depolarization front in the left ventricle will dominate the net current dipole. At birth, the left ventricular wall has not yet adapted and the fetal heart dipole is still seen, in which the right side dominates over the left side. Although, the vector ECGs of children show a large variety, all data seem to indicate that the largest vector is pointing towards the right, anterior-inferior octant, with a wide variety of angles.

A wide variety of values is also obtained for P-waves. For instance the amplitude of the P-wave after birth ranges from 0.05 mV to 0.3 mV, the direction varies as well [DePasquale and Burch, 1963]. However, in general the same direction as in the adult heart is observed pointing from the right to the left atrium. The vector ECGs of newborns show a ratio of about one to six for the amplitude of the P-wave and the R-wave, each measured in the direction of that of the QRS-complex.

After birth, the T-wave shows the largest variety in duration and amplitude in the PQRST complex. Several hours after birth it may point in any direction, but after 30 hours it settles down in a direction towards the left-inferior quadrant either pointing anteriorly or posteriorly. After one month the range in which the T-wave is pointing varies from 20 degrees anteriorly or 60 degrees posteriorly in the horizontal plane [Namin and Miller, 1966]. The data show that it is likely that both P and T-wave point in more or less the same direction and that the R-peak is more or less under an angle of 90 degrees with these other two. Present-day computer heart models used to solve the forward problems for adults explain the features of the T-wave by taking into account the difference in duration of the action potential difference of endocardial, epicardial and M-cells. In fetuses, the ventricular wall is supposed to be homogeneous.

8. SIMULATIONS

Fetal MCGs are influenced by the current distribution in the volume conductor. This influence can be studied by means of simulations. Simulations can be helpful to determine which features are reflected in the measurements. For instance, an enlarged P-wave may be due to atrial hypertrophy but also due to a large distance between the fetal heart and the point of observation or due to a condition in which the amount of amniotic fluid is very low. Moreover, simulations may help to find the optimal measuring positions. Another reason for studying the volume conduction would be the solution of the inverse problem, so that from the fetal MCG measurements the heart vector (i.e. the equivalent current dipole) can be reconstructed. A first and fruitful reconstruction of the equivalent dipole from fetal MCG measurements was carried out by Horigome et al. [2001]. The depth of the dipole was measured by ultrasound and the volume conductor was described as a homogeneous half-space. The strength of the dipole turned out to be dependent on the gestational age. In case of cardiac hypertrophy in the fetus, the dipole was clearly enlarged. Consequently, the inverse solution can be used to diagnose prenatal hypertrophy. In the next sections, simulations are discussed that were carried out at the University of Twente [Stinstra and Peters, 2002].

8.1. Simulations of MCGs of Fetuses in Weeks 20 to 30 of Gestation

The fetal heart is represented by a current dipole situated in the center of the fetal heart. A four-compartment volume conductor model is chosen describing the fetus with a conductivity of 0.2 S/m, the amniotic fluid with a conductivity of 1.7 S/m, and the surrounding maternal abdomen with a conductivity of 0.2 S/m, comprising a layer of subcutaneous fat with a conductivity 0.02 S/m. The compartment of fat is estimated to have a thickness of about 2 cm near the abdominal wall. Towards the bottom and top of the model, the layer is thicker and has an average thickness of 3 cm. A cross section of the model is given in Fig. 16A. The surface potential and the magnetic field strength perpendicular to the abdominal surface as well as the current distribution within the volume conductor are calculated by means of the boundary element method. In Fig. 16B, the current density distribution in a vertical cross-section through the abdomen is depicted, showing that most currents are confined to the fetus and amniotic fluid. The current density in the maternal abdomen is

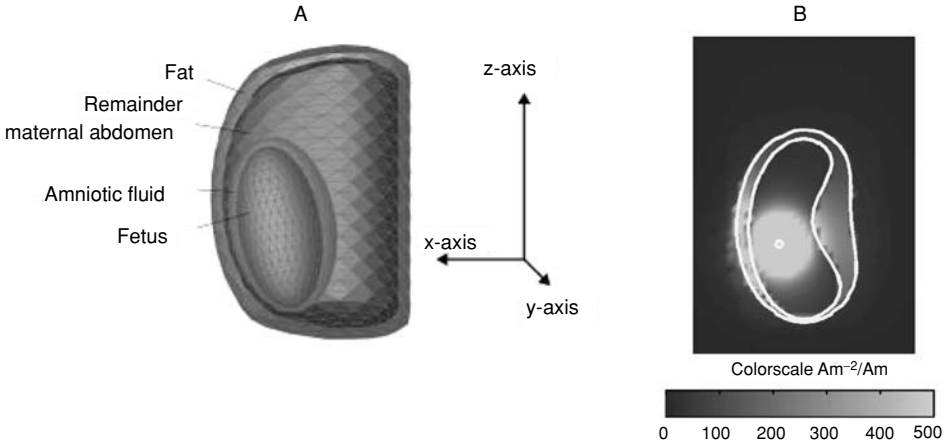

Figure 16. Cross section of a four compartment abdominal model and the current distribution within a cross section.

very low. This result explains why fetal ECGs are difficult to measure as the potential differences at the abdominal surface are small when the local current density is small. The maps shown depict the case for a current dipole along the x-axis. In case the dipole points in another direction, similar results are obtained. In conclusion, it is found that due to the presence of the amniotic fluid, the currents are confined within the uterus. Hence, it is to be expected that currents in the abdominal compartment play a minor role in the computation of the magnetic field. Consequently, it is unnecessary to subdivide this compartment. This expectation is confirmed by simulations [Stinstra, 2001].

To study the volume conduction in a realistically shaped model three MR-images were obtained from pregnant women in the period ranging between 21 to 30 weeks of gestation. Using these images, models were created that consisted of three compartments, representing the fetus, the amniotic fluid and the remainder of the abdominal volume (see Fig. 17). The amniotic fluid and the structures within the fetus could be reasonably well distinguished in the MR-images. Details in the maternal abdomen like a layer of fat or skin could not be distinguished. However, the results mentioned previously showed that these regions of the maternal abdomen hardly influence the magnetic field and thence a further subdivision of the maternal abdomen is not necessary. The placenta and the amniotic fluid were both white in the MR-images; nevertheless, a distinction could be made between both. In order to keep the computational effort within the limits of the computer used, no separate placental volume was included in the model. The placental volume was divided between both the amniotic fluid and the maternal abdomen. In order to avoid the use of large amounts of elements the volume of arms and legs of the fetus were divided between fetus and amniotic fluid in a similar procedure. Apart from avoiding a huge computational effort, the arms and legs were difficult to distinguish as some parts fall within the gap between two MRI-slices, which make it difficult to define the location of a hand or a foot. The position of the heart could be obtained without any problem and the current dipole was positioned at the center of the heart. The transfer functions for these models were computed and are depicted in Fig. 18.

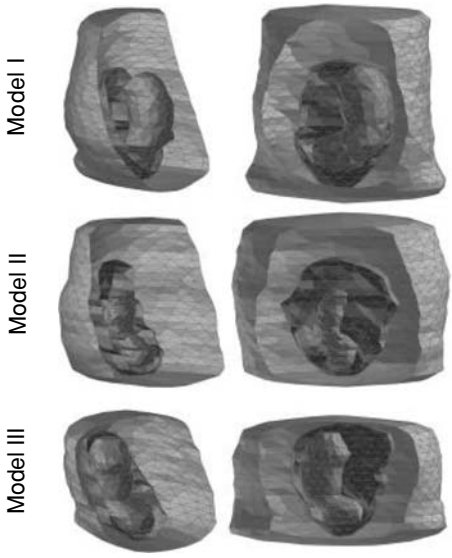

Figure 17. Models that were used in the simulations of MCGs of fetuses in week 20 to 30 of gestation.

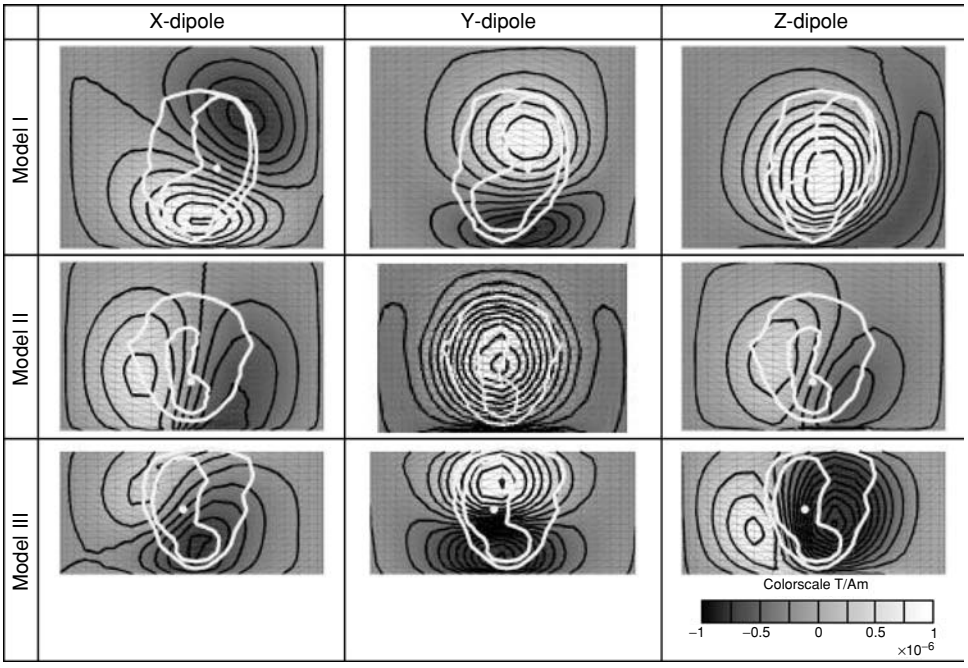

Figure 18. The distribution of the z-component of the magnetic field due to a dipole in the x, y or z direction. Models are shown in Fig. 17.

8.2. Simulations of MCGs and ECGs of a Fetus in Weeks 30 to Term

The vernix caseosa has a large influence on the volume conduction problem. As this layer develops at the end o f the second trimester (from week 28 and onward), it marks a significant change in the volume conduction problem. Some investigators claim that the vernix caseosa first covers the fetus completely and that afterwards holes appear in the layer [Oostendorp, 1989]. This assumption is based on the fact that only in about 20 to 30 percent of the fetal ECGs measured in this period a usable recording is obtained in which fetal R-peaks can be discerned. One hole is probably near the mouth. Simulations show that when one hole is present in the poorly conducting layer, it still confines the currents within the fetus. In order to obtain larger current densities in the volume outside the vernix caseosa at least two holes are needed, so that the currents induced by the fetal heart leave the fetus at one side and return at the other side. A second hole is expected at the onset of the umbilicus.

In the model, the layer of vernix caseosa was assigned a value of 2×10^{-5} S/m. The layers outside the fetus do not have a profound influence on the magnetic field, but do have an influence on the fetal ECG. Four realistically-shaped models have been constructed from MR-images made during the last period of gestation of four different women. In this period the mobility of the fetus within the uterus is small, the fetus is confined to certain positions and orientations in respect to the maternal abdomen. In all four cases examined, the fetuses were lying in a left occiput position. In order to include holes in the layer of vernix, the position of the mouth and the umbilicus were estimated. The first can be obtained easily, as the oronasal cavities are clearly visible, however the position of the umbilical chord is more difficult as it cannot be discerned on the MR images. Thence, it was estimated based on the position of the liver, lungs and heart within the fetus. In Fig. 19, the four models are depicted. The models include a layer of vernix caseosa with an estimated thickness of about 2 mm. Variations in thickness of such a high-resistive layer will not affect the magnetic field or electrical potential distribution at the surface [Stinstra, 2001].

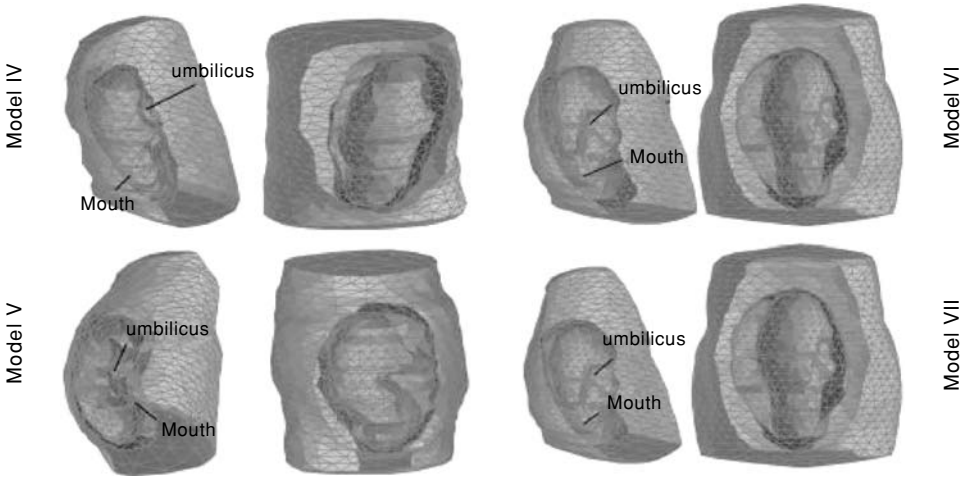

Figure 19. Models that were used in the simulations of MCGs of fetuses in week 30 to term.

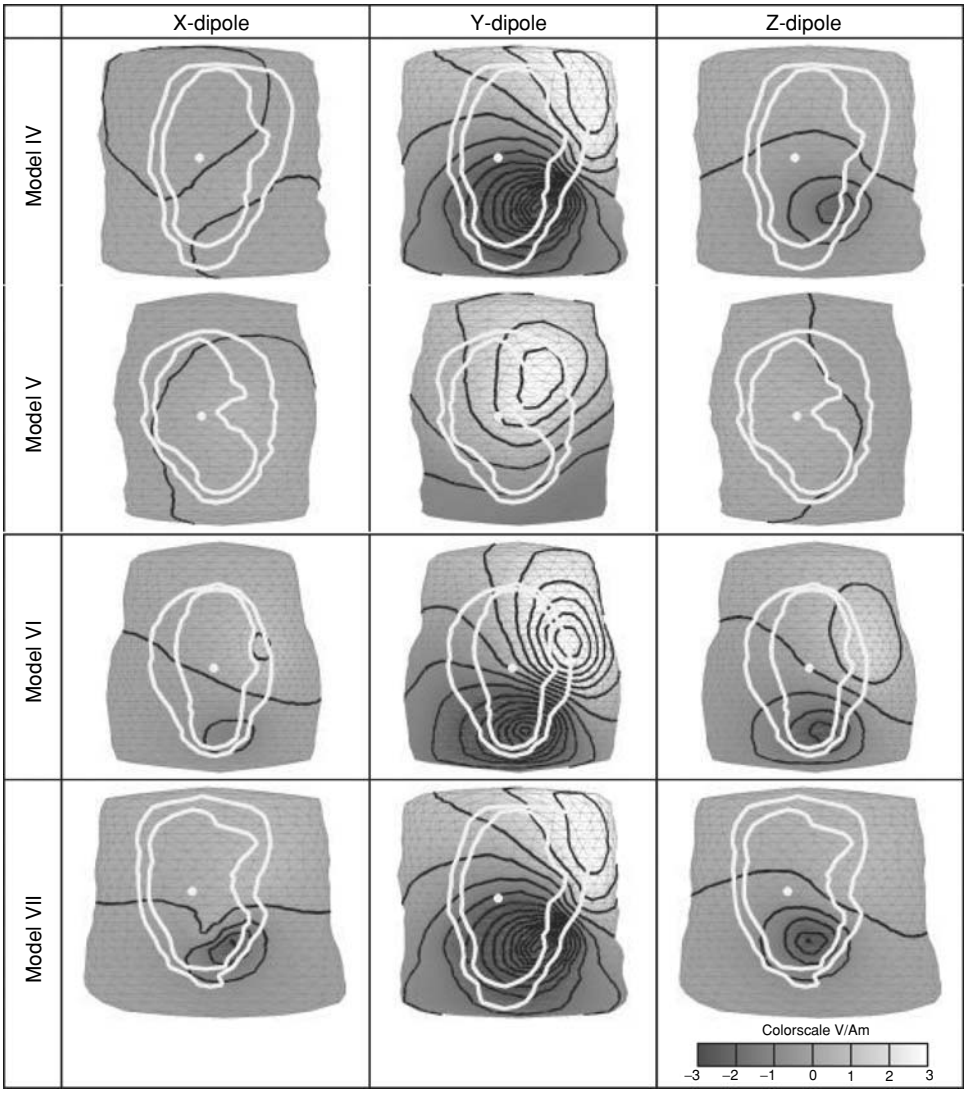

Figure 20. The electric potential distribution due to a dipole in the x, y or z direction. Models are shown in Fig. 19.

For all models, the abdominal surface potential and the magnetic field distribution were calculated. The latter was computed at a distance of 2 cm from the abdominal wall. In Fig. 20, the surface potential distribution is shown for all three components of the current dipole. Likewise, in Fig. 21 the x-component of the magnetic field is depicted for all three current dipole components. This x-component of the magnetic field is the component perpendicular to the front of the abdomen and is the one that is usually measured. The magnetic field maps display a wide variety in patterns. Not only do the patterns change, the amplitudes of the distributions vary over a wide range.

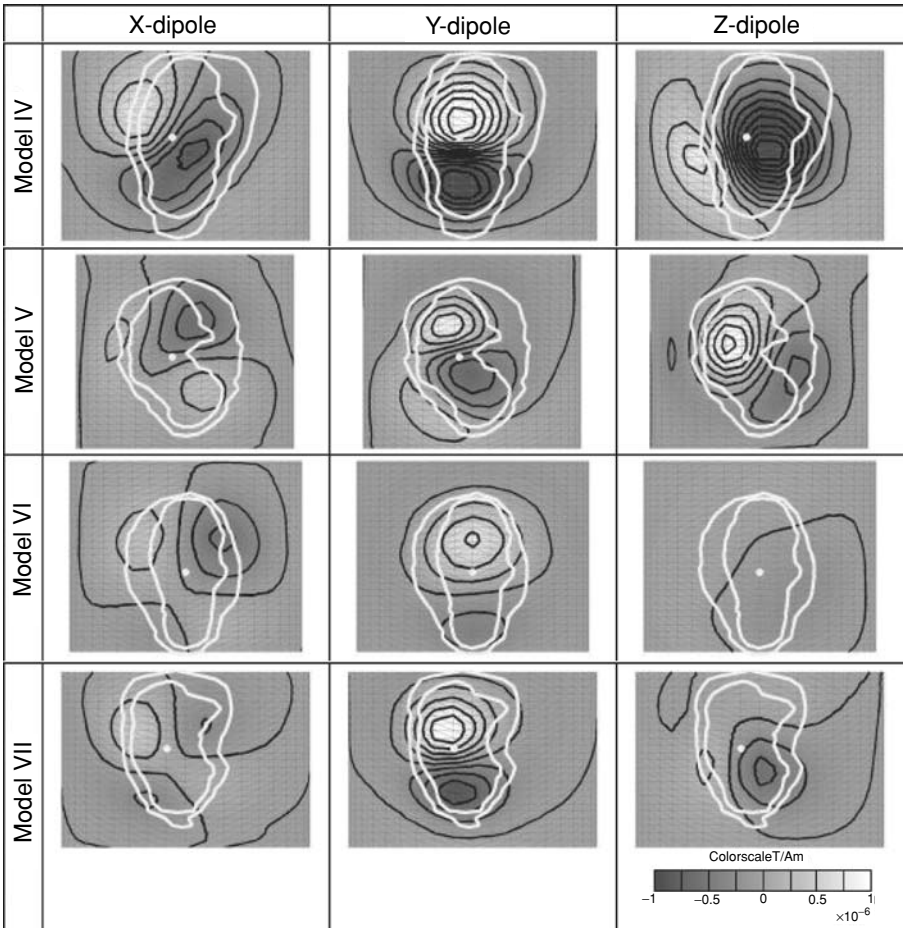

Figure 21. The distribution of the z-component of the magnetic field due to a dipole in the x, y or z direction. Models are shown in Fig. 20.

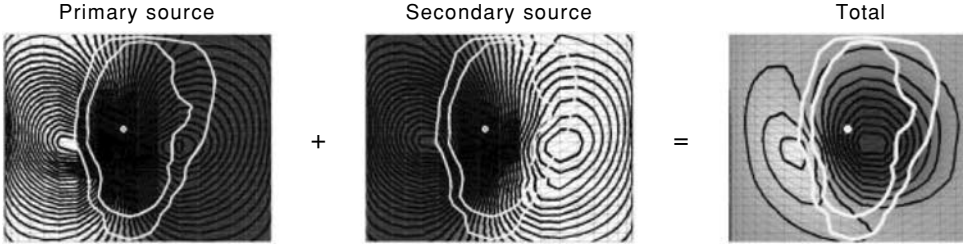

Figure 22. The magnetic field due to a current dipole oriented along the z axis split up a contribution of the primary source and that of the volume currents (i.e. the secondary sources).

In order to get a better understanding of the diversity in the magnetic field distribution shown by means of the simulations, the magnetic field is split up into a contribution of the primary source (current dipole) and a contribution of the secondary sources (volume conductor contribution). A typical result is given in Fig. 22 from which it is clear that both contributions tend to counterbalance each other. It turns out that small changes in the geometry of the volume conductor modify the degree in which both the primary and secondary source contribution tend to cancel each other. Hence, the extrema in the magnetic field distribution of the different models may be found at different positions.

9. DISCUSSION

Fetal MCG can be used to classify arrhythmias. Some information can only be obtained from fetal MCG, such a prolonged QT-interval. Fetal MCG is truly a noninvasive method in which the patient is not even touched, therefore, it would be an appropriate method to study the influence of drugs [Anastasiadis et al., 2001]. However, the measurement system is still too expensive for obstetric departments in peripheral hospitals. Moreover, skilled technicians are necessary to operate these systems. It would be advantageous to have an instrument that can be used at the bedside in a hospital setting. Fortunately, simple single-channel systems are under development, which are relatively cheap and easy to handle because they do not need a magnetically shielded room or liquid helium supply, because the cooling will be due to a closed-cycle refrigerator [ter Brake et al., 2002; Bachir and Dunajski, 2002]. Such systems will lead to better fetal monitoring and health care.

REFERENCES

Anastasiadis P.G., Anninos P., Assimakopoulos E., Koutlaki N., Kotini A. and Galaxios G., 2001, Fetal heart rate patterns in normal and ritrodine-treated pregnancies, detected by magnetocardiography, J. Matern. Fetal Med., 10(5):350–354.

Andelfinger G., Fouron J.C., Sonesson S.E. and Proulx F., 2001, Reference values for time intervals between atrial and ventricular contractions of the fetal heart measured by two Doppler techniques, *Am. J. of Cardiol*, 88(12):1433–1436.

Bachir W. and Dunajski Z., 2002, Flux transformer for fetal magnetocardiography in an unshielded environment, *Proc. 13th Int. Conf. on Biomagnetism*, H. Nowak, J. Haueisen, F. Gieszler and R. Huonker, eds., VDE Verlag GMBH, Berlin, pp. 627–629.

Baker P.N., Johnson I.R., Gowland P.A., Hykin J., Adams V., Mansfield P. and Worthington B.S., 1995, Measurement of fetal liver, brain and placental volumes with echo-planar magnetic resonance imaging, *Brit. J. Obstet. Gynaecol*., 102:35–39.

Bell A.J. and Sejnowski T.J., 1995, An information-maximization approach to blind separation and blind deconvolution, *Neural Computation*, 7:1129–1159.

Berul C.I., 2000, Neonatal long QT Syndrome and sudden cardiac death, *Progress in Pediatr. Cardiol*., 11: 47–54.

Brace R.A., 1998, Fluid distribution in the fetus and neonate, in: *Fetal and Neonatal Physiology*, R.A. Polin and W.W. Fox, eds., Saunders company, Philadelphia, second edn., pp. 1703–1713.

Brace R.A. and Wolf E.J., 1989, Normal amniotic fluid changes throughout pregnancy, *Am. J. Obstet. Gynecol.*, 161(2):382–388.

Brake H.J.M. ter, Rijpma A.P., Stinstra J.G., Borgmann J., Holland H.J., Krooshoop H.J.G., Peters M.J., Flokstra J., Quartero H.W.P. and Rogalla H., 2002, Fetal magnetocardiography: Clinical relevance and feasibility, *Physica C*, 368:10–17.

Clark J.M. and Case C.L., 1990, Fetal arrhythmias, in: *Pediatric Arrhythmias*, P.C. Gilette and A. Garson, eds., Saunders, Philadelphia, pp. 293–302.

Cooley R.L., Montano N., Cogliati C., van de Borne P., Richenbacher W., Oren R. and Somers V.K., 1998, Evidence for a central origin of the low frequency oscillation in R-R-interval variability, *Circulation*, 98(6):556–561.

Copel J.A., Buyon J.P. and Kleinman C., 1995, Successful in utero therapy of fetal heart block, *Am. J. Obstet. Gynecol*., 173(5):1384–1390.

Costa Monteiro E., Schleussner E., Kausch S., Grimm B., Schneider A., Hall Barbosa C. and Haueisen J., 2001, Fetal cardiac activity analysis during twin pregnancy using a multi-channel SQUID system, *Physica C*, 354:87–90.

Costarino A.T. and Brans Y.W., 1998, Fetal and neonatal body fluid composition with reference to growth and development, in: *Fetal and Neonatal Physiology*, R.A. Polin and W.W. Fox, eds., Saunders company, Philadelphia, second edn., pp. 1713–1721.

Dawes G.S., Moulden M. and Redman C.W.G., 1990, Limitations of antenatal foetal heart rate monitors, *Am. J. Obstet. Gynecol*., 162:170–173.

De Luca F., Cametti C., Zimatore G., Maraviglia B. and Pachi A., 1996, Use of low-frequency electrical impedance measurements to determine phospholopid content in amniotic fluid, *Phys Med Biol*, 41:1863–1869.

DePasquale N.P. and Burch G.E., 1963, The electrocardiogram, ventricular gradient and spatial vectorcardiogram during the first week of life, *Am. J. Cardiol*., 482 –493.

Gabriel S., Lau R.W. and Gabriel C., 1996, The dielectric properties of biological tissue: II Measurements in the frequency range 10Hz to 20GHz, III Parametric models for the dielectric spectrum of tissues, *Phys. Med. Biol.*, 41:2251–2293.

Geddes L.A. and Baker L.E., 1967, The specific resistance of biological material–A compendium of data for the biomedical engineer and physiologist, *Med. Biol. Eng*, 5:271–293.

Grimm B., Haueisen J., Huotilainen M., Lange S., van Leeuwen P., Menéndez T., Peters M.J., Schleussner E. and Schneider U., 2002, Recommended standards for fetal magnetocardiography (fMCG), submitted to *Circulation*.

Hamada H., Horigome H., Asaka M., Shigemitsu S., Mitsui T., Kubo T., Kandori A. and Tsukada K., 1999, Prenatal diagnosis of long QT syndrome using fetal magnetocardiography, *Prenatal. Diag*., 19(7):677–680.

Haykin S., 2002, *Adaptive Filters*, Prentice Hall.

Hosono T., Chiba Y., Shinto M., Miyashita S., Muramaki K., Kandori A. and Tsukada K., 2001, A case of fetal complete heart block recorded by magnetocardiography, ultrasound and direct fetal electrocardiography, *Fetal. Diag. Ther*., 16:38–41.

Hosono T., Kawamata K., Chiba Y., Kandori A. and Tsukada K., 2002, prenatal diagnosis of long QT syndrome using magnetocardiography: a case report and review of the literature, *Prenat. Diagn*., 22:198–200.

Horigome H., Shihono J., Shigemitsu S., Asaka M., Matsui A., Kandori A., Miyashita T. and Tsukada K., 2001, Detection of cardiac hypertrophy in the fetus by approximation of the current dipole using magnetocardiography, *Pediatric. Res*., 50:242–245.

Kähler C., Grimm B., Schleussner E., Schneider A., Schneider U. and Nowak H., 2001, The application of fetal magnetocardiography to investigate fetal arrhythmia and congenital heart defects, *Prenat. Diagn.*, 21:176–182.

Kahn A.R., 1963, Transmission characteristics in fetal electrocardiography, pp. 134–135 In: 16th annual conference on engineering in medicine and biology.

Kariniemi V., Ahopelto J., Karp J.P. and Katila T.E., 1974, The fetal magnetocardiogram, J. Perinat. Med. 2(3):214–216.

Lange S., Van Leeuwen P., Klein A., Leven A., Hatzmann W. and Grön emeyer D., 2002, Heart rate variability in growth retarded fetuses as determined by fetal magnetocardiography, in: *Proc. 13th Int. Conf. on Biomagnetism*, H. Nowak, J. Haueisen, F. Gieszler and R. Huonker, eds., VDE Verlag GMBH, Berlin, pp. 633–635.

Leeuwen P. van, Lange S., Bettermann H., Grönemeyer D. and Haltzmann W., 1999[a], Fetal heart rate variability and complexity in the course of pregnancy, *Early Hum. Devel*., 54: 259–269.

Leeuwen P. van, Hailer B., Bader W., Geissler J., Trowitzsch E. and Grönemeyer D.H., 1999[b], Magnetocardiography in the diagnosis of fetal arrhythmia, *Brit. J. Obstet. Gynaecol*., 106(11):1200–1208.

Leeuwen P. van and Schüszler, 2000, Fetal magnetocardiography in twin pregnancy, *Proc. 10th Int. Conf. on Biomagnetism*, C.J. Aine et al., eds., Springer, New York, 585–588.

Leeuwen P. van, Klein A., Geue D., Lange S., and Grönemeyer D., 2001[a] , Bestimmung der fetalen Herzzeitenintervalle anhand der Magnetokardiographie: Einfluss der Anzahl der evaluierten Messkanäle, *Biomed. Tech.*, 43 Suppl 1:256–257.

Leeuwen P. van, Lange S., Hackmann J., Klein A., Hatzmann W. and Grönemeyer D., 2001[b], Assessment of intra-uterine growth retardation by fetal magnetocardiography, in: *Biomag2000 Proc. 12th Int Conf on Biomagnetism*, pp. 603–606.

Leuthold A, Wakai R.T. and Martin C.B., 1999, Noninvasive in utero assessment of PR and QRS intervals from the fetal magnetocardiogram*, Early Hum. Dev.*, 54(3), 235–243.

Li Z., Wakai R.T., Strasburger J.F., 2002, Amplitude of the P and QRS components of the fetal MCG in normal and fetal arrhythmia subjects, in: *Proc. 13th Int. Conf. on Biomagnetism*, H. Nowak, J. Haueisen, F. Gieszler and R. Huonker, eds., VDE Verlag GMBH, Berlin, pp. 636–638.

Magann E.F., Bass J.D., Chauhan S.P., Young R.A., Withworth N.S. and Morrison J.C., 1997, Amniotic fluid volume in normal singleton pregnancies, *Obstet. & Gynecol*., 90(4):524–528.

Menéndez T., Achenbach S., Beinder E., Hofbeck M., Schmid O., Singer H., Moshage W. and Daniel W.G., 2000, Prenatal diagnosis of QT prolongation by magn etocardiography, *PACE*, 23: 1305–1307.

Menéndez T., Achenbach S., Beinder E., Hofbeck M., Klinghammer L., Singer H., Moshage W. and Daniel W., 2001, Usefulness of magnetotocardiography for the investigation of fetal arrhythmias, *Am. J. Cardiol*., 88:334–336.

Moshage W., Achenbach S., Gohl K. and Bachmann K, 1996, *Int. J. Card. Imaging*, 12:47–59. 1996.

Namin P.E., 1967, Pediatric Electrocardiography and Vectorcardiography.

Namin P.E. and Miller R.A., 1966, The normal electrocardiogram and vectorcardiogram in children, in: Electrocardiography in Infants and Children, D.E. Cassel and R.F. Zugler, eds., pp. 99–115.

Oldenburg J.T. and Macklin M., 1977, Changes in the conduction of fetal electrocardiogram to the maternal abdominal surface during gestation, *Am. J. Obstet. Gynecol*., 129(4):425–433.

Oostendorp T.F., 1989, Modeling the fetal ECG, Ph.D. thesis, University of Nijmegen, The Netherlands. Oostendorp T.F., van Oosterom A. and Jongsma H.W., 1989, Electrical properties of biological tissues involved in the conduction of foetal ECG, *Med. Biol. Eng. Comput*., 322–324.

Oudijk M.A., Michon M.M., Kleinman C.S., Kapusta L., Stoutenbeek P., Visser G.H. and Meijboom E.J., 2000, Sotalol in the treatment of fetal dysrhythmias, *Circulation*, 101(23):2721–2726.

Peters M.J., Stinstra J.G. and Hendriks M., 2001, Estimation of the electrical conductivity of human tissue, *Electromagnetics*, 21:545–557.

Piéri J.F., Crowe J.A., Hayes-Gill B.R., Spencer C.J., Bhogal K. and James D.K., 2001, Compact long-term recorder for the transabdominal foetal and maternal electrocardiogram, *Med. Biol. Eng. Comput*, 39:118–125.

Podt M, van Duuren M.J., Hamster A.W., Flokstra J. and Rogalla H., 1999, Two-stage amplifier based on a double relaxation oscillation superconducting quantum interference device, Appl. Phys. letters, 75(15):2316–2318.

Quartero H.W.P., Stinstra J.G., Golbach E.G.M., Meijboom E.J. and Peters M.J., 2002, Clinical implications of fetal magnetocardiography, *Ultrasound Obstet Gynecol*, 20(2):142–153.

Richter M., Schreiber T. and Kaplan D.T., 1998, Fetal ECG extraction with nonlinear state-space projections, *IEEE Trans Biomed. Eng.*, 45(1):133–137.

Roche J.B. and Hon E.H., 1965, The fetal electrocardiogram, *Am. J. Obstet. Gynecol*., 92:1149–1159.

Rush S., Mehtar M. and Baldwin A.F., 1984, Normalisation of body impedance data: a theoretical study, *Med Biol Eng Comput*, 22:285–286.

Schwartz P.J., Stramba-Badiale M., Segantini A., Austoni P., Bosi G., Giorgetti R., Grancini F., Marni E.D., Perticone F., Rosti D. and Salice P., 1998, Prolongation of the QT interval and the sudden infant death syndrome, *New Engl. J. Med*., 338(24):1709–1714.

Shier D., Butler J. and Lewis R., 1996, *Hole's Human Anatomy & Physiology*. WCB McGraw-Hill., Boston. Stinstra J.G., 2001, The reliability of the fetal magnetocardiogram, PhD thesis, University of Twente, The Netherlands.

Stinstra J.G. and Peters M.J, 2002, The influence of fetoabdomenal tissues on fetal ECGs and MCGs, *Arch. Physiol. Biochem.*, 110 (3): 165–176.

Stinstra J.G., Krooshoop H.J.G., Muis B., Huirne J.A.F., Quartero H.W.P. and Peters M.J., 1999[a], The influence of the vernix caseosa on foetal magnetocardiograms, in: *Recent Advances in Biomagnetism*, T. Yoshimoto, M. Kotani, S. Kuriki, H. Karibe and N. Nakasato, eds., Tohoku University Press, Sendai, pp. 1070–1073.

Stinstra J.G., Golbach E.G.M., Peters M.J. and Quartero H.W.P., 2001[a], Extracting reliable data from the fetal MCG, in: *Biomag2000 Proceedings 12th Int Conf on Biomagnetism*, pp. 591–594.

Stinstra J.G., Golbach E.G.M., van Leeuwen P., Lange S., Menéndez T., Moshage W., Schleußner E., Kähler C., Horigome H., Shigemitsu S. and Peters M.J., 2002, Multicentre study on the fetal cardiac time intervals using magnetocardiography, Br. J. Obstet, Gyneacol., 109:1235–1243

Stoll C., Garne E., Clementi M. and EUROSCAN study group, 2001, Evaluation of prenatal diagnosis of associated congenital heart diseases by fetal ultrasonographic examination in Europe, *Prenat. Diagn*., 21:243–252.

Strasburger J.F., 2000, Fetal arrhythmias, *Progress in Pediatr. Cardiol*., 11:1–17.

Vrba, J., 1996, SQUID gradiometers in real environments, in: *SQUID Sensors: Fundamentals, Fabrication and Application*, H. Weinstock, ed., Kluwer, Dordrecht, pp.117–178.

Wakai R.T., Leuthold A.C., Cripe L. and Martin C.B., 2000[a], Assessment of fetal rhythm in complete congenital heart block by magnetocardiography, *PACE*, 23:1047–1050.

Wakai R.T., Lengle J.M. and Leuthold A.C., 2000[a], Transmission of electric and magnetic fetal cardiac signals in a case of ectopia cordis: the dominant role of vernix caseosa, *Phys. Med. Biol*., 45:1989–1995.

Wakai R.T., Chen M., Zhao H., van Veen B. and Strasburger J., 2001, Assessment of fetal rhythm at 20 weeks' gestation by fetal magnetocardiography , *Biomed. Tech*., 46:188–190.

Wezel_Meijler G. van, Genderingen H.R. van, and Meijler F.L., 1997, Atrioventriculaire geleidingstijd bij te vroeg geborenen ongeveer de helft van die bij volwassenen, Ned. Tijdscr. Geneeskd., 141(5):244–247.

Zarzoso V., Millet -Roig J. and Nandi A.K., 2000, Fetal ECG extraction from maternal skin electrodes using blind source separation and adaptive noise cancellation techniques, *Comp. in Cardiol.*, 27:431–434.

Zarzoso V. and Nandi A.K., 2001, Noninvasive fetal electrocardiogram extraction: Blind separation versus adaptive noise cancellation, *IEEE Trans on Biomed. Eng.*, 48:12–18.

Zhao H., Wakai R.T., Strasburger J., Gotteiner N. and Cuneo B., 2002, Assessment of fetal heart rhythm and rate in complete congenital heart block by fetal magnetocardiography, in: *Proc. 13th Int. Conf. on Biomagnetism*, H. Nowak, J. Haueisen, F. Gieszler and R. Huonker, eds., VDE Verlag GMBH, Berlin, pp. 617–619.

Zhuravlev Y.E., Rassi D., Mishin A.A. and Emery S.J., 2002, Dynamic analysis of beat-to-beat fetal heart rate variability recorded by squid magnet ometer: quantification of sympatho-vagal balance, *Early Hum. Developm.*, 66:1–10.

Chapter 2

Microwave Thermoelastic Tomography and Imaging

James C. Lin

ABSTRACT

Microwave thermoelastic imaging uses microwave-pulse-induced thermoelastic pressure waves to form planar or tomographic images. Since the generation and detection of thermoelastic pressure waves depends on dielectric permittivity, specific heat, thermal expansion, and acoustic properties of tissue, microwave thermoelastic imaging possesses the characteristic features of a duel-modality imaging system. The unique attributes of the high contrast offered by microwave absorption and the fine spatial resolution furnished by ultrasound, are being explored to provide an imaging modality for noninvasive imaging characterization of tissues, especially for early detection of breast cancer. This chapter describes the research being conducted in developing microwave thermoelastic tomography (MTT) and imaging for medical diagnosis. It discusses the science of thermoelastic wave generation and propagation in biological tissues; the design of prototype microwave thermoelastic tomographic imaging (MTTI) systems; and the reconstruction of tomographic images using filtered-back projection algorithms; as well as the performance of prototype microwave thermoelastic tomographic systems in phantom models and human subjects.

James C. Lin Department of Electrical and Computer Engineering, and Department of Bioengineering, University of Illinois at Chicago, Chicago, IL 60607-7053 USA

Advances in Electromagnetic Fields in Living Systems, Volume 4, edited by James C. Lin, Springer Science+Business Media, New York, 2005.

1. INTRODUCTION

In spite of the remarkable progress that has been made against cancer, the battle is far from over. It is estimated that there are 175,000 new female breast cancer cases, annually, and 40,000 deaths resulting from it in the U.S. In fact, breast cancer incidence rates have shown little change in the 1990s, while breast cancer death rates have been declining about 2 percent per year since 1990 [Ries et al., 1999]. Modern mammography is relied upon most often for breast cancer screening. Mammograms can detect most breast cancers, but they miss some. Its accuracy and sensitivity are age and breast density dependent. For example, the false negative rate is about 25% for women under age 50, with invasive breast cancer [Kerlikowske et al., 1996; 1997]. It reduces to 10% for women more than 50 years of age. Although the amount of radiation exposure during mammography is minimal - about the same as receiving a dental x-ray, the radiation from mammograms can cause additional breast cancer deaths [Feig, 1996; NIH, 1997]. (It has been estimated that if 10,000 women have yearly mammograms for ten years, the radiation from mammograms will cause one additional breast cancer death.) Because the absolute benefit of screening women aged 40 to 49 years is small and there is concern that the harm may be substantial, there have been suggestions that these women should be informed about the potential benefits and risks of screening mammography [Kerlikowske, 1997].

A majority of imaging devices and systems, including mammography, used by medical practitioners to facilitate the visualization of diseases are based on sources such as gamma particles and x-rays, which are different forms of ionizing electromagnetic energy. They provide the crucial pictorial information to assist the diagnosis of normal and abnormal developments in the practice of many medical specialties. The documented benefits are so overwhelming and ubiquitous that the experience is often taken for granted. They are found in the routine use of bone radiography by orthopedic surgeons and are relied upon by neural specialists. The impact of computed tomography on the discipline of neurology and neurosurgery is enormous. However, there is a small, but finite risk in their use: gamma particles and x-rays are known to be carcinogenic and can produce a variety of malignant neoplasia, especially at higher doses.

Magnetic resonance imaging (MRI) depends on the nonionizing static and radio frequency (RF) magnetic fields as energy sources for image formation, and has been shown to offer distinct advantages in a multitude of disease processes, when compared to ionizing radiation imaging modalities. The current generation of MRI machines use magnetic fields of 1.5 Tesla (T), for imaging of hydrogen protons in tissue [Ueno and Iriguchi, 2000]. The frequency of the applied RF field is about 63.9-MHz according to Larmor resonance. MRI is the preferred imaging technique in the diagnosis of soft tissue disorders of the head, neck and spinal regions (An example is shown in Fig. 1 for MR images of the brain). Also, it has been shown to be important in the evaluation of disease progression [Stark et al., 1999]. The use of MRI is increasing for diagnostic evaluation of cardiovascular diseases, metabolic illnesses, and abdominal disorders in the methods of MR-angiography, or functional MRI. While cardiovascular evaluation may soon become the next major domain of application for MRI, after neurological studies [Nield et al., 2002; Plein et al., 2002], the problem of motion artifact remains as a significant challenge for MRI of the abdomen.

Since MRI is based on the nuclear magnetic resonance of water molecules, a strong applied static magnetic field is required to induce the magnetic dipole moments associated

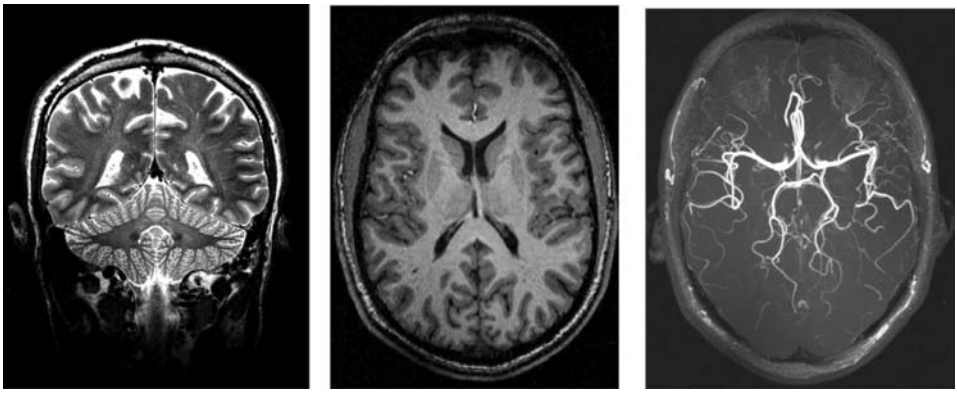

A B C

Figure 1. MRI images of brain anatomy with different MR techniques: (a) A coronal T2 weighted image obtained with a spin echo technique; (b) An axial T1-weighted image obtained with a gradient echo technique; and (c) An axial maximum intensity projection (MIP) vascular image obtained with a 3D time of flight technique. (Courtesy of Noam Alperin, Department of Radiology, University of Illinois-Chicago).

with hydrogen protons in tissue to be aligned in the direction of the applied field. The magnet used to produce the 1.5 T DC magnetic field represents a major cost disadvantage for MRI systems. Nevertheless, it should be emphasized that since its inception, advances in MRI have proceeded exponentially. The tremendous improvements in image quality and imaging time, during the past 20 years, suggest that the field of MRI still has an enormous potential for growth, especially in the measurement of tissue chemistry and function under normal or disease conditions.

Several other tomographic techniques for tissue imaging are currently under investigation, which exploit the cost differential and at the same time, utilize the nonionizing and noninvasive advantages of electric and magnetic fields [Franchois, et al., 1998; Guerquin-Kern et al., 1985; Larsen and Jacobi, 1979; Meaney et al., 1996; Semenov et al., 1996, 2002]. Of late, a great deal of emphasis has been directed toward the area of breast cancer detection. It is noteworthy that the contrast in terms of dielectric constant and electrical conductivity between normal and malignant tissue is higher for the breast than any other tissue type. Breast tissues have higher fat content, whereas cancer cells are perfused more abundantly by blood and have higher water content [Foster and Schwan, 1989]. The wide range of dielectric property variations offers a potential for higher contrast and better opportunities for tissue characterization at microwave frequencies. For this reason, microwave imaging and tomography have been explored to reconstruct images associated with variations of permittivity in body tissues. However, the same high contrast in tissue permittivity induces diffraction in the propagation of microwaves in tissue, which greatly complicates its use as a source for tissue imaging. Another constraint has been the limited spatial resolution afforded by microwave frequencies cir 1000 MHz. While a near-field approach might help to alleviate some of this limitation – and to enhance its imaging capability of small tissue targets – the inhomogeneity of human tissues combined with the high contrast in tissue permittivity brings on diffraction in the propagation of microwaves in tissue. This makes the use microwave energy as a tissue imaging modality a very difficult task indeed.

It has frustrated most, if not all efforts to date, to develop a clinically feasible imaging modality.

Another imaging modality, which uses nonionizing radiation to interrogate body tissue with considerable success, is diagnostic ultrasound. Acoustic energy in the ultrasonic region of 0.5 to 10 MHz is capable of making images of soft tissues, in the body, with less than 0.5 cm spatial resolutions. The attenuation of ultrasonic energy in tissue is approximately proportional to the acoustic frequency. Thus, frequencies below 5 MHz are commonly used for most organs. However, for superficial and in thin tissue media or, in intra-operative environments, images have been made with frequencies as high as 20 MHz. Moreover, localized motion in the field of view of an ultrasonic beam introduces a Doppler shift into the propagating ultrasonic waves. Ultrasound imaging provides a valuable means to measure circulatory and other movements in their normal or diseased states. Indeed, the capability to image motions in the body such as blood flow enables ultrasound modality to occupy a unique position in clinical imaging procedures. In contrast to transmission x-ray images, in ultrasound, reflection images are produced because of the distinct reflections that occur at the interfaces between organs, and from between tissue components within the organs.

An innovative method, microwave thermoelastic tomography (MTT), was first proposed about two decades ago. It employs microwave-pulse-induced thermoelastic pressure waves to form planar or tomographic images of biological tissues [Chan, 1988; Chan and Lin, 1988; Lin and Chan, 1984; Olsen, 1982; Olsen and Lin, 1983; Su, 1988]. The modality is based on the observation that sonic and ultrasonic waves can be generated in biological tissues by deposition of short high power microwave pulses. Absorption of the pulse microwave energy causes a rapid rise in tissue temperature. A thermoelastic pressure wave is launched in response, which propagates away in all directions, and can be detected with an acoustic sensor or ultrasonic transducer array. The detected acoustic waves are processed to form images of the tissue media.

The principle of microwave thermoelastic tomography and imaging (MTTI), and some results have been available in archival literature and published conference papers since the early 1980's. It was conjectured at that time that the potential contrast advantage of microwave imaging and the resolution advantage of ultrasonic imaging could combine to make thermoelastic imaging of biological tissues a potentially useful *duel modality* for diagnostic imaging. In particular, the wavelengths in muscle equivalent tissues for microwaves are 17.5 mm at 2450 MHz and 95.2 mm at 433 MHz. On the other hand, for ultrasonic energy, it is a mere 0.5 mm at 3 MHz and 1.5 mm at 1 MHz. Thus, the potential gain in spatial resolution is tremendous for tissue imaging by only relying on using microwave radiation.

In recent years, this potential has attracted considerable interest with an aim toward developing a microwave thermoelastic tomographic imaging system for near real-time detection and imaging of mammary tumors, especially for early breast cancer detection [Kruger et al., 2000]. The task is complex due to the intrinsic heterogeneity of normal breast tissues, which are composed of fat, connective tissue, glandular tissue, muscle, and blood vasculatures. Moreover, the tissue compositions may differ across patients of various age groups. Subjects in different stages of menstruation, pregnancy or lactation have different compositions. Normal breast tissues have different water or fat content. Moreover, malignant breast tissues often are actually composed of small parts of malignant cells infiltrating within a large part of normal cells, which obviously, renders imaging of mammary tumors and early detection of breast cancers a challenge.

2. THE DISCOVERY OF MICROWAVE THERMOELASTIC WAVES IN TISSUE—THE MICROWAVE AUDITORY PHENOMENON

The discovery of microwave thermoelastic or thermoacoustic wave generation in biological tissues by deposition of short microwave pulses came about as an intense effort was launched in search of a mechanism to help understand a newly observed biological response to microwave radiation.

When a short pulse of microwave radiation with high peak power – a 2.45 GHz rectangular pulse of one microseconds and a peak power of 10 kW, equivalent to 0.01 joules of energy impinges on a mass of biological tissues – absorption of the short pulse of microwave energy causes a rapid rise in tissue temperature. The elastic tissue rapidly expands, and launches a thermoelastic pressure wave in response in the tissue, which propagates away from the absorbing tissue, in all directions. This phenomenon was first reported by human subjects exposed to radar pulses as clicking or buzzing sounds, in the 1950's, and it has since been referred to as the microwave auditory phenomenon or microwave hearing effect.

The microwave auditory phenomenon effect pertains to the hearing of short-pulse, modulated microwave energy at high peak power by humans and laboratory animals [Frey, 1961; 1962; 1971; Frey and Messenger,1973; Guy et al., 1975a,b; Lin, 1978; 1980; 1981]. The effect can arise, for example, at an incident energy density threshold of 400 mJ/m^2 for a single, 10-μs-wide pulse of 2450 MHz microwave energy, incident on the head of a human subject. It has been shown to occur at an SAR threshold of 1.6 kW/kg for a single 10-μs-wide pulse of 2450 MHz microwave energy. A single microwave pulse can be perceived as an acoustic click or knocking sound, and a train of microwave pulses to the head can be sensed as an audible tune, with a pitch corresponding to the pulse repetition rate.

The hearing of microwave pulses is a unique exception to the airborne or bone-conducted sound energy, normally encountered in human auditory perception. The hearing apparatus responds to acoustic or sound pressure waves in the audible frequency range, but the hearing of microwave pulses involves electromagnetic waves whose frequency ranges from hundreds of MHz to tens of GHz. Since electromagnetic waves (e.g., light) are seen but not heard, the report of auditory perception of microwave pulses was at once astonishing and intriguing. Moreover, it stood in sharp contrast to the responses associated with CW microwave radiation. Initially, the microwave auditory effect had been interpreted to imply a direct microwave interaction with the neurophysiological system [Frey, 1961; 1962; 1971; Frey and Messenger, 1973].

On many sites along the auditory neural pathway, small electrodes may be inserted to record electrical potentials that arise in response to acoustic-pulse stimulation. If the electrical potentials elicited by a microwave pulse exhibited characteristics akin to those evoked by conventional acoustic pulses, this would vigorously support the argument that pulsed microwaves are acoustically perceptible. Furthermore, if microwave-evoked potentials were recorded from each of these loci along the auditory neural pathway, this would lend further support to the contention that the microwave auditory phenomenon is mediated at the periphery, as is the sensation of a conventional acoustic stimulus.

An early study has shown that the classical components of the action potential from the auditory branch of the eighth cranial nerve and the round window of the cochlea appeared in both microwave and acoustic pulse cases [Guy et al., 1973; Taylor and Ashleman, 1974].

This suggested that the site of initial interaction of a pulse-modulated microwave radiation with the auditory system is at or outside the cochlea of the inner ear.

A peripheral interaction should involve displacement of tissues in the head, with resultant dynamic effects in the cochlear fluids, hair cells, and central nervous system: auditory activities that have been well described for the acoustic case. In fact, the cochlear microphonic response - a signature of mechanical disturbances in the cochlear hair cells, has been demonstrated in cats and guinea pigs subjected to microwave pulse exposure [Chou et al., 1975; 1976].

Furthermore, evoked-potential recordings have been obtained from the vertex of the head and from the central auditory nervous system of cats. Specifically, responses recorded from the vertex represent volume-conducted electrical events that occur in the auditory brainstem nuclei, within the first 8 ms after the onset of an acoustic stimulus [Lin et al., 1978; 1979]. Indeed, essentially identical microwave and acoustic pulse evoked neural electrical events were recorded from five levels of the central auditory system: the primary auditory cortex, medial genicular, inferior colliculus, lateral lemniscus, and the superior olivary nuclei [Lin et al., 1979]. Thus, the same pathway through the central auditory nervous system is activated by both microwave and acoustic pulses.

This interpretation was augmented by observations made in systematic studies of loci involved, through production of coagulative lesions in ipsilateral auditory nuclei and bilateral ablation of the cochlea, the known first stage of transduction for acoustic energy into nerve impulses [Chou and Galambos, 1979]. Also, successive lesion production in the inferior colliculus, lateral lemniscus, and superior olivary nuclei resulted in a drastic reduction of the recorded response amplitude [Lin et al., 1978; 1979]. The consequence of cochlear disablement was abolishment of all potentials recorded from three levels of the auditory nervous system (the primary auditory cortex, brainstem nucleus, and the eighth nerve), evoked by both microwave and acoustic pulses. These data indicate that peripheral site of initial interaction of pulse-modulated microwave radiation with the auditory system was, indeed, distal to the cochlea of the inner ear.

These results confirmed that the microwave auditory effect was mediated by a physical transduction mechanism, initiated outside the inner ear, and involves mechanical displacement of biological tissues. Concurrent to the electrophysiological research activities, an intense effort was devoted to identifying the physical transduction mechanisms responsible for microwave hearing. Among the several competing physical transduction mechanisms suggested that involve mechanical displacement, thermoelastic expansion had emerged as the most effective mechanism.

Although not directly related to microwave hearing, two earlier publications: one by White [1963], and another by Gournay [1966], had described the conversion of electromagnetic (laser) energy to acoustic energy by surface heating of fluids. Taking the finding as a cue, Foster and Finch [1974] had observed that microwave pulses in water produced acoustic pressure transients with peak amplitude, which are within the auditory frequency range of 200 Hz to 20 kHz, and are well above the expected threshold for perception by bone conduction. They presented the observation as evidence for thermoacoustic auditory stimulation by pulsed microwaves. After examining the mechanical forces generated by electrostriction, radiation pressure, and thermoelastic stress in brain tissue, thermoelastic pressure in tissue was found to be three orders of magnitude greater than the other competing mechanisms [Lin, 1976a,b].

A series of detailed mathematical analyses was initiated by combining the electromagnetic and thermoelastic formulations, and by using spherical head models of animals and humans [Lin, 1976c; 1977a,b,c; 1978]. The analyses showed that the minuscule ($\sim 10^{-60}$C) – but a rapid rise (1–10 μs) in temperature – as a result of the absorption of pulse microwave energy, creates a thermoelastic expansion of tissue matter, which then launches an acoustic wave of pressure that travels to the cochlea, and there it is detected by the hair cells and then relayed to the central auditory system. Specifically, the thermoelastic theory of auditory perception of pulsed microwave radiation delineated the acoustic waves: frequency, pressure, and displacement generated, as functions of head size, in the head, and the characteristics of impinging and absorbed microwave energies. In addition to the expected dependence of sound pressure on the strength of microwave pulses, it prescribed the dependence of induced sound pressure (or loudness of perceived sound) on pulse width, and the dependence of induced sound frequency on head size. For example, the thermoelastic theory predicted a fundamental sound frequency that varies inversely with head radius – the smaller the radius, the higher the frequency. For rat-size heads, it predicted acoustic frequencies in the ultrasonic range of 25 to 35 kHz, which rats can perceive. For the size of human heads, the theory predicted frequencies between 7 and 15 kHz, which are within the audible range of humans.

To acquire biophysical confirmation of the predicted thermoelastic pressure and frequency, a series of measurements was conducted using a hydrophone transducer (3-mm in diameter), implanted in the brains of cats, rats, and guinea pigs, and in brain-equivalent, spherical head models. The results showed sound or pressure frequencies as expected from that predicted by the thermoelastic transduction theory [Olsen and Lin, 1981; 1983; Su and Lin 1987]. Moreover, a propagation speed of the thermoelastic pressure wave of 1523 m/s was measured, in the brain of cats irradiated with pulsed microwaves [Lin et al., 1988], which confirmed the acoustic nature of the microwave-induced thermoelastic pressure waves.

The thermoelastic mechanism had given rise to a rather surprising prediction - a sound pressure or loudness that initially increases with pulse width but soon reach a peak, and then with further increases in pulse width, it gradually oscillates to a lower value [Lin, 1977a,b,c; 1978]. While some indirect experimental evidence had come from the measured amplitudes of evoked auditory responses of animal subjects [Lin, 1980; 1981], a direct measure of the sound pressure or loudness, which would verify the prediction, had to come from another direction. A study conducted in Moscow, which had been reported to disprove the thermoelastic theory [Tyazhelov et al., 1979], and yet, in the end, the data provided in that paper supported the theory [Lin, 1981; 1990; 2001]. The Tyazhelov et al. study investigated the variation of loudness perception with pulse width on human subjects exposed to microwave pulses. The experimental data were presented as curves showing the subject's sensitivity to microwave-induced auditory sound - the inverse of perceived sound loudness or pressure. When properly interpreted, the results showed remarkably similar loudness characteristics as the predictions of the thermoelastic theory. Thus, instead of disproving it, the study from Moscow, actually furnished direct evidence in support of the thermoelastic theory.

We now know that the microwave auditory phenomenon does not arise from an interaction of microwave pulses directly with the auditory nerves or neurons along the auditory neurophysiological pathway of the central nervous system. Instead, the microwave pulse,

upon absorption by soft tissues in the head, launches a thermoelastic wave of acoustic pressure that travels by bone conduction to the inner ear. There, it activates the cochlear receptors via the same process involved for normal hearing [Lin, 1990; 2001]. The microwave auditory effect is the most widely accepted biological effect of microwave radiation – aside from tissue heating – with a known mechanism of interaction: the thermoelastic theory of the microwave-induced acoustic pressure waves in the head. A thorough discussion of the phenomenon and mechanism of microwave hearing is given in a book [Lin, 1978], a review paper [Lin, 1980], and two book chapters [Lin, 1981; 1990], on the subject.

One more digression before moving to the subject of imaging, the thermoelastic theory for hearing microwave pulses was developed on the basis of bulk absorption of pulsed microwave energy in the brain, which was assumed to be spherical for analytically clarity and simplicity [Lin, 1977a,b,c; 1978]. Recently, a numerical analysis was presented by a group from Tokyo, using the finite-difference, time-domain (FDTD) computational algorithm, which is capable of detailed anatomic modeling of the brain and head structure [Watanabe et al., 2000]. In addition to confirming the characteristics of a microwave pulse induced acoustic waves such as sound frequency and pressure amplitude – previously obtained using a homogeneous spherical head, the recent numerical computation graphically illustrated the sequence of pressure wave propagation inside the head, following absorption of pulse microwave energy. It is noteworthy that the pressure wave initially reverberated, and then focused near the center of the head – consistent with the analytical observations showing an induced thermoelastic pressure wave, which varies from as functions of position and time inside the head [Lin, 1977a,b,c; 1978].

3. PHYSICAL PROPERTIES OF BIOLOGICAL MATERIALS MICROWAVE THERMOELASTIC IMAGE FORMATION

The objective of microwave thermoelastic imaging and tomography is the improvement of the diagnostic capability. The hypothesis is that microwave thermoelastic waves can serve as the basis for a unique, novel, nonionizing, and noninvasive tomographic imaging modality to complement current x-ray mammography for early detection of malignancies, especially, breast cancer. It is emphasized that the duel modality, microwave thermoelastic tomography is based on a fundamentally unique mechanism, i.e., the selective absorption of microwave energy and differential emission of acoustic energy by normal and malignant tissues. Moreover, the component cost for this microwave thermoelastic tomographic system would be very modest compared to modalities currently in clinical usage. It therefore could provide an imaging modality capable of early detection of breast cancer, with a potential to offer it on more widely available basis and with minimal radiation risk to the patient. Clearly, in order to advance microwave thermoelastic imaging and tomography, it would be important to examine the phenomena of microwave interaction, thermoelastic pressure wave generation and propagation in biological tissue, and the detection of acoustic or ultrasonic pulses. Since the generation and propagation of microwave thermoelastic pressure waves are governed by the microwave, thermal, and acoustic properties of biological tissues, the following sections include brief summaries of these properties as related to the subject at hand.

3.1. Microwave Dielectric Permittivity of Biological Materials

The electromagnetic properties of tissue media, specifically, permittivity and permeability strongly influence the interaction of microwave fields with biological materials. At microwave frequencies, biological materials have permeability values close to that of free space, such that $\mu = \mu_0 = 4\pi \times 10^{-7}$ H/m, and they are independent of frequency. The permittivity, dielectric constant and conductivity, displays unique dependence on frequency. Typically, dielectric constants decrease while conductivities increase with increasing frequency. This occurs because biological tissues are composed of cells and water. As the frequency increases, changes associated with cell membranes stabilize, the rotational and vibrational behaviors of polar molecules in water become more significant. However, the electrical conductivity of biological tissues behaves in a disparate manner. Cell membranes become progressively short-circuited for higher frequencies, allowing the intracellular and extracellular fluids to participate in electric current conduction. This causes the conductivity to increase as the frequency increases. Moreover, at microwave frequencies, the rotation of water molecules is accompanied by viscous friction that accounts for the principal mechanism of increased conductivity.

In general, the permittivity of biological tissues may be classified by their water content. For example, tissues such as fatty and skeletal tissues have low water contents. Blood is characterized by high water content, while muscle has intermediate water content. Typical values of microwave dielectric constant and conductivity at 37°C are given in Table 1 for such tissues as fat, muscle and blood [Foster and Schwan 1989; Michaelson and Lin, 1987; Lin, 2004]. It can be seen that there is a modest change in dielectric constant and electrical conductivity as a function of frequency for all the tissues in the spectrum range of most interest to thermoelastic tissue imaging. However, differences among the three types of tissues are quite large. At 915 MHz, the dielectric constant for muscle is 15% lower than blood, but is about ten times higher than for fat. While conductivities for blood and muscle are approximately the same, they are about 15 times higher than for fat.

As mentioned previously, the prospect for breast cancer detection has been a major impetus for the research and development effort in microwave thermoelastic tomographic imaging. This came about, in part, from the contrast in the numerical value of dielectric permittivity and electrical conductivity between normal and malignant tissues. The contrast is quite high for the breast than many other tissue types due to the breast's high fat content compared with the higher water and blood content of tumor cells. Normal breast tissues are composed mainly of fat, connective tissue, and glandular tissue.

Table 1. Dielectric Constant and Conductivity of Biological Tissues with High and Low Water Contents in the Frequency Range of Interest

	Dielectric Constant			Conductivity (S/m)		
Freq. (GHz)	Blood	Muscle	Fat	Blood	Muscle	Fat
0.433	62	53	5.6	1.2	1.4	0.08
0.915	60	51	5.6	1.4	1.6	0.10
2.45	58	49	5.5	2.1	2.2	0.16
5.80	51	43	5.1	5.3	4.7	0.26

Table 2. Dielectric Constant and Conductivity of Normal and Malignant Breast Tissues at Microwave Frequencies

	Dielectric Constant			Electrical Conductivity (S/m)		
Freq. (GHz)	Breast Fat	Breast Tumor	Fat	Breast Fat	Breast Tumor	Fat
[b]0.40	17	67		0.25	0.74	
[h]0.40	45	58		0.18	0.96	
[j]0.40	18.6	58.3		0.18	0.88	
[g]0.433	5.6		5.6	0.05		0.08
[b]0.900	8.3	62.5		0.25	0.9	
[h]0.900	42	49		0.36	1.1	
[j]0.900	15.7	57.5		0.23	1.17	
[g]0.915	5.4		5.6	0.07		0.10
[b]2.0	8	50		0.325	1.22	
[h]2.0	39	47		0.67	1.46	
[g]2.45	5.1		5.5	0.14		0.16
[c]3.0	5.7	60		1.0	3.0	
[a]3.2	10–50	10–50		0.35–3.5	0.35–3.5	
[g]5.70	4.8		5.1	0.37		0.26
[c]9.2	4.3	40		5.0	10	

[a][Campbell and Land, 1992] (Human at 24° and 3.2 GHz)
[b][Chaudhary et al., 1984] (Human at 24° and 3 MHz–3 GHz)
[c][England et al., 1949]; 1950 (Human *in vitro* at 37° and 3–24 GHz)
[g][Gabriel et al., 1996] (Human at 37°C)
[h][Joines et al., 1980] (Rat in vivo at 37°C and 30 MHz–2 GHz)
[j][Joines et al., 1994] (Human at 24°C and 50 MHz–900 MHz)

A summary of published dielectric constant and conductivity values, for normal and malignant breast tissues, at the microwave frequencies of interest is presented in Table 2. It can be seen that a significant difference exists in the relative permittivity and conductivity between the normal and tumor tissues. Moreover, many of the reported values for breast fat are comparable to those for un-infiltrated fat tissue. Nevertheless, it should be noted that one published study suggests a close similarity of the dielectric properties between benign and malignant breast tumors, instead of a large difference. If these measurements are correct, the results suggest that microwave imaging methods will have limited practical use since it would not be capable of distinguishing benign and malignant breast tumors [Campbell and Land, 1992]. However, most reports in the literature have shown that the dielectric properties of cancerous tissues differ from those of surrounding normal tissues, *in vitro*. It can be seen from Table 2 that, while the contrast generally is greater than 100% between normal and malignant tissues in terms of dielectric permittivity and electrical conductivity, the variability of data reported by different investigators also is very large for most microwave frequencies. It is noteworthy that fatty breast tissue has essentially the same dielectric constant and conductivity [Gabrial et al., 1996], as tissues of low-water content listed for fat in Table 1.

This state of inconsistency in measured data, while troublesome, is not entirely unexpected since tissue dielectric permittivity and electric conductivity are negatively correlated

with variations in temperature - a low tissue temperature will give rise to lower values than at body temperature. It is didactic to recognize other possible causes for the variability in order to enhance the prospect for using microwaves to image biological tissues. Indeed, given the intrinsic inhomogeneity of breast tissues, which normally are composed of fat, connective tissue, glandular tissue, etc. there is no lack of parameters that can influence the quantities of measured permittivity and conductivity. Some malignant tissues actually are composed of small parts of malignant cells infiltrating within a large part of normal cells, which may decrease the mean value of the malignant tissue samples. The age and specific type of breast tissue, the particular stage of tumor development, handling and treatment of tissue samples, as well as whether the measurements were conducted *in vivo* or *in vitro* have considerable influence on these values. Likewise, the experimental techniques and protocols will affect the measured results. Clearly, given the paucity of data, there is a need for more extensive efforts to characterize the dielectric behavior of both normal and malignant breast tissues - to reduce the range of uncertainty.

Nevertheless, a majority of studies indicate a significant difference in the relative permittivity between the normal and cancerous breast tissues. Moreover, several studies in the literature also report that the dielectric permittivity and conductivity of other cancerous tissues – human gliomas and mouse fibrosarcomas – consistently differ from those of their normal counterparts [Lu et al., 1992; Roger et al., 1983]. The difference generally has been attributed to an increase in blood perfusion; water content in cancerous tissues is higher relative to their normal counterparts. This difference has been employed to theoretically demonstrate the promise of imaging of breast cancers with microwaves. Although there has been extensive experimental work attempting to exploit this prospect for medical imaging applications, a microwave medical imaging device has not yet come close to competing successfully with existing radiological imaging modalities. A prime handicap has been the diffraction effect associated with microwave propagation through inhomogeneous biological media, and limitations on the spatial resolution produced by the microwave modality, as mentioned previously.

3.2. Thermal Properties of Biological Tissues

The thermal properties of biological tissues are characterized by the specific heat and thermal conductivity. Table 3 lists some of these thermal properties and the coefficients of thermal expansion for tissues with high and low water content. Note that it is the thermal expansion in response to deposition of pulsed microwave energy that gives rise to the thermoelastic waves. It can be seen from the values of thermal conductivity that biological

Table 3. Thermal Properties of Biological Tissues*

Tissues	Thermal Conductivity (kcal/sec °C)	Specific Heat (kcal/kg °C)	Coefficient of Thermal Expansion (10^{-5}/°C), ϕ
Fat	0.05	0.62	2.76
Muscle	0.12	0.75	4.14
Water	0.15	1.0	6.9

*[Lin, 1978]

tissues are relatively poor thermal conductors. Moreover, values for these properties are directly proportional to the water content of tissue. The thermal capacitance is given by the product between the tissue specific heat, c (kcal/kg°C or Joule/(kg°C) and density, ρ(kg/m^3). The following are some typical values of these parameters for muscle tissue: $\rho = 1000$ (kg/m^3), c = 3500 (J/kg°C), and $\eta = 0.508$ (W/(°C m^3)). However, heat transfer by blood convection is considerably faster in well perfused tissue, as is seen by a high $V_s = 7.780 \times 10^6$ {W/(°C m^3)}.

The increase - or decrease - in temperature per unit time is influenced by the phenomena of heat transfer that rakes place inside the body. These events are closely related to the above parameters, which determine the amount of heat accumulated (or lost) per unit time and per unit mass, at a point inside the biological tissue.

3.3. Acoustic Properties of Biological Tissues

The properties that determine the behavior of ultrasounds in biological tissue are the propagation velocity and coefficient of attenuation of acoustic waves in the medium. The acoustic properties also can be expressed in terms of Lame's constants, χ and ξ, and the density of tissue ρ, so that the velocity v, of acoustic wave propagation is given by (Lin, 1978):

$$v = [(\chi + \xi)/\rho]^{1/2} \tag{1}$$

Table 4 summarizes the acoustic properties at 0.5, 1.0, and 3.0 MHz for representative tissues. It can be seen that the velocity is about 1550 m/s for most tissues: it is lower for fat tissue and higher for tendon-like tissues. Note that the sole measured value for microwave thermoelastic waves showed a velocity of propagation of 1550 m/s in brain tissue [Lin et al., 1988]. The coefficient of attenuation in fat is lower than in muscle or tendon. A comprehensive compilation of the acoustic properties of biological tissue showed large discrepancies between values reported by different investigators [Goss at el., 1978; 1980].

Table 4. Acoustic Properties of Biological Tissues*

		Attenuation Coefficient at Frequency (MHz)		
Tissues	Bulk Velocity at 1 MHz (m/s)	0.5	1.0 (Np/cm)	3.0
Fat	1440		0.07	0.18
Blood	1500		0.03	0.07
Brain	1520	0.03	0.07	0.24
	1550[a]			
Liver	1546	0.04	0.08	0.29
Muscle	1580	0.12	0.16	0.45
Tendon	1750	0.33	0.56	1.30

* [Goss et al., 1978; 1980]
[a] Measured value for microwave thermoelastic waves, [Lin et al., 1988]

4. MICROWAVE THERMOELASTIC PRESSURE WAVE GENERATION

4.1. Microwave Fields in Biological Media

Electromagnetic energy in the microwave frequency region between 300 MHz and 300 GHz has wavelengths between 1 mm and one m in air. They produce photons of low energy, therefore, under ordinary circumstances, they are too weak to produce ionization or excitation in biological materials. Consequently, they are often referred to as *nonionizing radiation*. Microwaves propagate or advance through a material medium at a constant speed in that medium. In particular, it propagates through air or vacuum at the speed of light, 2.998×10^8 m/s, and at a lower speed in all material media, including biological materials. To understand the interaction of electromagnetic fields with biological systems in particular, and with all materials in general, one can begin with the theoretical statements known as Maxwell equations - the physical laws describing the characteristics and behavior of electromagnetic waves in biological media. These equations capture our understanding of basic electromagnetic process and theorize mechanisms of interaction through experimental observations. They provide a set of principles for working with abstract ideas and for the logical deduction of all macroscopic phenomena of electromagnetic interaction with material media.

When components of the microwave fields oscillate harmonically, at a *frequency*, f, and angular frequency $\omega = 2\pi f$, Maxwell equations may be combined to derive two second order differential equations which describe the propagation of microwaves, one containing the electric field strength, **E** and the other containing the magnetic field strength, **H** such that:

$$\nabla^2\mathbf{E} + \omega^2\mu\varepsilon\mathbf{E} = 0 \tag{2}$$

$$\nabla^2\mathbf{H} + \omega^2\mu\varepsilon\mathbf{H} = 0 \tag{3}$$

in the free space, air or where the electric charge density is zero. The other parameters are the *dielectric permittivity*, ε; the *magnetic flux density*, and the *magnetic permeability*, μ.

Solutions for the wave equations characterize the propagation of microwaves with a *speed,* $\mathrm{v} = (\mu\varepsilon)^{-1/2}$, and its corresponding *wavelength* λ specified by v/f.

In biological media, or a medium with finite electrical conductivity σ, a conduction current $\mathbf{J} = \sigma\mathbf{E}$, will flow – giving rise to energy loss by Joule heating – the wave equations in these media contain a loss term, and take the form of

$$(\nabla^2\mathbf{E} + \omega^2\mu\varepsilon - \mathrm{j}\omega\mu\sigma)\mathbf{E} = 0 \tag{4}$$

$$(\nabla^2\mathbf{H} + \omega^2\mu\varepsilon - \mathrm{j}\omega\mu\sigma)\mathbf{H} = 0 \tag{5}$$

As the wave propagates in this type of medium, a part of the incident energy is extracted from the propagating microwave and absorbed by the biological tissue with conductivity σ, which ultimately dissipates into heat energy. The dissipated or absorbed power density is equal to the rate of energy absorption by the medium or, *specific absorption rate*, SAR, and it is quantified by

$$\mathrm{SAR} = \left({}^{1}/_{2}\right)\sigma\mathrm{E}^2 \tag{6}$$

where σ is electrical conductivity of the medium, and E is the electric field in the medium. It is noteworthy that the configuration and frequency of the microwave source, tissue dielectric permittivity, and the geometry and composition of the biological body will influence the absorption and distribution of the wave as it impinges and propagates in the biological body. Moreover, the absorption is directly proportional to σ, the higher the conductivity the higher the absorption.

The energy radiated from a microwave antenna is dictated by the frequency, size and configuration of the antenna. For a physically small antenna - dimensions that are small compared to a wavelength, the radiated energy is in the form of a spherical wave in which the wavefronts are concentric shells. The spherical wavefront expands as the wave propagates outward from the source. At distances far from the source, the radius of curvature of the spherical shells becomes so large that the wavefront would essentially appear as a plane. They are therefore referred to as plane waves. Plane waves are important since their behavior is well quantified - the power density varies only in the direction of propagation and the fields are uniform in planes normal to the direction of propagation. In this case, both electric and magnetic fields of the propagating wave lie in the plane of the wavefront. Moreover, the electric and magnetic fields are orthogonal in space and both are perpendicular to the direction of wave propagation. In practice, most sources have radiating behaviors that fall between a spherical wave and a plane wave.

As a first order approximation, the plane-wave configuration is often used for its simplicity to assess of microwave interaction with biological tissue. In a plane wave, the electric and magnetic field components are related by the *intrinsic impedance* (η) of the medium, which is a constant for the medium, and is given by

$$\eta = (\mu/\varepsilon)^{1/2} \tag{7}$$

The microwaves propagating in a homogeneous biological medium are exponentially attenuated, and the exponential attenuation is characterized by a *complex propagation factor* γ such that

$$\gamma = \alpha + \mathrm{j}\beta \tag{8}$$

where α and β are the *attenuation* and *propagation coefficients*, respectively. They are all functions of the frequency of the impinging microwave, and of the medium's electrical conductivity, dielectric permittivity, and magnetic permeability, and are given by

$$\alpha + \mathrm{j}\beta = [\mathrm{j}\omega\mu(\sigma + \mathrm{j}\omega\varepsilon)]^{1/2} \tag{9}$$

$$\alpha = \omega\{(\mu\varepsilon/2)[(1 + \sigma^2/\omega^2\varepsilon^2)^{1/2} - 1]\}^{1/2} \tag{10}$$

$$\beta = \omega\{(\mu\varepsilon/2)[(1 + \sigma^2\omega^2\varepsilon^2)^{1/2} + 1]\}^{1/2} \tag{11}$$

The amplitude decreases exponentially as the wave advances in an oscillating manner, in the biological medium. If the medium is highly conducting, α and β reduce to

$$\alpha = \beta = (\omega\mu\sigma/2)^{1/2} \tag{12}$$

Clearly, from the dependence of α on ω and σ, it can be seen that the rate of amplitude reduction is proportional to source frequency and conductivity. The quantity δ, known as the *depth of field penetration* or *skin depth*, and is given by

$$\delta = 1/\alpha \tag{13}$$

Therefore, the skin depth is inversely proportional to the attenuation coefficient, and to the frequency and conductivity. It is noted that the microwave field does not cease to penetrate beyond the depth of σ; this is merely the point at which the field has decreased to e^{-1}, or 37% of its initial quantity.

When the microwaves propagating in one medium impinge on a second medium, tissue or other materials having a different dielectric permittivity, reflection and transmission of microwave energy occur at the boundary between the two media. The reflected field is characterized by the reflection coefficient Γ, which is defined as the ratio of the reflected electric field strength tot he incident electric field strength at the boundary and is given by

$$\Gamma = (\eta_2 - \eta_1)/(\eta_2 + \eta_1) \tag{14}$$

where η_1 and η_2 are the intrinsic impedance of medium one and two, respectively. In a similar manner, the *transmission coefficient* T is defined as the ratio of the transmitted electric field to that of the incident electric field at the boundary,

$$\mathrm{T} = 2\eta_2/(\eta_2 + \eta_1) \tag{15}$$

If intrinsic impedances of the two media are approximately equal, most of the energy is transmitted into the second medium and the reflected field is relatively small. Conversely, if intrinsic impedances differ greatly, the transmitted field is small and the quantity of reflected energy is large.

When the wave impinges normally on the boundary, the resulting reflected wave propagates back toward the source, but the transmitted wave will propagate in the second medium along the same direction as the incident wave. If angle of incident upon a boundary surface is other than normal, the angle of reflection is equal to the angle of incidence, θ_i, while the angle of transmission, θ_t, is found by Snell's law of refraction,

$$\sin\theta_\mathrm{t} = (\varepsilon_1/\varepsilon_2)^{1/2} \sin\theta_\mathrm{i} \tag{16}$$

If $\varepsilon_1 < \varepsilon_2$, for example, in air and biological medium, θ_t becomes smaller than the incident angle, creating a focusing effect - bending the transmitted wave more along the direction normal to the boundary surface. However, in most prototype microwave thermoelastic tomographic systems, the antennas are configured for the microwave to incident at a normal angle. For this reason, an antenna system or array structure that conforms to the shape of the human breast is more advantageous compared to a planar antenna structure. In general, the transmitted wave undergoes a wavelength contraction such that $\lambda_\mathrm{t} = \lambda_\mathrm{o}/(\varepsilon)^{1/2}$, where λ_t is the wavelength in tissue, and λ_o = wavelength in free space.

A plane wave of microwave radiation, polarized in the plane of incidence (i.e., parallel polarization), is almost completely transmitted into a tissue medium. Most, if not, all of the energy carried by the incident plane wave in air would be deposited inside the tissue medium. The magnitude of the reflected microwave is reduced to a minimum at the Brewster angle,

$$\theta_\mathrm{b} = \tan^{-1}(\varepsilon_2/\varepsilon_1)^{1/2} \tag{17}$$

where the wave impinges from medium 1. For example, depending on the tissue types, the Brewster angle is between 45 and 90 degrees for air-tissue interfaces at 2.5 GHz.

Another phenomenon of importance is *total internal reflection*, which occurs when the planar microwave impinges at a large incident angle from a medium with higher dielectric

permittivity onto one with a lower permittivity (i.e., $\varepsilon_1 > \varepsilon_2$). Specifically, for all angles of incidence $\theta_i > \theta_{c,}$ where the critical angle θ_c, corresponding to $\theta_t = 90^\circ$, is given by

$$\theta_c = \sin^{-1}(\varepsilon_2/\varepsilon_1)^{1/2} \tag{18}$$

there is total internal reflection. In this case, $\theta_t > \theta_i$, there is no transmission into the second medium for large angles of incidences, regardless of the polarization of the incident wave. As the microwave field propagates in a tissue medium, energy is extracted from the field and absorbed by the medium. This absorption will result in a progressive reduction of the microwave power intensity as it advances in the tissue in planar tissue media according to equations (9–11).

4.2. Microwave Absorption in Biological Bodies

The coupling or absorption of microwave energy in biological bodies is controlled by the frequency and configuration of the source, as well as the geometry and contour of the exposed body. In biomedical imaging applications, a beam, or beams, of microwaves is directed toward the body or target organ. In addition to the frequency dependence of dielectric properties of different tissues, the coupling of microwave energy into organs of different size and contour also varies with frequency, or the relative size of the organ compared with a wavelength. The wavelength λ, is inversely proportional to frequency f, according to

$$\lambda = (1/f)(\mu\varepsilon)^{-1/2} \tag{19}$$

where $(\mu\varepsilon)^{-1/2}$ is the speed of microwave propagation in the tissue or organ. The coupling mechanisms for a plane wave or a beam wave are different, particularly for regions beyond the center of the beam. A brief account is presented for plane wave coupling to the biological body or organ, as a function of frequency. Note that the plane approximation is especially relevant if the beam width is large compared to the size of the target organ, and can serve as a first-order approximation in other cases. The frequency dependence of microwave absorption or SAR by a 7-cm radius, homogeneous spherical model of organs with brain- and muscle-like materials was given in volume 3 of this book series [Lin, 2000]. The computation from the Mie theory showed that while SARs vary greatly with frequency. For the microwave frequencies of interest (0.433 and 6.00 GHz), SARs are nearly constant, although average SAR decreases or increase slightly in proportion to frequency for the higher and lower frequencies, respectively. The increase in peak SAR at higher frequencies reflects the fact that at these frequencies the same amount of incident power is deposited in decreasingly thinner superficial layers of the tissue model.

The SAR distributions – computed using the finite difference, time domain (FDTD) method – in a 2-cm diameter, homogeneous spherical model of muscle equivalent tissue are shown in Fig. 2 for 433, 915 and 2450 MHz. Clearly, the distribution of SAR inside the muscle sphere is not uniform, and they differ for different frequencies. At the lower frequencies, i.e., 433 and 915 MHz, the SAR is the highest near the front surface and decreases towards the far surface. At 2450 MHz, the highest microwave absorption peaks near near the center of the tissue volume. The coupling of 2450 MHz plane microwave radiation into variously sized spherical model of muscle tissues is illustrated by Fig. 3. It can be seen that the SARs induced by the same plane wave inside models of 1.0 to 10 cm in

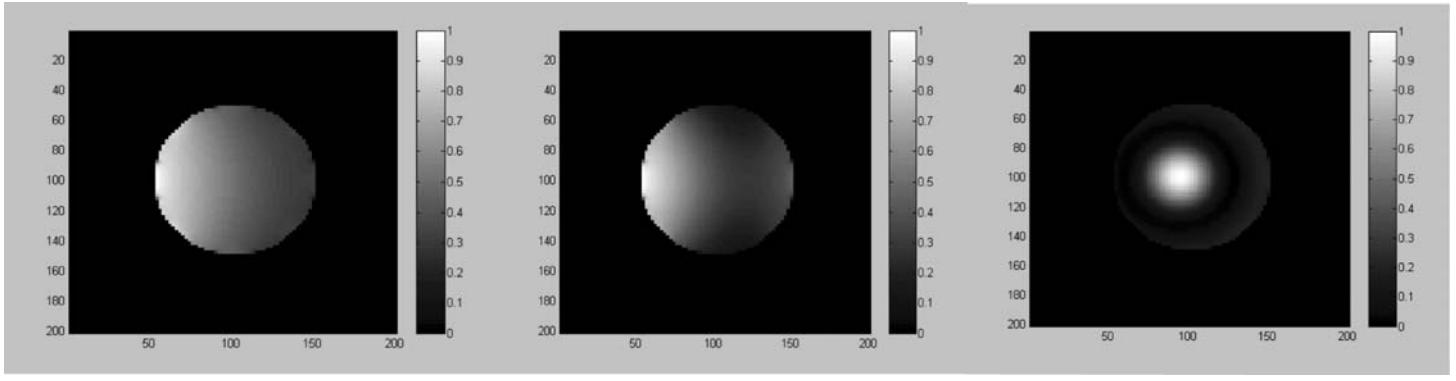

433 MHz 915 MHz 2450 MHz

Figure 2. Computed SAR distributions in a 2-cm diameter, homogeneous spherical model of muscle equivalent tissue at 433, 915 and 2450 MHz. The plane wave incidents from the left.

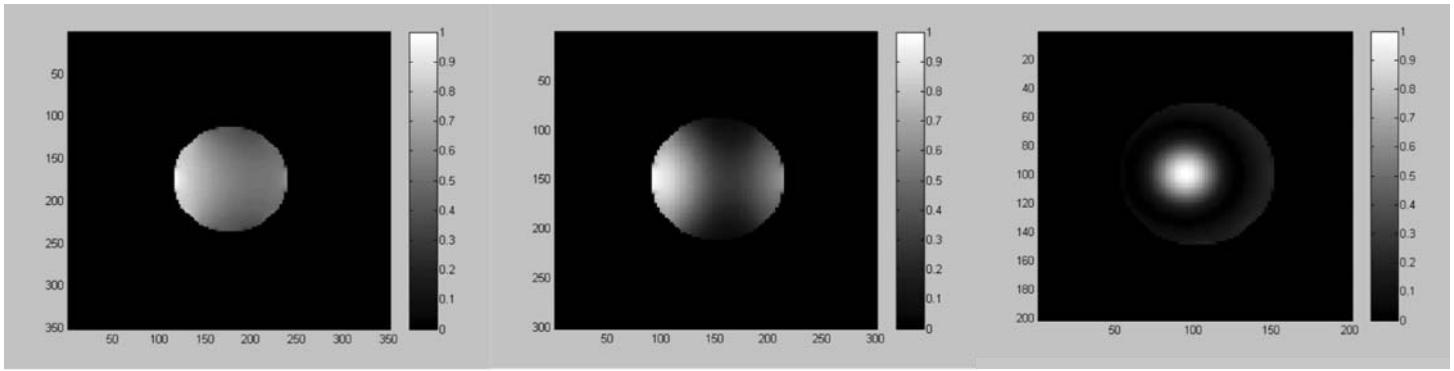

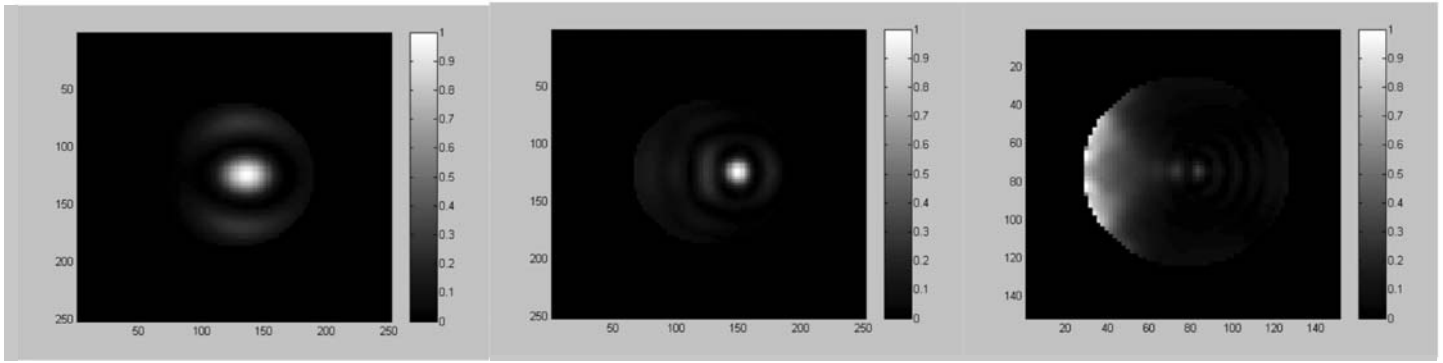

Figure 3. The distribution of 2450-MHz microwave energy (SAR) inside spherical models of muscle tissue with diameters of 1.0 to 10 cm. The plane wave is incident from the left.

diameter vary from a simple monotonic decrease away from the source to a very complex pattern of multiple peaks. The sharp change in SAR or power deposition as the model size is increased indicates an initial increase in the coupling of microwave energy into the tissue model. However, the increase is followed by some resonant absorption until the size of the model becomes larger than the wavelength. It is then followed by a falloff in SAR as the incident power is deposited in decreasingly thinner superficial layers of the model. (See [Taflove 1995; Kunz and Luebbers 1993; Lin and Gandhi, 1996] for FDTD computations.)

4.3. Thermal Response in Tissues

The dynamic temperature variation in tissue is a function of tissue composition, heat convection, thermal conduction, and heat generation due to metabolic processes, in addition to microwave energy absorption. The Pennes approximation to biological heat transfer via diffused conduction and blood convection in tissue can provide useful insights into microwave-induced rises in tissue temperature [Pennes, 1948]. Specifically, the Pennes bio-heat transfer equation states that

$$\rho c(dT/dt) = SAR + \zeta \nabla^2 T - V_s(T - T_o), \tag{20}$$

where T is the tissue temperature (°C), T_o is the ambient temperature in tissue (°C), ρ is the density, c is the specific heat, SAR is the heating potential generated by microwave power deposition, ζ is the coefficient of heat conduction, and V_s is the product of flow rate and heat capacity of blood. Note that this equation neglects metabolic heat production since in this present application the duration of microwave application is μs – a duration insufficient for significant metabolic heat contribution to tissue temperature elevation.

The heat conduction term, $\zeta \nabla^2$ T in equation (20) is a passive phenomenon that takes place slowly in biological tissues. Therefore, the rate of temperature rises in tissue is only weakly augmented by heat conduction. The convective heat exchange term, $V_s(T - T_o)$ in equation (20) can serve to moderate temperature elevation in tissues because heat is actively transported away from the generating site. However, in the case of a short μs-wide pulse of microwave application, heat transfer by blood convection – with finite blood velocity, would have an insignificant contribution to tissue temperature elevation. Thus, the rise in tissue temperature during the initial or a transient period of microwave energy absorption is linearly proportional to the value of SAR, such that

$$\rho c(dT/dt) = SAR \tag{21}$$

Thus, under these circumstances, SAR, as given previously,

$$SAR = (1/2)\sigma E^2 = \rho c(dT/dt) \tag{22}$$

is equal to the rate of energy absorption by the medium, and can be derived from the rise in tissue temperature during a brief transient period of microwave energy deposition.

4.4. Microwave Induced Thermoelastic Pressure Waves in Tissue

In the process of microwave propagation in tissue medium, a portion of the microwave energy is absorbed and converted into heat that produces a temperature rise in the tissue. If the temperature rise occurs abruptly and takes place in a very short (μs) time, it results in a

rapid expansion of the tissue and generates strains in the elastic tissue medium, which leads to formation of stress waves that propagate away from the site of generation. The amplitude of the thermoelastic pressure, p, in a planar tissue medium is given by [Lin, 1978],

$$\mathrm{p} = [2\alpha \mathrm{P}\tau(3\chi + 2\xi)\phi]/(\rho \mathrm{c}) \tag{23}$$

where α being the microwave attenuation coefficient, τ is the pulse width, χ and ξ are Lame's constants, ϕ is the coefficient of thermal expansion, P is the incident power density, ρ is tissue density, and c is the specific heat. Note that αP is the microwave energy absorption term, and is related to SAR by the tissue density so that $\alpha \mathrm{P}/\rho = \mathrm{SAR}$. Thus, equation (23) can be expressed in terms of SAR as,

$$\mathrm{p} = [2(\mathrm{SAR})\tau(3\chi + 2\xi)\phi]/\mathrm{c} \tag{24}$$

The amplitude of microwave-pulse-induced thermoelastic pressure in a spherical model of tissue with free surfaces, is given by [Lin, 1976a,b,c; 1977a; 1978],

$$\mathrm{p} = [4\xi(\mathrm{SAR})\upsilon\tau]/[(\chi + 2\xi)(\rho \mathrm{c})] \tag{25}$$

where υ = velocity of acoustic wave propagation. If the surface of the tissue model is constrained, such as for brain matter inside a bony skull, the amplitude of microwave-pulse-induced thermoelastic pressure changes to [Lin, 1977b],

$$\mathrm{p} = [4\mathrm{a}\xi(\mathrm{SAR})\upsilon\tau]/[(\chi + 2\xi)(\rho \mathrm{cr})] \tag{26}$$

where a and r are the radius and radial variable for the spherical model. Observe that the strength of thermoelastic generated pressures in biological tissues, in general, is a function of the microwave pulse width, SAR, thermoelastic properties of tissue, and dimensions of tissue media.

The frequency of microwave-pulse-generated thermoelastic pressure waves, for a spherical tissue model with a stress-free surface, is given by [Lin, 1976c; 1977a; 1978],

$$\mathrm{f_m} = \mathrm{m}\upsilon/(2\mathrm{a}), \tag{27}$$

where the frequency modes are associated with integers, $\mathrm{m} = 1, 2, 3, \ldots$, and for a spherical tissue model with a constrained surface, the pressure wave frequencies are,

$$\mathrm{f_m} = \mathrm{k_m}\upsilon/(2\pi \mathrm{a}) \tag{28}$$

where $\mathrm{k_m} = 4.49, 7.73, 10.9, 14.1, 17.2, 20.4, \ldots$ for $\mathrm{m} = 1, 2, 3, 4, 5, 6, \ldots$ [Lin, 1977b; 1978]. Note that the frequencies of thermoelastic pressure waves are functions of tissue size, acoustic property and boundary condition associated with the tissue medium.

Some computed acoustic frequencies, as a function of the size of tissue models, for a velocity of thermoelastic pressure waves at 1550 m/s in tissue spheres are provided in Table 5. It shows that the fundamental acoustic frequencies and harmonics are all higher for a constrained tissue surface compared to that for a free surface. For tissue spheres ranging in radii from 1 to 50 mm, the fundamental acoustic frequencies vary from 160 to 780 kHz for free surfaces, and 0.22 to 1.11 MHz for constrained surfaces. Note that frequencies of the 5^{th} harmonic cover the range from 0.78 to 3.88 MHz for free surfaces, and 0.85 to 4.25 MHz for constrained surfaces in tissue spheres whose radii are 1 to 50 mm. Since, *in vivo*, most tissues or organ surfaces are neither completely free, nor rigidly constrained, pulse-microwave generated thermoelastic pressure waves inside the human body

Table 5. Computed Acoustic Frequencies of Thermoelastic Pressure Waves in Spherical Models of Biological Tissues

	Frequency (MHz)			
	Free Surface		Constrained Surface	
Radii of Tissue Model (mm)	f_1	f_5	f_1	f_5
1	0.78	3.88	1.11	4.25
3	0.26	1.29	0.37	1.42
5	0.16	0.78	0.22	0.85
10	0.08	0.39	0.11	0.43
20	0.52	0.19	0.055	0.21
30	0.26	0.13	0.037	0.14
40	0.019	0.97	0.028	0.11
50	0.016	0.78	0.022	0.08

*f_1 = fundamental frequencies; f_5 = frequencies of 5^{th} harmonic

most likely would have acoustic frequencies or wavelengths somewhere in between those presented here.

For applications like imaging, it is useful to examine the thermoelastic acoustic frequency spectra produced by microwaves of different combinations of frequency and pulse width, impinging on a flat surface. Fig. 4 illustrates variations of the peak thermoelastic pressure intensity as a function of microwave pulse width for up to 25 μs and for microwave frequencies of 0.433, 0.915, 2.45, 5.0 and 8.0 GHz [Chan, 1988]. Note that for microwave energies at frequencies lower than 2.45 GHz, the peak intensity does not depend on microwave pulse width. Fig. 5 displays the intensity variation - as a function of acoustic frequency over range of 1 kHz to 1 MHz - for microwaves of 0.433, 2.45, and 8 GHz, at a pulse width of 2 μs [Chan, 1988]. It can be seen that the bandwidth, band-shape, and

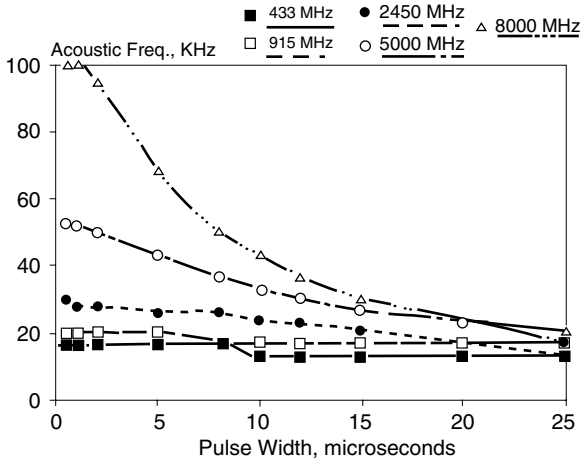

Figure 4. Variation of peak thermoelastic pressure intensity as a function of microwave pulse width for up to 25 μs and for microwave frequency [From Chan, 1988 by Permission].

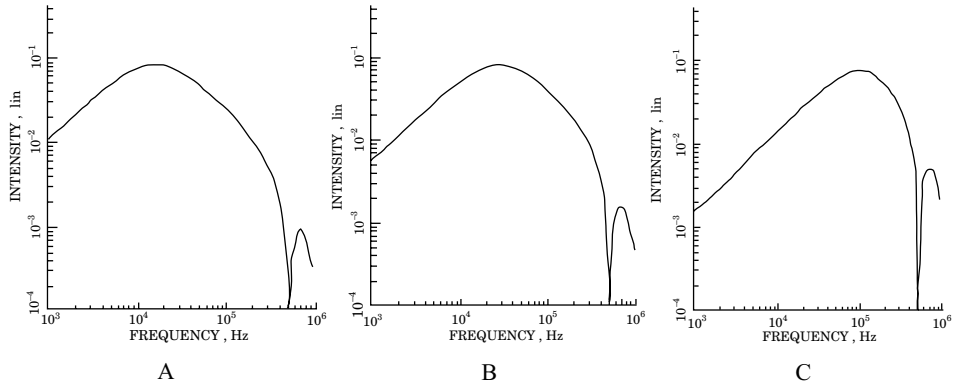

Figure 5. Thermoelastic pressure intensity variations as a function of acoustic frequency over range of 1 kHz to 1 MHz for microwaves of 0.433, 2.45, and 8 GHz at a pulse width of 2 μs [From Chan, 1988 by Permission].

maximum intensity do not vary much with the frequency of microwave energy. However, a significant influence by the microwave pulse width is shown in Fig. 6. As exhibited in Equations (23) and (24), the thermoelastic pressure amplitude increases with longer pulse width. In contrast, the bandwidth is inversely proportional to microwave pulse width, and the band shape also is more smooth for shorter pulse widths.

5. MICROWAVE THERMOELASTIC IMAGE FORMATION

Clearly, a high-peak-power microwave pulse – upon absorption by soft tissues in the body – can launch a thermoelastic wave of acoustic pressure in the tissue medium, which propagates away from the launching site in all directions. The thermoelastic pressure can

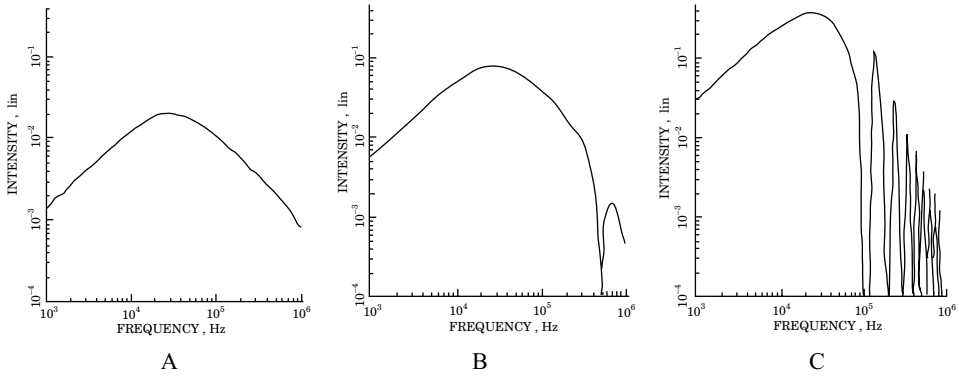

Figure 6. Influence of the microwave-pulse width.on the thermoelastic pressure intensity variations at 0.5, 2.0, and 10 μs. [From Chan, 1988 by Permission].

be detected with an acoustic or ultrasound sensor or transducer. Indeed, a duel modality for tissue imaging was proposed that employs the microwave pulse-induced thermoelastic pressure waves to form planar and/or tomographic images, as mentioned previously. Specifically, there is an explicit relation between the absorbed microwave pulses, the thermal characteristics of tissue, and the induced thermoelastic pressure waves in biological tissues. Different regions and organs with differing dielectric permittivity would exhibit differential absorption of microwave energy and varying characteristics of generated thermoelastic pressure waves. Thus, MTT possesses the unique features of differential dielectric absorption of microwave energy and finer spatial resolution of ultrasonic energy. These unique features may allow microwave thermoelastic imaging and tomography to become a competitive modality, and to permit noninvasive imaging of tissue characteristics, which are not easily identifiable by other modalities.

As mentioned, the general principles of MTT, and some results have been described in published literature and conference papers since the early 1980's. In recent years, the uniqueness of MTT has attracted considerable interest to develop a microwave thermoelastic imaging and tomography system for near real-time detection and imaging of mammary tumors, especially for the early detection of breast cancers.

5.1. Preliminary Investigations of Microwave Thermoelastic Imaging

The researches on thermoelastic imaging of gross anatomical structures that began in the early 1980's were essentially feasibility studies. [Olson, 1982; Olsen and Lin, 1983b]. There also was an effort attempting to apply it as a probe of local variations of SAR distribution in conjunction with the use of radio frequency energy for hyperthermia treatment of cancer [Caspers and Conway, 1982]. Nevertheless, most of the investigations reporting imaging studies aimed toward anatomical structures. The first study had employed a system consisting of a model of the human hand with dielectric properties of muscle (Fig. 7). The hand model was immersed in a tank of water, and at its surface, an open-waveguide applicator delivered the microwave pulses to the hand-in-water phantom. Microwave-induced thermoelastic pressure waves were detected by using a square of piezoelectric transducer array located at the bottom of the tank.

In our laboratory, we constructed a thermoelastic projection imaging system [Lin and Chan, 1984; Chan, 1988]. Cylindrical phantom models with dielectric properties, similar to that of normal and maligna nt breast tissues, were immersed in a tank of water at whose surface microwave pulses were applied. Microwave-induced thermoelastic pressure waves were detected by a 20×20 piezoelectric transducer array (ITC, lead zirconate titanate), located at the bottom of the tank. These transducers have a free field voltage sensitivity of -220 dB (re:1V/μPa), at 70 kHz. For each data point, a waveform was captured on the oscilloscope screen and stored on disk (Fig. 8). The received signals were then amplified, filtered and converted into digital form, off line, using a 2-MHz Nicolet oscilloscope. The maximum peak of each waveform was then read off the oscilloscope and key into the computer. For each image, 400 data points were acquired. This resulted in 400 image-pixel values (produced by a 0.9×0.9 cm hydrophone transducer). Fig. 9 illustrate a time-of-flight thermoelastic image obtained by the microwave pulse - hydrophone transducer array

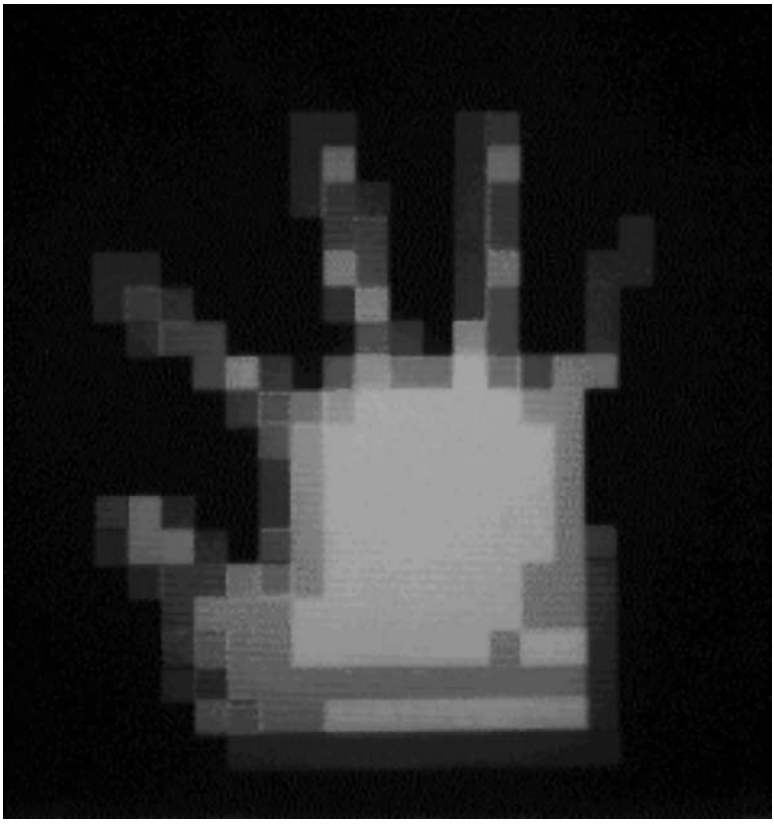

Figure 7. Computer display of the thermoelastic image of a model of the human hand with dielectric properties of muscle [From Olsen and Lin, 1983].

arrangement, with no object present in the field. The rings seen in the image correspond to different propagation times, the shortest of which is seen in the middle and longest at the corners.

Fig. 10 gives the thermoelastic image of a phantom which was produced interactively, where the processing techniques of subtraction, normalization, convolution filtering, grey scale transformation, and thresholding were used to enhance the image. Briefly, the phantom consisted of two glass test tubes 0.9 cm in diameter, filled with tissue equivalent materials, and they were placed 1.0 cm apart. The equivalent dielectric materials were an ethylene glycol in saline mixture and a semisolid mixture consisting of polyethylene powder, saline, and a gelling agent. It can be seen from Fig. 10 that the test objects could be clearly differentiated. Note that the ratio between the amplitude of the acoustic signals from the phantoms was 6.75 to 3.51 or nearly 2-to-1, which approximates the difference in dielectric permittivity between malignant and normal mammary tissues. It also demonstrates the above-mentioned prediction that malignant breast tissues would generate significantly higher amplitude of thermoelastic pressure waves - a better signal-to-noise ratio, which should render greater discriminations between malignant and normal breast tissues. Preliminary investigation of

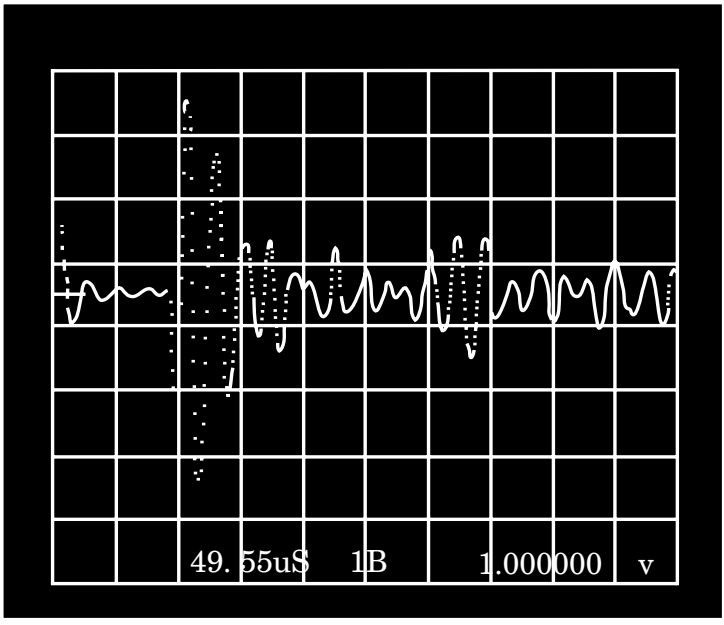

Figure 8. A representative waveform from each hydrophone transducer captured on the oscilloscope screen and stored on disk.

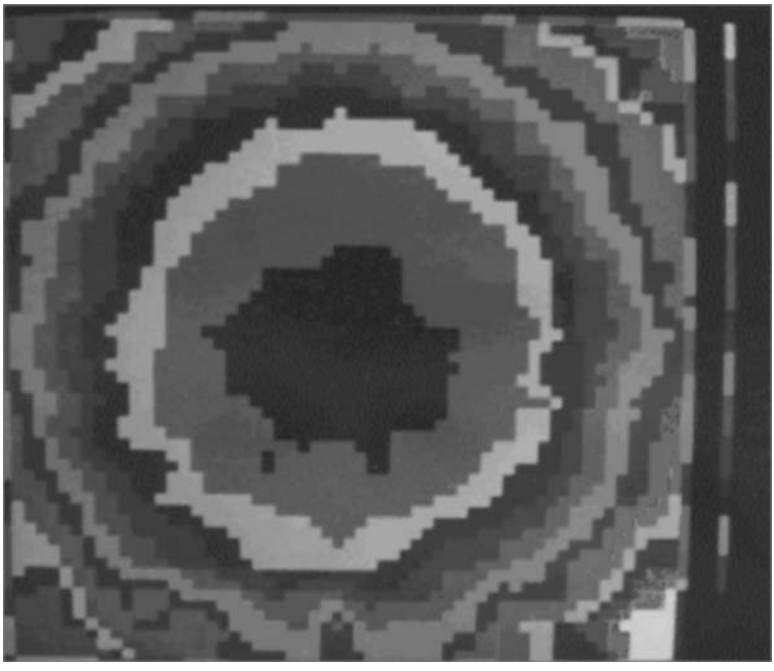

Figure 9. A time-of-flight thermoelastic image obtained by the microwave pulse - hydrophone transducer array arrangement, with no object present in the field.

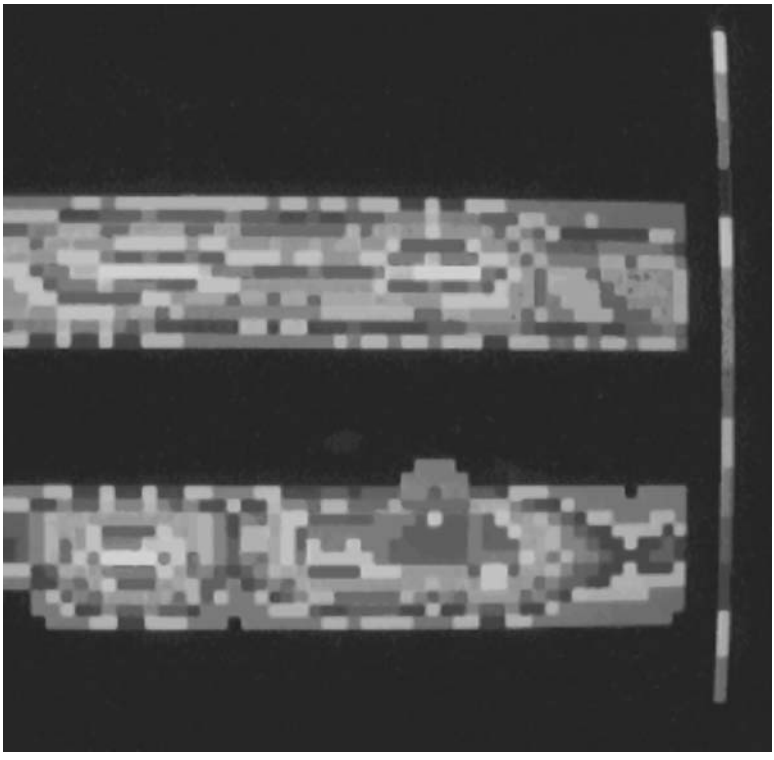

Figure 10. Microwave thermoelastic image of a phantom consisted of two glass test tubes 0.9 cm in diameter, filled with tissue equivalent materials, and they were placed 1.0 cm apart [From Chan, 1988 by Permission].

the spatial resolution indicated that the system is capable of resolving objects, which are of a one-unit transducer size, separated by a distance of one-transducer unit. This translates into about 1 cm in the above studies [Chan, 1988]. It suggests that decreasing the size of the transducer may lead to better spatial resolution.

5.2. Early Investigations of Microwave Thermoelastic Tomography

Tomography involves the formation of internal images of an object through which beams from a radiant energy source have passed through, and the measurement of the transmitted beams from many different directions within a plane through the body. From these measurements, an image of the cross section of the body is mathematically reconstructed using a computer algorithm, and then formatted to display on a screen. A tomographic system typically consists of two major components: a signal-detection component consisting of a radiant energy source and the detector system, and computer-based system, which manages the process and processes the collected data, reconstructs the image, and manipulates the image for display on a viewer. Clearly, the source-detector part is the salient component of any tomographic system, which provides the physical means to acquire the raw information

for image formation. Thus, MTT as a duel modality imaging system is unique in that the source is pulse-microwave energy and the detector is ultrasound.

Our investigations on microwave thermoelastic tomography were initiated by first conducting a series of computer simulations of microwave thermoelastic tomographic imaging of tissue phantoms consisting of one, two or three circular cylinders. Both parallel and fan beams, along with a filtered back projection algorithm were used in conjunction with the Shepp-Logan filter for the reconstruction [Su, 1988; Su and Lin, 1991]. In addition, we simulated both the transmission and emission cases for the tomographic reconstruction, using the same phantoms. As mentioned previously, tissues and organs with different dielectric, thermal, and elastic properties, upon absorption of pulse-microwave energy would emit acoustic waves at different strengths and frequencies. Results showed that in shape, size and location, the reconstructed images correspond well with to the original phantoms. The grey levels of the reconstructed images corresponded well to the attenuation constants in the transmission case. In the case of emission tomography, however, they were proportional to the ratio of the emitted signal strength and the attenuation constant. It was found by experimenting with the phantoms for varying numbers of projections - measurement from different directions - that 16 projections are the minimum number required to yield a reasonably accurate reconstruction. Fig. 11 shows the reconstructed cross sectional images using 16 projections assuming perfect data and absence of noise.

A prototype microwave thermoelastic tomographic system - essentially based on the same design described above [Fig. 12, see also Lin and Chan, 1984; Chan, 1988; Su, 1988],

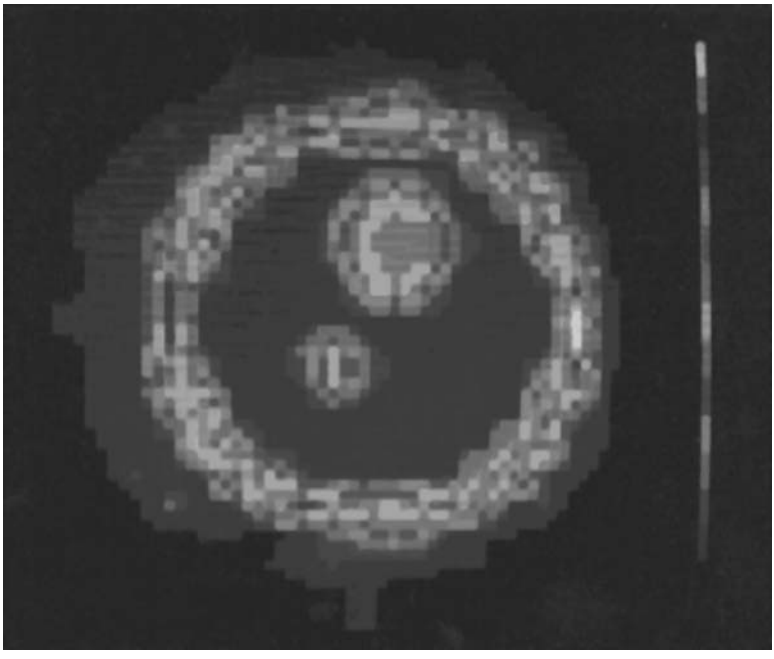

Figure 11. A reconstructed cross sectional image using 16 projections assuming perfect thermoelastic data and absence of noise [From Su, 1988 by Permission].

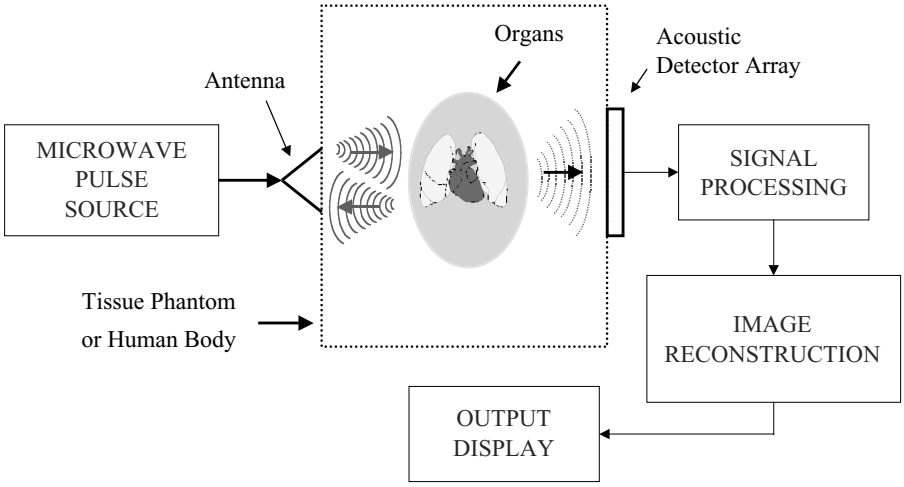

Figure 12. A schematic diagram of the microwave thermoelastic tomography and imaging system.

with the addition of a mini-gantry platform for rotating the phantom, was constructed. The pulse microwave energy was provided by a microwave pulse generator (Epsco PH40K) with a 2450-MHz plug in. The duration and the peak power of the microwave pulse were externally controllable from 0.4 to 25 μs and up to 40 kW, respectively. For a majority of the experiments, a 2-μs pulse width and a peak power of 30 kW were used. The projections were obtained by rotating the phantom through calibrated $\pi/16$ positions in a specially fabricated Delrin mini-gantry phantom platform. The same 20×20 element piezoelectric transducer array, in a water tank, was used for data collection. The data used to reconstruct the images were pre-processed to reduce noise in the signals by applying a smoothing filter, which also would reduce the sharpness of the images. Furthermore, a thresholding technique was applied for better object differentiation.

Reconstructed tomographic images from phantoms with one, two, and three muscle-equivalent cylinders are given in Fig. 13. The left figure is for a cylinder, 1.5 cm in diameter, located at the middle of the reconstruction region. The center image represented two

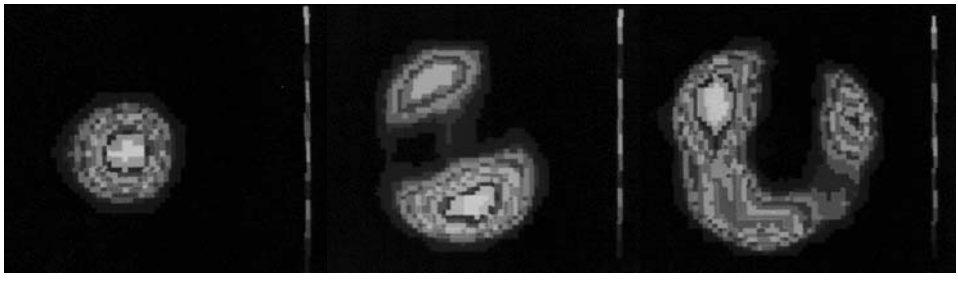

A B C

Figure 13. Reconstructed tomographic images from phantoms with one, two, and three muscle-equivalent cylinders [From Su, 1988 by Permission].

cylinders, 1.2 and 1.8 cm in diameter, respectively, separated 1 cm apart. The image on the right is for three 1.5-cm cylinders, separated by 1 or 2 cm. Clearly, the phantom locations are well represented in the tomographic images, especially for an object at the middle of the reconstruction zone. Also, the objects with separation distances of 1 cm are easily resolvable. The relative shape and size, and object location and property are consistently displayed. For three objects, the images were degraded by the phenomena of wave diffraction and refraction, and umbrae of objects in the field. Moreover, the images are distorted when objects in the phantoms are off center. Some of these difficulties may be minimized by choosing a different set of microwave frequencies and pulse widths. They also could be mitigated by using a microwave antenna, which can provide a more parallel beam for the projections, or a finer array of smaller ultrasonic detectors. It is noted that the prototype MTT system was able only to demonstrate the feasibility of MTT in the transmission mode. The potential advantages of an emission operation, with the possibility of yielding unique information on tissue characteristics was not tested in the prototype system. Nevertheless, the results showed that biological materials with high, moderate, and low water contents can be differentiated from reconstructed MTT images.

5.3. Further Developments

Recent efforts have reaffirmed that a microwave thermoelastic tomographic system that combines microwave energy absorption and ultrasonic energy emission is a unique nonionizing imaging modality. A majority of current investigation is targeting MTT as a modality that may complement mammography for early detection of breast cancer. In addition, there have been some studies aimed toward a more exact reconstruction of microwave properties [Ku and Wang, 2000; Xu and Wang, 2002]. However, although it is an approximation, the often used filtered back projection algorithms have given reconstructed images that agree well with the original specimens.

Some very promising results were provided in a series of studies using pulses of 434 MHz microwave energy. They had named their system thermoacoustic computed tomography (TCT). Over the last few years, the group has experimented with several variations of the instrument design. The systems were specifically targeted for human breast imaging [Kruger et al, 1999; 2000], and consist of a hemispherical, 300-mm-diameter bowl in which 64 piezo-ceramic transducers were attached in a spiral pattern. The bowl was mounted on a cylindrical shaft, and could be rotated 360° about its axis using a stepper motor. The entire device was immersed in deionized water contained in a cylindrical tank. For human breast imaging, the tank itself was placed beneath an examination table, in which a circular hole was cut and mated to the top of the TCT imaging tank. Initially, a helical RF antenna was installed at the base of the transducer array. A semi-rigid coaxial cable, which passed through the center of the shaft, was used to feed microwave energy to the helical antenna. This antenna arrangement produced circularly polarized microwaves, and a slowly varying spatial intensity pattern within the imaging volume. Microwave pulses (0.5-μs wide at a peak power of 25 kW) were delivered at a nominal repetition rate of 4,000 Hz. More recently, an updated version of the system replaced the helical antenna with waveguide antennas [Kruger et al., 2001; 2002]. The waveguide antennas produced linear polarization, and had averted the strong, thermoelastic signals generated at the surface of the helical antenna. These unwanted, thermoelastic signals overlapped in time with the much weaker thermoelastic signals from the microwave absorbing tissues. A schematic diagram

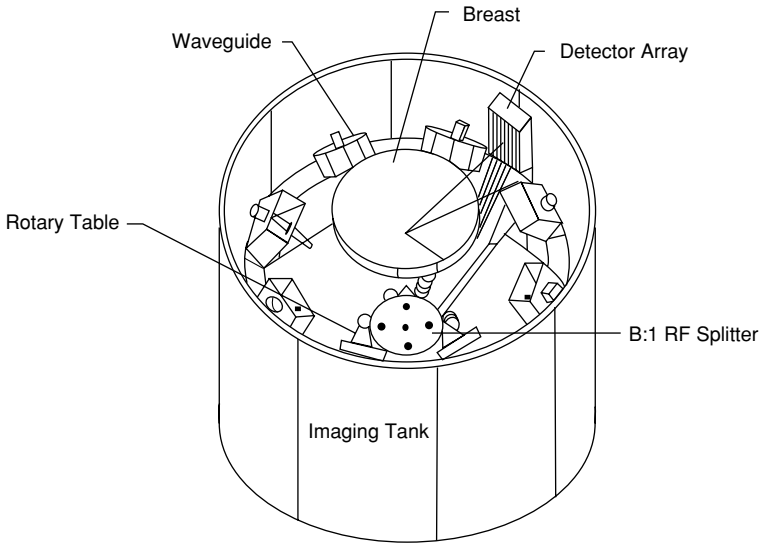

Figure 14. A schematic diagram of the thermoacoustic tomography (TCT) system. This system has eight waveguide antennas and 128 ultrasonic transducers arrayed on the hemispherical surface[From Kruger et al., 2002 by Permission].

and a photograph of the latter system are shown in Figs. 14 and 15. Note that this system has eight waveguide antennas and 128 ultrasonic transducers arrayed on the hemispherical surface.

A series of coronal sections and one sagittal section of the TCT images from a patient's breast in the region of the cancerous mass are shown in Fig. 16. The arrows in these

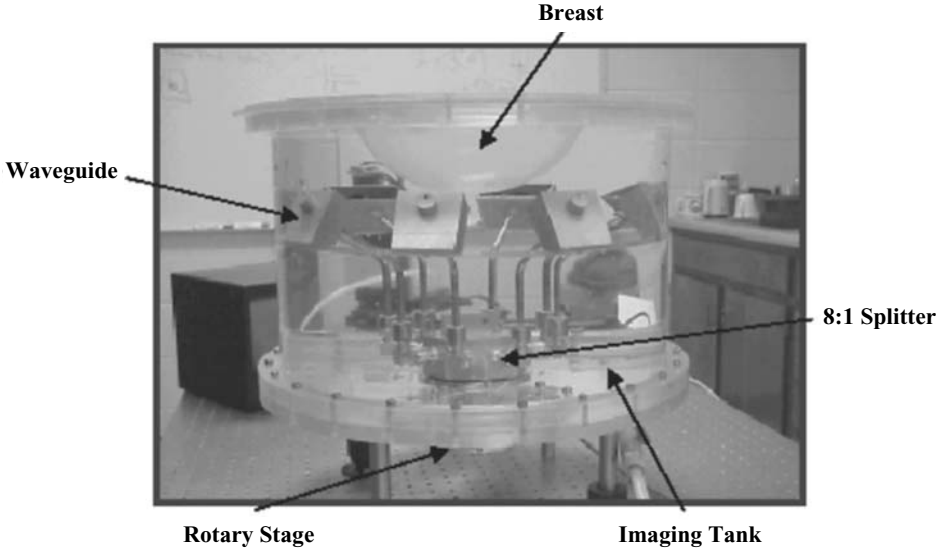

Figure 15. A photograph of the thermoacoustic tomography (TCT) system [From Kruger et al., 2002 by Permission].

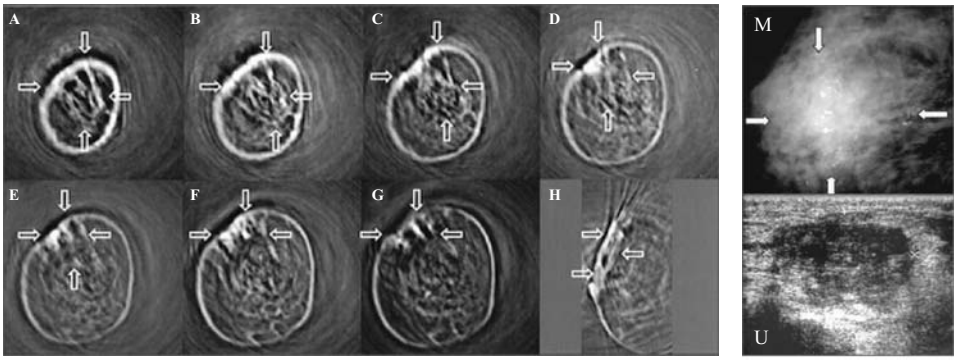

Figure 16. A series of coronal sections and one sagittal section of the TCT images from a patient's breast in the region of the cancerous mass are shown in M and U. The arrows in these images indicate a large, lobulated mass. An increase in contrast of approximately twofold was seen in the region of this large mass [From Kruger et al., 2000 by Permission].

images indicate a large, lobulated mass. An increase in contrast of approximately twofold was seen in the region of this large mass [Kruger et al., 2000]. The x-ray mammogram (Fig. 16, M) from the same patient indicated a large, poorly defined mass in the upper right breast. The transverse ultrasonographic scan (U) showed the same mass (indicated by calipers). Examples of cysts, fibroadenomas, and ductal carcinomas in TCT images are given in Fig. 17 [Kruger et al., 2001]. In Fig. 17a, the cysts can be readily visualized as dark regions surrounded by brighter glandular tissue, with higher microwave absorption. Fibroadenomas absorb microwave energy less, and are represented by a weaker contrast enhancement in TCT images. Fig. 17c illustrates the appearance of ductal carcinoma *in situ*. Thus, fibrocystic disease was well seen - cysts appearing as areas of low microwave absorption. Fibroadenomas did not demonstrate contrast enhancement In general, cancer displayed higher microwave absorption than surrounding tissues.

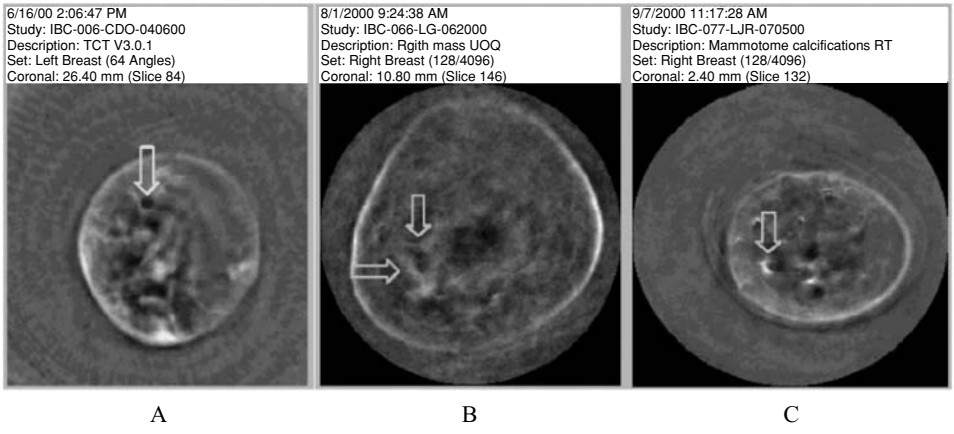

Figure 17. Examples of TCT images of (a) cysts, (b) fibroadenomas, and (c) ductal carcinomas [Kruger et al., 2001 by Permission].

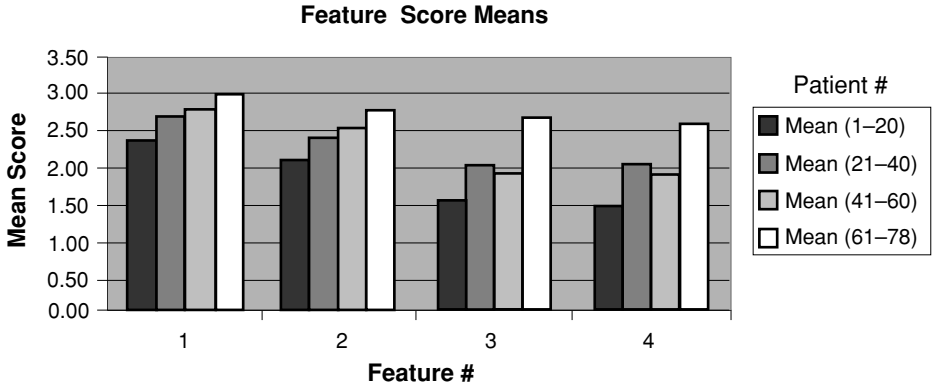

Figure 18. Results of image quality evaluation for four features: (1) areolar complex, (2) skin margin, (3) glandular tissue, and (4) Cooper's ligament, averaged for patients number 1–20, 21–40, 41–60, and 61–78. [From Kruger et al., 2001 by Permission].

The potential clinical utility of using TCT to image the breast was assessed in a retrospective pilot study of 78 patients [Kruger et al., 2001]. The patient volunteers were classified into three age groups (<40, 40–50, >50 years). The study population was further segregated into normal and suspicious groups, based on the previous x-ray mammography and ultrasound. Image quality was evaluated qualitatively by consensus of two trained mammographers using a 4-point scale (1 = not visualized; 2 = poorly visualized; 3 = adequately visualized; and 4 = excellently visualized). The appearance of normal anatomy, cysts, benign disease and cancer was noted. Fig. 18 gives results of image quality evaluation for four features (areolar complex, skin margin, glandular tissue, and Cooper's ligament), averaged for patients number 1–20, 21–40, 41–60, and 61–78. Two trends were evident. In general, image evaluation scores improved throughout the course of the study. Also, the scores of the four features followed the pattern: areolar complex > skin margin > glandular tissue > Cooper's ligament. The mean scores of all four features were averaged for patients with different density of breast. Fig. 19 shows that the more dense the breast the better the TCT images were scored.

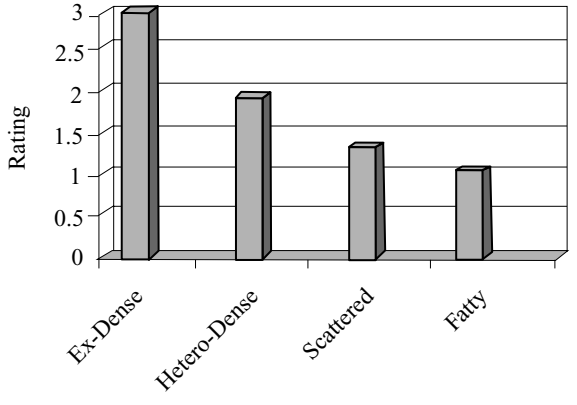

Figure 19. Image quality as a function of breast density; the more dense the breast the better the TCT images were scored [From Kruger et al., 2001 by Permission].

Likewise, the TCT images of breasts of younger women were judged to be better than those of older women. These data from a preliminary, retrospective, not-blinded study indicated that TCT image quality was dependent upon both patient age and breast density, and the quality improved with both increasing breast density and decreasing patient age - contrary to X-ray mammography. These findings also suggest that microwave thermoelastic tomographic imaging could potentially complement X-ray mammography to detect breast cancers when they are small, before they have spread and become incurable.

SUMMARY

Microwave thermoelastic tomography and imaging are a unique, noninvasive, duel imaging modality, which depends on microwave-pulse-induced thermoelastic pressure waves to form planar or tomographic images. Thermoelastic pressure waves are generated by absorption of pulsed microwave energy and are detected by ultrasonic transducers to form planar and tomographic images. Since the generation of thermoelastic pressure waves depends on dielectric permittivity, specific heat, and elastic properties of tissue, MTT combines the advantages of high contrast offered by microwave absorption and the fine spatial resolution furnished by ultrasound. These unique features are being explored as an imaging modality for noninvasive imaging and characterization of biological tissues. This chapter discussed the science of thermoelastic wave generation and propagation in biological tissues and the design of prototype tomographic imaging systems. I provided illustrations of reconstructed tomographic images using filtered-back projection algorithms and discussed preliminary evaluations of the performance of microwave thermoelastic tomography in phantom models, and normal and tumorous breast tissues. In spite of the advances made to date, and the theoretical promise of imaging the breast with MTT, extensive developmental works are still ahead in order to produce a medical imaging device that can compete successfully with alternative imaging technologies.

ACKNOWLEDGMENTS. I wish to take this opportunity to thank Dr. Robert .A. Kruger at IUPUI, and of Optosonics Indianapolis, for providing some of the TCT figures used as illustrations, and Dr. Noam Alperin at UIC, for providing the MRI images, and Zhangwei Wang, my Ph.D. student, and my former Ph.D. students: Karen H. Chan, and Jeng-Lung Su for their efforts and dedication. Also, I wish to express my gratitude to all the sponsors of our research activity, especially, NSF and ONR.

REFERENCES

Campbell, A.M., Land, D.V., 1992, Dielectric properties of female human breast tissue measured in vitro at 3.2 GHz. *Phys. Med. Biol*. 37:193–210.

Chan, K.H., 1988, Microwave-induced thermoelastic tissue imaging. PhD dissertation, University of Illinois, Chicago, 1988.

Chan, K.H. and Lin, J.C., 1988 Microwave induced thermoelastic tissue imaging. *Proc. IEEE/EMBS Annual International Conference*, New Orleans,1988, pp. 445–446.

Chaudhary, S.S., Mishra, R.K., Swarup, A., and Thomas, J.M., 1984, Dielectric Properties of normal & malignant human breast tissues at radiowave & microwave frequencies. *Indian Journal of Biochemistry & Biophysics*, 21:76–79.

Chou, C.K. and Galambos, R., 1979, Middle ear structure contribute little to auditory perception of microwaves. *J. Microwave Power* 14:321–326.

Chou, C.K., Guy, A.W., and Galambos, R., 1976, Microwave induced cochlear microphonics in cats. *J. Microwave Power* 11:171–173.

Chou, C.K., Guy, A.W., Galambos, R., and Lovely, R., 1975, Cochlear microphonics generated by microwave pulses. *J. Microwave Power* 10:361–367.

Caspers, P. and Conway, J., 1982, Measurement of power density in a lossy material by means of electromagnetically induced acoustic signals for noninvasive determination of spatial thermal absorption in connection with pulsed hyperthermia. *Proc. 12th European Microwave Conf.*, Helsinki, Finland, pp. 565–568.

England, T.S., 1950, Dielectric properties of the human body for wave-lengths in the 1–10 cm range. *Nature*, 166:480–481.

England, T.S. and Sharples, N.A., 1949, Dielectric properties of the human body in the microwave region of the spectrum. *Nature*, 163:487–488.

Feig, S.A., 1996, Assessment of radiation risk from screening mammography. *Cancer*, 77:818–822.

Foster, K.R. and Finch, E.D., 1974, Microwave hearing: evidence for thermoacoustic auditory stimulation by pulsed microwaves. *Science*, 185:256–258.

Foster, K.R. and Schwan, H.P., 1989, Dielectric properties of tissues and biological materials: a critical review. *Crit. Rev. Biomed. Eng*. 17:25–104.

Franchois, A., Joisel, A., Pichot, C., and Bolomey, J.C., 1998, Quantitative microwave imaging with a 2.45-GHz planar microwave camera. *IEEE Trans. Med. Imaging* 17:550–561, 1998.

Frey, A.H., 1961, Auditory system response to radio frequency energy. *Aerospace Medicine*. 32:1140–1142.

Frey, A.H., 1962, Human auditory system response to modulated electromagnetic energy. *J. Applied Physiology.* 17:689–692.

Frey, A.H., 1971. Biological function as influenced by low-power modulated rf energy. *IEEE Trans. Microwave Theory and Tech.* 19:153–164.

Frey, A.H., and Messenger, R., 1973, Human perception of illumination of pulsed UHF electromagnetic energy. *Science*, 181:356–358.

Gabriel, S., Lau, R.W., and Gabriel, C., 1996, The dielectric properties of biological tissues: II. Measurements in the frequency range 10 Hz to 20 GHz. *Phys. Med. Biol*. 41:2251–2269.

Goss, S.A., Johnston, R.L., and Dunn, F., 1978, Comprehensive compilation of empirical ultrasonic properties of mammalian tissues. *J. Acoust. Soc. Am.* 64:423–457.

Goss, S.A., Johnston, R.L., and Dunn, F., 1980, Compilation of empirical ultrasonic properties of mammalian tissues II. *J. Acoust. Soc. Am.* 68: 93–108.

Gournay, L.S., 1966. Conversion of electromagnetic to acoustic energy by surface heating. *J. Acoustic Society of Am.,* 40:1322–1330.

Guerquin-Kern, J.L., Gautherie, M., Peronnet, P., Jofre, L., and Bolomey, J.C., 1985, Active microwave tomographic imaging of isolated, perfused animal organs. *Bioelectromagnetics*, 6:145–156,1985.

Guy, A.W., Taylor, E.M., Ashleman, B., and J.C. Lin, 1973, Microwave Interaction with Auditory Systems of Human and Cats, *Proc. IEEE International Microwave Symp.* Boulder, Colo., 1973, pp. 231–232.

Guy, A.W., Lin, J.C., Chou, C.K, 1975a, Electrophysiological effects of electromagnetic fields on animals. In: Michaelson et al., editors. *Fundamentals and Applied Aspects of Nonionizing Radiation*. Plenum Press, New York. pp. 167–211.

Guy, A.W., Chou, C.K., Lin, J.C., Christensen, D., 1975b. Microwave induced acoustic effects in mammalian auditory systems and physical materials. *Annals NY Academ. Sciences*, 247: 194–218.

Joines, W.T., Jirtle, R.L., Rafal, D., and Schaefer, J., 1980, Microwave Power Absorption Differences Between Normal and Malignant Tissue, *Int. J. Radiation Oncology Biol. Phys.*, 6:681–687.

Joines, W.T., Zhang, Y., Li, C. and Jirtle, R.L., 1994, The measured electrical properties of normal and malignant human tissues from 50 to 900 MHz", *Medical Physics*, 21:547–550.

Kerlikowske, K., Grady, D., Barclay, J., Sickles, E.A., and Ernster, V., 1996, Effect of age, breast density, and family history on the sensitivity of first screening mammography. *JAMA* 276:33–38.

Kerlikowske, K. and Barclay, J., 1997, Outcomes of modern screening mammography. *Monogr Natl Cancer Inst* 22:105–111.

Kerlikowske, K., 1997, Efficacy of screening mammography among women aged 40 to 49 years and 50 to 69 years: comparison of relative and absolute benefit. *J Natl Cancer Inst Monogr* 22:79–86.

Kruger, R.A., Kopecky, K.K., Aisen, A.M., Reinecke, D.R., Kruger, G.A., Kiser, W.L. Jr., 1999, Thermoacoustic CT with radio waves: a medical imaging paradigm. *Radiology*. 211:275–8.

Kruger, R.A., Miller, K.D., Reynolds, H.E., Kiser, W.L. Jr, Reinecke, D.R., and Kruger, G.A., 2000, Breast cancer in vivo: contrast enhancement with thermoacoustic CT at 434 MHz-feasibility study. Radiology. 216:279–283.

Kruger, R.A. and Kiser, Jr W.L., 2001, Thermoacoustic CT of the Breast: pilot study observations. *Proc.* SPIE 4256:1–5.

Kruger, R.A., Stantz, K,M., Kiser, Jr W.L., 2002. Thermoacoustic CT of the Breast. *Proc. SPIE* 4682:521–525.

Ku, G. and Wang, L.V., 2000, Scanning thermoacoustic tomography in biological tissue. *Med Phys*. 27:1195–1202, 2000.

Kunz, K.S., Luebbers, R.J., 1993., The Finite Difference Time Domain Method for Electromagnetics. CRC Press, Boca Raton, FL.

Larsen, L.E. and Jacobi, J.H., 1979, Microwave scattering parameter imagery of an isolated canine kidney, *Medical Physics.* 6: 394–403, 1979.

Lin, J.C., 1976a, Microwave auditory effect–a comparison of some possible transduction mechanisms. *J. Microwave Power*. 11:77–81.

Lin, J.C., 1976b, Microwave induced hearing sensation: some preliminary theoretical observations. *J. Microwave Power*. 11:295–298.

Lin, J.C., 1976c, Theoretical analysis of microwave-generated auditory effects in animals and man. In: Johnson CC, Shore ML, editors. *Biological Effects of Electromagnetic Waves*, BRH/DEW, vol. I, pp. 36–48.

Lin, J.C., 1977a, On microwave-induced hearing sensation. *IEEE Trans. Microwave Theory Techniques*. 25:605–613.

Lin JC. 1977b, Further studies on the microwave auditory effect. *IEEE Trans. Microwave Theory Techniques*. 25:936–941.

Lin, J.C., 1977c, Calculations of frequencies and threshold of microwave-induced auditory signals. *Radio Science* 12/SS: 237–252.

Lin, J.C., 1978, *Microwave Auditory Effects and Applications*. Springfield, Illinois: Charles C Thomas.

Lin, J,C., 1980, The microwave auditory phenomenon. *Proceedings of IEEE*. 68: 67–73.

Lin, J.C., 1981, The microwave hearing effect. In: Illinger KH, editor. *Biological Effects of Nonionizing Radiation*, Amer. Chem. Soc., pp. 317–330.

Lin, J.C., 1990, Auditory perception of pulsed microwave radiation. In: Gandhi OP, editor. *Biological Effects and Medical Applications of Electromagnetic Fields*. Prentice-Hall, New York, Chapter 12, pp. 277–318.

Lin, J.C., 2001, Telecommunications health and safety: Hearing microwaves: the microwave auditory phenomenon, *IEEE Antennas & Propagation Magazine*, 43/6:166–168.

Lin, J.C., 2004, "Biomedical Applications of Electromagnetic Engineering," In: R. Bansal, ed., *Handbook of Engineering Electromagnetics,* Marcel-Dekker, pp.

Lin, J.C. and Chan, K.M. Microwave thermoelastic tissue imaging–system design. *IEEE Trans. Microwave Theory Tech*. 32: 854–860, 1984.

Lin, J.C. and Gandhi, O.P., 1996, Computational methods for predicting field intensity, In: C. Polk and E. Postow, eds. *Handbook of Biological Effects of Electromagnetic Fields*. (), CRC Press, Boca Raton, FL. pp. 337–402.

Lin, J.C., Meltzer, R.J., and Redding, F.K., 1978, Microwave-evoked brainstem auditory responses. *Proc. Diego Biomed. Symp*. Academic Press, 17:451–466.

Lin, JC., Meltzer, R.J., and Redding, F.K., 1979a, Microwave-evoked brainstem potential in cats, *J. Microwave Power*. 14: 291–296.

Lin, J.C., Su, J.L., and Wang, Y.J., 1988, Microwave-induced thermoelastic pressure wave propagation in the cat brain. *Bioelectromagnetics* 9: 141–147.

Lu, Y., Li, B., Xu, J., and Yu, J., 1992, Dielectric properties of human glioma and surrounding tissue. *Int J Hyperthermia.* 8: 755–760.

Meaney, P.M., Paulsen, K.D, Hartov, A., and Crane, R.K., 1996, Microwave imaging for tissue assessment: initial evaluation in multitarget tissue-equivalent phantoms. *IEEE Trans. Biomed. Eng.* 43:878–890, 1996.

Michaelson, S.M. and Lin, J.C., 1987, *Biological Effects and Health Implications of Radiofrequency Radiation*, Plenum Press, New York, pp.120–134.

Nield, L.E., Qi, X., Yoo, S.J., Valsangiacomo, E.R., Hornberger, L.K., and Wright, G.A., 2002, MRI-based blood oxygen saturation measurements in infants and children with congenital heart disease. *Pediatr Radiol.* 32:518–522.

NIH Consensus Development Panel., 1997, National Institutes of Health Consensus Development Conference Statement: Breast Cancer Screening for Women ages 40–49, *J Natl Cancer Inst* 1997;89:1015–26.

Olsen, R.G., 1982, Generation of acoustical images from the absorption of pulsed microwave energy, *Acoustical Imaging*, vol. 11, J.P. Powers, ed., Plenum, New York, pp. 53–59.

Olsen, R.G. and Lin, J.C., 1981, Microwave pulse-induced acoustic resonances in spherical head models. *IEEE Trans. Microwave Theory Techniques* 29: 1114–1117.

Olsen, R.G. and Lin, J.C., 1983a, Microwave-induced pressure wave in mammalian brain, *IEEE Trans. on Biomedical Engineering* 30: 289–294.

Olsen, R.G. and Lin, J.C., 1983b, Acoustical imaging of a model of a human hand using pulsed microwave irradiation. *Bioelectromagnetics* 4: 397–400.

Pennes, H.H., 1948, Analysis of tissue and arterial blood temperatures in resting forearm," *Journal of Applied Physiology*, 1:93–122.

Plein, J.S., Ridgway, P., Jones, T.R., Bloomer, T.N., and Sivananthan, M.U., 2002,. Coronary artery disease: assessment with a comprehensive MR imaging protocol–initial results. *Radiology.* 225:300–307.

Ries, L.A.G., Kosary, C.L., Hankey, B.L., Miller, D.S., and Edwards, B.K., eds. *1999, The SEER Cancer Statistics Review*, 1973–1996. National Cancer Institute, Bethesda, MD.

Rogers, J.A., Sheppard, R.J., Grant, E.H., Bleehen, N.M., and Honess, D.J., 1983, The dielectric properties of normal and tumor mouse tissue between 50 MHz and 10 GHz *Br J Radiol*.; 56(665): 335–338.

Semenov, S.Y., Svenson, R.H., Boulyshev, A.E., Souvorov, A.E., Borisov, V.Y., Sizov, Y., Starostin, A.N., Dezern, K.R.,Tatsis, G.P., and Baranov, V.Y., 1996, Microwave tomography-two-dimensional system for biological imaging. *IEEE Transactions on Biomedical Engineering* 43:869–877.

Semenov, S.Y., Svenson, R.H., Bulyshev, A.E., Souvorov, A.E., Nazarov, A.G., Sizov, Y.E., Posukh, V.G., Pavlovsky, A., Repin, P.N., Starostin, A.N., Voinov, B.A., Taran, M., Tatsis, G.P., Baranov, V.Y., 2002, Three-dimensional microwave tomography: initial experimental imaging of animals. *IEEE Trans Biomed Eng*. 49:55–63.

Stark, D.D. and Bradley Jr., W.G., 1999, *Magnetic Resonance Imaging*, 3rd ed., St. Louis: Mosby-Year Book, 1999.

Su, J.L., 1988, Computer assisted tomography using microwave-induced thermoelastic waves.*PhD dissertation*, University of Illinois, Chicago.

Su, J.L. and Lin, J.C., 1987, Thermoelastic signatures of tissue phantom absorption and thermal expansion. *IEEE Transactions on Biomedical Engineering* 34:179–182.

Su, J.L. and Lin, J.C., 1991, Computerized Thermoelastic Wave Tomography, *World Cong. Med Physics and Biomed Engg*, Kyoto, Japan, July, 1991.

Taflove A. 1995, *Computational Electrodynamics: the Finite Difference Time Domain Method.* Artech House, Norwood, MA.

Taylor, E.M. and Ashleman, B.T., 1974, Analysis of central nervous involvement in the microwave auditory effect. *Brain Research* 74:201–208.

Tyazhelov, V.V., Tigranian, R.E., Khizhnian, E.P., and Akoev, I.G., 1979, Some pecularities of auditory sensations evoked by pulsed microwave fields. *Radio Science* 14(supp 6):259–263.

Ueno, S. and Iriguchi N., 2000, Principles and Horizons of Magnetic Resonance Imaging, In *Advances in Electromagnetic Fields in Living Systems*, vol. 3, Lin, J.C., ed., Kluwewr/Plenum, New York, pp. 39–71.

Watanabe, Y., Tanaka, T., Taki, M., and Watanabe, S.I., 2000, FDTD analysis of microwave hearing effect, *IEEE Trans. Microwave Theory Techniques* 48:2126–2132.

White, R.M., 1963, Generation of elastic waves by transient surface heating. *J. Applied Physics* 34:3559–3567.

Xu, M. and Wang, L.V., 2002, Pulsed-microwave-induced thermoacoustic tomography: filtered backprojection in a circular measurement configuration. *Med Phys*. 29:1661–1669.

Chapter 3

Diffuse Optical Imaging

Ilkka Nissilä, Tommi Noponen, Jenni Heino, Timo Kajava, and Toivo Katila

ABSTRACT

Diffuse optical imaging is a functional medical imaging modality which takes advantage of the relatively low attenuation of near-infrared light to probe the internal optical properties of tissue. The optical properties are affected by parameters related to physiology such as the concentrations of oxy- and deoxyhemoglobin. Instrumentation that is used for optical imaging is generally able to measure changes in the attenuation of light at several wavelengths, and in the case of time- and frequency-domain instrumentation, the time-of-flight of the photons in tissue.

Light propagation in tissue is generally dominated by scattering. Models for photon transport in tissue are generally based on either stochastic approaches or approximations derived from the radiative transfer equation. If a numerical forward model which describes the physical situation with sufficient accuracy exists, inversion methods may be used to determine the internal optical properties based on boundary measurements.

Optical imaging has applications in, e.g., functional brain imaging, breast cancer detection, and muscle imaging. It has the important advantages of transportable instrumentation, relatively high tolerance for external electromagnetic interference, non-invasiveness, and applicability for neonatal studies. The methods are not yet in clinical use, and further research is needed to improve the reliability of the experimental techniques, and the accuracy of the models used.

Ilkka Nissilä, Tommi Noponen, Jenni Heino, Timo Kajava, and Toivo Katila Laboratory of Biomedical Engineering, Helsinki University of Technology, P.O. Box 2200, 02015 HUT, Finland.

Advances in Electromagnetic Fields in Living Systems, Volume 4, edited by James C. Lin, Springer Science+Business Media, New York, 2005.

In this chapter, we describe the interaction between light and tissue, light propagation models and inversion methods used in optical tomography, and instrumentation and experimental techniques used in optical imaging. The main applications of optical imaging are described in detail, with results from recent literature.

1. INTRODUCTION

Near-infrared light penetrates relatively easily into tissue due to the existence of the so-called optical window of tissue in the wavelength range from 650 to 950 nm. A significant absorber in this wavelength range is hemoglobin. Jöbsis (1977) demonstrated that it is possible to monitor changes in the blood volume and tissue oxygenation in the brain non-invasively by measuring the attenuation of near-infrared light at several wavelengths. Hoshi and Tamura (1993) showed that the increased blood flow and oxygenation due to brain activation can also be detected using near-infrared spectroscopy (NIRS).

The nature of light propagation in tissue is complicated by the strong scattering of most tissue types. In order to develop an imaging modality based on the measurement of the characteristics of the light that has traveled through tissue, a model which accurately describes scattering and absorption in tissue should be used. Most researchers have used models based on the radiative transfer equation (RTE) or approximations derived from it. Most applications of near-infrared measurements to the human body require the measurement of the light that has traveled through several centimeters of tissue. In this case, light propagation can be considered to be diffuse.

Optical imaging using diffuse near-infrared light is primarily a functional imaging modality. The goal is to obtain quantitative information about changes in the optical properties inside the tissue using boundary measurements. The light is guided into tissue using source optodes distributed on the surface of the tissue, and detected using optodes typically placed in between the source optodes (Fig. 1a). In addition to the intensity of light, datatypes which describe the distribution of photon travel times through the tissue can be measured using time-resolved techniques.

In order to resolve the optical properties inside the tissue, model-based reconstruction techniques are needed. The sensitivity of optical measurements to changes in the internal

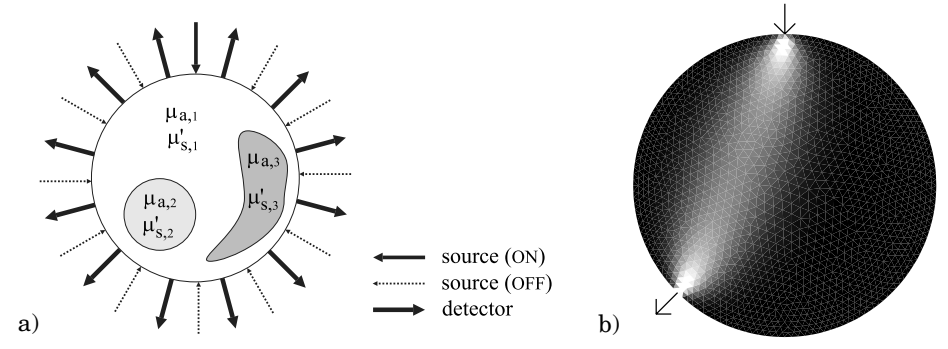

Figure 1. a) Principle of optical tomography. b) The sensitivity of the amplitude to changes in the absorption coefficient.

optical properties can be calculated based on the light propagation model. An illustration of the result of sensititivity analysis in the two-dimensional case is shown in Fig. 1b. The forward model and sensitivity analysis can be used in an iterative manner to search a distribution of optical properties which explains the boundary measurements. The inverse problem is ill-posed in the sense that small errors in the measurements may lead to large errors in the reconstructed images.

In addition to the anatomical contrast due to different optical properties of tissue types, diffuse optical imaging can be used to image changes in perfusion and oxygen consumption. This is especially important since the spatial resolution of diffuse optical imaging is not comparable with anatomical medical imaging modalities such as X-ray imaging or magnetic resonance imaging (MRI).

Instruments for diffuse optical imaging can be classified into three groups: time-domain systems which measure the full temporal point spread function of tissue to a pulse of light (Chance et al., 1988; Delpy et al., 1988, Eda et al., 1999; Schmidt et al., 2000), frequency-domain systems which measure the amplitude and phase shift of the detected light with respect to an intensity-modulated source light (Lakowicz and Berndt, 1990; Chance et al., 1998b; McBride et al., 2001; Nissilä et al., 2002a), and continuous wave systems, which measure the DC intensity of detected light (Schmitz et al., 2002). The primary advantage of time- and frequency-domain techniques is that they may provide enough information for the separation of features in scattering and absorption.

Advantages of optical imaging as a functional imaging modality include non-invasiveness, insensitivity to external electromagnetic interference, portability of the instrumentation, and suitability for neonatal studies. Problems in the local perfusion of the head of premature neonates may be revealed using optical tomography (Hebden et al., 2002). Optical tomography shows promise as a non-ionizing method for the detection of breast cancer (Franceschini et al., 1997; Pogue et al., 2001; Deghani et al., 2002). The oxidative metabolism of muscle tissue can also be studied with diffuse optical imaging.

In section 2, we discuss the basic mechanisms of light-tissue interaction especially in the near infared, as well as some physiological background. Section 3 reviews the mathematical models used for light transport in tissue-like highly scattering media. Techniques for image reconstruction are also discussed. In section 4, the different types of instruments used for diffuse optical imaging are described. In section 5, we review some of the most important applications of diffuse optical imaging and present some of the newest results from the literature.

2. TISSUE OPTICS AND PHYSIOLOGY

Proper interpretation of the data of diffuse optical imaging requires the understanding of optical properties and physiology of the underlying tissue. These issues are briefly presented in this section.

2.1. Photon and Single-Particle Interactions

The propagation of electromagnetic waves in a medium is traditionally modeled using the Maxwell equations. In diffuse optical imaging, such a complete description is not necessary because most tissues are strongly scattering in the near-infrared (NIR) region

so that the wave properties such as polarization and interference of light can be ignored after the light has traversed a few millimeters of tissue. Light-tissue interactions can also change the structure of tissue or even destroy it. Such interaction mechanisms are utilized, e.g., in phototherapy and laser surgery. In optical imaging, the intensity levels are so low (mW/mm^2) that these destructive processes do not occur. Furthermore, inelastic scattering has a negligible effect on the propagation of NIR light so that the contribution of processes such as fluorescence, phosphorescence, and Raman scattering can be neglected. Therefore, absorption and elastic scattering are the dominant photon-tissue interaction mechanisms in the NIR region.

2.1.1. Absorption

Absorption in tissue is often due to a chromophore, which is a special group in a molecule. The absorbed electromagnetic energy is usually converted into thermal energy. The absorption properties of chromophores depend on environmental factors, such as the type of host molecule, pH, and temperature.

2.1.1a. Basics of Absorption. Absorption properties of a material can be characterized by the specific extinction coefficient α. The product $c\alpha$, where c is the concentration of the absorbing compound, is proportional to its absorption coefficient. It represents the probability that a photon is absorbed within a unit length in the medium and is typically given in mm^{-1}. In the case of a single absorbing compound and no scattering, the intensity of light I as a function of pathlength x is obtained from the Beer-Lambert law as

$$\frac{I(x)}{I_0} = e^{-\mu_a x}, \tag{1}$$

where I_0 is the intensity of incident light.

The concentrations of absorbers in tissue can vary both spatially and temporally and the extinction coefficient is generally wavelength dependent. Because several chromophores contribute to the total absorption, the absorption coefficient is expressed as

$$\mu_a(\mathbf{r}, t, \lambda) = ln(10) \sum_i c_i(\mathbf{r}, t)\alpha_i(\lambda). \tag{2}$$

The specific extinction coefficient is usually defined using base 10 logarithms and μ_a using natural logarithms.

2.1.1b. Absorption in Tissue. Approximately 75% of the human body is water (Woodard and White, 1986). Due to its abundance, water is a considerable absorber of NIR light. Fortunately, the absorption of water is relatively low in the wavelength range of 200–950 nm (see Fig. 2).

Lipids have absorption properties similar to those of water. 1–80% of tissue is lipids, depending on the location within the body (Woodard and White, 1986). Because of their lower relative concentration, lipids do not typically contribute significantly to the total light attenuation. However, this does not apply to adipose tissue of the breast for example, which is mostly composed of lipids.

In surface tissues, the absorption of light, and especially of ultraviolet light, is relatively strong. In the NIR region, melanin is the dominant absorbing chromophore of the epidermis

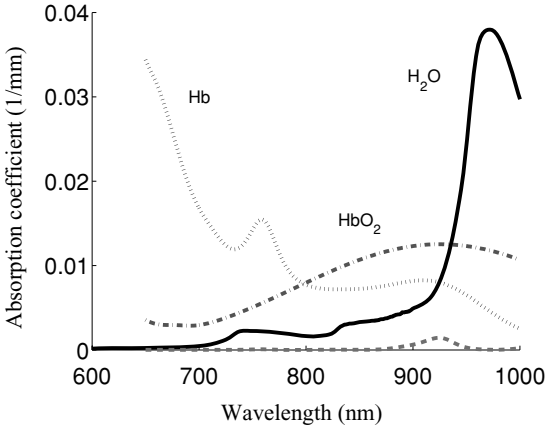

Figure 2. Scaled absorption coefficients of water (solid), Hb (dotted), HbO_2 (dashdot), and lipids (dashed) in the NIR region (Matcher et al., 1994; Cope, 1991; Quaresima et al., 1998).

layer of skin. However, the epidermal layer of the body is rather thin so that its contribution to the total attenuation of NIR light is relatively low.

Especially in brain and muscle studies, the local concentrations of water and lipids, as well as the optical properties of some surface tissues and bones, whose absorption of NIR light is relatively low, are often considered constant. These substances with several weaker absorbers comprise the group of fixed background absorbers. However, the local variations in the concentration of hemoglobin (an oxygen carrier molecule in the erythrocyte) can be relatively large. Its absorption properties depend on the oxygenation state, because the absorption spectra of oxygenated (HbO_2) and deoxygenated (Hb) hemoglobin are notably different in the NIR region (see Fig. 2). These properties are fundamental to functional NIR imaging of tissue. The absorption coefficient of hemoglobin is also rather low above 650 nm. This fact together with the absorption properties of water limit the suitable wavelength region to 650–950 nm when thick objects ($\sim$ cm) are studied. In this region, non-invasive studies of local concentration changes of Hb and HbO_2 are possible provided that the true mean pathlength of photons in the tissue is known and at least two wavelengths are used (Jöbsis, 1977).

Cytochrome oxidase is an enzyme in the mitochondrial membrane taking part in the cellular respiratory chain. Its absorption properties depend on its redox state. The oxidized and reduced forms of the enzyme have different absorption spectra and its total concentration stays relatively constant in tissue. It might be therefore possible to use a single additional NIR wavelength to estimate the redox state changes of cytochrome oxidase, provided that the difference spectrum of the specific extinction coefficients of different forms of the enzyme is known (Cope, 1991).

2.1.2. Scattering

The dominant light-tissue interaction in the NIR region is elastic scattering, where the energy of a photon stays constant but its direction changes. Scattering theories provide

many useful methods for modeling light propagation in tissue (Ishimaru, 1978; Bohren and Huffman, 1983). The Rayleigh scattering theory is frequently used when the size of the scattering particle of any shape is much less than the wavelength of light. The Mie scattering theory can be applied to particles of any size as long as they have a spherical shape. Also, more advanced theories are used in tissue optics (see Sect. 3).

2.1.2a. Basics of Scattering. The scattering properties of a single particle are expressed by a scattering cross section σ. The total scattering coefficient μ_s of a medium which is composed of different scatterers is given by

$$\mu_s = \sum_i \sigma_i \frac{N_i}{V}, \tag{3}$$

where N_i is the number of scatterers in a volume V. The scattering coefficient is a quantity which describes the probability per unit length that a photon is scattered and is expressed usually in mm^{-1}. The reciprocal $1/\mu_s$ characterizes the mean free path between consecutive scattering events. In the case of single scattering events, an exponential attenuation law similar to Eq. (1) can be defined for scattering. However in a larger volume of tissue, multiple-scattering effects have to be taken into account, which requires more advanced modeling (see Sect. 3).

Scattering in tissue is usually anisotropic. A measure of the directional dependency of scattering is given by the normalized scattering phase function $f_{\hat{\mathrm{s}}}(\hat{\mathrm{s}}, \hat{\mathrm{s}}')$. This is a probability density function of $\hat{\mathrm{s}}$ for scattering from an incident direction $\hat{\mathrm{s}}'$ into a new direction $\hat{s}$. If the scattering is independent on the absolute direction of the incident light, $f_{\hat{\mathrm{s}}}(\hat{\mathrm{s}}, \hat{\mathrm{s}}')$ depends only on the angle θ between the incident and scattered directions and $f_{\hat{\mathrm{s}}}(\hat{\mathrm{s}}, \hat{\mathrm{s}}')\, d\hat{\mathrm{s}} = f_{\cos\theta}(\cos\theta)\, d\cos\theta$. This is a commonly used approximation for many tissue types.

The mean cosine of the scattering phase function can be written as

$$g = 2\pi \int_{-1}^{1} \cos\theta f_{\cos\theta}(\cos\theta)\, d\cos\theta. \tag{4}$$

This parameter is zero for isotropic scattering. When $g \to 1$, scattering vanishes, and when $g \to -1$, scattering becomes completely backward directed. The g parameter is often called the anisotropy factor.

If scattering is anisotropic, the effective scattering properties of a medium can be described with an effective (or reduced or transport) scattering coefficient. It is defined as

$$\mu_s' = (1 - g)\mu_s. \tag{5}$$

In addition to the absorption coefficient, the effective scattering coefficient is a material parameter often estimated in diffuse optical tomography.

2.1.2b. Scattering in Tissue. Scattering takes place at each boundary where the refractive index n changes.[†] In tissue, such boundaries exist, e.g., between the intra- and extracellular fluid and between the cytoplasm and the interior fluid of organelles. On a macroscopic scale the differences in refractive indices are relatively small and their values are about 1.4 in most tissues (Bolin et al., 1989). The significant differences can mainly be found at air-skin interfaces. Therefore n is often considered to be constant throughout the medium.

[†] The refractive index determines, e.g., the speed of light in a medium.

Scattering in tissue is slightly wavelength dependent, because it is mostly due to particles whose dimensions are close to the incident wavelength. Also the shape and density of particles as well as environmental variables such as temperature typically influence scattering (Laufer et al., 1998). The spatial origin of μ_s' is not easy to specify. Cellular membranes compose a large fraction of the total volume of tissue and they contain scattering boundaries so that they should contribute extensively to scattering (Cope, 1991). Mitochondria and other cellular organelles have appropriate sizes for NIR scattering and they are distributed all over the body as well (Beauvoit and Chance, 1998; Mourant et al., 1998). Scattering due to red blood cells is probably rather insignificant because their solid content in the body is rather low (about 2%) (Cope, 1991).

The macroscopic structure of some tissues may produce a preferred direction for light propagation. In muscle tissue, light tends to propagate along muscle fibers because of structural anisotropy (Marquez et al., 1998). The same may apply to the white matter of the brain due to the axon bundles.

2.1.3. Determination of Concentration Changes in Tissue

In near-infrared spectroscopy (NIRS), total attenuation of light is often modeled using the modified Beer-Lambert law,

$$A = log_{10}\frac{I_0}{I} = \alpha \cdot c \cdot d \cdot DPF + G, \tag{6}$$

where d is the geometrical distance between the observation points and the parameter G represents attenuation due to scattering. DPF is the so–called differential pathlength factor, which characterizes the average pathlength of photons in the tissue, given by $d \cdot DPF$. The documented values of DPF for human tissue typically vary between 3.5 and 6.5 (Elwell, 1995).

For simplicity, the attenuation due to scattering and background absorption is often considered constant. Then, the concentration changes of a chromophore can be estimated from Eq. (6). When a medium contains N chromophores of interest and the number of measurement wavelengths is $M (N \leq M)$, these changes are given by

$$\Delta \mathbf{c} = (\alpha^T \alpha)^{-1} \alpha^T \frac{\Delta \boldsymbol{A}}{d \cdot DPF}, \tag{7}$$

where $\Delta \mathbf{c}$ is a N×1 vector and $\Delta \mathbf{A}$ is a M×1 vector containing the changes in attenuation. The matrix α (M×N) contains the specific extinction coefficients for each chromophore at each wavelength.

Equation (7) is widely used in NIRS. In addition to the assumption of fixed scattering and background absorption, the DPF is often taken as a constant. In practice, however, it depends on the wavelength, the measurement geometry, and the μ_a and μ_s' of the medium.

2.2. Optical Properties of Tissues

A priori information of the optical properties of tissue can be used to study the feasibility of optical imaging, such as the expected contrast between benign and malignant tissue. It

can also be applied, e.g., to select appropriate measurement and modeling techniques and reconstruction algorithms, and to verify results.

2.2.1. Measurement and Modeling Techniques

Techniques for the determination of optical properties can be divided into direct and indirect methods (Wilson et al., 1987). Direct methods produce the material parameters directly from measurement data applying rather simple modeling techniques such as exponential laws. Therefore, direct methods are limited to cases where a single or only a few scattering events occur, making possible only the studies of thin tissue samples (often $\leq$100 μm). Direct methods can be used to measure, e.g., the total attenuation coefficient ($\mu_t = \mu_a + \mu_s$) of tissue and values of the scattering phase function.

Indirect methods usually require advanced light propagation models (Cheong et al., 1990). The integrating-sphere technique is a classic indirect measurement setup (Pickering et al., 1993). The simplest model for such measurements is based on the Kubelka-Munk theory. However, it requires a nearly isotropic diffuse flux inside the sample and may produce significant errors if the model and the measurement setup are inconsistent (Cheong et al., 1990; van der Zee, 1992). Therefore, other modeling techniques such as the adding-doubling method and Monte Carlo simulation are often applied to integrating sphere measurements (Prahl et al., 1993; van der Zee, 1992). The integrating sphere technique is suitable for *in vitro* samples only and edge effects in the measurement setup limit the sample thickness (typically $\leq$ 1 mm).

In vivo techniques allow measurements through thicker tissue samples (normally $\geq$ 1 cm), in which case μ_a and μ_s' are appropriate material parameters. In practice, such measurements are often preferred. Organs are, however, more difficult to access and the estimation of the measured volume is not straightforward. *In vivo* studies also require advanced measurement techniques and light propagation models (see Sects. 3 and 4).

2.2.2. Parameters of Some Tissue Types

There are some compilations of optical properties of different tissue types (Cheong et al., 1990; van der Zee, 1992; Tuchin, 2000). In Table 1, we have listed the optical properties of relevant tissues from recent studies. The data shows that practically all tissues are strongly scattering ($\mu_a \ll \mu_s'$). Only in cerebrospinal fluid (CSF) μ_a is considerably larger than μ_s'. In most cases tissue is also strongly forward scattering (typically $0.70 < g < 0.995$).[‡]

2.3. Physiological and Structural Changes Measured in Diffuse Optical Imaging

The functional imaging capability of diffuse optical imaging is mostly based on changes in the attenuation of NIR light due to the changes in oxidative metabolism in tissue. The

[‡] There is some variation in tissue properties reported by different authors. This may be due to differences in measurement setups, instrumentation, *in vivo* versus *in vitro*, modeling, preparation of tissue samples, and/or environmental factors such as temperature. The composition and heterogeneity of samples can also contribute to these variations.

Table 1. Optical Properties of Some Tissues Studied Using Diffuse Optical Imaging. Some Values in the Table Have Been Calculated from the Available Data (+), Whereas Other Values Have Been Approximated from Graphs (*).

Tissue	$\mu_a(\text{mm}^{-1})$	$\mu_s'(\text{mm}^{-1})$	g	λ (nm)
Muscle (abdominal)$^+$	0.0052–0.017	0.64–0.95	–	674–956[1]
Muscle (abdominal)$^+$	0.025–0.17	0.58–0.94	–	618–950[2]
Muscle (back)$^+$	0.0082–0.017	0.55–1.2	–	674–956[1]
Brain (grey matter)$^+$	0.0090–0.026	0.42–1.2	–	674–956[3]
Brain (white matter)$^+$	0.013–0.097	0.68–1.5	–	674–956[3]
Brain (grey matter)*	0.02–0.07	1.8–3.0	0.95–0.97	650–950[4]
Brain (white matter)*	0.005–0.04	7–10	0.78–0.86	650–950[4]
Brain (neonatal, grey mat)*	0.02–0.05	0.4–0.7	0.98–0.99	650–900[4]
Brain (neonatal, white mat)*	0.03–0.05	0.7–1.3	0.97–0.98	650–900[4]
Brain (CSF, approx. by pure water)$^+$	0.0013–0.029	~ 0	–	650–900[5]
Breast (adipose)$^+$	≤ 0.035	0.48–1.2	–	749–836 [6]
Breast (fibrous)$^+$	≤ 0.032	0.58–1.2	–	749–836[6]
Breast (average)*	0.002–0.008	0.6–1.4	–	750–830[7]
Blood*	0.13–0.49	2.5–4.0	0.99–0.995	665–960[8,9]
Bone (pig skull)$^+$	0.022–0.052	1.2–2.8	0.91–0.96	650–950[10]
Bone (human skull)$^+$	0.02–0.07	0.75–1.2	–	674–956[3]
Skin (dermis, Caucasian)$^+$	0.0053–0.049	1.3–3.4	–	618–950[2]
Skin (dermis, black)$^+$	0.025–0.46	1.1–5.5	–	617–949[2]
Subdermal fat$^+$	0.0040–0.024	0.8–1.7	–	617–949[2]

[1] Fishkin et al., 1997; [2]Simpson et al., 1998; [3]Bevilacqua et al., 1999; [4]van der Zee et al., 1993; [5]Matcher et al., 1994; [6]Troy et al., 1996; [7]Durduran et al., 2002; [8]Cheong et al., 1990; [9]Lovell et al., 1999a; [10]Firbank et al., 1993

activity of neurons and muscle cells is controlled by electrical impulses (i.e., action potentials) along their cellular membranes. This activation is accompanied by increased nutrient and oxygen demand of cells, which tends to increase also the local blood flow.

In a typical brain-activation measurement using NIRS, $[HbO_2]$ and [totHb] in tissue increase and [Hb] decreases (Fig. 3).[§¶] It is generally accepted that during activation, blood flow and oxygen delivery in tissue increase more than oxygen consumption (Villringer and Dirnagl, 1995). An increase in blood velocity increases the $[HbO_2]$ and decreases the [Hb]. The blood volume can also increase regionally in capillaries. However, a local increase in blood volume would increase the $[HbO_2]$ and [totHb], but the [Hb] would stay practically constant. Changes in oxygen consumption can affect both $[HbO_2]$ and [Hb]. The increased oxygen consumption decreases the $[HbO_2]$ and increases the [Hb] and vice versa. The probed region in NIRS measurements is typically so large (>1 cm^3) that all the hemodynamic and oxygenation phenomena mentioned above can contribute to the measured signal.

The optical properties of cytochrome oxidase may enable an estimation of tissue oxygenation and cellular oxygen metabolism. The redox-active copper center Cu_A is mostly responsible for the absorption of NIR light in the cytochrome oxidase, but it is only indirectly responsible for the oxygen consumption. There is evidence that in addition to the cellular oxygen consumption, other processes can change the redox state of Cu_A (Cooper

[§] The brackets indicate the concentration of substance and the abbreviation totHb refers to the total hemoglobin.
[¶] The drop in [Hb] also creates the so-called BOLD-contrast (blood oxygen level-dependent), which is mostly responsible for the signal changes in functional magnetic resonance imaging (fMRI).

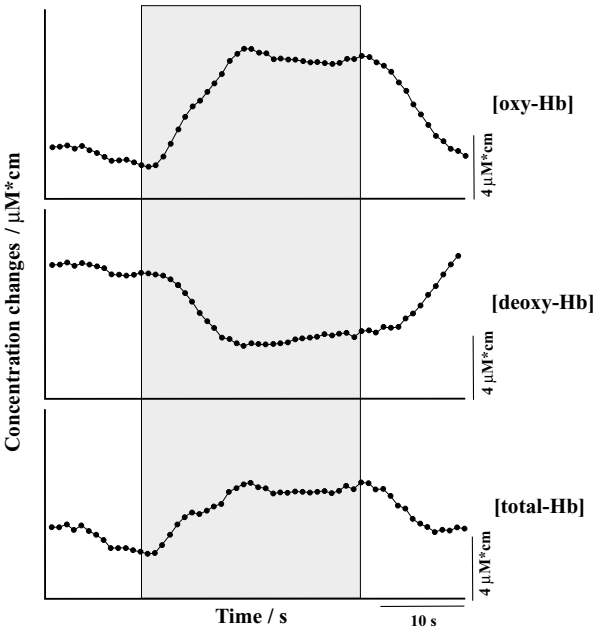

Figure 3. Typical NIRS response of a) [HbO_2], b) [Hb], and c) [totHb] to a visual randomly moving stimulus. The stimulus is on during the gray interval. NIRS signals were recorded above the right occipital cortex and the responses have been averaged over 8 subjects. Reproduced with permission from (Obrig and Villringer, 1997).

et al., 1994). The absorption spectrum of HbO_2 also resembles the difference spectrum of cytochrome oxidase (Cope, 1991). These facts complicate the non-invasive determination of changes in the redox-state of cytochrome oxidase (Cooper and Springett, 1997).

Variations in the scattering properties of tissue can also be detected using optical techniques. The signals attributed to scattering changes can be categorized into fast and slow signals (Villringer and Chance, 1997). The published research on scattering changes is mostly from animal studies using invasive methods (Hill and Keynes, 1950; Frostig et al., 1990; Macvisar and Hochman, 1991). The fast scattering signals are related to neuronal activity and action potentials providing direct information on the electrical activity of tissue (Stepnoski et al., 1991). The time scale of these changes is typically milliseconds (Rector et al., 2001). The geometrical changes of cells and organelles in tissue have also been shown to produce changes in scattering (Poe et al., 1996). Geometrical changes can be quite fast (tens of milliseconds), but they have been typically used to explain slower scattering changes (Rector et al., 2001; Villringer and Chance, 1997). When absorption and scattering changes are simultaneously measured, one should be aware of the link between them. When scattering increases, photons tend to propagate longer distances in tissue, which increases the probability for absorption in the tissue and vice versa.

Vascular, metabolic, and neuronal systems produce periodic changes, which may show up in the optical signal. While at rest, the frequency of oscillations due to the heartbeat and the pulsation of arterial blood is approximately 1 Hz. This fluctuation has been utilized to monitor the oxygen saturation of arterial blood (Franceschini et al., 1999). Features at

respiratory frequencies (0.2–0.3 Hz) may also be seen in the optical signal (Elwell et al., 1996). Furthermore, the cognitive activation of the frontal lobe has been demonstrated to induce recurrent oscillations in the range of 0.5–5 Hz (Chance et al., 1993). Living tissue also produce low-frequency (LFO, around 0.1 Hz) and very-low-frequency oscillations (VLFO, around 0.04 Hz), which have been proposed to arise from vascular (such as vasomotion), metabolic and/or neuronal fluctuations (Obrig et al., 2000).

In addition to functional images, diffuse optical imaging can be used to image the optical structure of tissue at a low resolution (around 1 cm^3). Structural imaging is based on the differences in the absorption and scattering coefficients between different tissue types (see Sect. 2.2.2). These differences can be utilized to detect, e.g., tumors, internal hemorrhages or hematomas (Zhang et al., 2000). Many studies of optical properties of malignant tissues have shown that the absorption and scattering coefficients may be larger than in benign tissues (Hargrave et al., 1996; Tromberg et al., 1997; Fantini et al., 1998).

3. THEORY AND MODELING

3.1. Problem Statement

The fundamental idea in optical tomography is that the internal distribution of μ_s and/or μ_a can be reconstructed based on a set of measurements of transmitted and/or reflected light between points on the boundary of an object. Reconstructing an image of optical parameters based on boundary measurements is an example of a so-called inverse problem. For solving an inverse problem, the solution to the respective forward problem is generally required.

Formally, the forward problem in optical imaging can be stated as: *Given the distribution of sources q on the boundary of the domain, and the distribution of the optical parameter values p in the domain, find the resulting boundary measurement set y*. The forward problem can be expressed with a non-linear forward operator:

$$y = F(p; q). \tag{8}$$

The inverse problem can be stated as: *Given the boundary measurements y and the distribution of sources q on the boundary, find the internal distribution of optical parameter values p*. Using the non-linear operator, the inverse problem can be written formally as:

$$p = F^{-1}(y; q). \tag{9}$$

3.2. Photon Transport Models

3.2.1. Radiative Transfer Equation

Based on the particle interpretation, light can be studied as a stream of energetic particles, i.e., photons. If the photon density is interpreted as proportional to the scalar field for energy radiance L, various differential and integrodifferential equations can be established based on energy conservation. The most widely applied equation in the field

of optical imaging is the Radiative Transfer Equation (RTE) (Case and Zweifel, 1967; Chandrasekhar, 1960)

$$\frac{1}{c}\frac{\partial L(\mathbf{r},t,\hat{\mathbf{s}})}{\partial t}+\hat{\mathbf{s}}\cdot\nabla L(\mathbf{r},t,\hat{\mathbf{s}}+(\mu_a+\mu_s)L(\mathbf{r},t,\hat{\mathbf{s}}) = \mu_s\int_{(4\pi)} f_{\hat{\mathbf{s}}}(\hat{\mathbf{s}},\hat{\mathbf{s}}')L(\mathbf{r},t,\hat{\mathbf{s}})d\hat{\mathbf{s}}'+q(\mathbf{r},t,\hat{\mathbf{s}}), \tag{10}$$

which describes the change in radiance $L(\mathbf{r},t,\hat{\mathbf{s}})$ in time at position $\mathbf{r}$ and in direction $\hat{\mathbf{s}}$. Above, c is the speed of light in the medium, $f_{\hat{\mathbf{s}}}(\hat{\mathbf{s}},\hat{\mathbf{s}}')$ is the normalized scattering phase function and $q(\mathbf{r},t,\hat{\mathbf{s}})$ is the spatial and angular distribution of the source.

The radiance L is defined so that the energy transfer per unit time by photons in a unit solid angle $d\hat{\mathbf{s}}$ through an elemental area da with a unit normal $\hat{\mathbf{n}}$, at position $\mathbf{r}$, is given by

$$L(\mathbf{r},t,\hat{\mathbf{s}})\hat{\mathbf{s}}\cdot\hat{\mathbf{n}}\,da\,d\hat{\mathbf{s}}. \tag{11}$$

The exitance Γ on surface, i.e., the energy transfer per unit time through a unit area with a normal $\hat{\mathbf{n}}$, is obtained from Eq. (11) by integrating over the solid angle:

$$\Gamma(\mathbf{r},t)=\int_{(4\pi)} L(\mathbf{r},t,\hat{\mathbf{s}})\hat{\mathbf{s}}\cdot\hat{\mathbf{n}}\,d\hat{\mathbf{s}}. \tag{12}$$

The units for the exitance are Wm^{-2} and for the radiance $\mathrm{Wm}^{-2}\mathrm{sr}^{-1}$, where sr is the unit for the solid angle. The units for the source term q in Eq. (10) are $\mathrm{Wm}^{-3}\mathrm{sr}^{-1}$.

For solving the inverse problem, a relatively fast and flexible solution to the forward problem is desirable. Although numerical solutions to the RTE have been presented, still normally simplified models derived from the RTE are used as a basis of image reconstruction.

3.2.2. The Diffusion Approximation

A standard approximation method for the RTE is the P_N approximation (Case and Zweifel, 1967). The P_N approximation consists of expanding the radiance $L(\mathbf{r},t,\hat{\mathbf{s}})$ and the source term $q(\mathbf{r},t,\hat{s})$ in Eq. (10) into spherical harmonics and taking terms only up to Nth order. Using the addition theorem of spherical harmonics, the scattering phase function can also be expanded into spherical harmonics (Arridge, 1999). Inserting these expansions in the RTE and some manipulation of the resulting expression yields in the general case N+1 coupled first-order partial differential equations (PDEs).

The diffusion approximation (DA) (for a more complete presentation, see (Case and Zweifel, 1967; Ishimaru, 1978)) is obtained from the P_1 approximation by making some additional simplifying assumptions. It is the most commonly applied model for optical tomography though there has also been some work on higher order approximations such as the P_3 approximation to the RTE (Arridge, 1999; Boas, 1996; Jiang, 1999).

We now define the energy fluence rate

$$\Phi(\mathbf{r},t)=\int_{(4\pi)} L(\mathbf{r},t,\hat{\mathbf{s}})\,d\hat{\mathbf{s}}, \tag{13}$$

and the energy current density

$$\mathbf{J}(\mathbf{r}, t) = \int_{(4\pi)} \hat{\mathbf{s}} L(\mathbf{r}, t, \hat{\mathbf{s}})\, d\hat{\mathbf{s}}, \tag{14}$$

both in the units of Wm^{-2}. In terms of the definitions (13) and (14), the P_1 approximation yields two coupled PDEs:

$$\frac{1}{c}\frac{\partial \Phi(\mathbf{r}, t)}{\partial t} + \nabla \cdot \mathbf{J}(\mathbf{r}, t) + \mu_a \Phi(\mathbf{r}, t) = q_0(\mathbf{r}, t), \tag{15}$$

$$\frac{1}{c}\frac{\partial \mathbf{J}(\mathbf{r}, t)}{\partial t} + \frac{1}{3}\nabla \Phi(\mathbf{r}, t) + (\mu_a + \mu_s(1-g))\mathbf{J}(\mathbf{r}, t) = \mathbf{q}_1(\mathbf{r}, t), \tag{16}$$

where g is the mean cosine of the scattering angle. The P_1 approximation is quite good when $\mu_s/(\mu_s + \mu_a$ is close to unity, i.e., $\mu_a \ll \mu_s$, the phase function is not too anisotropic, and the source-detector separation is large compared to the mean free scattering length $1/\mu_s'$ (Boas, 1996).

To derive the DA, we make the assumptions

$$\mathbf{q}_1(\mathbf{r}, t) = 0, \tag{17}$$

$$\frac{1}{|\mathbf{J}|}\frac{\partial |\mathbf{J}|}{\partial t} \ll c(\mu_a + \mu_s'). \tag{18}$$

The first assumption is justified if an isotropic source term is assumed. The second assumption effectively means that the left-hand-side term in Eq. (18) is taken to be zero. The implication of the second assumption is best seen in the frequency domain. The intensity of the source term is assumed to be sinusoidally modulated with angular frequency ω and the time dependence of the photon current $\mathbf{J}$ is thus of the form $e^{-i\omega t}$. The time derivatives can then be replaced by multiplying by $-i\omega$ and the second assumption (when $\mu_s' \gg \mu_a$) thus essentially becomes $\omega/(c\mu_s') \ll 1$. This means that the scattering frequency must be much larger than the modulation frequency (Boas, 1996). This assumption is considered to be a good approximation for biological tissues, if the source frequencies are less than $\sim$ 1 GHz (Haskell et al., 1994).

Substituting the assumptions (17) and (18) into Eq. (16) simplifies it to Fick's law,

$$\mathbf{J}(\mathbf{r}, t) = -\frac{1}{3(\mu_a(\mathbf{r}) + \mu_s'(\mathbf{r}))}\nabla \Phi(\mathbf{r}, t) = -\kappa(\mathbf{r})\nabla \Phi(\mathbf{r}, t), \tag{19}$$

where $\kappa(\mathbf{r})$ is the *diffusion coefficient*,

$$\kappa(\mathbf{r}) = \frac{1}{3(\mu_a(\mathbf{r}) + \mu_s'(\mathbf{r}))}. \tag{20}$$

Substituting Fick's law into Eq. (15) leads to the time-dependent diffusion equation (DE)

$$\frac{1}{c}\frac{\partial \Phi(\mathbf{r}, t)}{\partial t} - \nabla \cdot \kappa(\mathbf{r})\nabla \Phi(\mathbf{r}, t) + \mu_a \Phi(\mathbf{r}, t) = q_0(\mathbf{r}, t). \tag{21}$$

The exitance Γ defined in Eq. (12) can now, using Eq. (14) and Fick's law, be written as

$$\Gamma(\mathbf{r}, t) = -\kappa(\mathbf{r})\hat{\mathbf{n}} \cdot \nabla \Phi(\mathbf{r}, t). \tag{22}$$

3.2.2a. Validity of the Diffusion Approximation. The DA is a simple and the most widely applied model for light propagation in optical imaging. It is valid for most tissue types, though there are some important exceptions. For example, it cannot be used to model light transport in clear regions (e.g., the CSF), where the assumption of strong scattering is violated. Also, in the proximity of light sources more rigorous models could yield more accurate results. In (Hielscher et al, 1997), diffusion and transport calculations in a head model were compared. It was found that most differences occured in void-like regions and in regions where the absorption was comparable to scattering. Comparisons of diffusion calculations with experiments or Monte Carlo simulations based on the RTE show, however, that qualitatively and also quantitatively correct predictions of boundary measurements can be obtained using diffusion models when the required assumptions for the DA are met (Arridge et al., 1993; Okada et al., 1996; Rinzema et al., 1998).

3.2.2b. Frequency Domain. A common experimental approach is to modulate the intensity of the light source with a radio-frequency signal. Consider a point source modulated with an angular frequency ω:

$$q_0(\mathbf{r}, t) = \delta(\mathbf{r} - \mathbf{r}_s)(Q_0 + Se^{-i\omega t}), \tag{23}$$

where Q_0 is the average or the dc amplitude and S the modulation amplitude of the source. In a strongly scattering medium an intensity-modulated point source gives rise to a macroscopic wave of photon density propagating spherically outward from the source in the medium. In the literature, these waves are often referred to as diffuse photon density waves (DPDW) (Boas, 1996; Fishkin and Gratton, 1993; O'Leary et al., 1992). One approach to optical imaging is based on studying the refraction and reflection of these waves. The DE in the frequency domain is obtained by taking the Fourier transform of the time-dependent DE (21):

$$-\frac{i\omega}{c}\hat{\Phi}(\mathbf{r}, \omega) - \nabla \cdot \kappa(\mathbf{r})\nabla\hat{\Phi}(\mathbf{r}, \omega + \mu_a(\mathbf{r})\hat{\Phi}(\mathbf{r}, \omega) = \hat{q}_0(\mathbf{r}, \omega), \tag{24}$$

where $\hat{\Phi}(\mathbf{r}, \omega)$ is the complex fluence arising from the intensity modulated part $\hat{q_0}(\mathbf{r}, \omega)$ of the source term.

3.2.3. Boundary and Source Conditions

In order to achieve a better match between the light propagation model and the physical situation, the boundaries and sources must be carefully modelled (see, e.g., (Haskell et al., 1994; Schweiger et al., 1995)). A commonly applied approach in the literature is to use the zero or Dirichlet boundary condition (DBC), where the fluence is set equal to zero on the physical boundary:

$$\Phi(\mathbf{r}, t) = 0 \quad \forall \mathbf{r} \in \partial\Omega. \tag{25}$$

The DBC, although not physically accurate, is mathematically quite simple.

Another, physically more correct boundary condition can be derived from the requirement that no photons come into the tissue through the surface (except at the source position) (Ishimaru, 1978):

$$L(\mathbf{r}, t, \hat{\mathbf{s}}) = 0 \quad \forall \mathbf{r} \in \partial\Omega, \hat{\mathbf{s}} \cdot \hat{\mathbf{n}} < 0. \tag{26}$$

This condition, however, cannot be applied to the diffusion equation directly. Instead, we assume that the total inward directed current is zero:

$$\int_{\hat{\mathbf{s}}\cdot\hat{\mathbf{n}}<0} L(\mathbf{r}, t, \hat{\mathbf{s}})(\hat{\mathbf{s}} \cdot \hat{\mathbf{n}})\, d\hat{\mathbf{s}} = 0 \quad \forall \mathbf{r} \in \partial\Omega. \tag{27}$$

Within the diffusion approximation, the boundary condition becomes

$$\Phi(\mathbf{r}, t) + 2\kappa(\mathbf{r}) A \hat{\mathbf{n}} \cdot \nabla\Phi(\mathbf{r}, t) = 0 \quad \forall \mathbf{r} \in \partial\Omega, \tag{28}$$

where the term $A = (1 + R)/(1 - R)$ takes into account the differences in the refractive indices n and n' of the scattering medium and the surrounding medium (R is the reflection coefficient on the boundary). In the literature, the above boundary condition is known as the zero partial flux or the Robin boundary condition (RBC).

The RBC represents the physical situation more accurately, whereas the DBC has the advantage of leading to a simpler model. A compromise between these two is the extrapolated boundary condition (EBC), where an extrapolated boundary is introduced at a certain distance d_{ext} from the real physical boundary, and the DBC is then applied at this extrapolated boundary. Comparing with Monte Carlo simulations and experimental results, the RBC and EBC give much better agreement than the DBC (Okada et al., 1996; Schweiger et al., 1995).

In a measurement system for optical tomography, a laser light beam can be guided onto the surface of the tissue through an optical fiber. A common approach to model a collimated pencil beam incident on the surface is to represent it by an isotropic point source located at a depth $1/\mu_s'$ below the surface of the domain Ω. This approximation produces rather accurate results at distances larger than one mean free path, i.e., $1/(\mu_s' + \mu_a)$, from the source, but breaks down close to the source. In the DE, the isotropic point source can be represented as a δ-function source term.

Another approach is to treat the light source as a diffuse source on the surface of the domain. The source is represented as an inward-directed diffuse photon current over the illuminated area of the domain boundary $\partial\Omega$. The source can thus be incorporated directly into the boundary conditions.

3.2.4. Measurables

The measurable quantity on the boundary is the exitance Γ (see Eq. (22)). Using the RBC (28) Γ can be written as

$$\Gamma(\mathbf{r}, t) = \frac{1}{2A}\Phi(\mathbf{r}, t). \tag{29}$$

Although the time-resolved flux intensity $\Gamma(t)$ could be used for reconstruction directly, commonly one or a few data types derived from $\Gamma(t)$ are used. Possible data types are numerous: the total integrated intensity, time-gated integrals (early light as the integral over the first few nanoseconds, or windowed light) or integral transform type measurements (Fourier, Mellin or Laplace transform and their combinations), which can be used to obtain, e.g., the mean-time or higher-order moments. If frequency-domain measurements are considered, $\Gamma(\omega)$ is usually calculated from frequency-domain DA. Calculation of $\Gamma(\omega)$ is often much simpler than obtaining $\Gamma(t)$. Following the presentation in (Schweiger and Arridge,

1997; Schweiger and Arridge, 1999a), where the subject of data types is considered more profoundly, we give here the definitions of some of the common ones:

$$\text{time – gated integrated intensity:} \quad E = \int_{t_1}^{t_2} \Gamma(t)dt, \tag{30}$$

$$\text{integrated intensity:} \quad E = \int_0^{\infty} \Gamma(t)dt, \tag{31}$$

$$nth\,\text{temporal moment:} \quad \langle t^n \rangle = E^{-1} \int_0^{\infty} t^n \Gamma(t)dt, \tag{32}$$

$$nth\,\text{central moment:} \quad c_n = E^{-1} \int_0^{\infty} (t - \langle t \rangle)^n \Gamma(t)dt, \tag{33}$$

$$\text{normalized Laplace transform:} \quad L(s) = E^{-1} \int_0^{\infty} e^{-st} \Gamma(t)dt, \tag{34}$$

$$\text{Mellin – Laplace:} \quad ML_n(s) = E^{-1} \int_0^{\infty} t^n e^{-st} \Gamma(t)dt, \tag{35}$$

$$\text{AC intensity:} \quad |\Gamma(\omega)|, \tag{36}$$

$$\text{log intensity:} \quad \log \Gamma(\omega), \tag{37}$$

$$\text{modulation depth:} \quad \frac{\log \Gamma(\omega)}{E}, \tag{38}$$

$$\text{phase:} \quad \varphi = \arg\Gamma(\omega). \tag{39}$$

An important point is that all these data types except E and AC / log intensity are normalized, so knowledge of the absolute magnitude is not required, which makes them more robust against variations in source power and effects of fiber-tissue coupling.

3.3. Solving the Photon Transport

3.3.1. Stochastic Modeling

The most widely applied stochastic technique for photon transport is the Monte Carlo (MC) method. In MC models (Wilson and Adam, 1983; Prahl et al., 1989), the propagation of an individual photon or a photon packet (to improve the efficiency of the method) is simulated through the medium. This is done by following the photon's path and modeling sequentially each event the photon undergoes during its travel in the medium.

MC techniques provide a conceptually simple way of modeling light propagation in an inhomogeneous medium with complex arbitrary geometry at the expense of increased computational complexity. The statistical error of MC results decreases with the inverse square root of the number of detected photons. In order to achieve acceptable statistics, the number of photons or photon packages that have to be launched is often high, resulting in computational times that hinder the use of MC models as a basis for iterative image reconstruction algorithms. However, MC methods have been widely used for investigating the behaviour of light or some parameters related to light propagation in complex inhomogeneous conditions (Okada et al., 1997), as well as for the validation of PDE-based light transport models (Schweiger et al., 1995).

3.3.2. Deterministic Approach

In the deterministic approach, the RTE or PDEs derived from it are solved using either analytical or numerical methods.

Generally, numerical solutions to the RTE are computationally relatively expensive. Hence, most reconstruction algorithms rely on the diffusion approximation, though recently reconstructions based on the RTE have also been presented (Klose and Hielscher, 2002). Analytical solutions to the RTE are available only in some special cases, whereas for numerical solution, various computational techniques exist (Graaff et al., 1989; Kim and Ishimaru, 1998; Klose et al., 2002).

3.3.2a. Analytical Solutions to the DE. Analytical solutions to the diffusion equation are in general cases difficult to obtain. For some relatively simple geometries analytical solutions can be derived, but when dealing with arbitrary geometries or inhomogeneous media, one has to resort to numerical approaches.

For a point source in an infinite homogeneous medium, the solution of the DE is given by the Green function for infinite medium. For some other simple geometries, the solutions can be derived, e.g., using image sources and the infinite medium solution. Some geometries for which the DE has been solved in this manner include, e.g., semi-infinite half-space, an infinite slab or cylinder, and a two-dimensional circle or a three-dimensional sphere (Arridge et al., 1992; den Outer et al., 1993).

Some approaches for image reconstruction rely on studying the properties of the photon density field generated by an intensity-modulated light source (Boas et al., 2001; Boas et al., 1997; Chance et al., 1998; Ntziachristos et al., 1999). In a homogeneous medium, the frequency-domain diffusion equation (FDDE) (Eq. (24)) can be rewritten as the Helmholtz equation

$$(\nabla^2 + \kappa_{ac}^2)\hat{\Phi}(\mathbf{r}, \omega = -\frac{A}{\kappa}\delta(\mathbf{r} - \mathbf{r}_s), \tag{40}$$

with a complex wave number

$$\kappa_{ac}^2 = \frac{-c\mu_a + i\omega}{c\kappa}. \tag{41}$$

For an infinite homogeneous medium, the solution of Eq. (40) is an outgoing spherical wave:

$$\hat{\Phi}(\mathbf{r}, \omega) = \frac{S}{4\pi\kappa|\mathbf{r} - \mathbf{r}_0|} e^{i\kappa_{ac}|\mathbf{r}-\mathbf{r}_0|}, \tag{42}$$

where S is the source modulation amplitude, $\kappa_{ac} = \sqrt{(-c\mu_a + i\omega)/(c\kappa)}$ the complex wave number, and $|\mathbf{r} - \mathbf{r}_0|r$ the distance from the source.

Analytical solutions for the propagation and scattering of the DPDWs have been studied in various relatively simple geometries and both in a homogeneous medium and in the presence of spherical perturbations (Feng et al., 1995; Fishkin and Gratton, 1993; O'Leary et al., 1992).

3.3.2b. Finite Difference Method. Finite Difference Method (FDM) is a classical numerical approach for solving PDEs. In the FDM, the solution area is discretized using a regular grid, and the derivatives are approximated by finite-difference approximations

involving the values of the unknowns at adjacent grid points. Substituting the finite-difference approximations to the diffusion equation yields a discrete system equation.

FDM is conceptually simple and is often considered the easiest method to implement for regular domains. The system matrices have high degrees of symmetry, which makes the solution of the system equation easier. For complicated geometries, abrupt changes in material properties or complex boundary conditions, special modifications are, however, usually required. In optical tomography, the FDM is not the most common numerical method, but it has been used in inverse reconstruction schemes (Hielscher et al., 1999; Pogue et al., 1995).

3.3.2c. Finite Element Method. In the Finite Element Method (FEM), the discretization process begins from a variational formulation of the differential equation, where a set of so-called test functions is involved. The reduction to a finite-dimensional problem is made by replacing this (often infinite-dimensional) set by a set of functions depending only on a finite number of parameters and discretizing the solution area into a number of uniform or nonuniform finite elements. The result of this procedure can be reformulated to a system of equations with a sparse system matrix.

The FE formulation for the frequency-domain diffusion equation can be derived using the so-called Galerkin formulation. First, the FDDE is multiplied by a test function $\psi \in H^1(\Omega)$ (where $H^1(\Omega)$ is a predefined function space (Sobolev space)) and integrated over the solution domain Ω. The resulting equation is called the *weak formulation of* the FDDE. In the Galerkin approximation, the solution to the weak formulation is found in an N-dimensional subspace $U(\Omega) \subset H^1(\Omega)$, where N is finite. By defining a basis U: $\{\psi_i\}_1^N$ for the subspace $U(\Omega)$, the Galerkin approximation for $\hat{\Phi}$ can be expressed as

$$\hat{\Phi}^h(\mathbf{r}, \omega) = \sum_{i=1}^{N} \hat{\Phi}_i(\omega)\psi_i(\mathbf{r}). \tag{43}$$

Assuming, e.g., a Robin-type boundary condition (Eq. (28)), the Galerkin formulation finally yields a finite set of equations:

$$[\mathbf{A} + \mathbf{B} + \mathbf{C}]\hat{\Phi} = \hat{\mathbf{Q}}, \tag{44}$$

where

$$A_{ji} = \int_{\Omega} [-\frac{i\omega}{c} + \mu_a(\mathbf{r})]\psi_j(\mathbf{r})\psi_i(\mathbf{r})\, d\Omega, \tag{45}$$

$$B_{ji} = \int_{\Omega} \kappa(\mathbf{r})\nabla\psi_j(\mathbf{r}) \cdot \nabla\psi_i(\mathbf{r})\, d\Omega, \tag{46}$$

$$C_{ji} = \int_{\partial\Omega} \frac{1}{2A}\psi_j(\mathbf{r})\psi_i(\mathbf{r})\, d(\partial\Omega), \tag{47}$$

$$\hat{Q}_j = \int_{\Omega} \hat{q}_0(\mathbf{r}, \omega)\psi_j(\mathbf{r})\, d\Omega, \tag{48}$$

$$\hat{\Phi} = [\hat{\Phi}_1(\omega), \hat{\Phi}_2(\omega), \ldots, \hat{\Phi}_N(\omega)]^T. \tag{49}$$

In the time-dependent case, the FE formulation can be derived in a similar manner. The resulting FE matrix equation can be integrated with respect to time, the time variable discretized and the time derivatives approximated using the finite difference method.

The versatility of the FEM makes complicated geometries, complex boundary conditions or a highly heterogeneous material relatively easy to handle. In optical tomography, FEM is a very commonly used method for solving the DE numerically.

3.3.3. Hybrid Models

Solving the DE with FEM is relatively fast compared to some other methods such as Monte Carlo simulation. However, the drawback of the DE is that it is not valid, e.g., close to the sources. With Monte Carlo methods, however, more realistic solutions near the sources can be obtained at the expense of computational time. The speed of the DE-based FEM and the accuracy of the Monte Carlo method can be combined in a hybrid model. Wang and Jacques (1993) simulated light propagation near the source with a Monte Carlo model and used the results to form a distributed source for the diffusion model.

3.4. Inverse Problem

3.4.1. Uniqueness Issues

The inverse problem of optical tomography is extremely ill-posed making the image reconstruction a complicated task. The question of the existence of a unique solution to the inverse problem has recently received certain attention. In theorical considerations, the existence of a unique parameter distribution consistent with boundary data depends on the measurement technique (steady-state, time-domain or frequency-domain) and boundary data types used, the optical parameters considered as unknown (μ_a, μ_s, the refractive index) and the underlying model for light propagation.

Image reconstruction using a transport model and some considerations on simultaneous reconstruction of absorption and scattering within the transport framework have been presented, e.g., by Dorn (1998, 2000, submitted). Within the diffusion model, a proof the nonuniqueness of recovering both the scattering and absorption coefficient distributions using steady-state measurements was given by Arridge and Lionheart (1998). The authors showed that for a steady-state measurement, there exists an infinite set of optical parameters that give rise to identical data. The discussion was then extended to frequency/time domain. In these cases the uniqueness could be proved in the limit of continuous measurements and source distributions provided that the refractive index was known. However, if the refractive index distribution is considered unknown the uniqueness disappears. The discussion was continued by Matcher (1999) using a more exact P1-approximation. Within this time-dependent model it could be argued that the solution for μ_a, μ_s and refractive index distributions is almost certainly unique.

3.4.2. Data Types for the Image Reconstruction

The question of which data types to use for image reconstruction is closely related to the uniqueness issue. To our knowledge, formal results for different data types have not been derived. Some information on the usability of certain data types can, however, be obtained, e.g., by calculating the difference in the data caused by perturbations in the

optical parameters. In (Arridge 1999; Schweiger and Arridge, 1997) the maps of the error norms ε of the data were calculated in a homogeneous sphere with background parameters $\bar{\mu}_a$ and $\bar{\mu}'_s$ and perturbed parameters μ_a and μ'_s corresponding to a single perturbed area using:

$$\varepsilon(\mu_a, \mu'_s) = \sum_{i,j} \left(\frac{F_{i,j}(\bar{\mu}_a, \bar{\mu}'_s) - F_{i,j}(\mu_a, \mu'_s)}{\sigma_{i,j}} \right)^2, \tag{50}$$

where $F_{i,j}(\bar{\mu}_a, \bar{\mu}'_s)$ and $F_{i,j}(\mu_a, \mu'_s)$ are the homogeneous reference and the perturbed data, respectively, and $\sigma_{i,j}$ is the standard deviation for the measurement (i, j). The error maps were plotted against (μ_a, μ'_s) axes. The deduction from the maps was that for a single measurement type simultaneous reconstruction of both μ_a and μ'_s is ambiguous. However, combining measurement types in a suitable way can overcome the ambiguity between μ_a and μ'_s.

In order to employ a minimization scheme on Eq. (50), the standard deviations for the measurements need to be known. In experiments, the noise can be estimated based on the data. For simulated data, noise models have been established (Arridge et al., 1995; Schweiger and Arridge, 1997).

Yet another point to consider when choosing data types is the spatial sensitivity profile of the measurement. Different data types have slightly different spatial sensitivities, which can be accessed by calculating the sensitivity relations of the measurements with respect to parameter values.

3.4.3. Sensitivity Relations

The sensitivity relations between the measurement and the material parameters are utilized in many image reconstruction algorithms. For the forward model $y = F(\mathbf{r}_m, q, p)$ between the measurement y at $\mathbf{r}_m$ and the parameter values p and sources q, the sensitivity relation, often called as the Jacobian, can in general be defined as the rate of change of the measurement with p:

$$\mathcal{J}_p^y(\mathbf{r}_m, q, \mathbf{r}') = \lim_{\Delta p \to o} \frac{F(\mathbf{r}_m, q, p + \Delta p(\mathbf{r}')) - F(\mathbf{r}_m, q, p)}{\Delta p(\mathbf{r}')} \tag{51}$$

The Jacobians for different data types can be obtained from the Jacobian for the exitance Γ, e.g., for $\log \Gamma$ and $\varphi = \arg \Gamma(\omega)$ the Jacobians become

$$\mathcal{J}_p^{\log \Gamma} = \mathrm{Re}[\tfrac{1}{\Gamma} \mathcal{J}_p^{\Gamma}] \quad \text{and} \tag{52}$$

$$\mathcal{J}_p^{\varphi} = \mathrm{Im}[\tfrac{1}{\Gamma} \mathcal{J}_p^{\Gamma}], \tag{53}$$

where $\mathcal{J}_p^{\Gamma}$ denotes the Jacobian for Γ.

Analytical forms of the Jacobian have been studied using the known analytical forms for the Green functions in some simple geometries (Arridge, 1995; Schotland et al., 1993). For general geometries and inhomogeneous conditions, Monte Carlo and finite element techniques have been used. If the model we are considering is discretized, the Jacobian can

be written in a discrete form:

$$\mathcal{J}_p^y = \begin{pmatrix} \frac{\partial_{y_1}}{\partial_{p_1}} & \cdots & \frac{\partial_{y_1}}{\partial_{p_L}} \\ \vdots & \ddots & \vdots \\ \frac{\partial_{y_M}}{\partial_{p_1}} & \cdots & \frac{\partial_{y_M}}{\partial_{p_L}} \end{pmatrix}, \tag{54}$$

where y_i, are the measurements at locations $1 \ldots M$ and p_j are the parameter values in the discrete model. The computation of this Jacobian matrix is often burdensome and restricts the speed of image reconstruction algorithms.

There are several ways to calculate the Jacobian in a numerical framework such as the FEM. Conceptually the most straightforward way is to explicitly perturb regions in the numerical model and take the limit when the pertubation approaches zero. This scheme, however, is not very efficient. Another possilibity is to take the discretized weak form of the DE with a real source q_o as a starting point, and differentiate this with respect to a parameter value in a region (in the simplest form in one element). This results into a DE for the sensitivity values. Solving this form for each region (element), the Jacobian can be constructed. Considerable advantage in the speed of the calculation may be obtained by utilizing the reciprocity principle, stated as: *The measurement of the flux at* $\mathbf{r}_m$ *that is due to an isotropic source at* $\mathbf{r}_q$ *is equal to the measurement of the photon density at* $\mathbf{r}_q$ *produced by a source at* $\mathbf{r}_m$, *provided that the source is created by an adjoint measurement operator*. This leads to the so-called adjoint method (Arridge and Schweiger, 1995).

3.4.4. Methods for Solving the Inverse Problem

Various approaches for image reconstruction in optical tomography have been presented. An important tool in image reconstruction are perturbation approximations, which approximate the change in the field due to a change in the material parameters. Many image reconstruction algorithms are based on the first order Born or Rytov approximations. Let us consider perturbations in the material properties: $\mu_a = \mu_{a,\mathrm{o}} + \delta\mu_\mathrm{a}$ and $\kappa = \kappa_\mathrm{o} + \delta\kappa$. The Born approximation assumes that the perturbed field is obtained as:

$$\Phi = \Phi_0 + \Delta\Phi, \tag{55}$$

where Φ_0 is the field for unperturbed parameters $\mu_{a,0}, \kappa_0$ and the perturbation $\Delta\Phi$ in the field is obtained as:

$$\Delta\Phi = \int_\Omega \delta\kappa(\mathbf{r}')\nabla_{\mathbf{r}'} G_0(\mathbf{r}, \mathbf{r}', \omega) \cdot \nabla_{\mathbf{r}'}\Phi(\mathbf{r}', \omega) + \delta\mu_a(\mathbf{r}') G_0(\mathbf{r}, \mathbf{r}', \omega)\Phi(\mathbf{r}', \omega) d\mathbf{r}'. \tag{56}$$

The Rytov approximation assumes

$$\mathrm{In}\ \Phi = \mathrm{In}\ \Phi_0 + \delta u \tag{57}$$

for the perturbed field Φ, where δu is obtained as

$$\delta u = \frac{-1}{\Phi_0(\mathbf{r}, \omega)} \int_\Omega \delta\kappa(\mathbf{r}')\Delta_{\mathbf{r}'} G_0(\mathbf{r}, \mathbf{r}', \omega) \cdot \nabla_{\mathbf{r}'}\Phi(\mathbf{r}', \omega) + \delta\mu_a(\mathbf{r}') G_0(\mathbf{r}, \mathbf{r}', \omega)\Phi(\mathbf{r}', \omega) d\mathbf{r}'. \tag{58}$$

In the following, we shall outline some popular methods for image reconstruction.

3.4.4a. Analytical inversion. In (Markel and Schotland, 2001), analytical inversion formulas based on the FDDE were derived. In this analysis, small arbitrary-shaped perturbations $\delta\mu_a(\mathbf{r})$ and $\delta\kappa(\mathbf{r})$ on μ_a and κ, respectively, in a homogeneous background are considered. The difference in the boundary data due to these perturbations is written using the perturbation theory and Green's functions. Using the explicit forms of the analytical Green's functions in different geometries (planar, cylindrical, spherical), the boundary data function can be written in a form of a Fourier-Laplace transform of the perturbations $\delta\mu_a(\mathbf{r})$ or $\delta\kappa(\mathbf{r})$. Formal inversion of the transformation then leads to an inversion formula for the perturbation. These formulas can be used to implement a practical image reconstruction algorithm.

3.4.4b. Backprojection and Backpropagation. One approach for image reconstruction is to directly apply conventional computed tomography (CT) backprojection algorithms. In (Walker et al., 1997), a filtered backprojection algorithm using a straight line weight function (as in x-ray CT) was applied for optical measurements. The backprojection approach can be improved by using weight functions that take into account the diffuse propagation of light in turbid media.

The backpropagation approach can be developed based on diffuse light propagation and a linearizing approximation. In (Matson and Liu, 1999), a backpropagation algorithm was developed by writing an expression for the scattered wave produced by pertubations in μ_a and μ_s'. Under the Born approximation, the scattered wave was written as an integral over the perturbed domain involving the homogeneous solution to the wave equation and the appropriate Green functions.

The backpropagated wave inside the medium is then reconstructed by back-propagating the detected wave througout the turbid medium. Studying the explicit formulas for reconstructed waves, the authors note that the reconstructed wave is what would be obtained if the scattered wave would actually be measured in the reconstructed plane and that the planes of reconstructed wave can be used to localize objects. More complicated inhomogeneous structures could be reconstructed using a multiple-view backpropagation algorithm, which consisted of first reconstructing the backpropagated waves from all views used for measurement, and then coherently summing the backpropagated waves.

The advantage of backprojection and backpropagation algorithms is their speed, especially when the 3D case is concerned. They can provide structural information and have been suggested to be used as nearly real-time imaging algorithms. The results of these algorithms could also be used as a starting point for a more robust or quantitative reconstruction algorithm.

3.4.4c. Linear Methods. Linear single-step reconstruction methods can be developed based on integral or differential formulation of the first order perturbation approximation.

A linearized method using integral formulation (see e.g. O'Leary et al., 1995) is obtained assuming that the perturbed field due to perturbations $\delta\mu_a$ and $\delta\kappa$ is obtained as a first order Born approximation $\Delta\Phi_1$ by replacing Φ by Φ_0 on the right-hand side of Eq. (56). The resulting integral equation can then be discretized by rewriting the integral as a sum over voxels, leading to a set of coupled linear equations. This set can also be written in a matrix form $y = Ax$, where y is a vector containing measurements and x the optical parameter values in the image voxels, and then solved by matrix inversion or algebraic reconstruction techniques.

The differential formulation can be derived by expanding the forward model (Eq. (8)) as a Taylor series at point p_0, that is close to the ideal solution,

$$y = F(p_0) + F'(p_0)(p - p_0) + (p - p_0)^T F''(p_0)(p - p_0) + \ldots, \tag{59}$$

and neglecting the terms after first order. In the discrete case the term F' is represented by the Jacobian matrix $\mathcal{J}_p^y$ defined in Eq. (51). Writing $p - p_0 = \delta p$ and $y - F(p_0) = y - y_0 = \delta y$ we arrive at:

$$\delta y = \mathcal{J}_p^y \delta p. \tag{60}$$

The discretization is usually done using the finite difference or finite element methods. The matrix equation (60) is often ill-posed and large. Various methods have been used to solve this equation, including the truncated singular value decomposition (SVD) or the algebraic reconstruction technique (ART).

The linear perturbation method is valid only for small perturbations. Commonly, especially if quantitative reconstruction is desired, nonlinear methods are used.

3.4.4d. Nonlinear Optimization Methods. In (Ostermeyer and Jacques, 1997), an iterative reconstruction approach based on the integral formulation was presented. The method used the first-order Born integral formulation and proceeded by iterating successive higher order approximations Φ_n for Φ using the previously obtained estimate Φ_{n-1} in the integrand.

Most nonlinear optimization methods aim to minimize an objective function involving the measured data and the forward model between the data and the estimated parameters of a form

$$\mathcal{G}(p) = \|L(y - F(p))\|^2, \tag{61}$$

where L is a weighting matrix. Often a diagonal data scaling vector is used, e.g., $L(i,i) = \mathrm{I}/\sigma_i$, where σ_i is the standard deviation of the measurement.

Two popular types of optimizaton schemes are now considered (the discussion here follows Kolehmainen (2001) and Arridge and Schweiger (1998), see the references for details). First, Newton-type methods seek to minimize $\mathcal{G}(p)$ iteratively using the Taylor expansion of $\mathcal{G}(p)$ around the current estimate $p^{(\kappa)}$. The new estimate is obtained as

$$p^{(\kappa+1)} = p^{(\kappa)} - \left[\frac{\partial^2 \mathcal{G}}{\partial p^2}\left(p^{(\kappa)}\right)\right]^{-1} \frac{\partial \mathcal{G}}{\partial p}\left(p^{(\kappa)}\right). \tag{62}$$

Generally, this leads to a Newton-Raphson iteration involving a second-order derivative $\partial^2 F/\partial p^2$. In practical situations, the computation of the second order term may become too slow, so approximations to the Newton-Raphson method are needed. Two popular approximations are the Gauss-Newton method and Levenberg-Marquardt -type iteration. Denoting $\partial F/\partial p(p^\kappa) = \mathcal{J}_{(\kappa)}$ and $L^T L = W$, the Gauss-Newton iteration formula becomes

$$p^{(\kappa+1)} = p^{(\kappa)} + s_{(\kappa)} \left(\mathcal{J}_{(\kappa)}^T W \mathcal{J}_{(\kappa)}\right)^{-1} W \left(y - F\left(p^{(\kappa)}\right)\right). \tag{63}$$

The Levenberg-Marquart iteration involves a control term λI:

$$p^{(\kappa+1)} = p^{(\kappa)} + s_{(\kappa)} \left(\mathcal{J}_{(\kappa)}^T W \mathcal{J}_{(\kappa)} + \lambda I\right)^{-1} W \left(y - F\left(p^{(\kappa)}\right)\right). \tag{64}$$

where $\lambda \geq 0$ is a control parameter.

A second type of optimization schemes considered here are the gradient methods, which are preferable when the dimension of the optimization problem becomes very large. A prototype gradient method is the conjugate-gradient method, where a set of search directions is generated to minimize the objective function. The minimum is searched by an iteration where the objective function is minimized along the current search direction using one-dimensional line minimization and after that a new seach direction is generated. The procedure is repeated until a termination criterion is satisfied. In conjugate-gradient method, a new search direction $d^{(n+1)}$ is obtained as a weighted sum from the previous search direction $d^{(n)}$ and the gradient z of the objective function at the current estimate:

$$d^{(n+1)} = -z\left(p^{(n+1)}\right) + \beta^{(n+1)} d^{(n)}, \tag{65}$$

where $z\left(p^{(n+1)}\right) = \partial \mathcal{G}/\partial p = -2W\mathcal{J}^T\left(y - F\left(p^{(n+1)}\right)\right)$ and β determines the weighting.

Due to the ill-posedness of the inverse problem, often regularization is introduced. A commonly used regularization method is Tikhonov type regularization. In generalized Tikhonov regularization, the objective function to be minimized becomes

$$\mathcal{G}(p) = \|L(y - F(p)\|^2 + \alpha A(p), \tag{66}$$

where *A(p)* is regularizing function and $\alpha \geq 0$. For Newton-type optimization, a commonly used method is Tikhonov regularized Gauss-Newton iteration:

$$p^{(k+1)} = p^{(k)} + s_{(k)}\left(\mathcal{J}_{(k)}^T W \mathcal{J}_{(k)} + \frac{1}{2}\alpha H_A^{(k)}\right)^{-1}\left(\mathcal{J}_{(k)}^T W\left(y - F\left(p^{(k)}\right)\right) - \frac{1}{2}\alpha g_A^{(k)}\right), \tag{67}$$

where $H_A^{(k)} = \partial^2 A/\partial p^2\left(p^{(k)}\right)$ and $g_A^{(k)} = \partial A/\partial p\left(p^{(k)}\right)$. For the gradient methods, the gradient methods, the gradient z is modified to $z = -2W\mathcal{J}^T(y - F(p)) + \alpha \partial A/\partial p$.

3.4.4e. Statistical Methods. Recently, statistical inversion methods have received some attention in the field of optical imaging (Kolehmainen, 2001; Ye et al., 1999). In the statistical approach, the measurables and the parameters are treated as quantities that are either directly observable (measurables) or cannot be directly observed (parameters). These quantities are modelled as random variables with their respective probability densities, which can be joint as the quantities depend on each other through a more or less well known model. One interpretation of this method is that the uncertainty in parameter values is modeled through probability distributions. The solution to the inverse problem is the posterior probability density of the parameters in condition of the obtained measurements. This posterior density is derived using all available information on the measurements, the underlying model and prior information. Often point estimates, such as maximum a posteriori estimate, are drawn from the posterior density to obtain more intelligible solution, which in many cases involves tedious computing (Kaipio et al., 2000).

3.4.5. Absolute and Difference Imaging

Two different imaging strategies often identified are *absolute imaging* and *difference imaging*. Absolute imaging comprises a full modeling of the internal distributions of scattering and absorption of the object to be imaged and attempts to reconstruct the true distributions of absorption and/or scattering. In difference imaging, two states of the object

are compared, i.e., two data sets are obtained, one before and one after a change in the object, and image reconstruction aims to produce an image that reveals these changes. In practice, difference imaging is an easier approach than absolute imaging, and hence the more commonly applied one. Also, if time-varying data is measured, dynamic features of the states can be accessed (Barbour et al., 2001).

3.4.6. 3D Imaging

Nowadays 3D image reconstruction schemes are becoming increasingly common. As true measurements are always performed in 3D, realistic modeling and image reconstruction requires a full 3D approach. The requirements for the memory and the computational power are substantially higher in 3D, as the dimension of the discretized problem grows rapidly. Considering, e.g., FD or FE based modeling approaches, efficient matrix manipulation and inversion schemes become of great importance. For the commonly used FE modeling, another 3D challenge is mesh generation. Mesh generation, as well as checking the validity of the generated meshes, becomes essentially harder in 3D. Yet another complication in 3D is the visualization of the parameter distributions and solutions.

4. INSTRUMENTATION AND EXPERIMENTAL METHODS

In optical imaging, the instruments can be classified into three categories by the type of data they provide: the continuous wave (CW, DC) method in which the intensity is measured, the frequency domain method (FD) in which the light is modulated and the amplitude and phase shift are measured, and the time domain method (TD) in which the full time-of-flight distribution of the photons is measured.

4.1. Instrumentation for the Measurement of DC Intensity

The measurement of intensity (corresponding to Eq. 36 at $\omega = 0$) can be performed with relatively simple continuous-wave light sources and detectors. To include several wavelengths and light source positions, either modulated or pulsed light is used.

4.1.1. Modulated Systems

Intensity modulation of the light source and subsequent amplitude measurement has the advantage of reduced low-frequency-noise. This includes 1/f noise in the electronics and stray light from external light sources. (Fig. 4.)

Multiple wavelengths can be implemented by encoding them with different modulation frequencies, or by time-multiplexing.

If a fully parallel measurement is desired, each source can be assigned a different modulation frequency. However, the system complexity increases quickly with the number of optodes, and the dynamic range is compromised. This technique is most useful for dynamic two-dimensional imaging of the cortex.

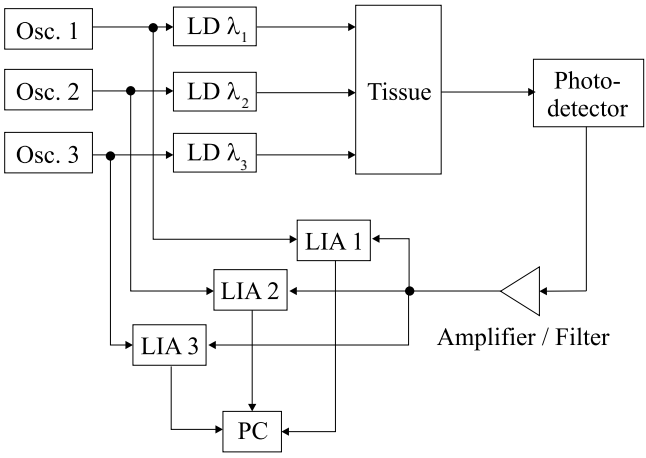

Figure 4. An intensity-modulated continuous-wave instrument with three wavelengths. Osc. = oscillator, LD = laser diode, LIA = lock-in amplifier, PC = personal computer.

4.1.2. Time-Multiplexed Systems

To solve the problem of dynamic range in optical tomography, time-multiplexing of the light sources is necessary.

A laser diode can be switched on and off using the injection current, and this can be combined with modulation if necessary. Another possibility is to use mechanical shutters for each laser diode. This has the advantage of a high switching speed (∼1 ms). A disadvantage is the large number of laser diodes required in a tomographic system. If only one laser diode is used for each wavelength, the light can be directed to the active source fiber using a fiberoptic or a mirror-based switch (DiCon FiberOptics, 1998; Schmitz et al., 2002). A time-multiplexed system is illustrated in Fig. 5.

4.1.3. Detectors in Continuous-Wave Systems

Most NIR-sensitive detectors can be used in continous-wave systems. Speed is usually not a problem, although there are a few detector types which are too slow for modulated light (∼kHz). In applications which require relatively small interoptode distances, silicon photodiodes (SiPD) are typically used. The high quantum efficiency (∼70%) results in a high signal-to-noise ratio and these detectors are not easily damaged by excessive incident light. If high speed is not required, detectors with a large sensitive area (>10 mm^2) may be used. A disadvantage of SiPDs is that normally they have no integrated current amplification, and thus noise of the subsequent electronics may overwhelm the dark current, increasing the detection limit of the system. Newer detectors with integrated amplifiers are available, but their speed at a given photosensitive area is not as good. To increase dynamic range, gain-programmable amplifiers can be included (Schmitz et al., 2002).

At very low (<1 pW) light levels, photomultiplier tubes (PMTs) are usually the best choice of detector. They use a secondary emission cascade to increase the current from a

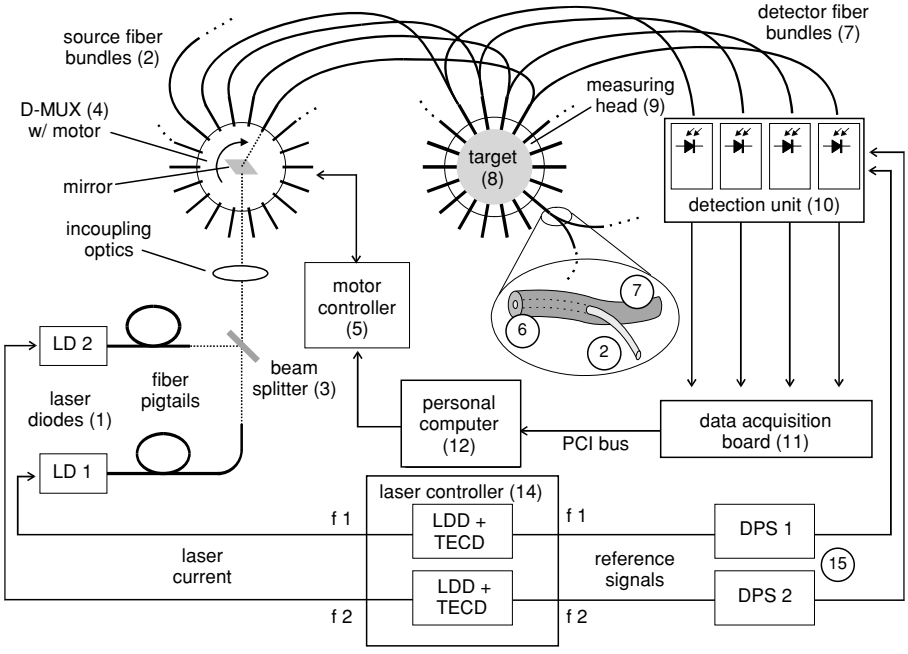

Figure 5. A continuous wave instrument with time-multiplexed source fibers. LDD = laser diode driver, TECD = thermoelectric cooling driver, f1, f2: laser diode modulation frequencies, LD1, LD2: laser diodes, D-MUX: optical demultiplexer, DPS1, DPS2: digital phase shifters. Reproduced with permission from (Schmitz et al., 2002).

single detected photon. PMTs have a relatively low quantum efficiency for near infrared light ($\leq$10%), but they have a very low dark current and the noise figure of the dynode chain is very low ($\sim$1.2). They are somewhat vulnerable to high intensities and anode currents. The photosensitive area is quite large ($\geq$50 mm^2) and they can be made with a fast response time (electron transit time spread (TTS) $\sim$200 ps). Due to the relatively large size and the high voltage required, PMTs are not ideal for direct-contact measurements with tissue.

The instrumentation is compact and simple enough for the implementation of multichannel systems which can be placed on the surface of the tissue without optical fibers (Vaithianathan et al., 2002). The light sources and large-area photodiodes can be (almost) in direct contact with the tissue, yielding a very high signal-to-noise ratio.

4.1.4. Light Sources

Laser diodes and light-emitting diodes (LEDs) are used in CW systems. Laser diodes have a narrower spectral bandwidth and they can be driven with lower electrical current than LEDs, thus they are usually preferred.

4.1.5. Calibration and the Use of Data

The separation of scattering and absorption in general requires the measurement of intensity along with at least one other feature of the TPSF, such as the mean time. Thus, while

the changes in the measured intensities reflect both changes in scattering and absorption, it is not possible to identify these changes as one or the other based on intensity alone (Arridge and Lionheart, 1998). Usually, it is assumed that scattering is not time-varying and changes in the absorption coefficient can then be spatially resolved based on the measured intensities. Since the background optical properties cannot be uniquely determined, the initial assumption is that the medium is homogeneous.

Intensity provides a high contrast-to-noise ratio to changes in the absorption of tissues close to the surface. Unfortunately, it is also very sensitive to the contact between the optodes and tissue. To reduce the variability of the contact, it may be preferable to attach the optodes at a distance of a few millimeters from the skin. If dark hair is present, a contact measurement may be a good choice, as it reduces the motion of hair under the optodes. A pressure sensor can in some cases be used to measure changes in the contact.

Intensity data is usually not explicitly calibrated, instead, a reference measurement is made. The reference can be a phantom with known optical properties and geometry. In the ideal case, the shape and dimensions of the reference are exactly the same as that of the tissue. The differences between the logarithms of intensities in the two states (reference and tissue) are used to reconstruct a map of the differences in the optical properties between the two states.

If desired, a calibration of the data can be performed with a homogeneous cylindrical phantom. By measuring the data corresponding to each source-detector pair, the coupling coefficients and the differences between the channels can be resolved based on symmetry. (Schmitz et al., 2000) It is also possible to solve for the calibration parameters together with the optical properties in the reconstruction (Boas et al., 2001a).

4.2. Instrumentation for the Measurement of the TPSF

The most flexible of the three instrument types is the time-domain instrument, which measures the flight time of each detected photon emitted by a pulsed light source.

4.2.1. Measurement Principle

In a time-resolved instrument, the light is emitted to the tissue in a rapid train ($\sim$100 MHz) of very short pulses (1–100 ps). The photons that are transmitted through the tissue are detected at several locations on the surface of the tissue. The signal for each detected photon is amplified in the PMT and preamplifier. The resulting electrical pulse is timed using a constant fraction discriminator (CFD) and a unit which compares the timing of the CFD-generated TTL pulse and the earlier electrical pulse produced by the pulsed laser. The time-comparison is usually realized with a time-to-amplitude converter (TAC) or a picosecond time analyzer (PTA). The pulses are then added to a histogram in digital electronics. The histogram of the photon flight times is then the uncalibrated TPSF. (Fig. 6.)

An advantage of the photon-counting technique is the possibility of selecting only those analog pulses, the heights of which are within a preselected range. The pulse heights due to cosmic rays is higher than average. Lower-energy pulses are likely to be the result of thermal excitation, while the remaining pulses are likely to be caused by true photoelectron emissions in the PMT.

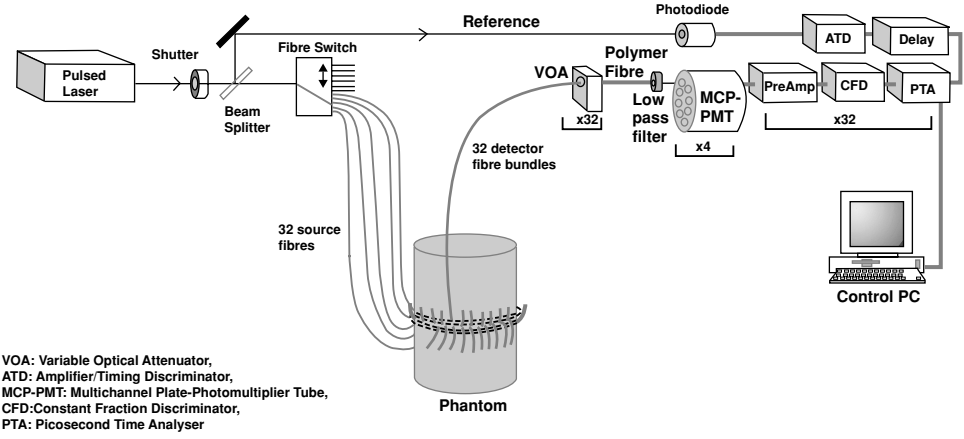

Figure 6. A time-resolved instrument (Schmidt et al., 2000). Reproduced with permission from (Hillman, 2002).

4.2.2. Detectors in Time-Resolved Systems

Since the electron transit time spread in PMTs is of the same order of magnitude as the TPSF, a fast PMT should be used to minimize distortion of the TPSF shape. Metal-channel PMTs such as the Hamamatsu R7400 series have a TTS of ∼230 ps, and microchannel plate (MCP) PMTs have a TTS of ∼45 ps. MCP-PMTs can be implemented with multiple anodes but interchannel crosstalk and high cost limit the use of this detector type in imaging systems.

Photon-counting systems have a limited dynamic range; the photon count rate is limited by the electronics to a value which is usually under 10^6 counts per second (cps). While this is high enough for large interoptode distances in a transmission geometry, it limits the signal-to-noise ratio available in the reflection geometry. For example, a typical intensity detected in activation imaging with a 3-cm interoptode distance is 50 pW (depending on the source power, hair, the diameter, and the numerical aperture of the optical fiber bundles), which corresponds to approximately $20 \cdot 10^6$ cps.

In order to reduce the intensity that can reach the detector, a variable optical attenuator (VOA) can be used to attenuate light in a controlled way (Eda et al., 1999; Schmidt et al., 2000). It consists of a disk with a set of holes of different sizes, or neutral density filters with different optical densities. The attenuation is controlled with a stepping motor. A VOA increases the time-multiplexing time and may affect the reproducibility of the measurements. Also, the calibration of the instrument becomes more difficult. In a pure transmission geometry, which is sometimes used in breast imaging, the required optical dynamic range may be small enough so that attenuation is not necessary even in a time-resolved system.

4.2.3. Light Sources

Time-resolved imaging systems use a pulsed light source, generally capable of emitting pulses in the range from 1 ps to 100 ps. Typically, the average power is about 10 mW,

although some systems operate at powers below 0.1 mW to comply with FDA's eye-safe classification (Ntziachristos et al., 1998).

In laboratory conditions, mode-locked picosecond Ti:Sapphire lasers are often used, but they are impractical for clinical use. Pulsed laser diodes can be used to generate $\sim$ 50-ps pulses, which may be adequate with appropriate calibration. Mode-locked and frequency-doubled fiber lasers (manufactured by IMRA America) are also available. They are potentially more stable and compact than Ti:Sapphire systems.

4.2.4. Calibration

The TPSF is distorted to some extent by the instrument. The optical fibers have temporal dispersion, the detector has a finite TTS and the finite laser pulse width also contributes to the instrument response function (IRF). If the full TPSF is used for reconstruction, it is necessary to measure the IRF and correct the measured TPSF by deconvolution. If only data types such as mean time, integrated intensity, variance and the Laplacian are used, a simpler calibration procedure can be used (Hillman et al., 2000). For example, the mean time is shifted by a constant (equal to the mean time of the IRF), and this is true for the variance of the TPSF as well. The normalized Laplace transform can be calibrated by dividing it by the transform of the IRF.

In practice, calibration is only needed for absolute (static) imaging of the optical properties. Calibration is usually performed in steps. Absolute calibration of temporal data types can be performed using a tool which holds the source fiber and detector fiber bundle at a fixed distance from each other. A diffusing paper is used between them to excite all the modes in the multimode detection fiber bundle. The tool should not produce temporal broadening of the pulse. Interchannel variations in the IRF can be measured using a separate relative calibration tool or simply by measuring each fiber in the absolute calibration tool.

If the source and detector fibers are combined into a single optode, it is possible to perform a part of the calibration *in situ*. Each source is switched on sequentially to illuminate the surface of the tissue under the corresponding detector fiber bundle. The TPSF measured is an approximation of the IRF of the instrument. The lengths of the source fibers must be measured separately. The diffuse reflection by the tissue and the characteristics of the surface should be accounted for. Since the procedure can be performed on-line, interchannel drift is reduced. (Hebden et al., 2003).

If a reference phantom with identical dimensions to the tissue to be imaged exists, and if its optical properties are known, it is possible to avoid explicit calibration by reconstructing difference images based on the differences in the data measured on the tissue vs. the data measured on the phantom. If a nonlinear reconstruction algorithm is used, the resulting images should be equivalent to those obtained with absolute calibration.

Another way to use the time-resolved data is to divide the TPSF into temporal windows and look at the intensity of light within each window. This allows the selection of photons that have travelled a short path or those that have travelled longer ones. The earlier photons travel more straightforward paths while the later ones have spread out more in the tissue. This can be used to estimate scattering and absorption. In a reflection geometry, the later photons provide higher sensitivity to changes in the deeper layers of tissue. (Steinbrink et al., 2001).

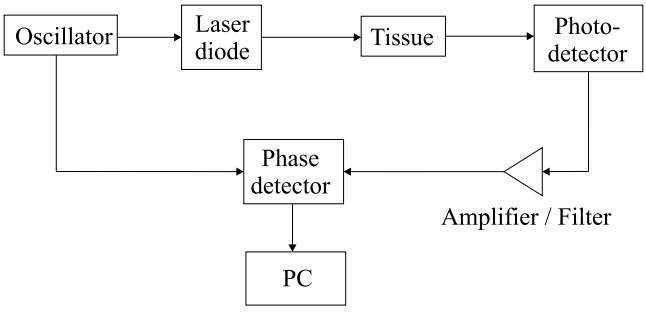

Figure 7. A homodyne frequency-domain instrument.

4.3. Instrumentation for the Measurement of Phase and Amplitude

In the time domain, the information of the TPSF is collected with a finite time resolution. The corresponding information may be obtained by measuring the phase and amplitude of modulated light at a set of modulation frequencies. While a few multifrequency implementations exist (Pham et al., 2000), the dynamic range and noise of a frequency-domain system can be improved by optimizing the electronics for a single frequency. The amplitude and phase at a single frequency (Eqs. 36 and 39) may be sufficient for the reconstruction of scattering and absorption images.

4.3.1. Homodyne Systems

In a homodyne system, the light source is modulated at a radio frequency, and the phase and amplitude of the detected and amplified signal are measured using a phase and amplitude detector, such as a lock-in amplifier (LIA) or an IQ circuit. A functional diagram of a homodyne system is shown in Fig. 7.

4.3.2. Heterodyne Systems

A heterodyne system consists of an RF part and an IF part. The modulation frequency f_{mod} is produced by an RF signal source. After the detected signal is amplified, it is down-converted to an intermediate frequency (IF, typically $\sim$10 kHz) with a mixer and a low-pass filter. The phase and amplitude can be measured using a LIA as usual. (Fig. 8.) The frequency that is used to drive the receiving mixer is $f_{LO} = f_{mod} + f_{IF}$. To provide a synchronized reference IF signal, the signals from the two rf sources are mixed and low-pass filtered. It is possible to syncronize the two rf sources with an external clock using a phase-locked loop (PLL). If a digital LIA is used, the reference signal should be synchronized with the sampling frequency of the analog-to-digital converter (ADC) in the LIA to reduce phase noise. (Nissilä et al., 2002a).

Advantages of the heterodyne design include lower phase noise and larger dynamic range afforded by the use of digital LIA technology, and a wider range of modulation frequencies.

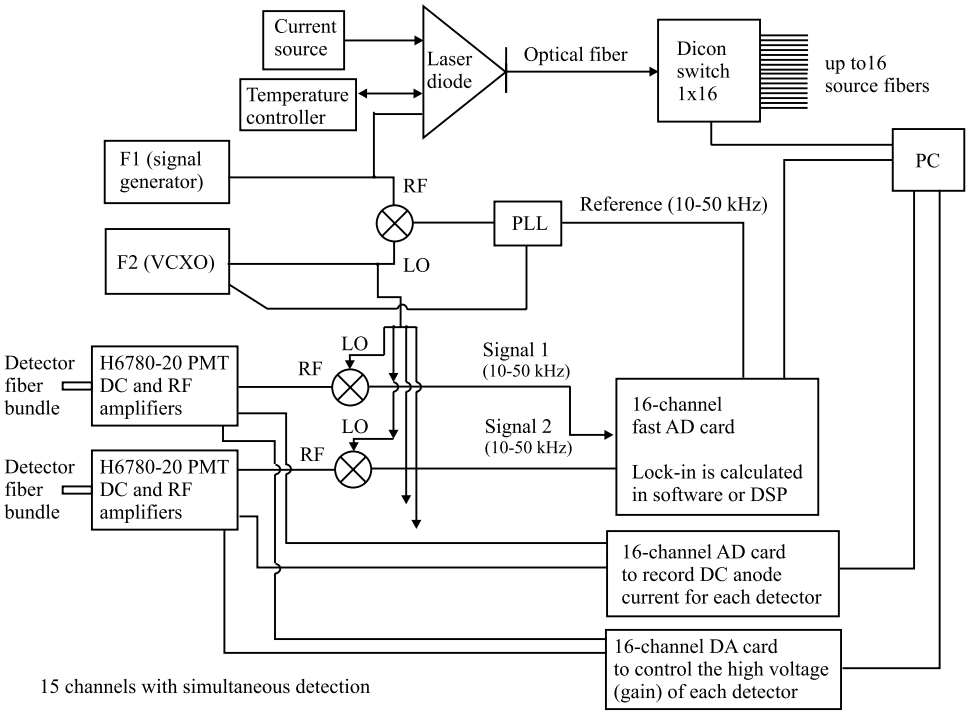

Figure 8. A heterodyne frequency-domain instrument.

4.3.3. Phased Array

A variation of the frequency-domain technique uses two light sources on opposite sides but at equal distances from the detector. The two light sources are modulated with a 180° relative phase shift. An interference pattern in the tissue is formed by the photon density waves. The measured phase is very sensitive to changes in the optical properties of the tissue in the equidistant plane from the two sources. To scan the probed volume of tissue, it is possible to modulate the amplitudes of the light sources slowly so that their relative amplitudes change in time. This bends the plane of sensitivity. The technique has been used, e.g., in activation studies on children (Chance et al., 1998a).

4.3.4. Detectors in Frequency-Domain Systems

Many continuous-wave detectors can be used in frequency-domain systems. The requirements are a fast rise time and the usual high NIR sensitivity and low noise. PMTs and APDs are normally used. For optical tomography, PMTs are preferred, while APDs are excellent in applications that only require measurements at relatively short interoptode separations (2–3 cm).

4.3.5. Light Sources

Although LEDs can also be used in a frequency-domain system, a better modulation efficiency can be obtained with laser diodes. Single-mode laser diodes are preferable, as their output is more stable against changes in temperature. Temperature stabilization should be implemented especially if the sensitivity of the photodetector depends strongly on wavelength. An impedance-matching circuit is required to obtain a good modulation efficiency.

4.3.6. Multiplexing

Frequency multiplexing of the light sources is not practical in the frequency domain as the number of simultaneous RF sources required is high, and the technology is already more complicated than in modulated CW systems. The different wavelengths can be frequency-encoded, however.

A practical solution is to illuminate the different source optodes sequentially. Normally, an optical switch is used for this. Since the signal-to-noise ratio of frequency-domain systems is comparable with that of DC systems, they can be used for dynamic imaging. The time constant of the LIA should be chosen so that it does not increase the effective switching time.

4.3.7. Dynamic Range

A difficulty in traditional phase measurement systems is that several components produce a phase shift which depends on the amplitude of the signal. This effect can be reduced by operating the components far below the top of their dynamic range. The phase-amplitude crosstalk in a photomultiplier tube depends on the relative magnitude of the anode current and the quiescent current through the voltage divider. Either by increasing the quiescent current, or by reducing the high voltage so that the anode current is much lower than the quiescent current, crosstalk can be reduced to an acceptable level.

While the crosstalk within the LIA and the crosstalk between the detection channels produce errors in measurements, these can easily be overwhelmed by the RF crosstalk between the source and the detector electronics. Both systems operate at precisely the same radio frequency, but their amplitudes can be different by as much as 170 dB. This problem can be solved by careful radiofrequency shielding and an appropriate selection of components up to about 200 MHz. Above this frequency, it becomes increasingly difficult to preserve the dynamic range. To extend the dynamic range of the system, gain switching or VOAs can be applied (Pogue et al., 1997; McBride et al., 2001; Nissilä et al., 2002a). With gain switching, phase can be measured accurately over a dynamic range of $1 : 10^6$.

4.3.8. Calibration

PMTs have an internal mechanism for gain adjustment. After the gain has been changed, there is a short transition period before the signal settles. In addition, changes

in the intensity of the incident light also cause hysteresis and the signal is slightly delayed. If absolute measurements are required, this needs to be taken into consideration.

Calibration of frequency-domain data in the general case requires the determination of the frequency response of the instrument. If a single frequency is used, this means that the amplitude and phase of the system for an object with known optical properties is to be measured. A direct measurement of the phase delay can be made just as for the mean time in the time domain (Sect. 4.2.4). Calibration of absolute amplitude is more difficult as the contact between the optodes and the tissue as well as the surface texture of skin have a large effect on the amplitude.

If gain switching by adjusting the high voltage of the PMT is used, it is necessary to calibrate the dependency of phase and amplitude on the high voltage separately for each detector.

4.3.9. Stability

The temporal (or phase) stability of frequency-domain instrumentation requires special attention. Phase noise and drift of the RF system can be minimized by precise synchronization of the two RF signal sources and the LIA. The temperature fluctuations of the laser diode should be minimized without compromising the RF shielding. The photodetector is also sensitive to temperature variations, and for optimal performance it should be cooled to a stable temperature. Temperature stabilized detectors are rarely used in frequency-domain instruments due to technical difficulties in retaining a low transmitter-receiver RF coupling in such a system. The RF components should not be used close to their maximum power ratings, as phase drift increases if the temperature of the components is not stable. It is possible to reach $\sim$2 ps/h stability in a closed laboratory environment.

4.4. Phantoms for Diffuse Optical Imaging

Optically tissue-equivalent phantoms have been developed by several groups. Liquid phantoms are usually made by diluting Intralipid into water and adding ink to obtain the desired absorption. A problem with this approach is the mismatch in the refractive indices at glass-liquid boundaries. To create heterogeneous phantoms with a uniform refractive index, transparent resin can be used together with a dye and a scattering material, such as titanium dioxide or microspheres. The dye and scatterer are diluted in alcohol and mixed with the resin. During the hardening process, care must be taken to avoid cracks and bubbles. The anisotropy factor g (Eq. 4) with TiO_2 particles is about 0.5 and with latex microspheres about 0.9, which is closer to that of tissue. (Firbank et al., 1993, 1995).

4.5. Techniques for the Attachment of Optodes on Tissue

The coupling of optical fibers with tissue is critical for the quality of the measured data. Various techniques have been proposed, ranging from a modified motorcycle helmet to a fiberbrush. Thermoplastic materials are commonly used for head measurements. They can be reshaped for each subject and measurement area separately (Fig. 9). In other body parts, which have a thicker layer of soft tissue, it may be more difficult to obtain a stable contact

Figure 9. Optical fibers mounted on a neonate using a thermoplastic mount.

between the tissue and the optical fibers. In such cases, it may be advantageous to avoid direct contact with the tissue and let the optodes stay at a distance from the skin. In this way, the optodes do not apply pressure to the skin, which would affect circulation as well as the boundary shape. It is also possible to bend the ends of the optodes to a 90° angle, which may be useful if space is constrained, such as when measuring inside a MR scanner. The angle may also help to reduce motion artifacts if the fiber bundles are attached to the body.

In the case of the head, hair is a major problem. Long and dark hair are particularly difficult. The hair may attenuate a large part of the light, which reduces the signal-to-noise ratio. The hair can also move under the optical fibers, causing large changes in the intensity of the measured signal. The temporal data types are less sensitive to this type of phenomena, but their contrast-to-noise ratio may not be sufficient to detect small changes such as those related to brain activity.

In hair-free cases, it is possible to utilize large-area SiPD detectors directly or almost directly on the surface of the tissue. This situation occurs in frontal studies with adults and often with neonates.

In optical mammography, several groups use the arrangement familiar from x-ray mammography, where the breast is compressed between two glass planes (Franceschini et al., 1997). The Philips optical mammography prototype (Colak et al., 1999) uses a scattering liquid to fill the gap between the breast and a cone containing the optodes. The optode geometry is fixed and the contact between the optodes and the liquid is constant, which should remove many artifacts. It is also possible to use precise mechanical positioners to place the optodes on the surface of the breast, as in the system by McBride et al. (2001).

4.6. Registration

Model-based reconstruction in optical tomography is sensitive to errors in the positions of the optodes. Markers can be placed on the skin at the optode positions, and photographed

from different angles using a digital camera. The images are then used to reconstruct the boundary of the object. A laser-scanning system or a measurement arm which tracks the 3D position of the pointing head can be used to measure the shape of the object. The latter also works if hair is present. It is also possible to obtain an approximate boundary based on indirect techniques such as digitizing the surface of the thermoplastic mount that was shaped to match the subject and hold the fibers.

A FE mesh can be generated based on the recovered boundary shape. If an anatomical MR image of the subject is available, it is possible to recover the boundary (as well as boundaries between different tissue types inside) from the segmented data and use it for mesh generation. Only the optode positions (as well as the positions of markers present in the MR imaging) need to be digitized.

5. APPLICATIONS

5.1. Muscle Studies

In skeletal muscle studies, the primary aim is to investigate the oxidative metabolism and its changes. NIRS systems with a single or a few channels have been applied to muscle measurements using continuous-wave (CW), spatially-resolved, time-domain, and frequency-domain techniques. Due to the commercial availability and lower price of instrumentation, CW studies have been most common (Ferrari et al., 1997; Boushel and Piantadosi, 2000).

Both healthy subjects and patients have been studied using single-channel continuous-wave NIRS devices. Muscle experiments usually involve a study group and a control group performing the same exercise test. During or after the test, the oxygen consumption and/or recovery is monitored by recording the changes in [HbO_2], [Hb], and [totHb]. The CW-NIRS technique has also been used in general studies of oxidative metabolism in skeletal muscles and it has been applied, e.g., to sports science to investigate differences in oxygen utilization of trained and untrained subjects (Ferrari et al., 1997). The CW-NIRS studies have been validated by comparing results, e.g., with ^{31}P magnetic resonance spectroscopy (MRS) measurements, and a correlation has been found between the techniques (Sako et al, 2001). Although the single-channel CW-NIRS technique has been widely used in research, it has not been established in clinical practice because of its limitations (see Sect. 4).

The spatial mapping of oxidative metabolism of skeletal muscles gives valuable information about the redistribution of blood, local changes in blood flow, and oxygen consumption at rest and during exercise. Multi-channel CW-NIRS instruments can be used to investigate these phenomena. Such devices typically contain 12–16 channels and are capable of imaging an area of $\sim$60 cm^2 (Nioka et al., 1999; Quaresima et al., 2001). The image-acquisition time of the system by Quaresima et al. (2001) is 0.1 s, which is fast enough for imaging changes in oxidative metabolism. Even a 200-channel system with an image-acquisition time of 0.2 s has been developed (Niwayama et al., 2002). However, the decreased acquisition time per channel tends to reduce the signal-to-noise ratio of the data. Results from these multi-channel CW-NIRS experiments indicate, e.g., that the vasculature in general and the capillary recruitment varies locally during an exercise. Although the variations of venous blood volume and oxygen saturation are considered the principal sources

of the optical signal, the exact contributions of different parts of vasculature are difficult to distinguish. Improvements in blood flow and venous saturation measurements using NIRS may open up new possibilities.

A typical CW-NIRS imaging system provides topographical images at a relatively low resolution. These images are often qualitative and/or relative, i.e., changes in [HbO_2], [Hb], and [totHb] with respect to an initial state. Utilization of tomographic reconstruction methods can provide quantitative data. A frequency-domain system has also been used to obtain topographical images using phase and amplitude data (Maris et al., 1994). With improvements in algorithms and utilization of diffusion theory, absolute values for μ_a and μ_s' were obtained locally (de Blasi et al., 1995). From this data, the absolute concentrations of [HbO_2], [Hb], and [totHb] and also the oxygen saturation were determined locally.

Using time-resolved instrumentation, a simultaneous tomographic reconstruction of μ_a and μ_s' may be possible. A 32-channel system has been applied to study cross-sectional imaging of an adult forearm (Hillman et al., 2001). In these measurements, 32 source fibers and 32 receiving fiber bundles were fixed around the forearm of the subject. The source fibers were at a 2-mm distance from the skin, e.g., to avoid fiber-tissue coupling artifacts and the receiving bundles gently touched the skin. Absolute images revealing the optical structure of the forearm were calculated. By using two wavelengths (780/790 and 820 nm), difference images showing the spatial changes in chromophore concentrations due to a finger exercise were obtained as well. The image reconstructions were carried out using a DE and FEM based algorithm in a 2D circular mesh using a 2D:3D correction for the measurement data. The mean time-of-flight data was used for the reconstructions (Fig. 10).

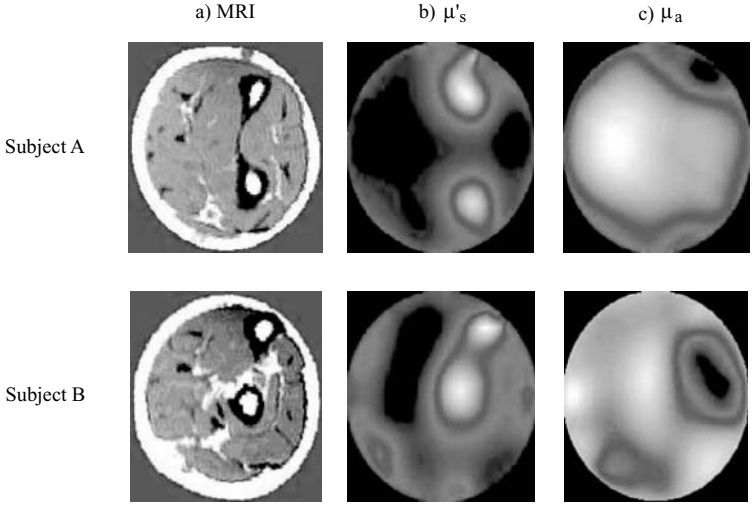

Figure 10. Absolute images of human forearms measured at 780 nm. The image area has a diameter of 7 cm. a) Cross-sectional MRI images of forearms of two volunteers. b) Spatial reconstruction of μ_s'. Bones are clearly visible because of their relatively high scattering coefficient. Also the more weakly scattering large muscles are resolved among skin and bones. c) The reconstructed absorption images correspondingly show maximum values for muscles, especially close to the largest arteries (UCL, 2001).

Tissue heterogeneity should be taken into account in muscle studies. It is a good practice to document the thickness of the adipose layer for each measured subject and, if possible, a multi-layer model should be used in the analysis (van Beekvelt et al., 2001). Also, the location and density of blood vessels in surface tissues may influence the results, because oxygenation and hemodynamic changes can occur in the skin and subdermal tissues. It may be possible to predetermine these changes using a short source-detector separation.

Myoglobin is another oxygen-carrier molecule in muscles having absorption properties similar to those of hemoglobin but with a significantly lower concentration. The changes in myoglobin volume and oxygenation have a small effect on the measurement signal and are typically superimposed on the absorption changes of hemoglobin. Also, only the concentration changes of hemoglobin are often measured, even though cytochrome oxidase may provide additional information on the oxidative metabolism of a muscle.

Movement artifacts and geometrical changes in muscles, especially during a dynamic exercise often cause severe problems. These experimental issues might be possible to include in modeling and reconstruction algorithms. So far, mostly forearm, thigh, and calf muscles have been studied because they are easily accessible, simple to exercise, and their blood circulation can be easily manipulated. Diffuse optical imaging of other muscles, such as the abdominal, back, or neck muscles, provide another set of challenges for experiments and modeling.

5.2. Optical Mammography

Traditionally, clinical techniques for breast cancer imaging or mammography exploit X-rays. The use of ionizing radiation causes a risk for the subjects and the technique has limitations regarding to its specificity and sensitivity (Moesta, 2002). MRI has also been used to diagnose breast cancer but is not in widespread use due to the cost of an examination. Optical mammography may complement the existing modalities.

Optical mammography is currently the most actively investigated application of diffuse optical imaging (OSA, 2002). Healthy breast tissue is optically relatively homogeneous, which makes it a suitable target for optical imaging. Because of its relatively low concentration of hemoglobin, it is possible to image through the whole breast. Optical mammography may offer unique information when compared with other breast imaging modalities such as X-ray, ultrasound, MRI, and isotopic imaging. Such information can be, e.g., the differences in the hemoglobin, water, and lipid concentrations and in the blood oxygen saturation between the carcinoma and healthy breast tissue. Angiogenesis and changes in the oxidative metabolism of breast tissue might be observed even before the structural changes detectable using X-rays have developed.

The Philips Medical Research Laboratory has carried out a research project using CW techniques (Colak et al., 1999). They have constructed a CW imager with 255 source fibers and 255 detector channels. In their setup, a patient lies down on an examination bed which includes a black conical cup where the optical fibers are mounted. During the imaging procedure, the breast is pendently held in the cup which is filled with a matching fluid to reduce coupling artifacts. The image reconstruction of the Philips system is based on a modified backprojection algorithm. The optical properties of the cup filled with the matching fluid are first imaged as a reference medium. Thereafter, the breast is imaged and the difference images of attenuation coefficient (i.e., $\sqrt{3\mu_a\mu_s}$) are generated. In clinical

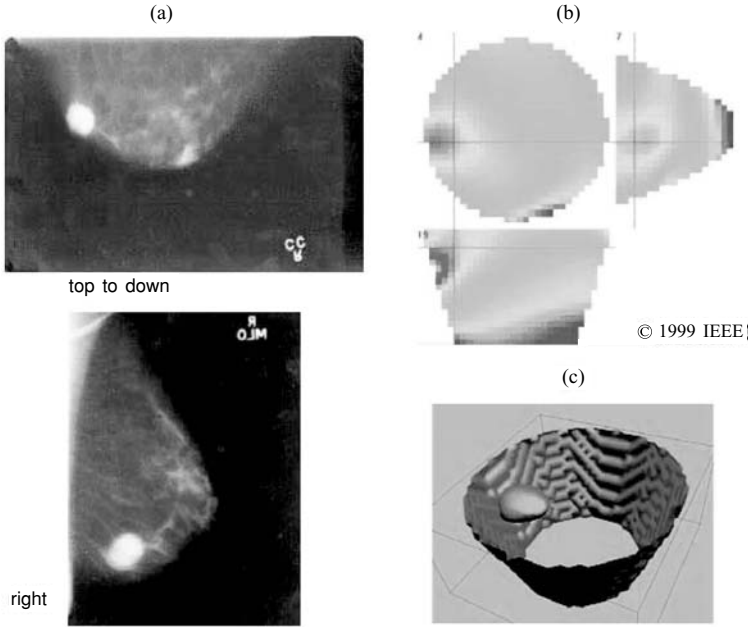

Figure 11. a) X-ray images of the right breast of a patient with Medullair carcinoma. b) Multiplanar cross-sectional optical images. The lesion is visible on the left showing a strong attenuation of light. c) A 3D isocontour image of the reconstructed cancerous tissue. The images have been reproduced with permission from (Colak et al., 1999).

tests, optical mammography was able to detect nine of the ten patients previously diagnosed to have a breast lesion using X-ray and ultrasonic imaging. In Fig. 11, a successful detection of a breast cancer is illustrated.

More comprehensive information on breast tissue can be obtained using time-and frequency-domain techniques. In the collaborative project between the Carl Zeiss company (Oberkochen, Germany) and Fantini et al., a frequency-domain instrument was used to image 69 breast cancer patients with a sensitivity of 73%. During the measurements, the breast was compressed between two glass plates and the scan was carried out by mechanically moving the source and the detector fiberbundle on opposite sides of the breast. In the system, two imaging projections (craniocaudal and mediolateral) were possible to acquire. The system produced the so-called normalized *N*-parameter maps where phase data was used for an edge correction only. In each scanning position, the parameter is related to the optical absorption of breast tissue. More recently, a similar system and algorithms have been applied to clinical tests of 131 breast cancer patients by Siemens AG, Medical Engineering (Erlangen, Germany). In these experiments, a sensitivity of 72% and specificity of 52% were obtained. (Fantini and Franceschini, 2002).

Grosenick et al. (1999) have developed a pulsed mammography system capable of measuring time-resolved transmittance images of the breast. In a typical experiment, 1500 scan positions in steps of 2.5 mm are collected. Normalized photoncount maps in a selected time window have been used to image the optical density of breast tissue. In addition, the μ_a and μ_s' have been calculated from an analytical solution of the diffusion equation in

an infinite slab assuming an optically homogeneous breast tissue. The optical properties of tumors are determined by including spherical inhomogeneities. In recent studies, random walk theory has been applied to estimate the material parameters of tumors (Grosenick et al., 2002). In clinical studies, the system has been tested using 35 suspected breast-cancer patients. The patients underwent X-ray and MRI examinations, where 26 of them were diagnosed to have breast cancer. Optical mammography was able to identify 17 cases. The nine undetected cases included a carcinoma *in situ*, a lymphoma, and several invasive ductal carcinomas. In some cases, the cancer was outside the imaged area but in other cases, the optical contrast between the cancerous and benign tissue was too low.

Tromberg et al. (2000) have investigated the optical properties of breast tissue, e.g., during different menopausal phases. They have developed a single-channel multi-wavelength multi-frequency instrument. In this system, the modulation frequency can be swept between 300 kHz and 1 GHz. Both the source fiber and the APD are mounted in a hand-held probe so that the measurement head is in direct contact with the patient. The optical parameters are resolved by fitting the measured amplitude and phase values to an analytical diffusion-equation model. From the resolved absorption coefficients at each wavelength, the concentrations of the four major absorbers in breast tissue, Hb, HbO_2, water, and lipids are determined. The studies of Tromberg et al. have shown that the absorption and scattering coefficients of premenopausal breast tissue are typically larger than the values of postmenopausal tissue. Furthermore, they have shown that cancerous tissue may have 1.25 to 3 times higher absorption coefficient compared to healthy tissue, which should give rise to contrast in optical mammography (Tromberg et al., 2000). In a recent study of 30 healthy women and a woman with fibroadenoma, the group has shown that the multi-wavelength measurement provides additional information to distinguish between normal and cancerous tissue. They demonstrated that the concentration changes of water and lipids might be better indicators of cancer than, e.g., the hemoglobin concentration or oxygen saturation (Cerussi et al., 2002).

The relatively poor spatial resolution of optical mammography has been attempted to overcome using multimodal imaging systems. The unique functional information of optical mammography has been coupled to spatially accurate X-ray and MRI images (Boas, 2002; Ntziachristos et al., 2002). In these approaches, the physiological data provided by optical mammography can be simultaneously registered with the anatomical data or, alternatively, the anatomical data can be used to guide the cancer detection in optical imaging. Also the optical contrast between a lesion and normal tissue can be enhanced using an absorbing contrast agent (Ntziachristos et al., 2000). Hybrid techniques employing fluorescent contrast agents (Hawrysz and Sevick-Muraca 2000; Ebert et al., 2001) and ultrasonic enhancement (Holboke et al., 2000) have been used to improve the sensitivity of optical mammography.

During the last few years, nonlinear inversion algorithms and FE models of the diffusion equation have been applied to *in vivo* data. The first published 3D FEM based reconstruction of breast tissue was based on DC data (Jiang et al., 2001) and the first FEM based reconstruction of quantitative hemoglobin concentrations in breast tissue in 2D was based on frequency-domain data (Pogue et al., 2001). The group at Dartmouth College has developed a frequency-domain imager with 16 time-multiplexed source channels and 16 parallel detection channels (McBride et al., 2001). The fibers are alternately fixed on a circular planar array so that the breast can be placed pendently in a central ring forming a firm contact with the tissue.

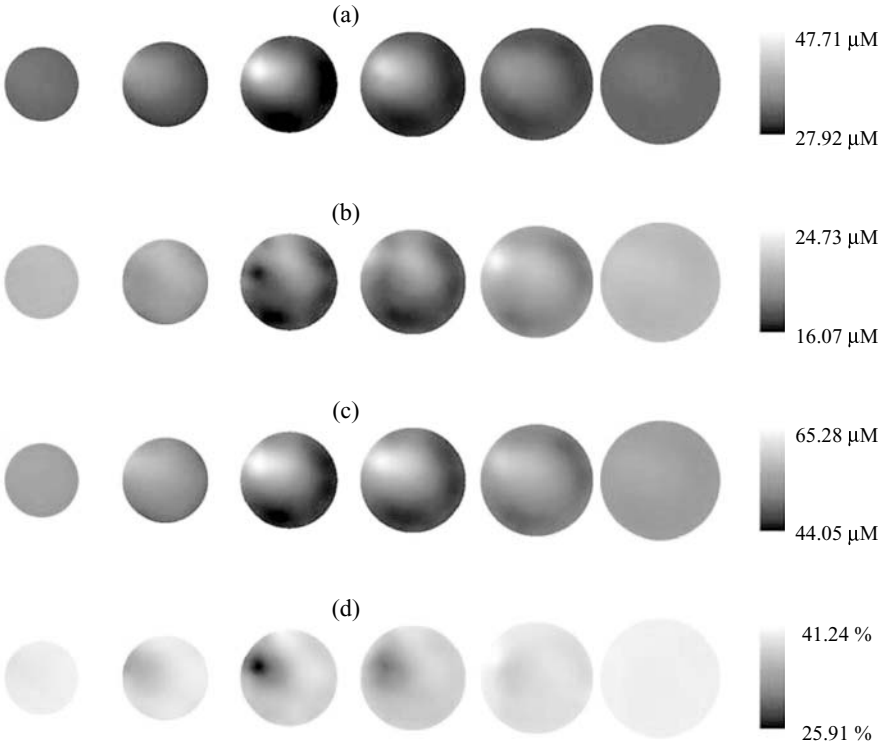

Figure 12. Maps of a) [Hb], b) [HbO_2], c) [totHb], and d) oxygen saturation. Each slice represents a different plane of the reconstruction mesh. In each case, cancerous tissue is clearly resolved in the third slice. The concentration of total hemoglobin is increased within the tumor area because of increased angiogenesis. Respectively, the oxygen saturation has decreased because of the increased oxidative metabolism due to the rapid grow of cancerous tissue. (Dehghani and Pogue, unpublished).

The Dartmouth group has recently developed a quantitative reconstruction method based on a 3D FE model (Dehghani et al., 2003). The calibration of the data at each wavelength is carried out using a reference phantom. In a recent experiment, the group imaged the breast of a subject with a malignant tumor of 11 mm in diameter. The phase and amplitude data were collected at four wavelengths from three planar slices (at the tumor site, at 12 mm above, and at 5 mm below the central slice). From the spatial distributions of absorption coefficient, maps of [Hb], [HbO_2], [totHb], and tissue oxygen saturation were obtained (Fig. 12).

5.3. Optical Imaging of the Brain

5.3.1. Activation Studies

5.3.1a. Introduction. Optical imaging can be used to study the hemodynamic changes induced in selective activation of the brain in a controlled activation task. Activation studies can be performed using a variety of existing brain imaging methods, such as

multichannel electroencephalography (EEG), magnetoencephalography (MEG), functional magnetic resonance imaging (fMRI) and positron emission tomography (PET). Although both the fast activation signal (which is probably due to a change in scattering) and the hemodynamic response (which is a change in absorption) contribute to the measured signal, the hemodynamic response is much easier to detect. The spatial resolution of optical imaging is not comparable to fMRI due to the diffuse spatial sensitivity of the measurements, but optical imaging can yield a higher sample rate and the temporal resolution is only limited by the signal-to-noise ratio. Current optical topography systems can record a complete set of data for a two-dimensional image several times per second (Franceschini et al., 2000, Kohl-Bareis et al., 2002).

The instrumentation used in optical imaging is relatively compact and it can be used without expensive shielding rooms. It is applicable to bedside monitoring. Optical imaging may become an important tool for the study of infants, which are difficult subjects for other neuroimaging modalities. Another advantage is that light and low-frequency electromagnetic fields do not interfere, allowing the use of optical imaging simultaneously with other imaging modalities.

Modeling in activation studies is generally based on the assumption that the medium is optically homogeneous. Backprojection and interpolation have been used to form two-dimensional activation maps (Chance et al., 1998a; Kohl-Bareis et al., 2002). The accuracy of these methods in the context of activation studies can be evaluated by comparing the images with fMRI. Phantoms can be used to study how well the algorithms work in the presence of a perturbation in a homogeneous or layered medium. The CSF layer may significantly affect the spatial sensitivity of the measurement.

5.3.1b. Imaging Paradigms. The hemodynamic response is relatively slow, reaching its maximum in approximately 5 s. It has been found in functional MRI studies that the strongest response can be elicited by using a rapid sequence of stimuli; the repeated stimuli cause a larger total response than stimuli separated by longer intervals. The block paradigm consists of periods of rest and stimulation interleaved with each other. The whole image area is normally scanned several times within each epoch. This allows the evaluation of the time course of the response. If the image frame rate is fast enough, it may be possible to identify and partially remove the oscillations in the oxyhemoglobin signal (Sect. 2.3.) since there is a strong temporal correlation between the signals at different positions. Normally, the signal is averaged for each source-detector combination, wavelength and task condition to obtain the change in the signal caused by the task. If several wavelengths are used and the DPF is known, the modified Beer-Lambert law can be used to calculate the changes in the average concentrations of the chromophores. Unfortunately, the approach cannot be used for the quantitative measurement of localised changes in the cortex. A localised change in the hemodynamic parameters in the adult cortex is likely to be seriously underestimated due to the small fraction of the measured volume being in the cortex (Boas et al., 2001b). The sensitivity calculations used in optical tomography may be used to improve the localisation of the activation and in the estimation of the magnitude of the true change if it is assumed to be concentrated in cortical tissue. However, since transmission measurements cannot be performed with adequate spatial resolution and signal-to-noise ratio, prior information is very important in the reconstruction of activation images.

In an event-related paradigm, the hemodynamic responses to individual stimuli are measured. This allows the study of the response of the brain to changes in the stimuli.

Using the event-related paradigm, is possible to avoid many of the problems in the block paradigm, such as low-frequency drift and oscillations. The effect of oscillations are reduced by randomizing the inter-stimulus intervals. A drawback is the loss of sensitivity as the signal is relatively weak and the time the signal is at its peak value is a small part of the total measurement time, thus prolonging the measurement time. An event-related auditory oddball study in adults was reported in (Kennan et al., 2002).

A few studies have been made, in which the event-related paradigm is applied to the fast signal presumably caused by scattering changes. The signal that can be detected transcranially is very small, and the time resolution requirement is quite high (10 ms). In principle, the spatial resolution of the scattering change should be better than that of the hemodynamic change since the spatial sensitivity of the optical measurements to scattering changes is narrower and the neural activation is more confined than the hemodynamic change. (Steinbrink et al., 2000; Gratton et al., 2001)

Of the hemodynamic parameters, the deoxyhemoglobin signal is less prone to show the oscillations in the vascular system and therefore it may provide a more robust measure of brain activity (Kohl-Bareis 2002). However, the oxyhemoglobin response is larger. Both the blood volume signal, which can be measured with a single wavelength, and the deoxyhemoglobin signal have been proposed to give the highest spatial resolution and best correspondence with brain activity of the hemodynamic signals (Culver et al., 2002; Kohl-Bareis et al., 2002).

5.3.1c. Instrumentation for Optical Activation Studies. An ideal instrument for optical topography is either a fast pulsed continuous-wave system or a frequency-multiplexed system because of their high speed and signal-to-noise ratio. Frequency-domain systems can be optimized for this application as well, with only a slight loss in signal-to-noise ratio due to the higher modulation frequency. Time-resolved systems have limited photon count rates and thus they do not give optimal signal-to-noise ratio at close source-to-detector distances. However, they can be used to differentiate between changes in different layers of the tissue by studying the different temporal windows. Photons that travel a longer time in general spend more time in cortical tissue than those that travel a short time. (Steinbrink et al., 2001)

In studies of neonates (or on the forehead of adults), it is possible to use specialized probes with large-area SiPD detectors and laser diodes or LEDs as light sources.

5.3.1d. Practical Applications. Motor, somatosensory and cognitive activity in neonates have been studied by Chen et al. (2000), Hintz et al. (2001), and Chance et al. (1998a) (Fig. 13). In the study by Kusaka et al. (2001), cerebral blood flow was measured using optical topography with a contrast agent (indocyanine green, ICG). In an asphyxiated neonate, the area of reduced blood flow was successfully localised.

In adults, motor/somatosensory, auditory, visual, and language processing have been studied. (Franceschini et al., 2000; Kennan et al., 2002; Colier et al., 2001; Obrig et al., 2002; Sato et al., 1999; Hoshi et al., 2000)

The compatibility of optical imaging with other neuroimaging methods has received wide interest. Optical measurements have been successfully combined with fMRI (Kleinschmidt et al., 1996; Toronov et al., 2001), MEG (Mackert et al., 2002), EEG (Kennan et al., 2002; Israel et al., 2002) and TMS (Oliviero et al., 1999; Iwata et al., 2000; Nissilä et al., 2002b).

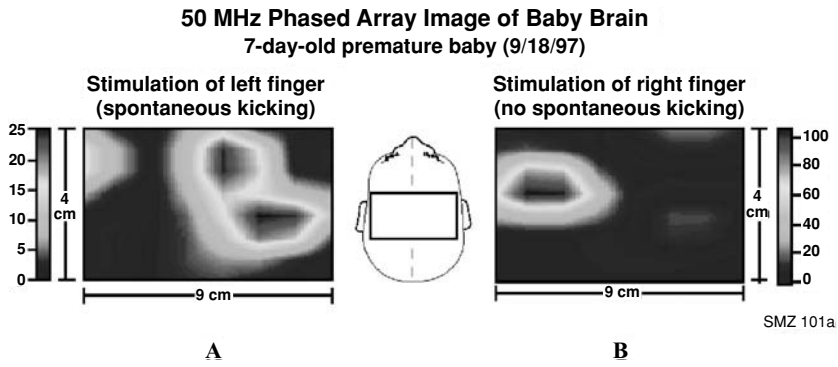

Figure 13. Somatosensory and motor activation in an infant. Reproduced with permission from (Chance et al., 1998a).

5.3.2. Optical Tomography of the Brain

The optical properties of the adult head and its large diameter limit the applicability of tomographic reconstruction methods. The smaller dimensions of the neonatal head together with more transparent optical properties and thinner CSF layer make it an easier problem.

The main clinical interest in optical tomography of the neonatal head is in the possibility of detecting and localising abnormalities in cerebral perfusion. If difference data between a reference phantom and the head at two or more wavelengths are available, it is possible to calculate three-dimensional images of the blood volume and oxygen saturation.

First results of the application of time-resolved optical tomography on a premature neonate are presented in (Hebden et al., 2002). The authors used a custom-made helmet with 31 sources and detectors to record data on a prematurely born neonate with cerebral haemorrhage primarily in the left ventricle. Three-dimensional images of absorption and scattering at two wavelengths were reconstructed based on differences in the mean time data type between a reference medium and the subject. The images reveal high absorption on the left side of the brain, which is consistent with ultrasonic localisation of the haemorrhage. The results are promising in that a model based on the diffusion equation was adequate to produce useful images. Improvements in the images can probably be obtained by more sophisticated modeling of scattering and the application of several data types.

Reconstructions of hemodynamic changes in the adult head based on intensity data have been reported in (Bluestone et al., 2001). The authors repeatably performed the Valsava maneuver on the subject, and reconstructed a time-series of images representing the changes in the concentrations of oxy- and deoxyhemoglobin in a volume under the forehead of the subject.

6. DISCUSSION

Optical imaging using diffuse near-infrared light is a promising functional imaging modality. Due to its sensitivity to changes in the blood volume and oxygen saturation, it can be used to study a variety of physiological processes in the brain, the breast and muscle

tissue. At present, much experimental research in the field is based on relatively simple models, but 3D finite-element numerical models are becoming more widespread.

In its most basic form, optical imaging is used to measure changes in the concentrations of oxy- and deoxyhemoglobin in an area of tissue by comparing the measured intensities of light between two different states of tissue ("active" vs. "rest"). A photon propagation model can be used to calculate the spatial sensitivity profiles for the different optode positions and this can be used to improve the accuracy of the functional maps. If both transmitted and reflected light can be measured from the tissue volume, and if a sufficient number of optodes are available, a tomographic reconstruction of the background optical properties is possible. This will further increase the accuracy of the localisation and quantification of the dynamic changes.

In addition to imaging dynamic processes, it is possible to reconstruct the static optical properties of tissue. The optical properties at several wavelengths can be used to reveal abnormalities such as haemorrhage or a tumor in tissue. Static recon-structions generally require either precise calibration or a reference measurement on a phantom. Both breast cancer and haemorrhage in a premature infant's brain have been successfully imaged using reference phantoms, thus indicating that difference imaging combined with nonlinear iterative inversion algorithms has considerable potential in clinical applications.

The standard modeling technique, numerical solution of the diffusion equation, is under pressure to be improved in several respects. The existence of nonscattering regions in the head calls for the solution of a hybrid model. Anisotropic scattering in the white matter or muscle tissue can be incorporated in form of a modified diffusion equation. The solution of the higher order approximations and RTE itself has also been considered. The disadvantage of these methods is the increase in the number of parameters to be solved in the inverse problem, necessitating the use of prior information. The computational requirements of the more sophisticated models are unfortunately quite high.

Although continuous-wave techniques are widely used, time- and frequency-domain techniques provide additional information which is likely to improve the quality of the images. The separation of scattering and absorption in breast and muscle studies is possible. In brain studies, only one data type has been used in most cases, producing inevitable crosstalk between the two optical properties. Further development of time-resolved instruments include improvements in the speed of data acquisition and the accuracy of measured data through better calibration procedures and improved system stability. Of great practical importance is the improvement of the instrument-patient interface.

In activation studies, the development of event-related protocols may increase the variety of cognitive phenomena that can be observed using optical imaging. It may also prove to be a more robust technique for observing brain activity, since high-pass filtering can be applied to reduce the effect of variable optode-tissue contact. Clinical applications of optical activation imaging are likely to be found for infants. Presently, the most practical instruments for activation studies are based on DC measurements.

In muscle imaging, valuable information of, e.g., local changes in the oxydative metabolism of skeletal muscle, can be obtained using only a few channels. Improvements in quantitative accuracy can be achieved by using multichannel instrumentation together with model-based reconstruction techniques.

In a layered structure, the measured change can be partly due to changes in the properties of other layers (e.g., dermis and adipose tissue) above the layer of interest (skeletal

muscle). A clinically useful imaging modality requires a higher spatial resolution than what is typically achieved today. Measurements at several source-detector distances and a tomographic reconstruction may allow the differentiation of the contributions from different layers.

Due to the non-invasive and non-ionizing nature of NIR light, diffuse optical imaging may provide new possibilities for mammography. Even continuous or regular monitoring is possible. The relatively small size and low price of the instruments together with the fact that no special operational environment is needed mean that optical mammography could be widely used in the clinical environment. Sensitivity for hemodynamic and oxygenation changes may enable an earlier detection of breast cancer and thereby an earlier start for treatment. This would increase the probability of recovery and reduce the need for the excision of the breast.

Despite the relatively low spatial resolution obtained with present optical mammography systems, preliminary results have already shown that the method can provide unique information for breast-cancer detection.

Research on optical mammography should focus on improving measurement and reconstruction techniques. Further testing is required to demonstrate its ability to detect different types of breast cancer, such as metastasis and lymphoma, and to distinguish cancerous tissues from benign lesions. The research of different endogenous chromophores is important as well. In addition to the changes in total hemoglobin and oxygen saturation, local changes in the concentrations of water and lipids may be of diagnostic interest. The concentration of water may increase (and lipids decrease) at the tumor site, indicating the replacement of the dominant adipose tissue by cancerous tissue containing more blood. Exogeneous contrast agents may further improve the contrast in optical mammography without a serious risk to the patient.

ACKNOWLEDGMENTS. The authors would like to acknowledge all the reserchers that allowed the reproduction of material and results from their research and publications.

This work was financially supported by the Academy of Finland, Jenny and Antti Wihuri Foundation, TES, the Finnish Cultural Foundation, and the graduate school Functional Studies in Medicine.

REFERENCES

Arridge, S. R., Cope, M., and Delpy, D. T., 1992, The theoretical basis for the determination of optical pathlengths in tissue: temporal and frequency analysis, *Phys. Med. Biol.* **37**:1531–1560.

Arridge, S. R., Schweiger, M., Hiraoka, M., and Delpy, D. T., 1993, A finite element approach for modeling photon transport in tissue, *Med. Phys.* **20**:299–309.

Arridge, S. R., 1995, Photon-measurement density functions. Part 1: Analytical forms, *Appl. Opt*. **34**:7395–7409.

Arridge, S. R., and Schweiger, M., 1995, Photon-measurement density functions. Part 2: Finiteelement-method calculations, *Appl. Opt*. **34**:8026–8037.

Arridge, S. R., and Lionheart, W. R. B., 1998, Non-uniqueness in diffusion-based optical tomography, *Opt. Lett*. **23**:882–884.

Arridge, S. R., and Schweiger, M., 1998, A general framework for iterative reconstruction algorithms in optical tomography, using a finite element method, in: *Computational Radiology and Imaging: Therapy and Diagnosis*, Borgers, C., and Natterer, F., ed., IMA Volumes in Mathematics and its Applications.

Arridge, S. R., 1999, Optical tomography in medical imaging, *Inv. Prob*. **15**:R41–R93.

Barbour, R. L., Graber, H. L., Pei, Y., Zhong, S., and Schmitz, C. H., 2001, Optical tomographic imaging of dynamic features of dence-scattering media, *J. Opt. Soc. Am. A* **18:**3018–3036.

Beauvoit, B., and Chance, B., 1998, Time-resolved spectroscopy of mitochondria, cells and tissues under normal and pathological conditions, *Mol. Cell. Biochem*. **184**:445–455.

Bevilacqua, F., Piguet, D., Marquet, P., Gross, J. D., Tromberg, B. J., and Depeursinge, C., 1999, *In vivo* local determination of tissue optical properties: applications to human brain, *Appl. Opt*. **38**:4939–4950.

Bluestone, A., Abdoulaev, G., Schmitz, C. H., Barbour, R. L., and Hielscher, A. H., 2001, Threedimensional optical tomography of hemodynamics in the human head, *Opt. Expr*. **9**:272–286.

Boas, D., 1996, *Diffuse Photon Probes of Structural and Dynamical Properties of Turbid Media: Theory and Biomedical Applications*, Ph.D. thesis, Univ. of Pennsylvania.

Boas, D., O'Leary, M. A., Chance, B., Yodh, A. G., 1997, Detection and characterization of optical inhomogeneities with diffuse photon density waves: a signal-to-noise analysis, *Appl. Opt*. **36**:75–92.

Boas, D. A., Gaudette, T., and Arridge, S. R., 2001a, Simultaneous imaging and optode calibration with diffuse optical tomography, *Opt. Expr*. **8**:263–270.

Boas, D. A., Gaudette, T., Strangman G., Cheng, X., Marota, J. J. A., and Mandeville, J. B., 2001b, The accuracy of near infrared spectroscopy and imaging during focal changes in cerebral hemodynamics, *Neurolmage* **13**:76–90.

Boas, G., 2002, Optical Breast Imaging: Mammography's next step? *Advance for Imaging and Radiation Therapy Professionals* **June 17**:30–31.

Bohren, C. F., and Huffman, D. R., 1983, *Absorption and Scattering of Light by Small Particles*, J. Wiley, New York.

Bolin, F. P., Preuss, L. E., Taylor, R. C., and Ference, J., 1989, Refractive index of some mammalian tissues using a fiber optic cladding method, *Appl. Opt*. **28**:2297–2296.

Boushel, R., and Piantadosi, C. A., 2000, Near-infrared spectroscopy for monitoring muscle oxygenation, *Acta Physiol. Scand*. **168**:615—622.

Case, K. M., and Zweifel, P. F., 1967, *Linear Transport Theory*, Addison-Wesley.

Cerussi, A. E., Jakubowski, D., Shah, N., Bevilacqua, F., Lanning, R., Berger, A. J., Hsiang D., Butler J., Holcombe R. F., and Tromberg B. J., 2002, Spectroscopy enhances the information content of optical mammography, *J. Biomed. Opt*. **7**:60–71.

Chance, B., Leigh, J. S., Miyake, H., Smith, D. S., Nioka, S., Greenfeld, R., Finander, M., Kaufmann, K., Levy, W., Young, M., Cohen, P., Yoshioka, H., and Boretsky, R., 1988, Comparison of time resolved and unresolved measurements of deoxyhemoglobin in brain. *Proc. Nat. Acad. Sci. USA* **85**:4971–4975.

Chance, B., Zhuang, Z., UnAh, C., Alter, C., and Lipton, L., 1993, Cognition-activated low-frequency modulation of light absorption in human brain, *Proc. Natl. Acad. Sci. USA* **90**:3770–3774.

Chance, B., Anday, E., Nioka, S., Zhou, S., Hong, L., Worden, K., Li, C., Murray, T., Ovetsky, Y., Pidikiti, D., and Thomas, R., 1998a, A novel method for fast imaging of brain function, noninvasively, with light. *Opt. Expr*. **2**:411–423.

Chance, B., Cope, M., Gratton, E., Ramanujam, N., and Tromberg, B., 1998b, Phase measurement of light absorption and scatter in human tissue, *Rev. Sci. Instrum*. **69**:3457–3481.

Chandrasekhar, S., 1960, *Radiative. Transfer*, Dover Publications, Inc., New York.

Chen, Y., Zhou, S., Xie, C., Nioka, S., Delivoria-Papadopoulos, M., Anday, E., and Chance, B., 2000, Preliminary evaluation of dual wavelength phased array imaging on neonatal brain function, *J. Biomed. Opt*. **5**:194–200.

Cheong, W., Prahl, S. A., and Welch, A. J., 1990, A review of the optical properties of biological tissues, *IEEE J. Quant. Elec*. **26**:2166–2185.

Colak, S. B., van der Mark, M. B., Hooft, G. W.'t, Hoogenraad, J. H., van der Linden, E. S., and Kuijpers, F. A., 1999, Clinical optical tomography and NIR spectroscopy for Breast Cancer Detection, *IEEE J. Quantum Electron*. **5**:1143–1158.

Cooper, C. E., Matcher, S. J., Wyatt, J. S., Cope, M., Brown, G. C., Nemoto, E. M., and Delpy, D. T., 1994, Near infrared spectroscopy of the brain: relevance to cytochrome oxidase bioenergetics, *Biochem. Soc. Trans*. **22**:974–980.

Cooper, C. E., and Springett, R., 1997, Measurement of cytochrome oxidase and mitochondrial energetics by near-infrared spectroscopy, *Phil. Trans. R. Soc. London Ser. B* **352**:669–677.

Cope, M., 1991, *The Development of a Near Infrared Spectoscopy System and its Application for Non Invasive Monitoring of Cerebral Blood and Tissue Oxygenation in the Newborn Infant*, Ph.D. thesis, University of London.

Culver, J. P., Siegel, A., Franceschini, M. A., Marota, J. J., Mandeville, J. B., and Boas, D. A., 2002, *OSA Biomedical Topical Meetings, OSA Technical Digest, (Optical Society of America, Washington DC)*, pp. 41–43.

Colier, W. N., Quaresima, V., Wenzel, R., van der Sluijs, M. C., Oeseburg, B., Ferrari, M., and Villringer, A., 2001, Simultaneous near-infrared spectroscopy monitoring of left and right occipital areas reveals contra-lateral hemodynamic changes upon hemi-field paradigm, *Vision Res*. **41**:97—102.

De Blasi, R. A., Fantini, S., Franceschini, M. A., Ferrari M., and Gratton, E., 1995, Cerebral and muscle oxygen saturation measurement by a novel frequency-domain near-infrared spectrometer, *Med. & Biol. Eng. & Comput*. **33**:228–230.

Den Outer, P. N., Nieuwenhuizen, T. M., and Lagendijk, A., 1993, Location of objects in multiple-scattering media, *J. Opt. Soc. Am. A* **10**:1209–1218.

Dehghani, H., Pogue, B. W., Poplack, S. P., and Paulsen, K. D., 2003, Multiwavelength threedimensional near-infrared tomography of the breast: initial simulation, phantom, and clinical results, *Appl. Opt*. **42**:135–145.

Delpy, D. T., Cope, M., van der Zee, P., Arridge, S., Wray, S., and Wyatt, J., 1988, Estimation of optical pathlength through tissue from direct time of flight measurement, *Phys. Med. Biol*. **33**:1433–1442.

DiCon FiberOptics, 1998, VX500 fiberoptic switch operation manual, Berkeley, USA.

Dorn, O., 1998, A transport-backtransport method for optical tomography, *Inv. Prob*. **14**:1107–1130.

Dorn, O., 2000, Scattering and absorption transport sensitivity functions for optical tomography, *Optics Express* **7**:492–506.

Dorn, O., submitted, Shape reconstruction in scattering media with voids using a transport model and level sets, *Canadian Applied Mathematics Quarterly*

Duncan, A., Meek, J. H., Clemence, M., Elwell, C. E., Tyszczuk, L., Cope, M., and Delpy, D., 1995, Optical pathlength measurements on adult head, calf and forearm and the head of the newborn infant using phase resolved optical spectroscopy, *Phys. Med. Biol*. **40**:295—304.

Durduran, T., Choe, R., Culver, J. P., Zubkov, L., Holboke, M. J., Chance, B., and Yodh, A. G., 2002, Bulk optical properties of healthy female breast tissue, *Phys. Med. Biol*. **47**:2847–2861.

Ebert B., Sukowski U., Grosenick D., Wabnitz H., Moesta T. K., Licha K., Becker A., Semmler W., Schlag P. M., and Rinneberg H., 2001, Near-infrared fluorescent dyes for enhanced contrast in optical mammography: phantom experiments, *J. Biomed. Opt*. **6**:134–140.

Eda, H., Oda, Ichiro, Yasunobu, I., Wada, Y., Oikawa, Y. Tsunazawa, Y., Takada, M., Tsuchiya, Y., Yamashita, Y., Oda, M., Sassaroli, A., Yamada, Y., and Tamura, M., 1999, Multichannel time-resolved optical tomographic imaging system, *Rev. Sci. Instrum*. **70**:3595–3601.

Elwell, C. E., 1995, *A practical users guide to near infrared spectroscopy*, UCL Reprographics, Lontoo.

Elwell, C. E., Owen-Reece, H., Wyatt, J. S., Cope, M., Reynolds, E. O., and Delpy, D. T., 1996, Influence of respiration and changes in expiratory pressure on cerebral haemoglobin concentration measured by near infrared spectroscopy, *J. Cereb. Blood Flow Metab*. **16**:353–357.

Fantini, S. and Franceschini, M. A., 2002, Frequency-domain techniques for tissue spectroscopy and imaging, in: *Handbook of Optical Biomedical Diagnostics*, V. V. Tuchin, ed., SPIE Press, Belllingham, Washington, pp. 405–453.

Fantini, S., Walker, S. A., Franceschini, M. A., Kaschke, M., Schlag, P. M., and Moesta, K. T., 1998, Assessment of the size, position, and optical properties of breast tumors *in vivo* by noninvasive optical methods, *Appl. Opt*. **37**:1982–1989.

Feng, S., Zeng, F., and Chance, B., 1995, Photon migration in the presence of a single defect: a perturbation analysis, *Appl. Opt*. **34**:3826–3837.

Ferrari, M., Binzoni, T., and Quaresima, V., 1997, Oxidative metabolism in muscle, *Phil. Trans. R. Soc. Lond. B* **352**:677–683.

Firbank, M., and Delpy, D. T., 1993, A design for a stable and reproducible phantom for use in near-infrared imaging and spectroscopy, *Phys. Med. Biol*. **38**:847–853.

Firbank, M., Oda, M., and Delpy, D. T., 1995, An improved design for a stable and reproducible phantom material for use in near-infrared spectroscopy and imaging, *Phys. Med. Biol*. **40**:955–961.

Firbank, M., Hiraoka, M., Essenpreis, M., and Delpy, D. T., 1997, Measurement of the optical properties of the skull in the wavelength range 650–950 nm, *Phys. Med. Biol*. **38**, 503–510.

Fishkin, J. B., and Gratton, E., 1993, Propagation of photon-density waves in strongly scattering media containing an absorbing semi-infinite plane bounded by a straight edge, *J. Opt. Soc. Am. A* **10**:127–140.

Fishkin, J. B., Coquoz, O., Anderson, E. R., Brenner, M., and Tromberg, B. J., 1997, Frequency-domain photon migration measurements of normal and malignant tissue optical properties in a human subject, *Appl. Opt*. **36**:10–20.

Franceschini, M. A., Moesta, K. T., Fantini, S., Gaida, G., Gratton, E., Jess, H., Mantulin, W. W., Seeber, M., Schlag, P. M., and Kaschke, M., 1997, Frequency-domain techniques enhance optical mammography: initial clinical results, *Proc. Natl. Acad. Sci. USA* **94**:6468–6473.

Franceschini, M. A., Gratton, E., and Fantini, S., 1999, Non-invasive optical method to measure tissue and arterial saturation: an application to absolute pulse oximetry of the brain, *Opt. Lett*. **24**:829–831.

Franceschini, M. A., Toronov, V., Filiaci, M. E., Gratton, E., and Fantini, S., 2000, On-Line Optical Imaging of the Human Brain with 160 ms Temporal Resolution, *Opt. Expr*. **6**:49–57.

Frostig, R. D., Lieke, E. E., Ts'o, D. Y., and Grinvald, A., 1990, Cortical functional architecture and local coupling between neuronal activity and the microcirculation revealed by *in vivo* high-resolution optical imaging of intrinsic signals, *Proc. Natl. Acad. Sci. USA* **87**:6082–6086.

Gibbs, E. L., Lennox, W. G., Nims, L. F., and Gibbs, F. A., 1942, Arterial and cerebral venous blood, arterial-venous differences in man, *J. Biol. Chem*. **144**:325–332.

Graaff, R., Aarnoudse, J. G., de Mul, F. F. M., and Jentink, H. W., 1989, Light propagation parameters for anisotropically scattering media based on a rigorous solution of the transport equation, *Appl. Opt*. **28**:2273–2279.

Gratton, G., and Fabiani, M., 2001, The event-related optical signal: a new tool for studying brain function, *Int. J. of Psychophys*. **42**:109–121.

Groenhuis, R. A. J., Ferwerda, H. A., and Ten Bosch, J. J., 1983a, Scattering and absorption of turbid materials determined from reflection measurements 1: theory, *Appl. Opt*. **22**:2456–2462.

Groenhuis, R. A. J., Ten Bosch, J. J., and Ferwerda, H. A., 1983b, Scattering and absorption of turbid materials determined from reflection measurements 2: measuring method and calibration, *Appl. Opt*. **22**:2463–2467.

Grosenick, D., Wabnitz, H., Rinneberg, H., Moesta, K. T., and Schlag, P., 1999, Development of a time-domain optical mammograph and first in vivo applications, *Appl. Opt*. **38**:2927–2943.

Grosenick, D., Wabnitz, H., Macdonald, R., Rinneberg, H., Mucke, J., Stroszczynski, C., Moesta, K. T., and Schlag, P., 2002, Determination of *in vivo* optical properties of breast tissue and tumors using a laser pulse mammography, in: *OSA Biomedical Topical Meetings, OSA Technical Digest*, Optical Society of America, Miami Beach, Florida, pp. 459–461.

Haskell, R. C., Svaasand, L. O., Tsay, T-T., Feng, T-C., McAdams, M. S., and Tromberg, B. J., 1994, Boundary conditions for the diffusion equation in radiative transfer, *J. Opt. Soc. Am. A* **11**:2727–2741.

Hargrave, P., Nicholson, P. W., Delpy, D. T., and Firbank, M., 1996, Optical properties of multicellular tumor spheroids, *Phys. Med. Biol*. **41**:1067–1072.

Hawrysz, D. J., and Sevick-Muraca, E. M., 2000, Developments toward diagnostic breast cancer imaging using near-infrared optical measurements and fluorescent contrast agents, *Neoplasia* **2**:388–417.

Hebden, J. C., Gibson, A., Yusof, R. M., Everdell, N., Hillman, E. M. C., Delpy, D. T., Arridge, S. R., Austin, T., Meek, J. H., and Wyatt, J. S., 2002a, Three-dimensional optical tomography of the premature infant brain, *Phys. Med. Biol*. **47**:4155–4166.

Hebden, J. C., Gonzalez, F. M., Gibson, A., Hillman, E. M. C., Yusof, R., Everdell, N., Delpy, D. T., Zaccanti, G., and Martelli, F., 2002b, Assessment of an in situ temporal calibration method for time-resolved optical tomography, *J. Biomed. Opt*. (In press).

Heino, J. and Somersalo, E., 2002, Estimation of optical absorption in anisotropic background, *Inv Prob*. **18**:559–573.

Hielscher, A. H., Alcouffe, R. E., Barbour, R. L., 1997, Transport and diffusion calculations on MRI generated data, in: *Optical Tomography and Spectroscopy of Tissue: Theory, Instrumentation, Model, and Human Studies*, B. Chance, and R.R. Alfano, ed., Proc. SPIE **2979**, pp. 500–508.

Hielscher, A. H., Klose, A. D., and Hanson, K. M., 1999, Gradient-based iterative image reconstruction scheme for time-resolved optical tomography, *IEEE Transactions on Medical Imaging* **18**:262–271.

Hill, D. K., and Keynes, R. D., 1949, Opacity changes in stimulated nerve, *J. Physiol*. **108**:278–281.

Hillman, E. M. C., Hebden, J. C., Schmidt, F. E. W., Arridge, S. R., Schweiger, M., Dehghani, H., and Delpy, D. T., 2000, Calibration techniques and datatype extraction for time-resolved optical tomography, *Rev. Sci. Instrum*. **71**:3415–3427.

Hillman, E. M. C., Hebden, J. C., Schweiger, M., Dehghani, H., Schmidt, F. E. W., Delpy, D. T., and Arridge, S. R., 2001, Time resolved optical tomography of the human forearm, *Phys. Med. Biol*. **46**: 1117–1130.

Hillman, E. M. C., 2002, *Experimental and Theoretical Investigations of Near Infrared Tomographic Imaging Methods and Clinical Applications*, Ph.D. thesis, University of London.

Hintz, S. R., Benaron, D. A., Siegel, A. M., Zourabian, A., Stevenson, D. K., and Boas, D. A., 2001, Bedside functional imaging of the premature infant brain during passive motor activation, *J. Perinat. Med*. **29**:335–343.

Holboke, M. J., Tromberg, B. J., Li, X., Shah, N., Fishkin, J., Kidney, D., Butler, J., Chance, B., and Yodh, A. G., 2000, Three-dimensional diffuse optical mammography with ultrasound localization in a human subject, *J. Biomed. Opt*. **5**:237–247.

Hoshi, Y. and Tamura, M., 1993, Detection of dynamic changes in cerebral oxygenation coupled to neuronal function during mental work in man, *Newrosci. Lett*. **150**:5–8.

Ishimaru, A., 1978, *Wave Propagation and Scattering in Random Media, Vol. 1, Single Scattering and Transport Theory*, Academic Press.

Israel, H., Obrig, H., Kohl, M., Uludag, K., Müller, B., Wenzel, R., Buckow, C., Arnold, G., Villringer, A., 2001, Is neurovascular coupling altered in interictal migraineurs? A combined visually evoked potential (VEP) and near infrared spectroscopy (NIRS) approach, *Neurolmage* **13**:S800.

Iwata N. K., Ugawa, Y., Watanabe, E., Yamashita, Y., Koizumi, H., and Kanazawa, I., 2000, Interhemispheric connection between bilateral hand motor areas studied with near-infrared spectroscipic (NIRS) mapping and transcramal magnetic stimulation (TMS), *Neurolmage* **11**:S520.

Jiang, H., 1999, Optical image reconstruction based on the third-order diffusion equations, *Optics Express* **4**:241–246.

Jiang, H., Xu, Y., Iftimia, N., Eggert, J., Klove, K., Baron, L., and Fajardo, L., 2001, Three-dimensional optical tomographic imaging of breast in a human subject, *IEEE Trans. Med. Imaging* **20**:1334–1340.

JöUbsis, F. F., 1977, Noninvasive, infrared monitoring of cerebral and myocardial oxygen sufficiency and circulatory parameters, *Science* **198**:1264–1267.

Kaipio, J. P., Kolehmainen, V., Somersalo, E., and Vauhkonen, M., 2000, Statistical inversion and Monte Carlo sampling methods in electrical impedance tomography, *Inv. Prob*. **16**:1487–1522.

Kennan, R. P., Horovitz, S. G., Maki, A., Yamashita, Y., Koizumi, H., Gore, J. C., 2002, Simultaneous Recording of Event-Related Auditory Oddball Response Using Transcranial Near Infrared Optical Topography and Surface EEG. *Neurolmage* **16**:587–592.

Kim. A. D. and Ishimaru, A., 1998 Optical diffusion of continuous-wave, pulsed, and density waves in scattering media and comparisons with radiative transfer, *Appl. Opt*. **37**:5313–5319.

Kleinschmidt, A., Obrig, H., Requardt, M., Merboldt, K. D., Dirnagl, U., Villringer, A., Frahm, J., 1996, Simultaneous recording of cerebral oxygenation changes during human brain activation by magnetic resoncance imaging and near - infrared spectroscopy, *J. Cereb. Blood Flow Metab*. **16**:817–827.

Klose, A. D., Netz, U., Beuthan, J., and Hielscher, A. H., 2002, Optical tomography using the time-independent equation of radiative transfer - Part 1: forward model, *Journal of Quantitative Spectroscopy & Radiative Transfer* **72**:691–713.

Klose, A. D. and Hielscher, A. H., 2002, Optical tomography using the time-independent equation of radiative transfer - Part 2: inverse model, *Journal of Quantitative Spectroscopy & Radiative Transfer* **72**:715–732.

Kohl-Bareis, M., Buckow, C., Zank, H., Obrig, H., Steinbrink, J., and Villringer, A., 2002, Multi channel NIR topography for the assessment of cortical activation, *OSA Biomedical Topical Meetings, OSA Technical Digest, (Optical Society of America, Washington DC)*, pp. 300–303.

Kolehmainen, V., 2001, *Novel Approaches to Image Reconstruction in Diffusion Tomography*, PhD thesis, University of Kuopio.

Kusaka, T., Isobe, K., Nagano, K., Okubo, K., Yasuda, S., Kondo, M., Itoh, S., and Onishi, S., 2001, *Neurolmage* **13**:944–952.

Laufer, J., Simpson, C. R., Kohl, M., Essenpreis, M., and Cope, M., 1998, Effect of temperature on the optical properties of ex-vivo human dermis, *Phys. Med. Biol*. **43**:2479–2490.

Lovell, A. T., Hebden, J. C., Goldstone, J. C., and Cope, M., 1999a, Determination of the transport scatter coefficient of red blood cells, *Proc. SPIE* **3597**:175–182.

Lovell, A. T., Owen-Reece, H., Elwell, C. E., Smith, M., and Goldstone J. C., 1999b, Continuous measurement of cerebral oxygenation by near infrared spectroscopy during induction of anesthesia, *Anaesthesiology and Analgesia* **88**, 554–558.

Mackert, B. M., Wübbeler, G., Leistner, S., Burghoff, M., Uludag, K., Obrig, H., Kohl, M., and Villringer, A., 2002, *Proceedings of the 13th International Conference on Biomagnetism*, August 10–14, Jena, Germany, p. 850.

MacVicar, B. A. and Hochman, D., 1991, Imaging of synaptically evoked intrinsic optical signals in hippocampal slices, *J. Neurosci*. **11**:1458–1469.

Maris, M., Gratton, E., Maier, J., Mantulin W., and Chance, B., 1994, Functional near-infrared imaging of deoxygeneted haemoglobin during exercise of the finger extensor muscles using the frequency-domain technique, *Bioimaging* **2**:174–183.

Markel, V. A. and Schotland, J. C., 2001, Inverse problem in optical diffusion tomography. I. Fourier-Laplace inversion formulas, *J. Opt. Soc. Am. A* **18**:1336–1347.

Marquez, G., Wang, L. V., Lin, S. P., Schwartz, J. A., and Thomsen, S. L., 1998, Anisotropy in the absorption and scattering spectra of chicken breast, *Appl. Opt*. **37**:798–805.

Matcher, S. J., Cope, M., and Delpy, D. T., 1994, Use of the water absorption spectrum to quantify tissue chromophore concentration changes in near infrared spectroscopy, *Phys. Med. Biol*. **39**:177–196.

Matcher, S. J., 1999, Nonuniqueness in optical tomography: relevance of the P1 approximation, *Opt. Lett*. **24**:1729–1731.

Matson, C. L. and Liu, H., 1999, Backpropagation in turbid media, *J. Opt. Soc. Am. A* **16**:1254–1265.

McBride, T. O., Pogue, B. W., Jiang, S., Österberg, U. L., and Paulsen, K. D., 2001, A parallel-detection frequency-domain near-infrared tomography system for hemoglobin imaging of the breast in vivo, *Rev. Sci. Instrum*. **72**:1817–1824.

Moesta, K. T., 2002, Clinical evaluation of optical breast imaging: what requirements of the clinician can be fulfilled, in: *OSA Biomedical Topical Meetings, OSA Technical Digest*, Optical Society of America, Miami Beach, Florida, pp. 432–434.

Mourant, J. R., Freyer, J. P., Hielscher, A. H., Eick, A. A., Shen, D., and Jonhson, T. M., 1998, Mechanisms of light scattering from biological cells relevant to noninvasive optical-tissue diagnostics, *Appl. Opt*. **37**:3586–3593.

Nioka, S., Miura, H., Long, H., Perry, A., Moser, D., and Chance, B., 1999, Functional muscle imaging in elite and untrained subjects, *Proc. SPIE* **3597**:282–290.

Niwayama, M., Yamamoto, K., Kohota, D., Hirai, K., Kudo, N., Hamaoka, T., Kime, R., and Katsumura, T., 2002, A 200-channel imaging system of muscle oxygenation using CW near-infrared spectroscopy, *IEICE Trans. Inf. & Syst*. **85-D**:115–123.

Nissilä, I., Kotilahti, K., Fallström, K., and Katila, T., 2002a, Instrumentation for the accurate measurement of phase and amplitude in optical tomography, *Rev. Sci. Instrum*. **73**:3306–3312.

Nissilä, I., Kotilahti, K., Komssi, S., Kähkönen, S., Noponen, T., Ilmoniemi, R.J., and Katila, T., 2002b, Optical measurement of hemodynamic changes in the contralateral motor cortex induced by transcranial magnetic stimulation, *Proceedings of the 13th International Conference on Biomagnetism*, August 10–14, Jena, Germany, pp. 851–854.

Ntziachristos, V., Ma, X., and Chance, B., 1998, Time-correlated single photon counting imager for simultaneous magnetic resonance and near-infrared mammography, *Rev. Sci. Instrum*. **69**:4221–4233.

Ntziachristos, V., Chance, B., and Yodh, A. G., 1999, Differential diffuse optical tomography, *Optics Express* **5**:230–242.

Ntziachristos, V., Yodh, A. G., Schnall, M., and Chance, B., 2000, Concurrent MRI and diffuse optical tomography of breast after indocyanine green enhancement, *Proc. Nat. Acad. Sci. USA* **97**:2767–2772.

Ntziachristos, V., Yodh, A. G., Schnall, M. D., and Chance, B., 2002, MRI-guided diffuse optical spectroscopy of malignant and benign breast lesions, *Neoplasia* **4**:347–354.

Obrig, H. and Villringer, A., 1997, Near-infrared spectroscopy in functional activation studies: can NIRS demonstrate cortical activation? *Adv. Exp. Med. Biol*. **413**:113–127.

Obrig, H., Neufang, M., Wenzel, R., Kohl, M., Steinbrink, J., Einhäupl, K. M., and Villringer, A., 2000, Spontaneous low frequency oscillations of cerebral hemodynamics and metabolism in human adults, *Neurolmage* **12**:623–639.

Obrig, H., Israel, H., Kohl-Bareis, M., Uludag, K., Wenzel, R., Muller, B., Arnold, G., and Villringer A., 2002, Habituation of the visually evoked potential and its vascular response: Implications for neurovascular coupling in the healthy adult, *NeuroImage* **17**:1–18.

Okada, E., Firbank, M., Schweiger, M., Arridge, S. R., Cope, M., and Delpy, D. T., 1997, Theoretical and experimental investigation of near-infrared light propagation in a model of the adult head, *Appl. Opt*. **36**:21–31.

Okada, E., Schweiger, M., Arridge, S. R., Firbank, M., and Delpy, D. T., 1996, Experimental validation of Monte Carlo and finite-element methods for the estimation of the optical path length in inhomogencous tissue, *Appl. Opt*. **35**:3362–3371.

O'Leary, M. A., Boas, D. A., Chance, B., and Yodh, A. G., 1995, Experimental images of heterogeneous turbid media by frequency-domain diffusing-photon tomography, *Opt. Lett*. **20**:426–428.

O'Leary, M. A., Boas, D. A., Chance, B., and Yodh, A. G., 1992, Refraction of diffuse photon density waves, *Phys. Rev. Lett*. **69**:2658–2661.

Oliviero, A., Di Lazzaro, V., Piazza, O., Profice, P., Pennisi, M. A., Della Corte, F., Tonali, P., 1999, Cerebral blood flow and metabolic changes produced by repetitive magnetic brain stimulation, *J. Neurol*. **246**:1164–1168.

Ostermeyer, M. R. and Jacques, S. L., 1997, Perturbation theory for diffuse light transport in complex biological tissues, *J. Opt. Soc. Am. A* **14**:255–261.

Pickering, J. W., Prahl, S. A., van Wieringen, N., Beek, J. F., Sterenborg, H. J. C. M. and van Gemert, M. J. C., 1993, Double-integrating-sphere system for measuring the optical properties of tissue, *Appl. Opt*. **32**: 399.

Poe, G. R., Nitz, D. A., Rector, D. M., Kristensen, M. P., and Harper, R. M., 1996, Concurrent reflectance imaging and microdialysis in the freely behaving cat, *J. Neurosci. Methods* **65**:143–149.

Pham, T. H., Coquoz, O., Fishkin, J. B., Anderson, E., and Tromberg, B. J., 2000, Broad bandwidth frequency domain instrument for quantitative tissue optical spectroscopy, *Rev. Sci. Instrum*. **71**:2500–2513.

Pogue, B. W., Patterson, M. S., Jiang, H., and Paulsen, K. D., 1995, Initial assessment of a simple system for frequency domain diffuse optical tomography, *Phys. Med. Biol*. **40**:1709–1729.

Pogue, B. W., Testorf, M., McBride, T., Osterberg, U., and Paulsen, K. D., 1997, Instrumentation and design of a frequency-domain diffuse optical tomography imager for breast cancer detection, *Opt. Expr*. **1**:391–403.

Pogue, B. W., Poplack, S., Mcbride, T., Wells, W., Osterman, K., Osterberg, U. L., and Paulsen, K. D., 2001, Quantitative hemoglobin tomography with diffuse near-infrared light: pilot results in the breast, *Radiology* **218**:261–266.

Prahl, S. A., Keijzer, M., Jacues, S. L., and Welch, A. J., 1989, A Monte Carlo Model of Light Propagation in Tissue, *SPIE Institute series* **5**:102–111.

Prahl, S. A., van Gemert, M. J. C., and Welch, A. J., 1993, Determining the optical properties of turbid media by using the adding-doubling method, *Appl. Opt*. **32**:559–568.

Quaresima, V., Matcher, S. J., and Ferrari, M., 1998, Identification and Quantification of Intrinsic Optical Contrast for Near-Infrared Mammography, *Photochem. Photobiol*. **67**:4–14.

Quaresima, V., Colier, W. N. J. M., van der Sluijs, M., and Ferrari, M., 2001, Nonuniform quadriceps O_2 consumption revealed by near infrared multipoint measurements, *Biochem. & Biophys. Res. Comm*. **285**:1034–1039.

Rector, D. M., Rogers, R. F., Schwaber, J. S., Harper, R. M., and George, J. S., 2001, Scattered-light imaging *in vivo* tracks fast and slow processes of neurophysiological activation, *NeuroImage* **14**:977–994.

Rinzema, K., Murrer, L. P. H., and Star, W. M., 1998, Direct experimental verification of light transport theory in an optical phantom, *J. Opt. Soc. Am. A* **15**:2078–2088.

Sako, T., Hamaoka, T., Higuchi, H., Kurosawa, Y., and Katsumura, T., 2001, Validity of NIR spectroscopy for quantitatively measuring muscle oxidative metabolic rate in exercise, *J. Appl. Physiol*. **90**:338–344.

Sato, H., Takeuchi, T., and Sakai, K. L., 1999, Temporal cortex activation during speech recognition: an optical topography study, *Cognition* **73**:B55–66.

Schmidt, F. E. W., Fry, M. E., Hillman, E. M. C., Hebden, J. C., and Delpy, D. T., 2000, A 32-channel time-resolved instrument for medical optical tomography, *Rev. Sci. Instrum*. **71**:256–265.

Schmitz, C. H., Graber, H. L., Luo, H., Arif, I., Hira, J., Pei, Y., Bluestone, A., Zhong, S., Andronica, R., Soller, I., Ramirez, N., Barbour, S.-L.S., and Barbour, R. L., 2000, Instrumentation and calibration protocol for imaging dynamic features in dense-scattering media by optical tomography, *Appl. Opt*. **39**: 6466–6486.

Schmitz, C. H., Löcker, M., Lasker, J. M., Hielscher, A. H., and Barbour, R. L., 2002, Instrumentation for fast functional optical tomography, *Rev. Sci. Instrum*. **73**:429–439.

Schotland, J. C., Haselgrove, J. C., and Leigh, J. S., 1993, Photon hitting density, *Appl. Opt*. **32**:448–453.

Schweiger, M., Arridge, S. R., Hiraoka, M., and Delpy, D. T., 1995, The finite element method for the propagation of light in scattering media: Boundary and source conditions, *Med. Phys*. **22**:1779–1792.

Schweiger, M. and Arridge, S. R., 1997, Optimal data types in optical tomography, *Information Processing in Medical Imaging (IPMI'97 Proceedings) (Lecture notes in Computer Science 1230)*, pp. 71–84.

Schweiger, M. and Arridge, S. R., 1999a, Application of temporal filters to time resolved data in optical tomography, *Phys. Med. Biol*. **44**:1699–1717.

Schweiger, M. and Arridge, S. R., 1999b, Optical tomographic reconstruction in a complex head model using a priori region boundary information, *Phys. Med. Biol*. **44**:2703–2722.

Simpson, C. R., Kohl, M., Essenpreis, M., and Cope, M., 1998, Near infrared optical properties of exvivo human skin and sub-cutaneous tissues measured using the Monte Carlo inversion technique, *Phys. Med. Biol*. **43**:2465–2478.

Steinbrink, J., Kohl, M., Obrig, H., Curio, G., Syre, F., Thomas, F., Wabnitz, H., Rinneberg, H., Villringer, A., 2000, Somatosensory evoked fast optical intensity changes detected non-invasively in the adult human head, *Neurosci. Lett*. **291**:105–108.

Steinbrink, J., Wabnitz, H., Obrig, H., Villringer, A., Rinneberg, H., 2001, Determining changes in NIR absorption using a layered model of the human head, *Phys. Med. Biol*. **46**:879–96.

Stepnoski, R. A., LaPorta, A., Raccuia-Behling, F., Blonder, G. E., Slusher, R. E., and Kleinfeld, D., 1991, Noninvasive detection of changes in membrane potential in cultured neurons by light scattering, *Proc. Natl. Acad. Sci. USA* **88**:9382–9386.

Toronov, V., Webb, A., Choi, J. H., Wolf, M., Safonova, L., Wolf, U., and Gratton, E., 2001, *Opt. Expr*. **9**:417–427.

Tromberg, B. J., Coquoz, O., Fishkin, J. B., Pham, T., Anderson, E., Butler, J., Cahn, M., Gross, J. D., Venugopalan, V., and Pham, D., 1997, Non-invasive measurements of breast tissue optical properties using frequency domain photon migration, *Phil. Trans. R. Soc. London Ser. B* **352**:661–668.

Tromberg, B. J., Shah, N., Lanning, R., Cerussi, A., Espinoza, J., Pham, T., Svaasand, L., Butler, J., 2000, Non-invasive *in vivo* characterization of breast tumors using photon migration spectroscopy, *Neoplasia* **2**:1–15.

Troy, T. L., Page, D. L., and Sevick-Muraca, E. M., 1996, Optical properties of normal and diseased breast tissues: prognosis for optical mammography, *J. Biomed. Opt*. **1**:342–355.

Tuchin, V. V., 2000, *Light scattering methods and instruments for medical diagnosis*, Tutorial texts series **TT38**, SPIE, Bellingham, Washington.

University College London, 2002, *Biomedical Optics Research Group. Muscle Imaging* (London, December, 2002); http://www.medphys.ucl.ac.uk/research/borg/research/monstir/muscle.htm.

Vaithianathan, T., Tullis, I., Meek, J., Austin, T., Delpy, D., 2002, A portable near infrared spectroscopy system for mapping functional activation on infants, *8th International Conference on Functional Mapping of the Human Brain*.

Van Beekvelt, M. C. P., Borghuis, M. S., van Engelen, B. G. M., Wevers R. A., and Colier W. N. J. M., 2001, Adipose tissue thickness affects *in vivo* quantitative near-IR spectroscopy in human skeletal muscle, *Clin. Sci*. **101**:21–28.

Van der Zee, P., 1992, *Measurement and modeling of the optical properties of biological tissues in the near infrared*, Ph.D., University of London.

Van der Zee, P., Essenpreis, M., and Delpy, D. T., 1993, Optical properties of brain tissue, *Proc. SPIE* **1888**:454–465.

Villringer, A. and Dirnagl, U., 1995, Coupling of brain activity and cerebral blood flow: basis of functional neuroimaging, *Cerebrovasc. Brain Metab. Rev*. **7**:240–276.

Villringer, A., 1997, Functional neuroimaging: optical approach, *Adv. Exp. Med. Biol*. **413**:1–18.

Villringer, A. and Chance, B., 1997, Non-invasive optical spectroscopy and imaging of human brain function, *Trends Neurosci*. **20**:435–442.

Walker, S. C., Fentini, S., and Gratton, E., 1997, Image reconstruction by backprojection from frequency-domain optical measurements in highly scattering media, *Appl. Opt*. **36**:170–179.

Wang, L. and Jacques, S. L., 1993, Hybrid model of Monte Carlo simulation and diffusion theory for light reflectance by turbid media, *J. Opt. Soc. Am. A* **10**:1746–1752.

Wilson, B. C. and Adam, G., 1983, A Monte Carlo model for the absorption and flux distributions of light in tissue, *Med. Phys*. **10**:824–830.

Wilson, B. C., Patterson, M. S., and Flock, S. T., 1987, Indirect versus direct technologies for the measurment of the optical properties of tissues, *Photochem. Photobiol*. **36**:601–608.

Woodard, H. Q., and White, D. R., 1986, The composition of body tissues, *Br. J. Radiol*. **59**:1209–1219.

Zhang, Q., Ma, H., Nioka, S., and Chance, B., 2000, Study of near infrared technology for intracranial hematoma detection, *J. Biomed. Opt*. **5**:206–213.

Chapter 4

Optical Biotelemetry

Koichi Shimizu

ABSTRACT

The usefulness of biotelemetry (remote measurement of biological information) has been recognized in clinical medicine and animal sciences. In biotelemetry, the radio wave has been commonly used as a transmission medium. To answer many new demands for biotelemetry and to overcome various problems of radio telemetry, a technological method called optical biotelemetry has been developed. Using light as a transmission medium, the bandwidth for signal transmission is greatly increased and many EMI problems can be solved. Technical considerations required to realize the optical biotelemetry were presented. On the devices for optical biotelemetry, the wavelength of light, light sources, light detecting elements and the measures for optical noises were discussed. On data transmission, analogue and digital communication, modulation methods, intelligent transmission and multiplexing methods were discussed. To develop an optical biotelemetry technique, we need to know the characteristics of light propagation. The optical characteristics of body surface tissue and the distribution of indirect light in a room were discussed for transcutaneous telemetry and ambulatory telemetry using indirect light, respectively. Two techniques were proposed for multi-channel optical biotelemetry. They were the applications of a pulse-burst method and the spread spectrum method. As concrete examples of optical biotelemetry, some applications of this method to practical use are presented. They are the transcutaneous ECG telemetry, non-contact measurement of body surface displacement, ambulatory telemetry,

Koichi Shimizu Graduate School of Engineering, Hokkaido University, N13, W8, Sapporo, 060-8628, Japan.

Advances in Electromagnetic Fields in Living Systems, Volume 4, edited by James C. Lin,
Springer Science+Business Media, New York, 2005.

multi-channel biotelemetry and data transmission between medical equipments. With its promising potential, it is expected that the optical biotelemetry opens new possibilities for further development of biotelemetry.

1. INTRODUCTION

Biotelemetry is defined as the measurement of biological signals from a remote place using a communication measure. In the history of the development of biomedical engineering, there were significant successes attained by applying engineering principles to clinical medicine. Biotelemetry is one of the typical examples of such a success, or the application of a telemetry technique to a biomedical measurement. From the first stage of the development of biomedical engineering, the biotelemetry technique has been applied in many areas of medicine. For instance, there have been different kinds of ECG transmission. Clinical applications include an ambulatory ECG measurement in an examination room, a centralized ECG monitoring in ICU, remote area transmission in telemedicine, etc. In research fields there have been well-known examples such as the radio capsule to measure various parameters in a digestive tract and the ECG/EMG measurement in sports medicine and in rehabilitation medicine.[1,2]

In biotelemetry we transmit the measured signal to a remote place by means of a medium for communication. A radio wave is a typical example of the medium. Since it has been used widely, people naturally think of it as radio telemetry when they say 'biotelemetry'. The use of different media for data-transmission has been attempted, i.e. light and ultrasound. The feasibility and the usefulness of optical biotelemetry have been suggested early.[3,4] However, few studies have followed them. It is one of the reasons that optical technology has not matured to support the new development of optical biotelemetry. For example, a high-power transmitter and a sensitive detector could not be made portable. Recently optical technology has been advancing greatly, and now we have had a reliable laser diode and photo diode in our hand. The background of new progress of optical biotelemetry has been maturing.

Figure 1 shows the fundamental principle of optical biotelemetry. Based on the telemetry principle, we can separate the data-acquisition part from the data processing/display part by means of communication. By this separation we can expect the following merits of biotelemetry.

1) We can make the data acquisition part very small and light. This makes the measurement possible with minimal perturbation on the object or the subject. The ambulatory measurement is a typical example.

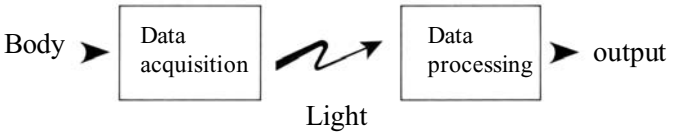

Figure 1. Basic principle of optical biotelemetry.

2) We can measure the signal in an environment which is not easily accessible, such as inside the body, deep in water and space.
3) We can monitor many subjects for a long period of time in the centralized system, such as an ICU.

Moreover, by use of light we can expect the following advantages over the conventional radio telemetry.

#1 We can achieve the wide-band signal transmission relatively easily. This corresponds to the possibility of information transmission with a good frequency characteristic or a high-speed temporal response. In another view, it indicates the possibility of high-speed large-capacity transmission of information.
#2 We can control the electromagnetic interference much easier than we can with radio telemetry. The signal light of the optical telemetry does not give interference to other instruments and does not receive interference from them. The shielding and securing safety can be done relatively easily.
#3 The legal restriction to use light for communication is not as strict as the radio wave.

There are of course some disadvantages with the optical biotelemetry. They are for example, the vulnerability to optical noises and the inability to reach the position out of the line of sight. However, they are not serious and can be overcome by technical measures which are discussed in the following sections.

The significances of the above advantages in biotelemetry are as follows. #1 means the improvement of the telemetry function itself over radio telemetry. It increases the practical value of the telemetry technique. With the wide-band transmission channel, we can use various intelligent techniques in the data-transmission. The significance of this advantage over radio telemetry is increasing with the progress of intelligent communication techniques. #2 is important for the serious problems of electromagnetic interference in a hospital. In a clinical environment, there are many sources of electromagnetic noise, such as an electric scalpel (radio knife, acusector), microwave hyperthermia and many devices with built-in microcomputers. Thus the telemetry system should not receive interference from them. Moreover, in a clinical environment, delicate equipments have increased such as life-support systems and centralized patient-monitoring systems. The trouble and malfunction of these system result in serious problems. Therefore, there are strict requirements to prevent a telemetry system from interfering with these systems. #3 becomes an important merit in the practical use of the telemetry system in a clinical environment and in field works.

As mentioned above, optical biotelemetry is a new technique with abundant potential. However the basic technology has not been sufficiently established compared with the radio telemetry. This chapter deals with the outline of the basic technologies necessary to use optical biotelemetry in practice. The common topics to radio telemetry such as the topics of electrodes and batteries are excluded. As concrete examples, some of the optical biotelemetry systems we have developed are introduced.

2. BASIC OPTICAL TECHNOLOGY FOR OPTICAL TELEMETRY

Optical biotelemetry is an integrated technology which consists of basic technologies such as optics, communication, biosignal measurement, and information processing. In the following sections, these basic technologies necessary for optical biotelemetry are outlined.

2.1. Selection of Wavelength

To design an optical biotelemetry system, the wavelength of optical communication has to be selected. Any wavelength of light, or ultraviolet-visible-infrared range, can be used for optical telemetry in principle. However, with ultraviolet light, the adverse effect on our health becomes a problem in a prolonged use. As for visible light, there may be a psychological effect on the subject. Further, in this wavelength, there are many sources of optical noise such as indoor lighting. With infrared light particularly of 700–1200 nm wavelength, such problems are few. Moreover, in this wavelength, the optical absorption of body tissue is relatively low, and we can expect high optical transmission through our body. Figure 2 shows the absorption spectra of the major constituents of a human body. In the ranges less than 700 nm and more than 1200 nm, the absorption of hemoglobin and water are predominant, respectively. Furthermore, this wavelength range has been used in optical fiber communication, and there are many kinds of sources and detectors available.

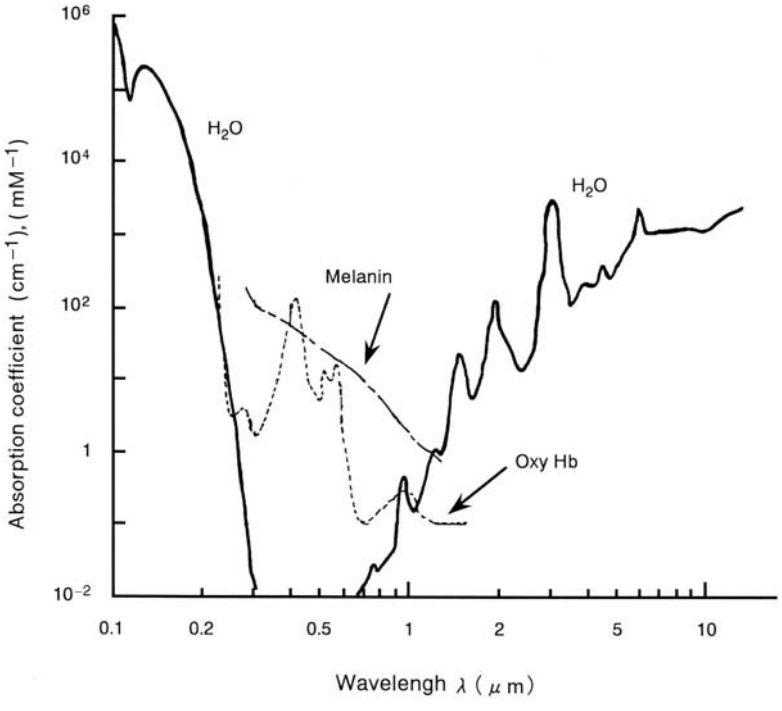

Figure 2. Absorption spectra of major constituents of human body.

2.2. Light Source

A basic part of the optical signal transmission consists of a light source and a photo-receiver. As a light source, a light emitting diode (LED) and a laser diode (LD) are used, generally. As semiconductor elements, they are small, light weight, operable with low voltage and with low power consumption. With each element, direct modulation is possible, as well. If we compared them, each has different merits in practical use. LED is generally inexpensive and easy to handle. LD is superior in monochromaticity, coherency and a response speed. These merits of LD become important in optical communication through an optical fiber and in the case of high frequency modulation (more than several hundreds MHz). However, these features are not necessarily required for the transmission of general biosignals such as an ECG (frequency range of 0-several hundreds Hz). In such a case, LED's are often used.

When a large amount of optical power is required like in the optical communication using indirect scattered light, many elements of the light source are used. To drive many elements simultaneously, we can connect the elements in series or in parallel at the last stage of a driver circuit. They are shown in Figures 3 (a) and 3(b). Since a current-source drive is a standard with LED, the series connection is preferable to make the light emission of each LED uniform. Moreover, the composite capacitance of LED becomes small in the series connection. It is advantageous when high-speed operation such as a pulse-wave drive is required. However in the series connection, the number of elements (n) cannot exceed a certain limit. This is because the forward voltage V_F times n cannot exceed the power-supply voltage V_{CC}. As a result, we often need to divide the series connection into some parallel connections of short series elements (Figure 3 (c)).

2.3. Light Detecting Elements

A light detector forms the front end of the receiver of data-transmission. As the detector, a photo diode (PD), a photo transistor (PTr), an avalanche photo diode (APD) or a photo-multiplier (PMT) is commonly used. To detect a low-level-light at a phton counting level, the detector with an internal gain such as APD and PMT are used. PTr is used as a

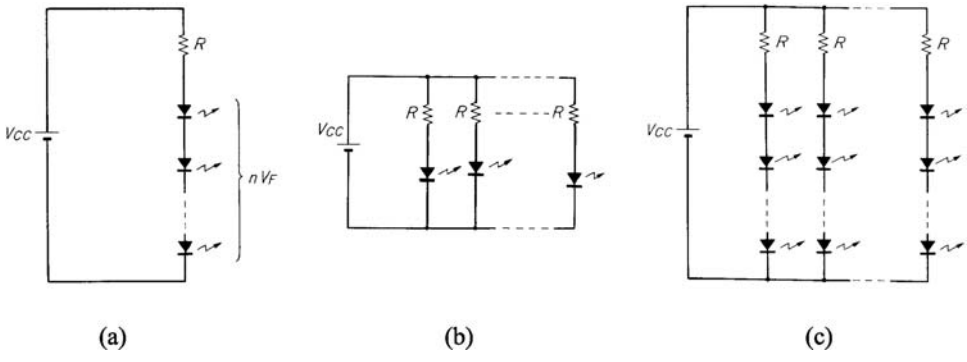

Figure 3. Driving of multiple light emitting elements: (a) series, (b) parallel, (c) mixed, V_{cc}: source voltage, n: number of elements, V_F: forward voltage.

photo-receiving part of such a composite element as a photo-coupler and a photo-interrupter. In optical biotelemetry, the PD is often used since it is easy to handle. Particularly a PIN photodiode can meet the requirement of high-speed operation (typically from some tens of MHz to some GHz) relatively easily. It is suitable for a wide-band digital data transmission system.

In optical telemetry, it is necessary to amplify the electric signal from PD and to process the signal in a wave-shaping circuit and a demodulation circuit. When high-sensitivity and high-speed operation are required, the performance of the whole receiver is often dominated by the first part of the receiver circuits rather than by the detector element itself. To solve this problem, new devices have been developed recently. They include the PD with built-in operational amplifiers as a preamplifier, and the OPIC (optical IC) which is an IC with a photodiode and signal processing circuit integrated on a single chip of IC.

2.4. Measures for Optical Noises

In practical application of biotelemetry, the measurement is particularly vulnerable to the foreign noise coming into the communication channel. Since optical telemetry uses light as the carrier of communication, it shows extremely high resistance to electromagnetic noise. However, it is certainly vulnerable to the effects of optical noise. To deal with this problem, two kinds of filters, or an optical filter and an electric filter are used. The noise source with the largest effect in a room is a fluorescent lamp. As shown in Figure 4, the major emission spectrum of a fluorescent lamp lies between 400–700 nm. Therefore we can greatly suppress its effect using the optical filter, which cuts the wavelength range shorter than a visible light. The filter is often called a black filter.

As for sunlight and the light of an incandescent lamp, we can eliminate a considerable part of the effect using an electronic filter. After the photo-electric conversion at the photo-detector, the frequency component of these lights is well-defined. They are either very low-frequency near DC or some harmonics of the power-line frequency (50 or 60 Hz). Thus, it is not difficult to eliminate them by an electronic filter. However, we have to be careful not to saturate the photo-detector in any case.

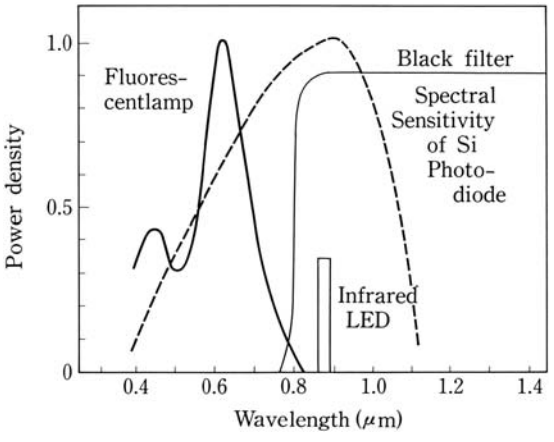

Figure 4. Spectral characteristics of optical elements.

3. BASIC COMMUNICATION TECHNOLOGY FOR OPTICAL TELEMETRY

Figure 5 shows a basic flow of the signal transmission in optical biotelemetry. A special consideration to optical biotelemetry is necessary in the part from the modulator to the demodulator. In this section, the communication technology concerning this part is described.

3.1. Analog/Digital Transmission

Most of the biomedical information can be measured as an analogue signal. A conventional medical telemeter such as an ECG telemeter transmits analogue information in an analogue signal. In analogue transmission the electronic circuit is generally simple. It is suitable to make the telemeter small in size and low in power consumption.

With the progress of digital technology and components, digital techniques have often been used in biotelemetry recently. It may sound meaningless to convert the analogue biological signal into a digital one and then back into an analogue signal at the receiving end. However, the advantage of the digital signal transmission is particularly significant in the intelligent data transmission as mentioned in a later section.

3.2. Modulation Method

In the conventional radio telemetry, a continuous wave modulation (AM, FM, etc.) and a pulse wave modulation (PPM, PIM, PCM, etc.) were used.[5] Commonly, in optical biotelemetry, we first modulate the electric signal using these modulation methods, and then modulate the light intensity by the modulated electric signal. Thus we express the modulation method as FM/IM (Frequency Modulation/Intensity Modulation) or PPM/IM (Pulse Position Modulation/Intensity Modulation) in optical telemetry.

To choose an appropriate modulation method, the characteristics of the biological signal, the multiplexing method and other practical factors have to be taken into account. In many of our applications, the PPM/IM and PIM/IM (Pulse Interval Modulation/Intensity Modulation) have been used. With pulse modulation, we can drive LED's

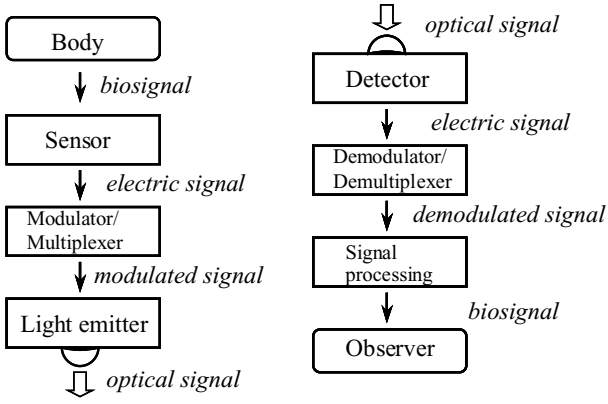

Figure 5. Signal flow in optical biotelemetry.

in higher luminance. With PPM and PIM, we can make the power consumption of the transmitter low by reducing the duty ratio of the light pulses.

3.3. Toward Intelligent Transmission

When we use light as a transmission medium, high-speed data communication becomes possible. The great advantage this brings is that we can use various techniques of intelligent communication. We can call this telemetry with intelligent communication, the telemetry of the next generation. It is compared with the conventional telemetry in which the measured biological signal is transmitted in the modulation signal of one-to-one correspondence.

As for the intelligent communication, the progress of the portable terminal which collects and displays a biological signal is remarkable. However, this article deals with the intelligent signal-transmission itself. There are two levels of intelligent communication, i.e. the level of a biological signal and that of a carrier signal. In the former case, the biological signal is processed using information processing techniques.

For example, the various redundancies such as noises and signal repetitions are eliminated in the transmission side.[6] In the receiving side, the necessary features of the biological signal are extracted from the transmitted signal. In the latter case, the communication part of the telemetry is made intelligent. It includes the error-control techniques in data transmission. Typical examples of the error-control techniques are the ARQ (automatic repeat request) and FEC (forward error correction). In both cases, we add some redundancy to the signal to transmit. Then, at the receiving side we detect the error caused in the transmission process, and take some measure for the detected error. With the ARQ, the system keeps requesting the repeated transmission of the data until no error is detected at the receiving side. With the FEC, the error is automatically corrected using the special code embedded (inscribed) in the transmitted signal.[5]

In such error-control processes, some duration of the data processing time is required. Generally, the longer time is required to use the more complicated error control to increase the reliability of data transmission. If this processing time exceeds the temporal capacity of the transmission system, the real-time operation is hindered. In biotelemetry, the real-time operation is often required. Therefore it is necessary to devise the error control method to secure high reliability while meeting the demand for the real-time operation. The balance between these contradicting requirements has been taken into account, for example by limiting the number of the repeated retransmissions in ARQ or by using a simple logic FEC such as a majority rule, etc.[7]

It should be noted that the difficulty of this problem has been gradually reducing due to the remarkable progress in the data-processing algorithm and the data-transmission speed.

3.4. Multiplexing Method

In optical biotelemetry, multi-channel data transmission is often required due to its large transmission capacity. To answer this, a multiplexing technique is necessary. The multiplexing techniques in optical communication are categorized largely into space-division multiplexing (SDM), wavelength-division multiplexing (WDM), time-division multiplexing (TDM), frequency-division multiplexing (FDM) and code-division multiplexing (CDM). Each has the following different characteristics and is chosen according to the purpose and the usage.

SDM uses the spatial difference in the light propagation path. It is effective for the telemetry using the direct-light transmission or the optical fiber transmission. With the indirect-light transmission, we have to separate the light-path by shading material, and the constraints in practical use are sometimes severe.

With WDM, we separate the channel by the difference of the wavelength of the transmission light. It can be realized relatively easily using light sources with different wavelengths and optical filters. It can be used in combination with other multiplexing techniques. Generally, it is difficult to have a large number of multiplexed channels due to the practical restrictions such as the monochromaticity of light source, the trade-off between the filter-bandwidth and the SN ratio of an optical signal, and so on. With the indirect light transmission, we cannot fully utilize the effective wavelength separability of the interference filter, since the orientation of light incidence to the optical detector is not constant.

With TDM, we allocate multiple channels on the time axis of the optical signal. With the recent rapid increase in the data transmission speed, the multiplexing of many channels has become possible. To perform efficient multiplexing in telemetry, the synchronization between multiple transmitters and receivers is necessary. For wireless synchronization, a two-way transmission is necessary and the receiving function is required for the apparatus equipped on a subject as well as the transmitting function. In biotelemetry, there is a fundamental demand to make the apparatus equipped on a subject as small as possible. Thus, the requirements of the synchronization often make it difficult to satisfy this demand.

With FDM, we differentiate multiple channels by the difference in the frequency of intensity modulation of carrier light. This can be done relatively easily. As mentioned above, a pulse modulation method is often used in optical biotelemetry. In the pulse modulation, the number of multiplexed channels is limited due to the higher harmonics of the pulse shape. With indirect-light transmission, the effect of multi-path transmission becomes non-negligible when the modulation frequency becomes large. Therefore, the bandwidth of signal transmission is limited.

With CDM, we encode the electric signal that modulates the light source, and differentiate multiple channels by the code. The spread spectrum is a typical example. This technique is suitable to the optical communication with which a broad band communication is possible. This technique has much useful potential such as strength against foreign noises and multi-path propagation. However, at present, some problems in practical use remain such as the complexity of the circuits both in a transmitter and a receiver.

4. PROPAGATION OF OPTICAL SIGNAL

For optical biotelemetry, it is necessary to understand the propagation of the optical signal in various conditions. This chapter summarizes the optical propagation in transcutaneous telemetry and ambulatory telemetry.

4.1. Optical Characteristics of Body Surface Tissue

In the transcutaneous signal transmission, the absorption and the scattering characteristics of body tissue are important. The optical absorption characteristics of biological tissue largely depend on the wavelength of light. Figure 6 shows the light attenuation in the tissues of body surface. This shows how the optical signal from the hypodermic (2 mm depth) light

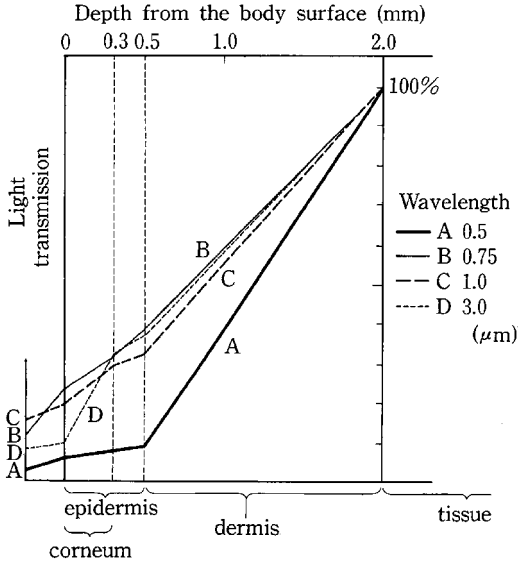

Figure 6. Attenuation of light in human surface tissue.

source is attenuated as the light propagates to the skin surface.[8] With near-infrared light, 10∼20% light transmission is expected through the 2 mm skin tissue.

An example of the measured scattering characteristics of the skin is shown in Figure 7. This is the case of a mouse, and we can see the effect of relatively thick white fur.[8] Even with the complex emission-pattern of LED in the air, the angular pattern of light transmitted through the skin becomes fairly uniform in all directions. This is due to the strong scattering at the body surface tissue, and is also expected with human skin with less hair. This orientational uniformity of signal transmission is a significant merit in biotelemetry in which the subject moves around freely. Other optical properties of mammalian tissue can be found elsewhere.[9]

4.2. Distribution of Indirect Light in a Room

In a closed space like a room, ambulatory telemetry is possible using the indirect light scattered from the ceiling, the wall and the floor, etc. To understand the behavior of the indirectly scattered light, the spatial distribution of received light-intensity is investigated in a computer simulation.[10]

Figure 8(a) shows the conditions of the simulation. A light emitter with a hemispherical emission pattern toward the ceiling is placed 1.5 m high (a shoulder height of a human adult) above each of the floor mesh points. The light intensity received by the detector which is placed at the center of the ceiling is calculated according to the position of the emitter. The positions of the emitter are set at each of the floor mesh points. The light receiver is hung 0.6 m down from the center of the ceiling and the detecting face is oriented toward the ceiling or the floor. Figures 8(b)–(c) and 9(b)-(c) show the spatial distribution of the received light or the intensity of the transmitted signal.

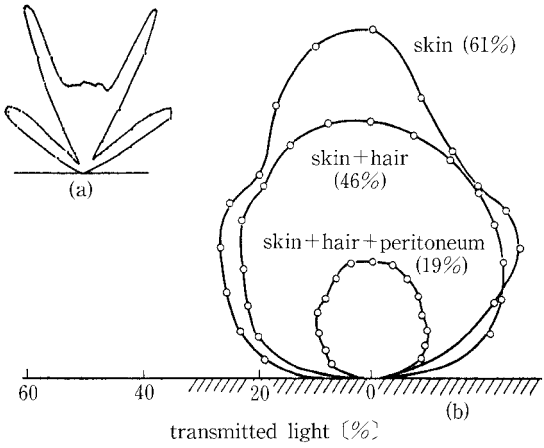

Figure 7. Scattering property of animal skin: (a) Radiation pattern of LED in air (wavelength 890 nm), (b) Radiation pattern of transmitted light through mouse skin (values are maximum transmission rates).

Figure 8(b) and 8(c) show the results with different orientations of the light detector. In both cases, sufficient amount of light for telemetry was received in all parts of the room even in a corner area due to the scattering effect. When the transmitter approaches to the central position of the floor, the received signal increases. In the case of Figure 8(c), the light-detecting face of the receiver is pointed up towards the ceiling and the variation of the received signal becomes relatively small. In ambulatory telemetry, the small variation is often more preferable than the high peak-intensity of the received signal. That is, we can

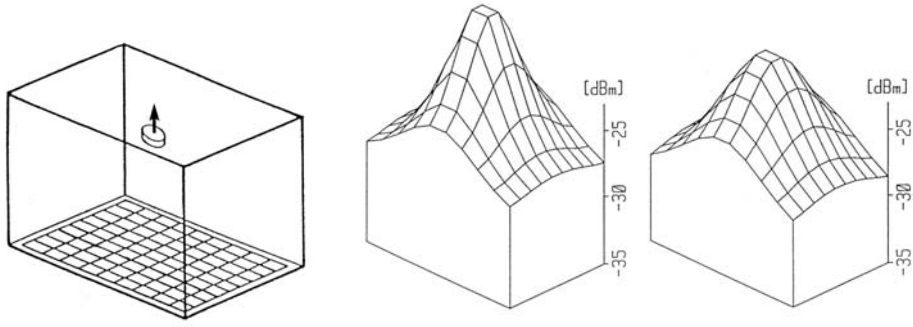

Figure 8. Conditions and results of simulation of indirect scattered light: (a) dimension of room 6.4 m width, 4.2 m length, 2.7 m height; reflection coefficient of inner surface of room 0.7 (Lambertian surface), optical power of transmitter 1 W; receiving area of receiver $10 \times 10\,\text{mm}^2$; directivities of transmitter and receiver are both cosine. (b) intensity distribution of signal transmission with receiver facing down toward floor, (c) intensity distribution of signal transmission with receiver (hung 0.6 m down from ceiling) facing up toward ceiling.

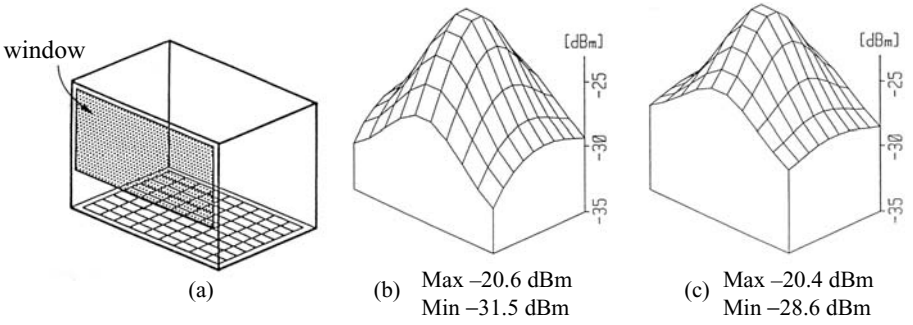

Figure 9. Change of signal transmission caused by window: (a) position of window, (b) with window, (c) without window.

expect stable telemetry with the light detector hung down from the ceiling with its receiving face pointed up towards the ceiling.

In the telemetry using indirect light transmission, the room is filled up with the signal light by the scattering from the ceilings and the walls. This is the basic principle of ambulatory telemetry. Thus, the signal strength is reduced considerably when there is an open-window or a dark curtain on the wall. To examine this effect, a simulation was conducted for the case when there is a large open-window (the wall with 0 reflection coefficient) covering most of one of the walls. Figure 9 shows the result. The signal strength decreases when the transmitter approaches the window. However, the decrease is small (2-3 dB) and there is little problem in practice. This example typically shows that the distribution of the indirectly scattered light is relatively stable against the change in environmental physical conditions.

The validity of this result of simulation was confirmed in the real measurement, as well.[10] An example of the measured result is shown in Figure 10. This is the spatial

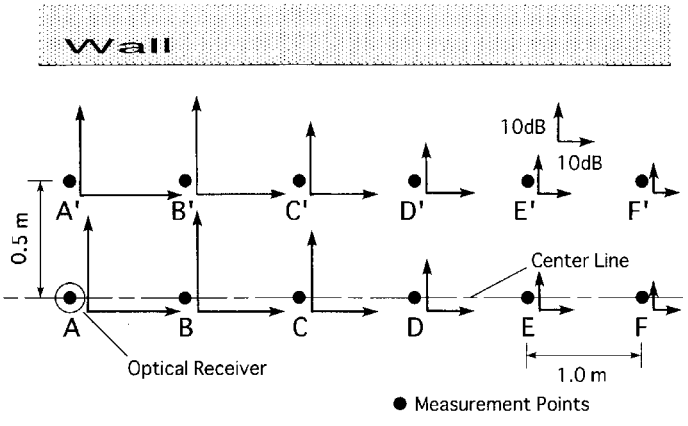

Figure 10. Measured distribution of signal transmission in corridor: length and orientation of vectors indicate CN ratio of received signal and direction of subject's face, respectively.

distribution of the received signal in the corridor in which two sides are considered as open space. (W2.1m × H2.7m × L30.0m) This shows the signal strength received at the ceiling at the position indicated in the figure. The subject equipped with a light emitter (1W optical power) on both shoulders stands at different points (A-F, A'-F') facing against a wall or facing along the center line of the corridor. The vectors in the figure indicate the orientation of the subject and the magnitude of the received optical signal in C/N (ratio between the strengths of carrier and noise). This result shows that we can expect more than 10 dB C/N in entire area by installing light detectors every 8–10m. Through these analyses it was confirmed that we can realize the ambulatory biotelemetry using indirect light transmission in a regular room with little effect from the subject's position and movement.

4.3. Optical Signal Propagation in Open Space

In the ambulatory measurement using indirect light transmission, the optical signal filled the closed space, generally. Therefore, it is considered to be effective in a patient's room, an examination room and a cabin of a vehicle, but not in an open space such as outdoors. Two techniques can be used to overcome this problem.

One is the use of direct light transmission with a tracking function. Using a beam of light, data can be transmitted by tracking either the transmitting side or the receiving side. Various systems that track a light spot automatically have been commercialized, and it is not difficult to follow the speed of a human movement. However, when we use direct light transmission, we always have to secure the light propagation path.

In another technique, we use the indirect light transmission available in an open space. For instance, the ambulatory measurement becomes possible to some extent using ground reflection effectively or using many receivers equipped with a diffuser or a reflector. An example of the unit of reflectors and a photo-detector is shown in Figure 11. 8–16 units of this structure are combined around the z-axis in the positions of rotational symmetry. With

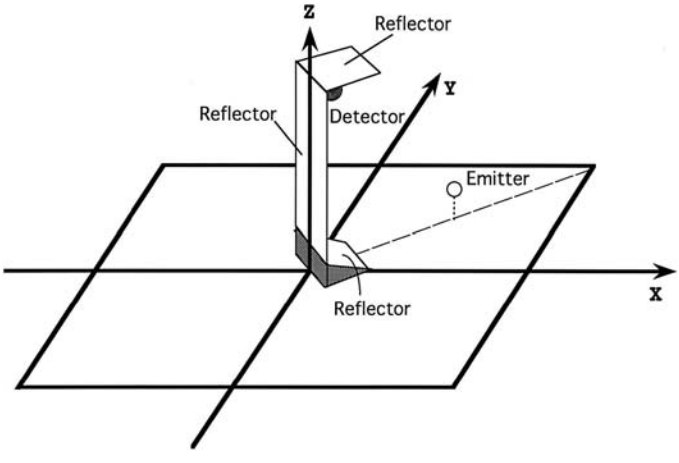

Figure 11. An example of reflector structure for indirect light transmission in open space.

this kind of receiver, we can achieve ambulatory measurement with a light emitter of 1W optical power within 10m distance from the receiving unit in an open space.

5. MULTIPLEXING IN OPTICAL TELEMETRY

As mentioned in Sec.3.4, there are various multiplexing techniques for optical telemetry. Every technique has problems to be solved in the practical use for optical telemetry. We have also developed the multiplexing technique suitable for the biotelemetry using indirect light transmission.[11] Here, we introduce two representative techniques.

5.1. Pulse Burst Method

In the optical data transmission in free-space, the pulse modulation technique is more advantageous than the CW modulation technique from the view points of optical transmission power and noise immunity. The pulse width modulation (PWM) is a typical method of the pulse modulation technique. We can use the PWM in a relatively simple manner, and the demodulation is easy, as well. However, the power consumption of PWM is generally high. So, we can modify the PWM as the pulse position modulation (PPM) by representing the positions of the rise and the fall of the PWM pulse by two short pulses. The first and the second pulses indicate the temporal positions of synchronization and modulation, respectively. In the proposed pulse-burst method, we make the above mentioned short pulse into a train of narrow pulses. This train of pulses consists of a few pulses to several tens of pulses. In multiplexing, each channel is distinguished by the frequency of the burst pulses. Figure 12(a) shows the principle of this technique, and Figure 12(b) shows the frequency spectra of the pulse burst signal with 500 kHz repetition of 1 μsec width pulses. As the number of the pulses increases, the spectral peak becomes narrow. In this case, we can expect several channels multiplexing with 8 pulses in a single burst. In experiments, the

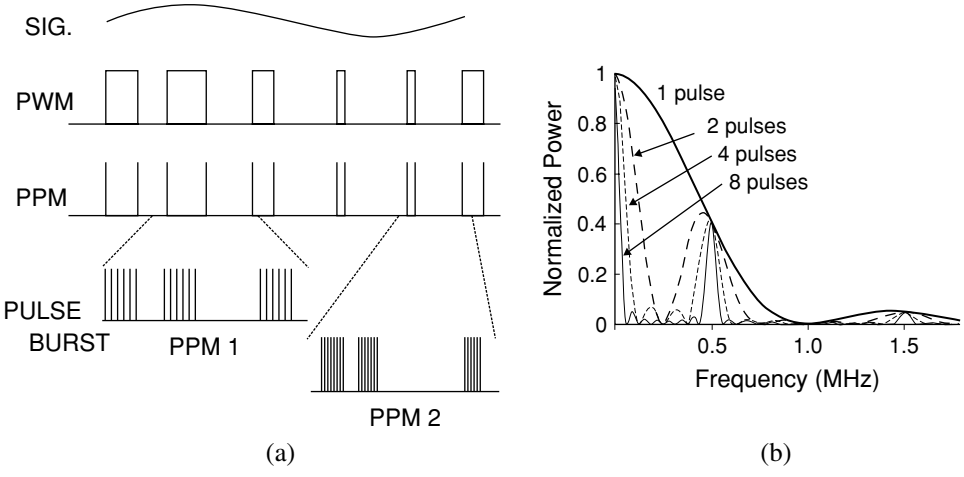

Figure 12. Pulse-burst multiplexing technique: (a) principle, (b) power spectra.

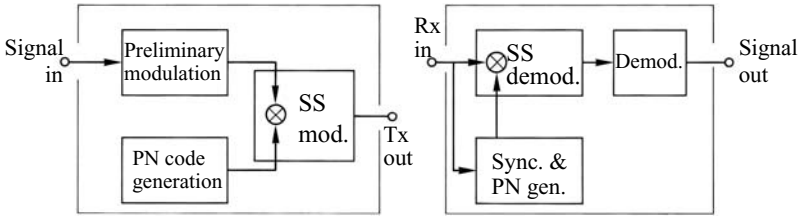

Figure 13. Telemetry system using spread spectrum technique.

effectiveness of this pulse-burst technique in the multiplexing of several channels has been confirmed.[11]

5.2. Spread Spectrum Method

For biotelemetry using indirect light transmission, we have proposed the application of the spread spectrum (abbreviated as SS) method as a promising multiplexing technique. With the SS method we modulate the signal to be transmitted into a much wider bandwidth than that required for the original signal.

Figure 13 shows the principle of the SS modulation system we have developed for the optical biotelemetry. In this system, we modulate the signal to be transmitted into a digital signal as the first modulation. Then, as the second modulation, we modulate the digital signal by multiplying it with a pseudo-noise signal generated in the transmitter. Since the pseudo-noise signal has much wider bandwidth than the original signal, the spectrum of the modulated signal is spread widely. In the receiving side, we take the correlation between the received signal and the same pseudo-noise signal as the transmitting side. As a result, we can obtain the digital signal of the first modulation. By demodulating the digital signal, we can recover the original signal. Through these processes, the effects of noises, interferences and multi-path propagation are greatly suppressed. With this SS method, we can multiplex more than several tens of channels relatively easily by using different kinds of the pseudo-noise. On the other hand, a wide-band transmission is required to utilize this technique effectively. Since the wide width of the transmission band is one of the typical merits of optical biotelemetry, it is suitable to the SS method. The detail of this technique and the results of experiments can be found in the reference[12].

6. APPLICATIONS OF OPTICAL TELEMETRY

We have applied the methods and techniques previously mentioned to realize the optical biotelemetry. Let us see some of them as concrete examples of optical biotelemetry.

6.1. Transcutaneous Biotelemetry

One of the techniques to take the internal information out of the body is the transcutaneous biotelemetry. The radio-capsule is one of the well-known examples. With this technique, we encapsulate pH electrodes or a temperature sensor in a swallowable small

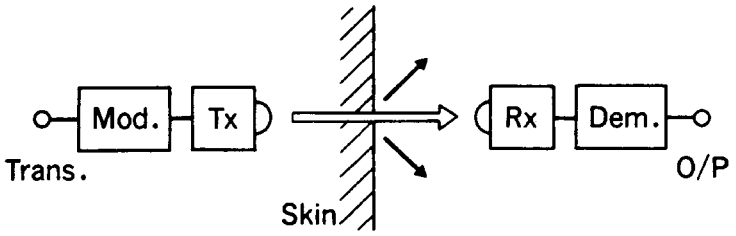

Figure 14. Principle of transcutaneous optical telemetry: Trans: transducer, Mod: modulator, Tx: transmitter, Rx: receiver, Dem: demodulator, O/P: output.

capsule. It transmits the pH or temperature information of the digestive tract from the inside to the outside of the body by a radio wave. We can apply the principle of optical telemetry to this purpose, also.

We place a light emitting element inside the body and receive the light propagated through the body tissue. Figure 14 shows this principle. We have confirmed the feasibility of this principle through various fundamental studies.[8] Then, a telemetry system was test-manufactured, and it was applied to an animal experiment.[8] Figure 15 illustrates the animal experiment. The electrodes, the transmitter and the light emitters were implanted inside the body of a rat. The light signal diffusely propagated through the skin was captured by the optical receiver placed outside the animal cage. In this way, the internal ECG can be measured remotely without restraining the animal. There is no need to attach any element on the body surface of the animal. This makes the animal experiment much easier than using many attachments on the body.

The size of the implanted transmitter was $40 \times 25 \times 15$ mm^3 and the weight was 16.6 g. The transmitter operates for about 100 hours in continuous use. We installed a power switch which can be driven by the illumination of near-infrared light pulses from outside the body. Therefore, the battery life was extended considerably by turning on the power only when it was necessary. The light emitters were two LED's with the optical power of 70 mW in total. The transmission range was 3 m in a free space. If there is a scattering object such as a wall or a human body within about 1 m, the telemetry was possible even when the direct propagation path was intercepted.

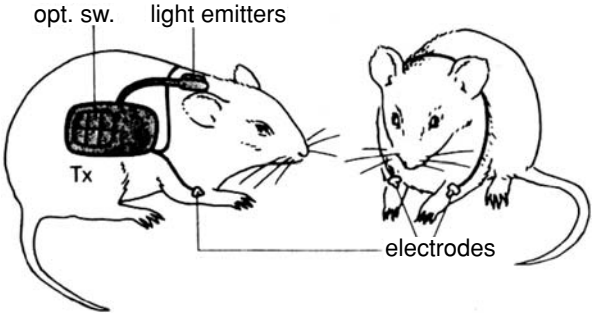

Figure 15. Animal experiment of transcutaneous optical telemetry: opt. sw.: optical switch.

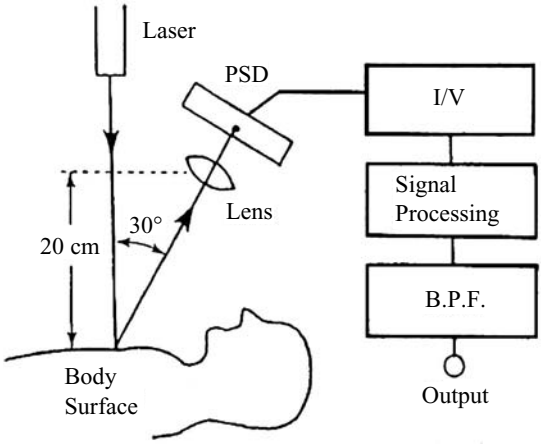

Figure 16. Principle of surface displacement measurement by light.

6.2. Non-contact Measurement of Body Surface Displacement

We can measure the displacement of the body surface without any direct contact by using light. Figure 16 illustrates the principle of this technique. This example shows that we can use light not only for the signal carrier but also for the sensor to obtain a biological signal.[13] When we illuminate the measurement point on the body surface with a thin parallel beam of light, a scattering light spot appears on the body surface. With a lens, the scattered light is focused on a solid-state position sensitive device (PSD) as a light spot. Since the body surface displacement in the direction of the light beam changes the position of the light spot on the PSD, we can measure the displacement as the current change of the PSD. We used a laser diode (1mW, 780 nm) as a light source, and a one-dimensional PSD (1×12 mm^2 effective receiving area) as a light receiver. The sensitivity and the accuracy were 200 mV/mm and 0.01 mm (frequency bandwidth 0.1–20 Hz), respectively.

This principle was applied to the respiratory and cardiac monitoring of neonates.[13] Figure 17 shows the concept of this technique. Figure 18 shows the result of the measurement

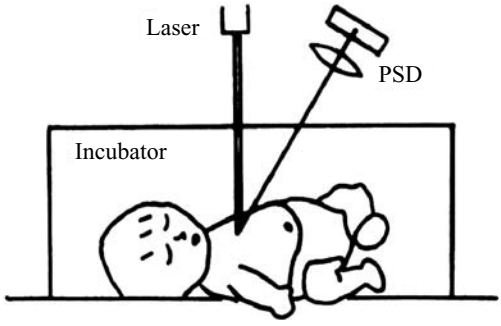

Figure 17. Respiration monitoring of neonate by light.

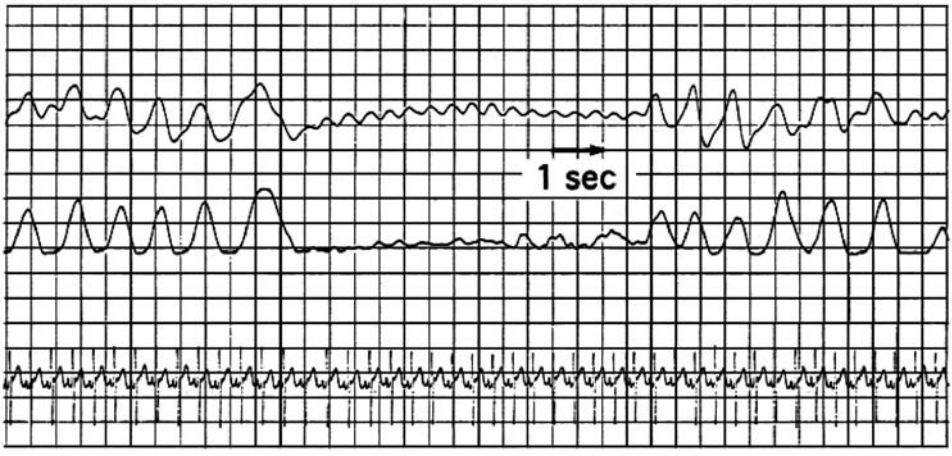

Figure 18. Measured results of chest movement of neonate: (a) optical technique, (b) impedance measurement, (c) ECG.

obtained with the neonate lying on the back. It shows the waveform obtained by the proposed technique (Figure 18(a), 0.1–3 Hz bandwidth), the respiration waveform obtained by an impedance measurement technique (Figure 18(b)) and the ECG (Figure 18(c)) for comparison. Figs.18(a) and 18(b) show the temporary apnea between normal respirations. Even with a simple band-pass filtering, the waveform obtained by the optical technique shows a good agreement with that obtained in the conventional impedance measurement. In Figure 18(a) we can observe the fluctuation in the apnea period. In comparison with Figure 18(c), it was found to be the cardiac movement of the chest wall. This shows that we can monitor the vital sign of neonate with a beam of light and without any electrodes and cables.[13]

There have been different applications of this technique, or the optical non-contact measurement of body surface movement. They include the measurements of a mechanocardiogram and the pulse propagation velocity.[14] It has been shown that this technique is also useful in detecting the blood vessel constriction due to physical and mental stress without any physical contact on the body.[14]

6.3. Ambulatory Telemetry

One of the most important purposes of biotelemetry is to measure physiological signals without any constraint on the natural activity of the subject. The ECG telemeter which has been used in clinical routines is a typical example. In hospitals and medical institutions, various kinds of telemeters have been used, such as integrated monitoring in ICU and CCU, and daily cardiac monitoring of hospitalized patients. In almost all the cases, a radio wave has been used as the transmission medium in these kinds of telemetry. Recently, EMI problems have become more serious than ever due to the deterioration of the electromagnetic environment in hospitals and the enforcement of legal restrictions.

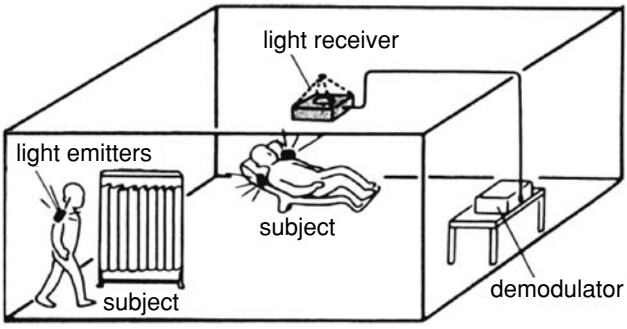

Figure 19. Principle of ambulatory telemetry using indirect light transmission.

Many of these problems can be solved by using light as a transmission medium for the biological information. If we use indirect light which has been reflected and scattered at a ceiling, a floor and walls, we can transmit a stable signal by light without the problem of interception of a direct path. Figure 19 shows the principle of this technique. The biological or physiological signals obtained from a subject are modulated for transmission. If multi-channel data transmission is required, they are multiplexed into a single channel of data. The modulated signal is converted into a light signal at a transmitter. The light signal is emitted, reflected and scattered at the inner surface of a room, and eventually fills the room. In this way, we can maintain the signal transmission by the indirect light transmission even if the direct light path between the transmitter and the receiver is intercepted.

Figure 20 shows the outline of the system to realize this technique. This system consists of a transmitter to collect and to transmit biological signals and a receiver to receive and to display/record the signals. To examine the effectiveness of this technique, an optical telemetry system was manufactured. Table 1 shows major characteristics of the system. The effectiveness and the usefulness of this technique have been confirmed in the measurement

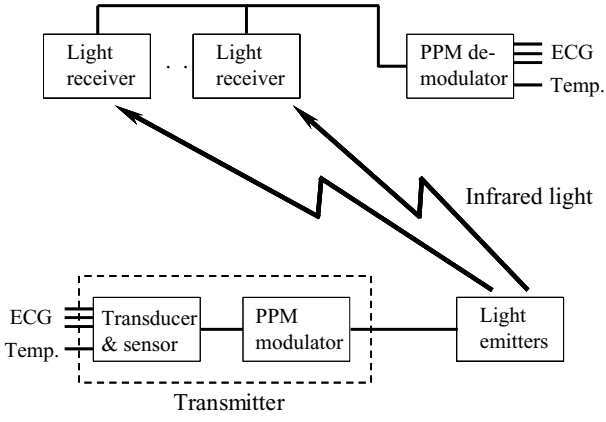

Figure 20. Telemetry system using indirect light transmission.

Table 1. Performance of Optical Biotelemetry System

TRANSMITTER			LIGHT EMITTERS (a set of two)	
ECG	3 ch. standard limb leads or precordial unipolar leads		Light emitter	80 IRLED's (940 nm)
signal bandwidth	0.05–100 Hz		Total optical output (when pulse on)	1 W
non-linearity	less than 4%		Current drain	20 mA
total gain	46dB		Dimension	L90 × W80 × H18 mm^3
Temperature	1 ch. thermistor		Weight	85 g
temperature range	0-–42 deg. C			
time constant	0.42 deg/s			
Modulation	4 ch. PWM/PPM/IM			
Pulse frequency	2.6 kHz		LIGHT RECEIVER	
Pulse interval	ECG ch.	0.3 ms	Photo detector	PIN Si photo diode (effective receiving area 100 mm^2)
	Temp. ch.	0.6 ms		
Pulse width	2μs		Optical filter	long pass filter (cut off wave length 800 nm)
Current drain	1.5 mA			
Dimension	L36 × W60 × H138 mm^3		Dimension	L100 × Wl20 × H50 mm^3
Weight	350 g		Weight	450 g

with a subject in various moving conditions. The optical telemetry system using indirect light transmission developed in this study has been used for the biological data acquisition of a payload specialist of a space shuttle in the space-lab.[15]

6.4. Multi-channel Biotelemetry

Using the biotelemetry technique, we can transmit biological signals and medical data to a remote place. The ECG transmission from isolated islands and remote rural areas using a public telephone network is a well-known example. With the optical technique, we can realize the large-capacity high-speed data transmission.

Figure 21 shows the principle. Different kinds of biological signals and medical data are multiplexed in a primary station. They are transmitted through an optical communication channel. The optical signal is received at the secondary station and demultiplexed

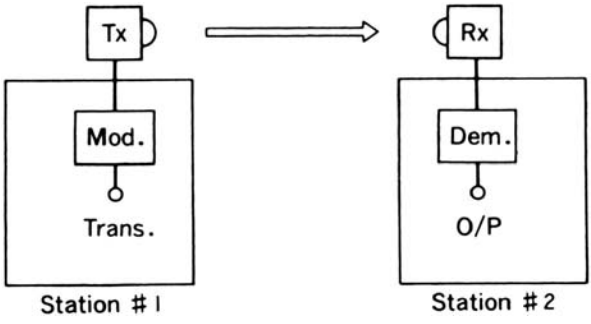

Figure 21. Principle of multi-channel data transmission to remote place by optical telemetry: Trans: transducer, Mod: modulator, Tx: transmitter, Rx: receiver, Dem: demodulator, O/P: output.

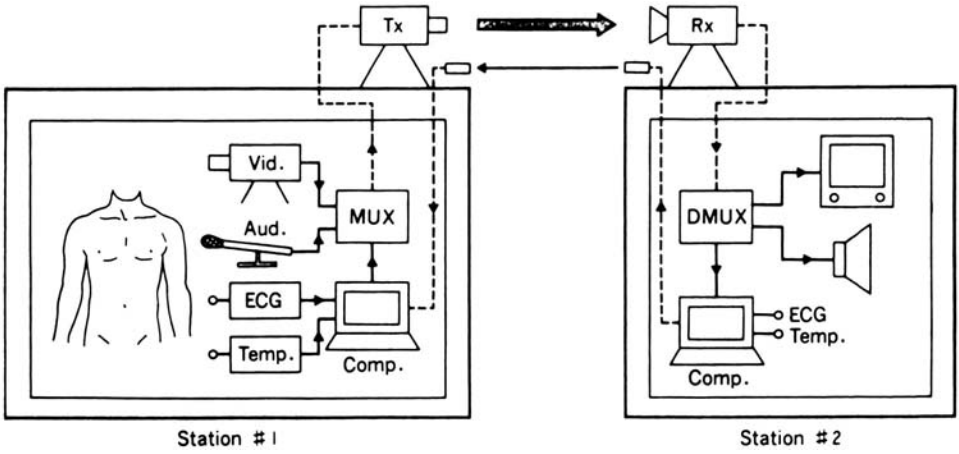

Figure 22. Developed system for multi-channel data transmission to remote place by optical telemetry: Vid: video signal, Aud: audio signal, MUX: multiplexer, Tx: transmitter, Rx: receiver, DMUX: demultiplexer, Comp: computer, broken line: optical fiber.

to reproduce the original signals and data. This technique not only enables us to separate the data collection site and the data analyzing site, but also enables us to transmit many different kinds of data to a remote place simultaneously in real time. In this way, we can significantly increase the mobility and the flexibility of each station. This is particularly important in the case of animal or human experiments and clinical practices. In these cases, it is generally difficult to bring large data collection/processing equipments into the measurement site. Since we can send multi-channel data including color moving images and audio signals in real time, this technique provides a powerful tool for telemedicine and home-care medicine.

Figure 22 illustrates the outline of the system test-manufactured to show the possibility of this technique. From the primary station to the secondary station, the biological signals (color video image, audio signal, ECG, EEG and body temperature) are modulated by the PPM/IM method and transmitted through open air. In the return-path, the signal for ARQ is transmitted back from the secondary station to the primary station. Since the capacity of the information through this return-path is very small such as the existence of channel disconnection and the state of receivability, four kinds of signals were enough. They were differentiated by the frequency in an FM/IM modulation.

An experimental system was developed and the effectiveness of this technique was examined.[16,17] In the experiment, a color moving image, an audio signal and three channels of biological signals (ECG, EEG, body temperature) were transmitted simultaneously to show the condition of a patient. In this experiment, the signals were transmitted by light through open air. The transmission distance up to 1 km was confirmed with our system. Using a laser with higher optical power, larger transmission distance is expected. If the mobility of the primary station is not required, we can use an optical fiber communication. Then, the transmission distance can be much larger than the open-air communication.

6.5. Data Transmission between Medical Equipments

With the recent increase of various electrical equipments in medical institutions, there has been a strong demand for them to be integrated into a small number of systems. Particularly in an operating room and an ICU, the centralized control and data processing are required among many monitoring, imaging, and automatically controlled equipments. However, such integration inevitably increases the number of electric wires connecting the equipments. This not only hinders the operation but also increases the risk of accidents such as the leakage of electric current. The wireless transmission of data and control signals is one of the solutions. However, the use of a radio wave in a hospital is not preferable due to the problem of electromagnetic interference. We have applied the optical biotelemetry technique to answer this demand.

For multiplexing we have used the SS method which is robust against various noises and can provide many channels for multiplexing. To examine the feasibility of this technique, we have developed a central part of the transmission system.[12] Figure 23 shows the outline of this system. The digital data to be sent is fed from computer A through an RS-232C interface. In the transmitter, the data is processed in the preliminary modulation circuit to be suitable for the next SS modulation. Then, it is multiplied with the pseudo-noise (PN) code generated in the transmitter. For the preliminary modulation and the PN code, we used the ASK (Amplitude Shift Keying) and the Gold series with 127 chips period. To make the data transmission rate at 9600 bps, the clock frequency of a chip was set at 7.315 MHz. The SS modulated signal is emitted from the LED array which consists of 60 LED's (nominal optical power 30 mW each, wavelength 850 nm). The indirect light scattered by a ceiling, a floor and walls reaches the Si-PIN photodiode and is transformed into an electric signal. The received signal is amplified and its frequency is shifted to 215 MHz in an up-conversion circuit using a double balanced mixer (DBM). This is the operating frequency of a surface acoustic wave (SAW) convolver. In the receiver, the time-reversed Gold series which is the same as that used in the transmitter is generated. This PN code is also frequency-shifted to 215 MHz and fed to the SAW device. In the SAW device, the received signal is convolved with the PN code, and the correlation data is obtained in real time. After this SS demodulation, the signal is demodulated according to the preliminary modulation. In the developed system, the signal is processed in the envelope detection

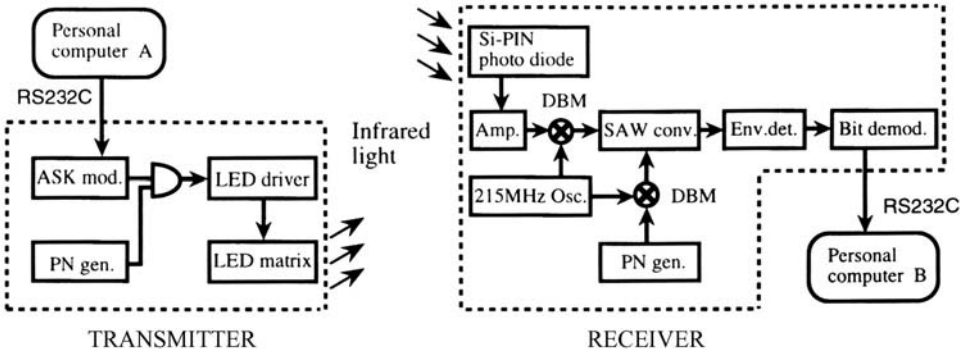

Figure 23. System for optical data transmission between medical equipments using SS technique.

and the bit demodulation circuits. The bit-data is fed to computer B through an RS-232C interface and an original signal is reproduced in the computer.

We have manufactured an experimental system which consists of two transmitters and one receiver. In the analysis of transmission characteristics, the practical feasibility of the proposed technique has been verified.[18,19]

7. CONCLUSIONS

A concept of optical biotelemetry has been proposed and summarized. Conventionally, a radio wave is commonly used for biotelemetry. However, optical biotelemetry is possible in various applications as shown in this chapter. Due to the recent progress in optical and electronic technologies, the introduction of the optical technique can realize new useful features. We do not intend to replace radio telemetry by optical biotelemetry. They should be used to support each other. For example, in a closed space such as in a building, optical telemetry has many useful merits. However, in open space such as outdoors, radio telemetry has much greater transmission range.

Until very recently, the applications of biotelemetry have been limited in a relatively small area, such as ECG telemetry and animal tracking. However, the demand for biotelemetry has been steadily expanding. There has been a notable change in our society. Cardiac and cerebral disorders are increasing rapidly as the elderly population increases. The necessity of homecare and telemedicine is higher than ever. The importance of rehabilitation medicine and sports medicine has been widely recognized. Health management and self-diagnosis have become common among the general public. The demand for providing emergency medical support to moving vehicles such as ships, aircrafts and space ships has been increasing, as well.[20] In these social trends, biotelemetry has been expected to play an important role as a key-technology. Optical biotelemetry is only one of the techniques of such biotelemetry. But it has promising potential to open a new possibility to answer the above demands.

REFERENCES

1. R.S. Mackay, *Bio-Medical Telemetry* (IEEE Press, New York, 1993).
2. International Society on Biotelemetry, *Biotelemetry*, Series of publications, http://www.biotelemetry.org.
3. K. Shimizu, Optical biotelemetry, *Japanese Journal of Medical Electronics and Biological Engineering* (in Japanese), **18**(7), 492–498 (1980).
4. H. P. Kimmich, Biotelemetry based on optical transmission, *Biotelemetry and Patient Monitoring*, **9**, 129–143 (1982).
5. K. Shimizu, Fundamentals for biotelemetry; Engineering, *Biotelemetry*, **11**, 179–184 (1991).
6. S. Tsuda, K. Shimizu and G. Matsumoto, Efficient application of coding technique for data compression of ECG, *IEICE Trans. Inf. & Syst.*, **E76-D**(12), 1425–1433 (1993).
7. H. Murakami, K. Shimizu, K. Yamamoto, T. Mikami, N. Hoshimiya, K. Kondo, Telemedicine using mobile satellite communication. *IEEE Trans. Biomed. Eng.,* **41**(5), 488–497 (1994).
8. N. Kudo, K. Shimizu and G. Matsumoto, Fundamental study on transcutaneous biotelemetry using diffused light, *Frontiers of Medical and Biological Engineering*, **1**(1), 19–28 (1988).
9. V. Tuchin, *Tissue Optics* (SPIE Press, Bellingham, 2000).

10. N. Kudo, K. Shimizu and G. Matsumoto, Optical biotelemetry using indirect light transmission, *Biotelemetry*, **9**, 55–58 (1987).
11. S. Matsuda, K. Shimizu, K. Yamamoto and T. Mikami, Multiplexing technique for the optical telemetry using indirect light transmission, *Biotelemetry*, **11**, 54–57 (1991).
12. K. Shimizu, N. Toya and K. Yamamoto, Application of spread spectrum technique for multichannel transmission in optical telemetry, *Biotelemetry*, **14**, 97–102 (1998).
13. K. Shimizu, K. Kobayashi and G. Matsumoto, Respiratory and cardiac monitoring of neonate by non-contact optical technique, *Biotelemetry*, **10**, 626–632 (1989).
14. K. Shimizu, Measurement of body surface displacement by light (in Japanese), *BME*, **4**(4), 33–43 (1990).
15. K. Shimizu, Optical biotelemetry (in Japanese). *Jap J. Physical Fitness and Sports Medicine*, **44**(2), 317–324 (1995).
16. H. Odagiri, K. Shimizu and G. Matsumoto, Free-space optical data link for multi-dimensional biological information (in Japanese), *Memoirs of Hokkaido Institute of Technology*, **16**, 1–8 (1988).
17. H. Odagiri, K. Shimizu and G. Matsumoto, Free-space optical data link for multi-dimensional biological information II(in Japanese), *Memoirs of Hokkaido Institute of Technology*, **17**, 1–9 (1989).
18. N. Toya, and K. Shimizu, Fundamental analysis of multichannel spread spectrum data transmission using indirect scattered light (in Japanese),*IEICE Trans.*, **J83–B**(6), 780–788 (2000).
19. N. Toya and K. Shimizu, Performance analysis of spread spectrum data transmission for biotelemetry using indirect IR light, *Biotelemetry*, **16**, in press.
20. K. Shimizu, Telemedicine by mobile communication, *IEEE Eng. Med. Biol.*, **18**(4), 32–44 (1999).

Chapter 5

Extremely Low Frequency Magnetic Fields (ELFMF) and Pain Therapy

Frank S. Prato, Alex W. Thomas, and Charles M. Cook

ABSTRACT

One of the most conspicuous results of extremely low frequency magnetic field (ELF MF) exposure in animal and human populations has been an effect upon pain behaviours. Pain is a multi-faceted construct having cellular, physiological and psychological domains of action and represents one of the most significant health issues that we deal with on a day to day basis. Our laboratory has been investigating ELF MF effects on pain for over twenty years after it was first noted how magnetic field exposure inhibited morphine induced analgesia. Our mission is to develop effective and efficacious specific pulsed magnetic field designs, initially for the treatment of pain. Although there is a rich body of research in studying animal models, there is a definite lack of well designed studies examining the effects of magnetic fields upon human pain responses. This chapter reviews the historical and current state of magnetic field therapies for the treatment of pain, as well as providing an overview of our current understanding of pain, nociception and the opioid system. We also review some of the current hypothesized mechanism(s) by which time-varying magnetic fields elicit behavioural and physiological responses and how this will provide us with the tools to design specific magnetic field pulses and delivery systems which will be used for chronic and acute pain treatment without the unwanted side-effects often associated with chemical/pharmaceutical therapies. We also hypothesize that the future of magnetic fields and pain therapy

Frank S. Prato, Alex W. Thomas, and Charles M. Cook Lawson Health Research Institute, London, ON N6A 4V2, Canada

Advances in Electromagnetic Fields in Living Systems, Volume 4, edited by James C. Lin, Springer Science+Business Media, New York, 2005.

lie in the rapid advancement of imaging technologies, such as magnetic resonance imaging (MRI), positron emission tomography (PET), electroencephalography (EEG) and magnetoencephalography (MEG). We advance the concept of image-guided magnetotherapy as the next step in therapeutics oriented bioelectromagnetics research.

1. INTRODUCTION

For over 100 years, researchers have been studying the effects of extremely low frequency magnetic fields (ELF MF) upon animal and human systems. Nearly every aspect of physiology and behavior have been examined in the pursuit of an explanation of how ELF MFs could exert a systemic effect. It is extremely well established that static magnetic fields of approximately earth-strength ($\approx$50 μT) affect animal behaviour. Birds, fish, salamanders, turtles, snails, bees, ants and many other animals use the Earth's magnetic field as one cue for orientation, migration and homing [see Deutschlander *et al.* 1999 for a review]. Interestingly, the biophysical mechanism of such a pervasive phenomenon remains largely unknown [Edmonds, 1996; Deutschlander *et al.* 1999; Ritz *et al.* 2000; Wiltschko *et al.*, 2002]. Less well known, but perhaps just as important, are the behavioural effects of extremely low frequency magnetic fields oscillating from between zero and 300Hz. Reproducing the positive results in this area has been difficult with mainly failures in replication, either pointing to the subtlety or simply the absence of a true effect. One of the more sensitive systems in the body to ELF MF exposure appears to be the pain system, with effects appearing independent of phylogeny. From snails to human subjects, there finally appears to be a replicable effect of weak, ELF MF exposure, that although subtle, appears to be reproducible within and between laboratories. It has now been reported, by three independent laboratories, that such fields strongly influence opioid-like behaviour in animals as diverse as rodents, pigeons, snails [Kavaliers *et al.* 1986; Betancur *et al.* 1994; Del Seppia *et al.* 2000; Kavaliers and Ossenkopp 1991; Papi *et al.* 1992; Thomas *et al.* 1997a,b, 1998; Jeong *et al.*, 2000] and perhaps even humans [Papi *et al.* 1995; Sartucci *et al.* 1997].

1.1. Scope of the Pain Problem

It is hard to estimate the economic/social impact of acute and chronic pain. Clearly, almost all humans suffer from pain and almost all humans seek treatment, particularly through pharmaceuticals [Jones and Wall, 1989]. The prototype agents used for severe pain management have been opioids such as morphine and codeine. However pharmaceuticals, by their very nature, have both cognitive and physiological side effects which can be severe. Hence, it is not surprising that patients experiencing pain on a daily basis seek out complementary and alternative treatments for their pain experience.

1.2. A Brief Historical (and Modern) Perspective on the Use of Magnetic Fields

The use of magnets and magnetic fields to treat pain is an ancient practice, steeped largely in superstition and belief, rather than sound, scientific data [Basford, 2001; Persinger, 1988]. This belief in the power of magnets continues unabated. One only has to examine the massive proliferation of internet sites that promote and sell magnets to treat every malady

known to humanity. A close examination of many of these websites indicates that most of the 'proof' of the effectiveness rests on a single cited study. This is unfortunate, as what has previously been seen as suspect has been parlayed into a respectable, reproducible effect. The continued growth of the pseudoscience associated with magnets only interferes with the acceptance of some very fine studies that have demonstrated that weak, ELF MFs seem to affect the processing of nociceptive behaviors and perception.

If the use of magnetic fields as therapeutic agents is to ever become a useful health tool to combat pain, what will be required to overcome this long and often erroneous history? In a recent paper by McLean *et al.* [2000], they sketch a number of caveats that should be undertaken to increase the validity and reliability associated with pain and MF studies. Taking a cue from pharmacology, if magnetic field therapy is to be embraced by the medical community and regulatory agencies as a whole, then a) magnetic fields must be properly characterized with the known depth of field penetration into tissue b) biological effects of magnetic fields should first be demonstrated in animal and cell models before introduction to human models c) effects of magnetic fields in human populations should be demonstrated first in pilot studies so that positive findings can be explored in greater depth within more controlled studies and d) larger controlled studies should include placebo and possibly the addition of a second magnetic field condition.

1.3. Chapter Outline and Purpose

Our laboratory's mission is to develop effective and efficacious specific pulsed magnetic field designs, initially for the treatment of pain. Our underlying goal is to have a research program which is both practical (e.g. experiment on human subjects) and also basic (i.e. directed towards discovery of mechanism). Knowledge of the mechanism(s) by which time-varying magnetic fields elicit behavioral and physiological responses will provide us with the tools to design specific magnetic field pulses and delivery systems which will be used for chronic and acute pain treatment without the unwanted side-effects often associated with chemical/pharmaceutical therapies. Over the last twenty years we have had the following specific objectives:

a) Establish that time-varying magnetic fields can affect behavioral and physiological responses associated with the opioid system.
b) Show that this is a scientifically valid result that is reproducible in more than one laboratory.
c) Having established a reproducible effect, use it to determine mechanism(s). In general, mechanism(s) involve(s) how and where. For us, "how" has meant the initial detection mechanism and how it is then coupled to the whole animal to produce a behavioral or physiological response. "Where" has meant seeking the molecular site of action to be established in animals and human cell lines.
d) Use these discovered mechanisms to predict which combination of magnetic fields will elicit the desired, i.e. analgesic, effect.
e) Establish whether there are side effects by using animal behavioral experimental protocol, which tests for a wide range of behaviours.
f) Scale from animal results to strategies for treating humans. Because of the cost and awkwardness of whole body exposure for humans, as has been used almost

exclusively in animal studies, we need to discover the human anatomical sites to be exposed for magnetic field therapy. We need to develop approaches to do this which are different than the ones we have had available in animals. Our best guess at this time is to use passive mapping of endogenous electrical and magnetic field activity using electro and magnetoencephalograpy (EEG and MEG) as well as active imaging methods, such as positron emission tomography (PET) and perhaps functional magnetic resonance imaging (fMRI).

g) Perform limited clinical trials to establish effects in humans (both normal controls and patients experiencing pain) and optimize the exposure parameters.
h) Perform multi-center clinical trials to validate the technology in conventional medicine, and establish third-party payment protocols.
i) Establish widespread availability of the technology through intellectual property protection and commercialization.
j) Use a significant fraction of the commercial profits to fund continuing research and development of specific pulsed magnetic field based therapies including, but not limited to: the treatment of chronic and acute pain, affective disorders and for cognitive counseling aids.

2. PAIN, NOCICEPTION, AND THE OPIOID SYSTEM

A comprehensive review of pain, nociception and the opioid system is obviously far beyond the scope of this review. What will be provided is a brief description of the basic concepts in pain research from a behavioural/systems perspective, concentrating on aspects of the pain system that have been shown to be most affected by exposure to ELF MFs. [For a more complete review of pain see Wall and Melzack, 2000].

The current definition of pain, according to International Association of Pain (IASP), is that pain is "An unpleasant sensory and emotional experience associated with actual or potential tissue damage or described in terms of such damage". Pain can also be described as nociceptive (arising from "physiological" stimulation of nociceptors) or neurogenic (arising from "pathological" lesions of the "pain pathway"). Acute pain is usually nociceptive, while chronic pain is usually neurogenic [McGrath and Rice, 1999]. The main function of the pain pathway is to detect potentially noxious stimuli and protect against tissue damage. Activity in the pain pathway (nociception) can be modulated by the nervous system. Therefore, pain is not necessarily a consequence of nociception. The electrical and chemical stimulation of several brain structures has confirmed the existence of descending pathways which exert an anti-nociceptive effect upon dorsal horn neurons. These effects are closely linked to opiate analgesia and autonomic regulation [McGrath and Rice, 1999].

2.1. Pain and Nociception

Pain is a unified, multidimensional experience. It is generally divided into the following categories: sensory-discriminative, affective-motivational and cognitive-evaluative [Melzack and Casey, 1968]. Experimental evidence has supported the notion of multiple parallel pain pathways representing different aspects of the pain experience. It is important to emphasize the temporal differences in the three aspects reinforcing the different pathways

and regions involved. Sensory pain occurs in a millisecond time scale, with affective-motivational occurring in the millisecond to second range and cognitive-evaluative is in the seconds range. Recent evidence suggests that there is a 'double dissociation' between the two systems responsible for the generation of sensory and affective pain [Hofbauer *et al.*, 2001].

In general, the pain experience can be divided into the following categories of *transduction*, *transmission, central representation* and *modulation* [Chapman and Nakamura, 1999]. The dissociation between sensory and affective pain occurs with the projection from the spinal cord to the cortex. The first step of the pain experience consists of the *transduction* of a tissue trauma energy into neural activity via nociceptors. Nociceptors are found in the skin, muscle, joints, tendons and visceral organs and in many other regions. The information from nociceptors travels via A and C fibers depending on the type of noxious stimuli. The A-fibers are thinly mylenated and travel quickly (*ca* 4–44 m/sec) and transduce thermal and mechanical stimuli, while the C fibers are unmylenated and travel more slowly (0.5–1 m/sec) and are multimodal, transducing various high intensity mechanical, thermal and chemical stimuli. The second step is the *transmission* of the nociceptive afferents to the spinal cord. The dorsal horn of the spinal cord, receives the information from projection neurons that will target cortical regions, facilitative interneurons that relay information to projection neurons and inhibitory interneurons that modulate the flow of information to the cortical regions. The third step refers to the *central representation* of the pain experience. This mostly consists of information relayed from the spinal cord through the thalamus, a large group of distinct neurons that widely project information to the limbic and cortical regions. For the sensory-discriminative aspect, the medial and ventrobasal thalamic nuclei receive nociceptive afferents that are processed, discriminated and then projected to the somatosensory cortices I and II. Another pathway for affective experience projects from the spinal cord to the parabrachial nucleus and from there projects to the amygdala and hypothalamus. The fourth step is the *modulation* of the pain. This refers to how the cortex and spinal cord are able to reduce or inhibit the flow of nociceptive information. There are a number of descending pathways from cortex to spinal cord that will act to 'gate' the noxious input to the dorsal horn. The periacqueductal grey (PAG) has a key role in the modulation of spinal cord activity. The PAG receives information from somatosensory cortices, insula and the anterior cingulate cortices (ACC) and is notably activated during the experience of acute pain [Rainville, 2002; Hsieh *et al.*, 1996].

Whereas the sensory-discriminative portion of pain could be described as a more objective measure of pain, as it is a factor of intensity, where the pain is transduced, transmitted and centrally represented in terms of intensity [Treede *et al.*, 1999], the affective-motivational component of the pain describes the quality or 'feel' associated with it [Chapman and Nakamura, 1999]. Pain is an emotional experience, usually a profoundly negative one, and has a definite 'feel', what philosophers have termed 'qualia'. Everyone understands what pain 'feels' like. Emotions are a complex mix of physiological arousal and hedonic labeling of experience, consisting magnitudes of positive/negative and high/low intensity. The intensity of emotional experiences are most closely associated with arousal and the autonomic nervous system. The labeling of the experience is due in part to the past experience of the organism and the current state of the external environment. The pathways responsible for the generation of the affective response are similar to the sensory pathways, but differ in terms of projection from the spinal cord with afferents mainly going to the limbic system. The affective pain portion is mediated cortically within a distributed network of limbic and

paralimbic regions that are responsible for the central autonomic nervous system (ANS) [Price, 2000; Rainville, 2002], which include the amygdala, hypothalamus, anterior cingulate and insular cortices. For the pain experience, the sympathetic portion of the ANS is most important, as it is the system that is responsible for 'fight or flight'. Sympathetic responses are governed in part by the hypothalamus, periacqueductal grey, amygdala, midbrain reticular formation; in response to tissue damage, the ANS increases heart rate, respiration, muscle tone and pupil dilation. This has recently been considered to underlie the early portion of the affective experience, as the autonomic activation leads to a defense response and would occur somewhat automatically [Price, 2000]. A second mechanism would consist of the 'integration' of the sensory and qualitative aspects, likely occurring in the posterior parietal, anterior cingulate and insular cortices receiving from the somatosensory cortices, S1 and S2. Of the listed structures, the ACC is considered to be of 'premier' importance for the integration of attentional and evaluative function with emotional experience [Devinsky *et al.*, 1995; Frankenstein *et al.*, 2001; Sewards and Sewards, 2002].

The third portion of the pain experience is the cognitive-evaluative. This is almost purely a central phenomenon, where pain itself can be modified by expectations and situational variables [Petrovic and Ingvar, 2002]. Three cognitive-evaluative experiences which result in the modulation of pain include attention and both placebo and hypnotic analgesia.

One of the most studied psychological variables associated with pain modulation is attention. It is well known that by simply not attending or being distracted from a painful stimulus can reduce the intensity of the experience [Villemure and Bushnell, 2002]. One interpretation of this phenomenon is that pain itself 'demands' attention and by dividing attention or allocating attentional resources elsewhere, the intensity of the pain is reduced. Current evidence suggested a significant role of the periaqueductal grey (PAG) in the attentional modualtion of pain [Tracey *et al.*, 2002].

Considering two of the more 'mysterious' modulators of the pain response, it is believed that placebo analgesia involves a degree of conditioning, expectations and suggestions to the person in pain, where an inert substance, such as a pill or a cream can induce a strong analgesic response to pain [Petrovic *et al.*, 2002]. While, hypnotic analgesia is the result of suggestions by the experimenter that the upcoming stimuli they will perceive will not be painful or that they should 'reinterpret' a painful stimulus in a non-painful manner. Without delving to far into proposed mechanisms which are a discussion unto themselves [Price and Barnell, 2000], it appears that hypnotic suggestions do have psychophysiological effects upon human pain due in part to a proper 're-evaluation' of a painful stimulus. Placebo analgesia is no less complex, as decidedly hard to define concepts such as 'belief' come into play [Brody, 1997]. Most importantly, is that a subject's past history and belief (or disbelief) in the 'healing' process can effectively reduce or even increase subjective pain responses [Spiegal, 1997]. There are numerous cognitive variables that will also affect pain perception, such as personality. Subjects classified as 'hostile' or 'difficult' often tend to 'suffer' more, meaning their affective dimension of pain seems vastly greater than those subjects displaying more effective coping mechanisms. Other cognitive factors include socio-cultural roles including gender, ethnic/cultural, spiritual/religious and age of the subject can all significantly influence the pain response. Similarly, as with placebo and hypnotic analgesia, the concept of belief remains very important for the cognitive-evaluative dimension of pain.

2.2. Acute vs. Chronic Pain

Most of the pain that has been discussed thus far has been the 'acute' forms. Pain researchers usually distinguish 'acute' from 'chronic' pain. Chapman and Stillman [1996] define chronic pain as a severe persisting pain of moderate or long duration that disturbs normal living, ceases to provide adaptive function and degrades health and functionality. Any persistence of pain which accompanies and outlasts inflammatory tissue or nerve damage, characterized by its spontaneous nature and is not elicited by external stimulation can be considered a 'chronic' pain. [Millan, 1999] Furthermore, the condition can be noted by the presence of hyperalgesia (the increase in pain sensitivity elicited by a noxious stimuli) and allodynia (increase in pain elicited by a normally benign stimulus) [Millan, 1999]. In contrast to acute pain, chronic pain is thought to serve no physiological or evolutionary purpose for the organism. Thus it is purposeful to divide chronic/acute pain into pathological vs. physiological forms.

2.3. Opioid System

What is of greatest interest with respect of ELF MFs has been the opioid system. As will be discussed later, most of the experiments indicating an influence of magnetic fields upon pain processing has been within the opioid system. Endogenous opioids are ubiquitous and present in varying densities with the central, peripheral and autonomic nervous systems of both animals and humans [Drolet *et al.*, 2001]. Opioid receptors are involved with many other functions and behavioural responses aside from pain, such as reinforcement and reward, neurotransmitter release and modulation of autonomic and endocrine functions [for an extended review see Vaccarino *et al.*, 1999].

Like pain itself, there are various types of opioids that suggest it is not a unitary system as it has different subtypes each having different functional significance. There are three families of endogenous opioids, enkaphalins, dynorphin and endorphins and there are three types of receptors through which opioids exert biological effects, the mu, delta and kappa opioid receptors. Although all three receptor types exert some analgesic/antinociceptive effect, their individual properties distinguish them.

Mu opioid receptors have been found in widespread CNS areas including cerebral cortex, limbic system (amygdala), hypothalamus, thalamus, brainstem and dorsal horn of the spinal cord. Delta and kappa opioids have been found in the cerebral and cerebellar cortices, thalamus, hippocampus and spinal cord. Morphine is the prototypical mu-opioid analgesic that serves as the drug against which all others have been compared [Zubieta *et al.*, 2001]. A number of studies have demonstrated that opioids from all three classes can modulate NMDA (N-methyl-D-aspartate) receptors, the main excitatory receptor in the CNS, as both opioids and NMDA receptors co-localize in many CNS areas including the dorsal horn [Mao, 1999]. A number of studies indicate that activation of NMDA receptors can likewise modulate the effect of opioid related antinociception, however, these results are conflicted as it isn't completely clear how NMDA antagonists increase and decrease opioid antinociception. This avenue of thinking precipitated a special issue in Pain Symptom and Management entitled 'Enhancing Opioid Analgesia with NMDA Antagonists' [Price *et al.*, 2000].

3. ELF MFs AND NOCICEPTION IN ANIMALS

3.1. Studies Using Rotating Magnets and 60 Hz fields

Studies utilizing animal models are often undertaken to evaluate new therapeutic medical procedures. In fact, it is often impossible to convince an institutional review board and raise sufficient funds to conduct evaluations in human subjects without positive results in animal models.

One of the first to establish the definitive link between ELF MF exposure and analgesic processing in animals was Kavaliers *et al.* [1984] establishing that exposure to a time-varying ELF MF of 0.5 Hz (0.2–0.4 mT) abolished the enhanced nocturnal analgesic response to morphine in mice. Over the course of a number of publications, it was determined that this effect could be replicated [Kavaliers and Ossenkopp, 1985ab], was evident in different strains

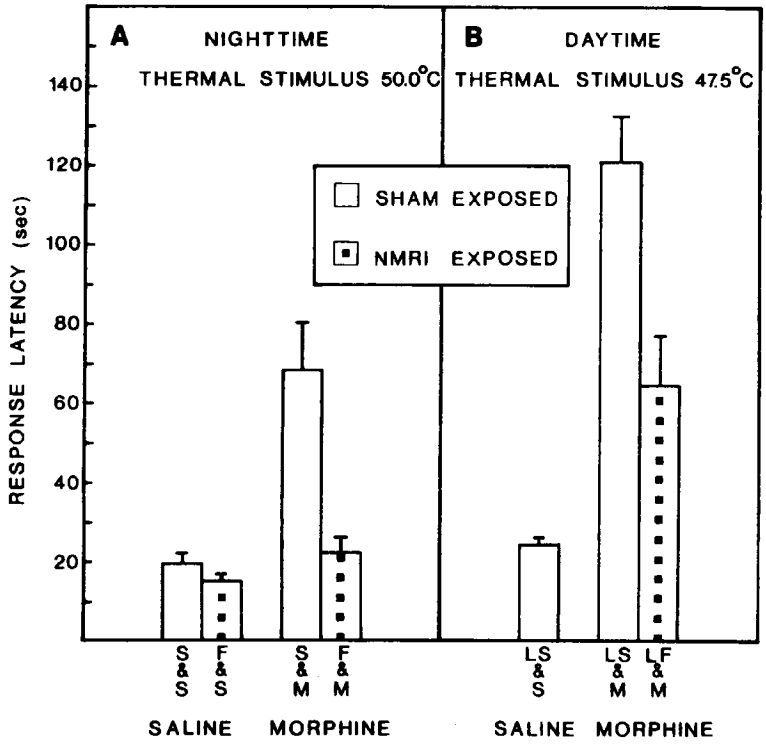

Figure 1. Mean response latencies for each of the groups tested during the nighttime (panel A) or the daytime (panel B) for reactivity to a thermal stimulus. During the nighttime morphine injection produced a pronounced analgesia effect in the sham imaged mice but not in the mice exposed to the NMRI procedure. During the daytime the NMRI exposure attenuated, but did not abolish the morphine-induced analgesia. The saline injected groups are indicated by the lower S and the morphine ones with the lower M. Sham exposed groups correspond to the upper S and MRI exposed by the upper F. The letter L before S or F indicate experiments done during the mid-light phase. The error bars are standard errors.

Taken with permission from: Ossenkopp K-P, Kavaliers M, Prato FS, Teskey GC, Sestini E, Hirst M: Exposure to nuclear magnetic resonance imaging procedure attenuates morphine-induced analgesia. *Life Sci* 1985; 37:1507–1514.

of mice [Kavaliers and Ossenkopp, 1985c] and different types of magnetic fields, such as the pulsed ELF MFs associated with magnetic resonance imaging [Ossenkopp *et al.*, 1985] and seemed to be light dependent [Kavaliers and Ossenkopp, 1987], a finding supported by Betancur *et al.* [1994] who found a light-dependent effect of magnetic field exposure on stress-induced analgesia in mice. It was also determined that ELF MF exposure could reduce endogenous stress-induced analgesia in mice [Kavaliers and Ossenkopp, 1986a], a finding also replicated by Del Seppia *et al.* [1995] who demonstrated that stress-induced analgesia in the pigeon was inhibited by ELF MF exposure.

The involvement of the opioid system in this effect appears to be a valid and reliable observation, further demonstrated by Kavaliers and Ossenkopp [1986b] demonstrating that the magnetic field exposure differentially inhibited mu, delta, kappa and sigma opiate-induced analgesia in mice. The general effect of ELF MF inhibition of opioid-mediated analgesia was also found in the common land snail, *Cepaea nemoralis* [Kavaliers and Ossenkopp, 1988], indicating a robustness of this effect across different phylogeny. Further support for the involvement of ELF MFs in opioid-mediated analgesia was recently put forth by Jeong *et al.* [2000], who found that exposure to MFs inhibits the increase of pain thresholds at night-time and produces hyperalgesia at day-time with the involvement of opioid and benzodiazepine systems.

The involvement of the calcium ion in this ELF MF mediated effect was described by Kavaliers and Ossenkopp [1986c] who found that a brief exposure (60 min) to a 0.5 Hz rotating magnetic field (1.5–90 G) significantly reduced the day-time analgesic effects of morphine, while injections of a calcium chelator (EGTA) blocked these effects and administration of the calcium ionophore (A23187) potentiated the inhibitory actions. These results suggest that exposure to magnetic stimuli affects the functioning of calcium channels and the distribution of calcium ions, thereby, altering the effects of opiates. Kavaliers *et al.* [1991] sought to examine the effects of protein kinase C (PKC), a calcium/diacylglycerol/phospholipid-dependent protein kinase, on opiate-induced analgesia and its involvement in mediating the inhibitory effects of exposure to magnetic fields and found that morphine-induced antinociception was reduced in dose-related manner by the PKC activator, SCH-9. Exposure of snails for 2 h to a low intensity (1.0 gauss rms) 60-Hz magnetic field also reduced morphine-induced analgesia. The inhibitory effects of the 60-Hz magnetic field on morphine-induced analgesia were significantly reduced by the PKC inhibitors, H-7 and H-9, and significantly enhanced by the PKC activator, SC-9. The non-specific protein kinase inhibitor, HA-1004, and the preferential calmodulin inhibitor, W-7, had no significant effects on either morphine-induced analgesia or the inhibitory actions of exposure to the magnetic fields. These results suggest that: (1) PKC has antagonistic effects on opiate-mediated analgesia in the snail, *Cepaea nemoralis*, and (2) that the inhibitory effects of magnetic fields on opiate-induced analgesia involve alterations in PKC.

Until this point, it was apparent the ELF MF exposure reduced morphine-induced analgesia, and the effect was mediated in part by calcium and protein kinase C, but the utility or ecological advantage posed by such an effect was not apparent. The possible therapeutic value of using ELF MFs to reduce pain was demonstrated by Kavaliers and Ossenkopp [1993]. They considered that animals repeatedly injected with the opioid antagonist, naloxone, acquire a hypoalgesic response to thermal nociceptive stimuli. Snails received daily injections of naloxone followed by measurements of thermal nociceptive sensitivity developed hypoalgesia. Daily brief (30-min) exposures to a weak 60-Hz magnetic field (1.0 gauss

or 0.1 mT), which acutely antagonize opioid-mediated nociception and antinociception in a manner comparable to that of naloxone, also led to the expression of a hypoalgesic responses. They concluded that opioid antagonist-induced thermal hypoalgesia may be a basic feature of opioid systems and this naloxone- and magnetic field-induced 'analgesia' may be consistent with either a facilitation of aversive thermal conditioning and/or antagonism of the excitatory, hyperalgesic effects of low levels of endogenous opioids.

3.2. Pain and the Zero Magnetic Environment

A number of recent studies in our laboratory have focused upon the behavioural effects of exposure to a shielded magnetic environment. Exposure to 0.5 Hz rotating magnetic fields, 60 Hz magnetic fields and ELF magnetic fields used in magnetic resonance imaging procedures reduces analgesia induced by both exogenous opiates (e.g. morphine) and endogenous opioids, such as those induced by stress. Interestingly, stress induced analgesia was similarly reduced in mice which had been kept in a μ-metal box, an observation first noted by Del Seppia *et al.*, [2000]. They found that after 120 minutes in a μ-metal box that included a 30 minute period of stress-inducing confinement, the mice did not show stress induced analgesia as compared to experiments carried out in a wooden box of identical dimensions. Using Del Seppia's apparatus, we have demonstrated that this effect is not from the approximate 100-fold reduction in the static magnetic field as the effect (i.e. the attenuation of stress-induced analgesia) does not occur when mice are placed in a wooden box in which the static magnetic field has been similarly attenuated using large, external Helmholtz coils [Choleris *et al.*, 2002]. This suggests that the mice might be responding to the shielding of the weak, ambient-time-varying magnetic fields, which were not zeroed by the Helmholtz coils. Alternatively, the mice could be sensitive to the μ-metal box shielding of the ambient electric fields.

We tested this latter hypothesis by placing mice in a copper box specifically designed to attenuate the ambient electric fields but not the static and ELF magnetic fields. Individual free-moving male Swiss CD1 mice were randomly assigned to 1 of 4 experimental groups. In group 1, mice were placed in a non-conductive fiberglass box and exposed to ambient magnetic and electric fields. For the second group, mice were placed in a μ-metal box and shielded from both ambient magnetic and electric fields (μ-metal). The third group of mice were placed in a non-conductive opaque fiberglass box and placed into the center of Helmholtz coils used to zero the static magnetic field. The fourth group of mice were placed in a copper box which attenuated the ambient electric field but not the ambient magnetic fields. For all mice, we measured their initial nociceptive responses (measured as the latency of foot-lifting or licking) for a pre-exposure baseline Mice were then placed into their respective boxes for 90 minutes and allowed to move freely. After exposure, mice were then immobilized for 30 minutes inside a modified translucent polypropylene 50ml centrifuge tubes inside their respective boxes. The nociceptive responses of mice after restraint stress were measured for a post-exposure reading (Figure 2). Statistical analysis of the data shows: that latency times significantly increased for animals in the control box. As has been found previously, stress-induced analgesia did not occur for mice in the μ-metal box. Also previously demonstrated was that zeroing the static magnetic field using the Helmholtz array had no effect on stress-induced analgesia. Most importantly though, zeroing the electric field had no effect on analgesia. If the attenuation of stress-induced

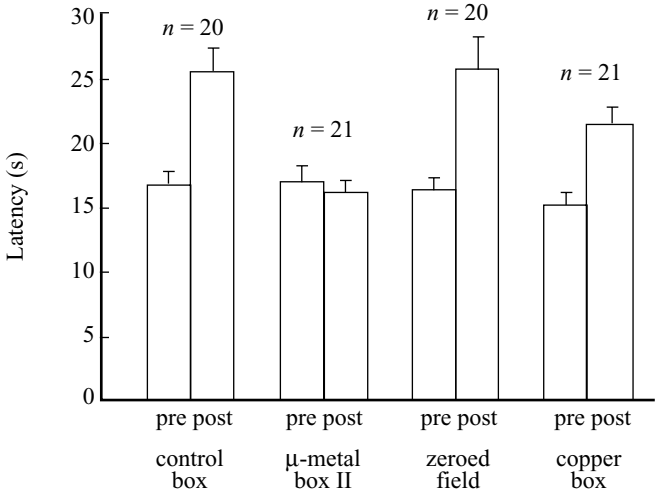

Figure 2. Replicate of μ-metal box effects and control for electric field effects (copper box). Mean ($\pm$SEM) latencies (sec), sample sizes, results of the repeated measure ANOVA and significant differences between post values are represented. Elimination of the electric field (copper box) did not reduce stress induced analgesia as occurred when mice were placed in the μ-metal box. The overall ANOVA revealed significant main effects of latency ($F_{1,78} = 55.57$, $p = 0.0001$) and exposure ($F_{3,78} = 3.70$, $p = 0.015$) and of their interaction ($F_{3,78} = 8.90$, $p = 0.0001$).

Taken with permission from: Choleris E, Del Seppia C, Thomas AW, Luschi P, Ghione S, Moran GR, Prato FS: Shielding, but not zeroing of the ambient magnetic field induces stress-induced analgesia in mice. *Proc R Soc Lond B Biol Sci* 2002; 269:193–201.

analgesia by μ-metal box shielding is not a result of the attenuation of the static magnetic field or the electric field, then it may be due to the shielding of the weak, ambient ELF fields. If this is correct, it indicates that mice demonstrate sensitivity to weak, ambient ELF MFs (which in our experiment were of the order of <0.1 μT rms, 60 Hz). This figure shows the elimination of the electric field (copper box) did not reduce the stress-induced analgesia that occurred when mice were placed in the μ-metal box. This suggests that mice demonstrate altered behaviour when they are shielded from ambient ELF magnetic fields of the order of 0.1 μT rms. The overall ANOVA revealed significant main effects of latency ($p < 0.001$), exposure ($p < 0.02$) and of their interaction ($p < 0.001$).

In our most recent experiment, [Desjardins *et al.*, 2002], the objective was to determine if daily repeated exposures of mice to the environment produced by a μ-metal box would induce analgesia. Adult male Swiss CD1 mice [Charles River, Canada] were placed in an opaque Plexiglas^{TM} lined μ-metal box or an opaque Plexiglas^{TM} box (sham condition) for 1 hour a day for 10 consecutive days. The μ-metal box attenuates ambient magnetic fields from 0 to 2500 Hz by a factor of 125 at 0 Hz down to 8.6 at 2500 Hz [Choleris *et al.*, 2002]. Nociception was measured as the latency of a foot lifting/lick to an aversive thermal stimulus ($50 \pm 0.5^{\circ}$ C) before (pre) and immediately after (post) placement in the boxes. Two experiments were conducted, one in which thermal latency was tested on each of the ten days and one in which testing was only performed on days 1, 5 and 10 but exposure was for 10 consecutive days as in the first experiment. Post "exposure" latency values

were normalized (post/pre) to pre-exposure values. Statistical analysis showed that those mice exposed to the μ-metal box showed a significant increase in latency as compared to the mice in the control condition. In the first experiment, statistical analysis showed a significant interaction between days of exposure and exposure condition. The latency times of the μ-metal exposed group dropped to 80% of pre-values after the first exposure, which corroborates former findings [Choleris *et al.*, 2002] and then increased to 160% as compared to pre-values after exposures of days 3, 4, and 5. By day 10 post values were not different from pre-values. These results were not seen in the control group. Results of the second experiment confirmed those of experiment one showing again a decrease in post latency values on day 1 (70% of pre-values), increase on day 5 (180% of pre-values) with a return to pre-latency values on day 10 [Desjardins *et al.*, 2002].

These experiments further suggest that shielding from ambient magnetic fields affects opioid related behaviours in a manner similar but not identical to effects from exposure to increased ELF MFs. The initial reduction on day 1 was consistent with previous data [Choleris *et al.*, 2002] as was the induction of analgesia on day 5 [Kavaliers and Ossenkopp, 1993]. Further experiments are needed to compare and contrast the effects of ELFMF exposure and ELFMF shielding on opioid function.

3.3. Studies Using Pulsed Magnetic Fields

The aim of developing a specific pulsed MF was to examine more the 'coupling' mechanism of magnetic field characteristics to biology and behaviour, and investigate the potential differential response of clinical populations. The assumption being that endogenous frequencies may be specific for certain tasks and that a specific pulsed field can match or entrain such a specific endogenous frequency. If we make the assumption that some theory or combination of theories of MF/biological detection explains the initial interaction, then we need to also understand the coupling or effect of that detection [Walleczek, 1995]. Hence, 'coupling' will result in biophysical events between this initial detection and the final physiological/behavioural response. This biological adaptation or alteration could then be related to an observable behaviour.

We initially demonstrated the efficacy of using weak, pulsed ELF MFs in the common snail *Cepaea nemoralis* [Thomas *et al.*, 1997ab]. We found fifteen minute exposures to a specific magnetic field ± 100 μT both increased enkephalinase inhibitor induced opioid analgesia and induced analgesia in untreated snails. Injection of the prototypic opioid antagonist naloxone, attenuated, but did not completely block, the pulsed magnetic field induced analgesia (Figure 4). Two other pulsed waveform designs failed to induce analgesia in untreated snails as did a pure 60 Hz sinuosoidal MF set to the same intensity and amplitude. These findings suggest that specific magnetic field exposure designs may be tailored to produce significant behavioural effects including, but certainly not limited to, the induction of analgesia [Thomas *et al.*, 1997a]. This also suggests that besides the initial detection mechanism, the coupling of detection to the behavioural response may be dependent on the higher order frequencies found in the pulsed field design (See Figure 3).

Further experiments with this pulsed MF design [Thomas *et al.*, 1997b] found that this analgesia was in part opioid mediated as it was significantly reduced, but not eliminated by the prototypic opiate antagonist, naloxone; the mu opioid receptor directed antagonists, naloxazine or beta-funaltrexamine, and the delta opioid receptor directed antagonists,

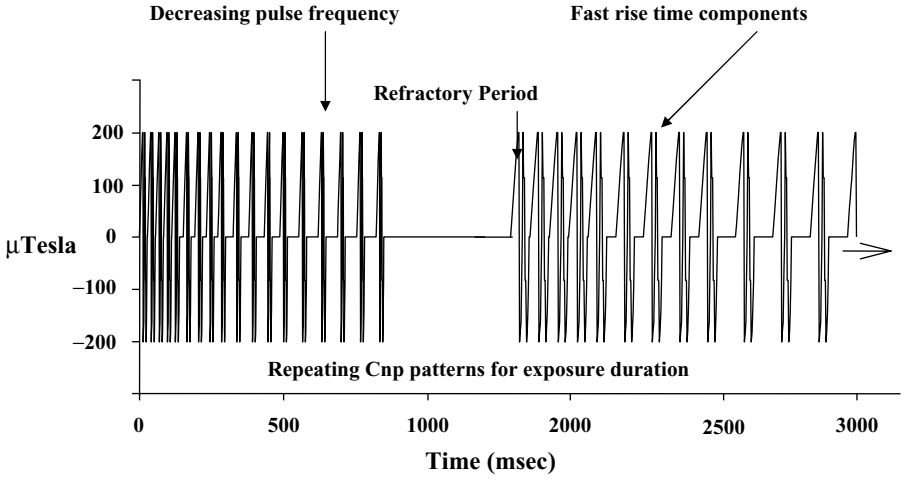

Figure 3. The complex neuroelectromagnetic pulse (Cnp) incorporates three basic components: (i) the pulse sequence starts at a specific set of frequencies; (ii) the frequency of the pulse is then either decreased, or increased, to alter the entrained endogenous system in a preferred direction; (iii) a refractory period allows for a partial stabilization of endogenous frequencies. The Cnp sequence is continually repeated during the exposure period.

Taken with permission from: Thomas AW, Kavaliers M, Prato FS, Ossenkopp K-P: Pulsed magnetic field induced "Analgesia" in the land snail, *Cepaea nemoralis*, and the effects of μ, δ, and κ opioid receptor agonists/antagonists. *Peptides* 1997; 5:7-3–709.

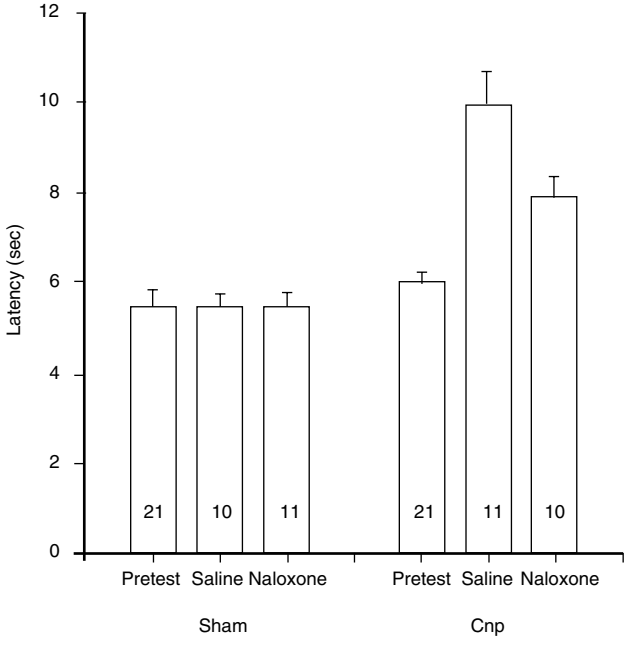

Figure 4. Response latencies of sham and Cnp exposed snails that were injected with either the opiate antagonist, naloxone (1.0 μg in 1.0 μl saline) or saline vehicle (1.0 μl) prior to the 15 min exposure. Response latencies recorded before (pretest) and after sham or exposures are also shown. Error bars represent SEM.

Taken with permission from: Thomas AW, Kavaliers M, Prato FS, Ossenkopp K-P: Antinociceptive effects of a pulsed magnetic field in the land snail, *Cepaea nemoralis*. *Neurosci Lett* 1997; 222:107–110.

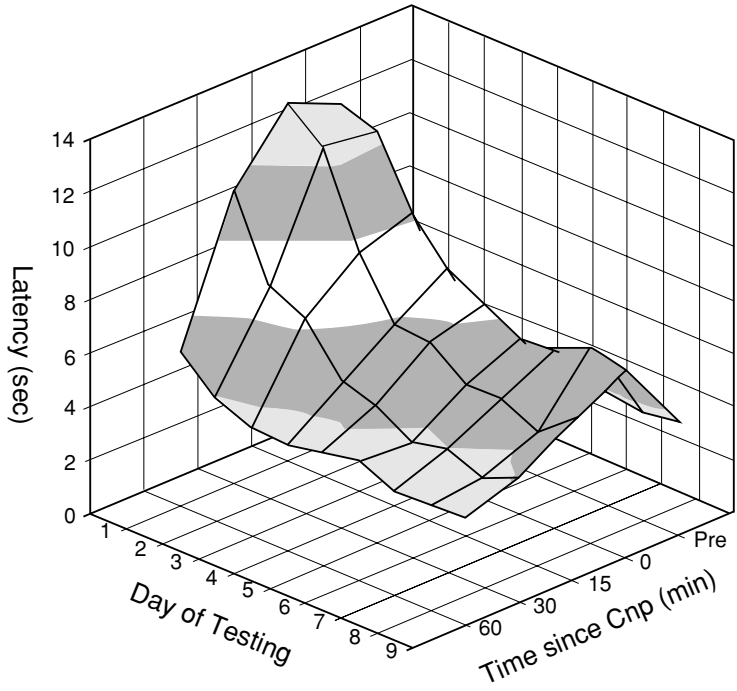

Figure 5. Effects of a 30-min daily repeated acute exposure to a specific pulsed magnetic field (Cnp) on the thermal (40 °C) response latencies of individual hydrated snails ($N = 30$), shown in 3-D perspective. Response latencies were recorded prior to (Pre) and after (0. 15, 30, and 60 min) exposure.

Taken with permission from: Thomas AW, Kavaliers M, Prato FS, Ossenkopp K-P: Analgesic effects of a specific pulsed magnetic field in the land snail, *Cepaea nemoralis*: Consequences of repeated exposures, relations to tolerance and cross-tolerance with DPDPE. *Peptides* 1998; 19:333–342.

naltrindole-5′-isothiocyanate or ICI 174,864. However the pulsed MF induced analgesia was unaffected by the kappa opioid receptor directed antagonist, nor-binaltorphimine. The delta 1 and delta 2 opioid receptor directed agonists DPDPE, ([D-Pen2,D-Pen5]enkephalin) and deltorphin, (D-Ala2,Glu4]), respectively, also had significant differential analgesic effects, supporting a functional delta opioid receptor mediated enkephalinergic mechanism in the snail. These results suggest that this specific pulsed magnetic field elicits significant analgesic effects through mechanisms that involve both delta opioid and to a lesser extent mu opioid receptors. This result was replicated further in snails [Thomas *et al.*, 1998a] and also demonstrated in mice [Thomas *et al.*, 1998b].

4. ELF MFs AND PAIN IN HUMANS

As stated recently by Valbonna and Richards [1999], there is a definite lack of well designed studies examining the effects of magnetic fields upon human pain responses. The question of what constitutes a ‘good’ study is difficult to quantify, however, if the

investigation is randomized, double-blind and placebo controlled with careful subject selection and well-defined clinical populations then the study is often considered 'good'. Unfortunately, it is often these very qualities that are absent when examining the effects of ELF MFs upon human pain. Furthermore, there are fewer studies examining ELF MF effects on pain where the goal of the study is an investigation of effect, rather than examining strict therapeutic benefits. While the pursuit of the potential therapeutic benefits of this research is certainly laudatory, it seems that fewer studies have appeared to replicate the many different animal experiments assessing the pain-MF relationship.

Most of the recent work concerning the use of ELF MFs as a therapeutic agents is characterized by the use of static magnetic fields (0 Hz). One of the most noted studies is by Vallbona [1997], who investigated post-polio pain, a chronic pain disorder characterized by diffuse muscle, joint pain and hyperalgesia. Using a 'Bioflex' device, a cocentric arrangement of 8 magnets (intensity 300 to 500 G ∼30 to 50 mT), subjects were randomly assigned to wear either the active or sham device on their person for 45 min. Subjects who wore the active device reported much less pain post-exposure compared to those who received a sham device. Further studies using different arrangements of static MFs have been found to be effective reducers of clinical pain in rheumatoid arthritis [Segal *et al.*, 2001] and in non-specific chronic pain [Holcomb *et al.*, 2000]. Sadly, the Vallbona *et al.* [1997] study, despite being a proper sham-controlled, blinded study, is most oft-cited by internet promoters of magnets as a 'cure-all' for many diseases and ills. What is required are more replications of results as well as an increased level of vigilance in how one's work is being represented.

In examining the effects of ELF MF exposure on nociception, Papi *et al.*, [1995] investigated pain perception (as defined by sensory thresholds) during MF exposure, and found that the dental sensory threshold was significantly reduced post-exposure. This is a similar effect to the hyperalgesia found in previous animal studies of ELF MF exposure. Sartucci *et al.*, [1997] found that a MF exposure (+70 to –20 μT; 0.026 Hz, 0.043 Hz and 0.067 Hz presented simultaneously on three nested orthogonal coil pairs) reduced the amplitude of pain-related somatosensory evoked potentials (N150 and P250 waves) compared to sham exposure. The exposure duration was 2 hrs and the complicated nature of these fields were chosen because they had previously been shown to produce orientation disturbances in pigeons [Ioale and Guidarini, 1985], affect the activity of the endogenous opioids [Papi *et al.*, 1992] and induce hyperalgesia in humans [Papi *et al.*, 1995].

A recent study by Rollman *et al.*, [2002] has determined that previous results, using pulsed magnetic fields in animal models, can also be seen in human subjects. That is, pulsed magnetic fields' analgesic effects were noted in a small pilot study with six volunteers. In this study, the electric current needed to produce a subjective rating of 'moderate' pain was increased in both male and female subjects exposed to pulsed MFs compared to those exposed to a sham field. The current was expressed as a ratio of mAmps under exposure condition to sham condition. A ratio greater than 1 could be interpreted as an induction of analgesia (or hypoalgesia), and less than 1, hyperalgesia. Individual subjects were randomly assigned to either an analgesia-inducing MF exposure group, or postural sway altering MF group. Sham and MF exposure trials were held at least 1 week apart, and both experimenter and subjects were kept blind to the exposure conditions until the completion of the study (double-blinded). Electric current recordings at each time point (15–60 min) were divided by the averaged baseline readings taken at time point 0 and 15.

Time point 15 was a second control time point, with exposures (sham or MF) starting at time point 25. The results demonstrated a significant interaction between MF type (analgesia vs. postural sway) and exposure condition (sham vs. MF exposed). It was found that subjects exposed to the analgesia MF required significantly more current to reach a 'moderate' subjective pain rating compared to sham exposure. Furthermore, subjects exposed to the 'postural sway' MF required less current to reach the 'moderate' subjective pain rating compared to the sham exposure. This is preliminary [unpublished, Cooper *et al.*, 2001] data and should not be construed as conclusive evidence of the MF induction of hypo- or hyperalgesia.

From the above studies we are somewhat optimistic that the effect that we have seen in animals may be a replicable human effect as well. We have recently confirmed that exposure to the pulsed magnetic field design used in the Thomas *et al.*, [1997ab; 1998ab] and in Rollman *et al.*, [2002] affects the human brain electrical activity as measured by electroencephalography (EEG) [Cook *et al.*, in review]. Exposure to the pulsed MF for a 15 min duration resulted in significantly higher 8–13 Hz (alpha activity) over posterior regions of the brain compared to a sham exposure. This result is very consistent with other studies examining ELF MF and ELF modulated RF [Cook *et al.*, 2002], leading us to conclude that perhaps the higher alpha activity is a non-specific result of MF exposure, independent of intensity and frequency. Another interesting result from that study was a significant decrease in alpha activity over frontal regions post-MF exposure compared to sham exposure. This pattern of response is similar to the EEG asymmetries in response to reward and punishment that is found over frontal electrodes, with less left frontal alpha power during reward than during punishment trials [Sobotka *et al.*, 1992]. As discussed previously, the magnetic field design used in this study has been found to be affect opioid-based analgesic processes [Thomas *et al.*, 1997ab; 1998ab], which may be related to 'reward' properties. Future studies are needed to address this hypothesis.

5. POTENTIAL OF ELF MFS IN PAIN THERAPY

It has been more than a century now since the discovery of x-rays and their potential use in diagnostic medicine. Since that time it has been determined that ionizing radiation can be used to effectively diagnose disease and treat cancer. It has also been established that ionizing radiation can be detrimental to health. Can we expect a similar capability from non-ionizing electromagnetic radiation? Clearly non-ionizing EM has a place in diagnostic medicine with the spectacular growth of Magnetic Resonance Imaging (MRI) over the last two decades. Also, recognizing that radiofrequency and microwave radiation can efficiently deposit significant energy into biological samples has resulted in the presence of a microwave oven in almost every home in the developed world. If non-ionizing electromagnetic fields can produce non-thermal, non-stochastic deterministic effects we predict that there will be significant use of these fields for therapeutic and diagnostic purposes. Of course, as with ionizing electromagnetic radiation, we will have to keep in mind the potential for detrimental effects. The establishment of such effects has been and will be very important. However, success in the application to therapy is very dependent on knowledge of the initial biophysical detection mechanism and the cascade of events from this initial event to the desired therapeutic result.

Multidisciplinary independent clinical trials must be undertaken if pulsed magnetic field therapy is to be accepted into conventional medicine and become reimbursable through government and private insurance. A number of limited pre-clinical trials will need to be performed firstly in a patient population with age-matched normal healthy subjects and trained actors as controls. Normal subjects would be utilized to establish that there are no obvious analgesic-typical deleterious side effects of exposure, such as the induction of drowsiness. Having established that there are no serious side effects, patients diagnosed with painful conditions (chronic or acute, depending on the target therapy) would be studied. Currently, we have selected two diagnostic criteria for patients suffering from chronic pain: rheumatoid arthritis and fibromyalgia (diagnosed and referred to the study through random selection from the files of a local rheumatologist) [Thomas *et al.*, 2001b]. Such small groups will need to be repeated as the technology evolves. Potential sources of subjects for these pre-clinical studies could include chiropractic, complimentary or alternative medicine, or rehabilitation clinics.

Having established safety in the pre-clinical trials, application to the US FDA, and comparable technology administration entities in other countries, should be made for approval to perform the clinical trials. Upon acceptance of the clinical trial design by the FDA and IRB of at least 3 independent academic centers, the trial should begin. Note that the double blind experimental protocol will need to ensure that a suitable sham treatment is performed due to the potentially large placebo effect.

The magnetic field technology, especially the ELF pulse sequence design, must be protected [Thomas *et al.*, 1999]. If not protected, the financial resources needed to develop the technology will not likely be forthcoming, as investors would not realize suitable gains from the investment. Of course, patent protection is an expensive and on-going cost and must be budgeted for as part of the research expense. Successful commercialization will be dependent on the success of the clinical trials and the demonstrated advantage of the new magnetic field technology over existing and soon-to-be competing technologies. With proper intellectual property protection, the technology can be licensed out (e.g. our pulse sequence can be implemented on a TENS unit), leased to existing pain clinics which use magnetic field therapy and finally, developed in whole as a device by a spin-off company such as FRALEX Therapeutics Inc. (www.fralex.com). Considerable research dollars are needed to remain competitive and further develop magnetic field therapy for other uses, including treatment of such widespread ailments as anxiety and depression. It is important that significant fractions of commercialization income can be re-invested into research and development.

6. MECHANISMS

6.1. Background

What must be further elucidated to bring magnetic field therapies to an acceptable place within the medical establishment are mechanisms. While the discovery of mechanism does not preclude the advancement of a working treatment, due to the past somewhat nefarious history of magnetic field therapies, the burden of proof necessarily falls onto the bioelectromagnetics community to demonstrate the physical and biological effects.

Energy transduction mechanisms considered to date fall into two general categories involving either the tissue effects of electric fields induced by exposure to ELF magnetic

fields, i.e. an indirect effect; or the direct detection of magnetic fields by some type of tissue or cell sensor [Weaver and Astumian, 1990; Polk, 1992]. There are at least three magnetic field direct detection mechanisms that have been proposed. Detection by biological magnetite particles (biomagnetite) [Kirschvink and Walker, 1985], detection by effects on free radical recombination rates [Till *et al.*, 1998; Timmel *et al.*, 1998] and detection by "ion resonance" models which involve ion-protein complexes [Liboff *et al.*, 1987; Lednev 1996a; Blanchard and Blackman, 1994].

Biomagnetite particles are small ($\approx$100 nm) single magnetic field domain crystals of ferric oxide. If the magnetic moment of such a particle or collection of particles arranged in a row is represented by $\boldsymbol{\mu}$ and the external magnetic field by $\mathbf{B}$, then there will be a torque on the particles represented by $\boldsymbol{\tau} = \boldsymbol{\mu} \times \mathbf{B}$. Therefore, it may be possible to qualitatively test a magnetite-based mechanism in a combined B_{DC} and B_{AC} exposure by assuming that $\boldsymbol{\mu}$ will align with an applied static field (B_{DC}), and the AC magnetic field component (B_{AC}) will have its greatest effect when it is oriented at right angles to B_{DC} [Adair, 1994; Polk, 1994]. Theoretical analysis indicates biomagnetite should be sensitive down to $<0.2\mu$T for static fields [Edmonds 1996] and of the order of 5 μT for ELF fields [Adair, 1994; Polk, 1994].

Free radical formation is either followed by recombination within microseconds or diffusion from the site of formation to react at some distant site. (Free radicals are highly reactive chemical species which contain unpaired electrons and the reaction at some distant site can induce cellular damage, e.g., DNA damage.) When free radicals are formed, they are usually formed in pairs and the pairs can usually recombine by sharing the unpaired electrons, i.e. they are in the singlet State. However, before recombining, the Spin State of one member of the pair can flip, i.e. in the triplet State, and then recombination will not be possible until one of the pair of electrons has a spin that flips. Exposure to a static magnetic field can change the probability of spin flipping and can therefore affect the probability of escape and consequently the amount of tissue damage. There is evidence that a number of potentially important biological reactions that have free radical intermediaries, e.g. vitamin B_{12} [Harkins and Grissom 1994; Canfield *et al.*, 1996] can have their reaction rates affected by exposure to a static magnetic field. Since recombination reaction times are of the order of microseconds, oscillating fields in the ELF range look like a static field for the lifetime of an individual free radical [Scaiano, 1994] and for this reason, this ELF mechanism is considered fast [Engstrom, 1997]. However, oscillation in the magnetic field can cause oscillation in the recombination rates of free radicals [Eichwald and Walleczek, 1996,1998; Carson, *et al.*, 1999]. Effects observed to date have an approximate threshold of 1.5 mT [Grissom, 1995] and therefore, the role of this mechanism for fields below 1 mT remains unknown, although lower field effects have been predicted [Till *et al.*, 1998; Timmel *et al.*, 1998].

Finally, there is a class of theoretical mechanism that predicts effects caused by direct coupling to the oscillations of the exposing ELF magnetic fields. The proposal is that metal ions are trapped in a potential well produced by a protein [Engstrom, 1996; Smith *et al.*, 1987; 1995; Lednev, 1991; 1993; 1994; Blanchard and Blackman, 1994; Blackman *et al.*, 1994; 1995; Liboff, 1987]. The positively charged ion within the well is oscillating and consequently, can interact with an external magnetic field. The linearly oscillating ion can be thought of as two circulating states, one clockwise and the other anti-clockwise. These two states have the same energy if they are in a zero magnetic field. But if placed in a static field (B_{DC}), Zeeman splitting of the states occurs and then the polarization of these states can be altered by further exposure to an ELF field. The

equations to describe this system have been developed in both classical mechanics and quantum mechanics [Lednev, 1996a; Engstrom, 1996]. Adair has been a strong opponent, arguing that the potential well of the protein cannot have the desired stable properties required by the theory [Adair, 1992; 1998]. Nevertheless, there is good experimental data supporting this model in cell free systems [Lednev 1994; Markov *et al.*, 1993], in cells [Smith *et al.*, 1995; Liboff, 1987, Blackman *et al.*, 1994; 1995] and in whole animals [Prato *et al.*, 1995; 1996ab; 1997; 2000]. The theory is characterized by a double resonance in which the static field (B_{DC}) is related to the frequency (ν), i.e. $\nu = B_{DC}/2\pi \bullet q/m$ where q/m is the charge/mass of the ion in question, and the effects of the AC field (B_{AC}) are predicted by: effect $= C_1 + C_2 J_n(n \bullet B_{AC}/B_{DC})$ where C_1 and C_2 are constants and J_n is the Bessel function of order n. To date, the theory specifically accounts for only the case in which B_{AC} and B_{DC} are parallel [Engstrom, 1996]. However, we have used a simple vector combination of B_{AC} onto B_{DC} to extend the model to supposed non-parallel B_{AC}, B_{DC} conditions [Prato *et al.*, 1996b]. Recently, Bowman and Engstrom [personal communication] have proposed a more general solution for non-parallel AC and DC fields.

There is very good evidence that animals use the earth's magnetic field to orient/home/navigate [Ritz *et al.*, 2002; Wiltschko *et al.*, 2002ab, Philips *et al.*, 2002]. Ever since magnetite has been found to be central to the mechanism of orientation in some bacteria [Blakemore, 1975], some have argued that it is responsible for all such effects [Kobayashi *et al.*, 1995; Kirschvink *et al.*, 1985; Dunn *et al.*, 1995; Edmonds, 1996; Wiltschko *et al.*, 2002a; Phillips *et al.*, 2002]. But with the discovery that some animal orientation is dependent on simultaneous light-exposure at a specific wavelength [Phillips *et al.*, 1992; 1993; Wiltschko, 1993; Deutschlander *et al.*, 1999; Ritz *et al.*, 2000, 2002], two other theories have been proposed. Leask [1977] predicts that a double resonance involving optical pumping of electrons in a photosensitive retinal pigment is involved. Interestingly, this mechanism has a number of similarities to the resonance models dependent on ion-protein complexes [Prato *et al.*, 1996a; 2000]. Another theory [Schulten, 1982; Canfield *et al.*, 1996; Ritz *et al.*, 2000] has similarities to the free radical mechanism. An interesting property of these latter two mechanisms is that the target molecules are fixed to a spatially oriented biological membrane, such as rhodopsin on the retina.

A question rarely addressed is the effect of lowering the environmental magnetic field background. Would this reduction of 'noise' affect the minimum ELF MF amplitude that would be needed to produce such an effect? In fact, there are suggestions that acute shielding of the ambient geomagnetic field could have an effect [Lednev, 1996] and that chronic shielding could have a severe effect upon development [Kopanev *et al.*, 1979].

It has been our goal to determine which, if any, of these detection mechanisms account for the effects of ELF magnetic fields on opioid mediated function.

6.2. Mechanism of the Opioid Effect

The ELF magnetic field detection mechanism for opioid effects is currently unknown. Knowing the mechanism(s) might: 1) make it possible to predict magnetic field exposure parameters which would *decrease* sensitivity to pain which could be of considerable clinical value, and 2) allow the prediction of the magnetic field intensity threshold needed to elicit an effect. This in turn will determine the feasibility of portable battery-powered magnetic field therapy devices.

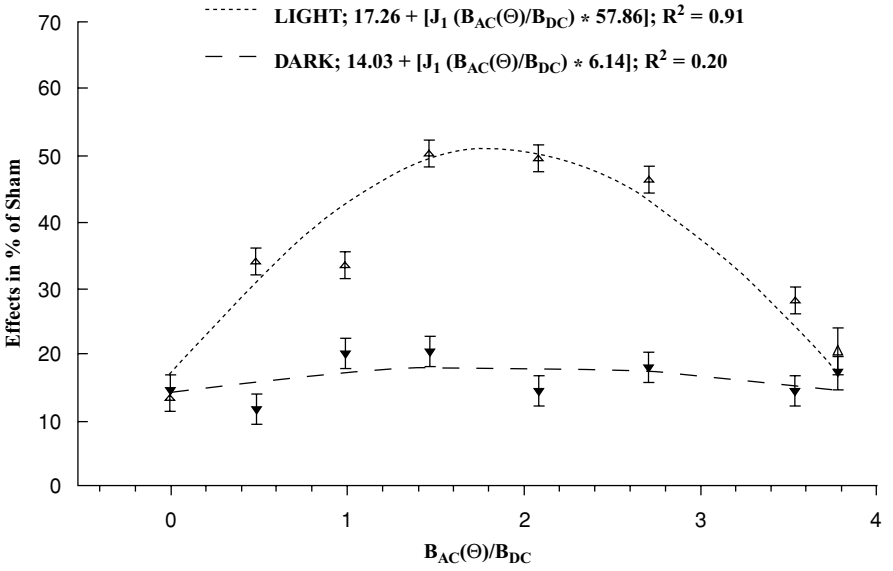

Figure 6. Effects of variations in the direction of the 60 Hz magnetic field on thermal (40°C) response latencies and levels of analgesia in snails injected with enkephalinase inhibitor SCH 34826 (1.0 μg/1.0 μl saline). Responses are expressed as percent inhibition of sham ((sham latency – 60 Hz exposed latency)/sham latency* 100). Data are shown for eight groups of snails when the direction of the static field is varied with respect to the 60 Hz vertical field (0°, 22.5°, 45°, 57°, 67.5°, 75°, 82.6°, 90°). For all angles, the magnitude of $B_{60\,Hz}$ and B_{STATIC} were fixed at 299 μT peak amplitude and 78 μT respectively. The upward pointing open triangles correspond to light (presence of light) exposed snails while the downward pointing filled triangles correspond to the dark exposed (absence of light) snails with the number of animals in each group also indicated. The horizontal axis was set equal to the cosine of the angle between the direction of the two magnetic fields. The solid and dashed lines correspond to the fit of the data to the predictions of the parametric resonance model as described in the text.

Taken with permission from: Prato FS, Kavaliers M, Carson JJL: Behavioural responses to magnetic fields by land snails are dependent on both magnetic field direction and light. *Proc R Soc Lond B Biol Sci* 1996; 263:1437–1442.

In a series of experiments [Prato *et al.*, 1995] we established that the opioid effect (attenuation of opioid-induced analgesia by ELF magnetic fields) was not proportional to the product of the frequency and amplitude of the ELF magnetic field. Therefore, the effect did not seem to depend on the potential of the magnetic field exposure to induce an electric field [Weaver and Astumian, 1990; Adair, 1991; Polk, 1992]. Further, as seen in Figure 6, if the ELF magnetic field was kept constant in amplitude and direction the size of the "opioid effect" could be altered by changing the direction of the static (B_{DC}) field [Prato *et al.*, 1996a, b]. These results provided evidence [Engstrom, 1999] that the underlying mechanism probably did not depend on magnetite as part of the direct detection mechanism for the attenuation of opioid induced analgesia in snails. The parametric resonance theory (PRM) of Lednev [1996; Prato *et al.*, 2000] seems to best predict these results, however this is a controversial conclusion with alternative explanations being offered by other ion resonance theorists [Liboff, 2002].

Betancur *et al.*, [1994] showed that attenuation of opioid-induced analgesia was light dependent in mice; the effect disappeared if the experiment was carried out in the dark.

Consequently, we have also found that the effect was significantly reduced, but not eliminated, if the ELF magnetic field exposures were carried out in the dark [see Figure 6] [Prato *et al.* 1996a; 1997; 1998a; 2000; Kavaliers and Prato, 1999]. This modulatory effect of light may occur at the primary magnetic field detection mechanism. However, it could also be argued that light just acts as a "post-detection amplifier", i.e. light could affect the responses of opioid systems to a fixed stimulus produced by the magnetic field exposure. In another study [Prato *et al.*, 1998a], we compared the effects of the presence and absence of light on the attenuation of opioid-peptide-induced "analgesia" in the snail by 1) an ELF magnetic field and 2) the prototypic opiate antagonist naloxone. Unlike the effects of ELF magnetic fields, light did not affect the sensitivity of the endogenous opioid system to naloxone antagonism, suggesting that the modulatory effects of light on the actions of the ELF magnetic fields probably affect the magnetic field detection mechanism prior to its coupling to the opioid system.

Our initial work with snails and combination of static and ELF magnetic fields compared predictions of the PRM for effects on the Ca^{2+} ion. However, the PRM also predicts effects associated with the K^+ ion. Since the effects of the K^+ ion are opposite to those of the Ca^{2+} with respect to the effects on the opioid system [Huang, 1995; Crain and Shen, 1990], we might expect that an exposure, predicted by the model for the K^+ ion, would *increase* opioid-induced analgesia; this was indeed the case, as shown in Figures 7–9 [Prato *et al.*, 2000]. As with the attenuation of opioid-induced analgesia, this increase was also light

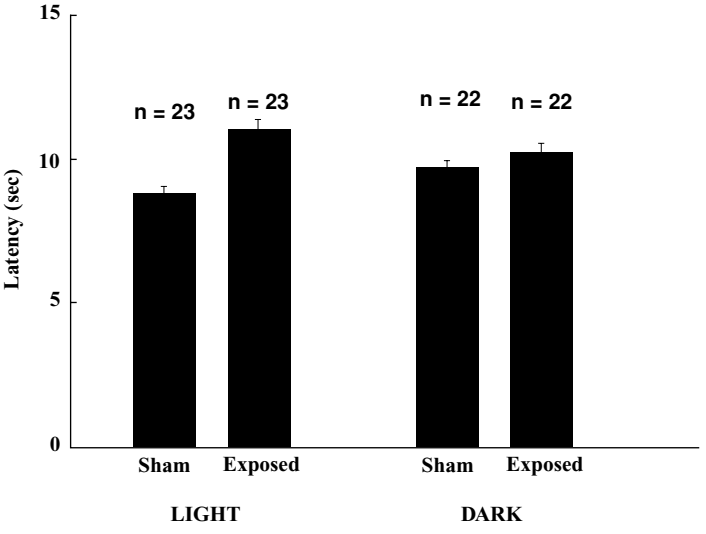

Figure 7. Thermal response latencies of snails injected with the enkephalinase inhibitor SCH34826 (1.0 μg/1.0 μl saline) and exposed for 15 min to either a 30 Hz, 190 μT (Exposed) or sham magnetic field in either the presence of light ("LIGHT") or absence of light ("DARK"). In the 30 Hz exposure, snails were exposed to a B_{AC} of 190 μT and a B_{DC} of 76 μT. In the sham exposure, snails were only exposed to a B_{DC} field of 76 μT and an ambient B_{AC} field <0.2 μT.

Taken with permission from: Prato FS, Kavaliers M, Thomas AW: Extremely low frequency magnetic fields can either increase or decrease analgaesia in the land snail depending on field and light conditions. *Bioelectromagnetics* 2000; 21:287–301.

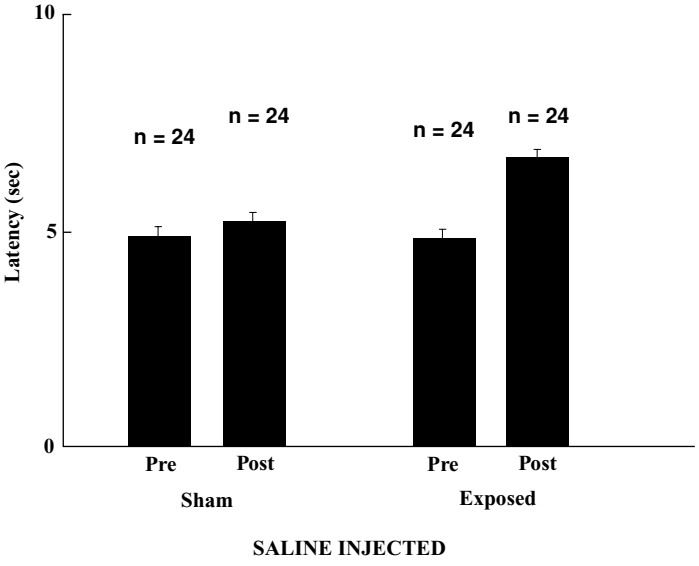

Figure 8. Thermal response latencies of snails injected with saline vehicle (1.0 μl) and exposed for 15 min to either a 30 Hz (Exposed, $B_{DC} = 76\,\mu T$, $B_{AC} = 190\,\mu T$) or sham (Sham, $B_{DC} = 76\,\mu T$, $B_{AC} < 0.2\,\mu T$) magnetic field. Latency values after sham exposure (Post) were not significantly different than measurements done before injection and exposure (Pre), whereas the 30 Hz exposure significantly increased latency.

Taken with permission from: Prato FS, Kavaliers M, Thomas AW: Extremely low frequency magnetic fields can either increase or decrease analgaesia in the land snail depending on field and light conditions. *Bioelectromagnetics* 2000; 21:287–301.

dependent. In addition, we found that this field could also *induce* analgesia. This is the first time, using a single simple sinusoidal exposure, that we have been able to *increase* drug-induced analgesia and, more importantly, *induce* analgesia in drug-naive animals. Note that Parris *et al.*, [1994] showed that *repeated* simple sinusoidal ELF magnetic field exposures could increase analgesia in rats and Kavaliers and Ossenkopp [1993] have shown similar results in snails. In summary, we have been able to use the predictions of the PRM to define the ELFMF that would *increase* analgesia. This was only possible because we have made some progress in understanding one possible underlying energy transduction mechanism.

Results of experiments recently reported have shed some light on the relationship between the cellular site of action and the detection mechanism [Kavaliers and Prato, 1999; Kavaliers *et al.*, 1998]. Results of experiments with nitric oxide (NO) releasing agent (S-nitro-N-acetylpenicillamide; SNP) and NO synthase (NOS) inhibitor (N^G-nitro-L-arginine methyl ester; L-NAME) indicate that NO and NOS are involved in the inhibitory effects of exposure to ELF magnetic fields in the land snail, *Cepaea nemoralis*. Low doses of L-NAME (0.1 μg/snail) which did not alter opioid-induced analgesia, eliminated the field effects when combined with ELF MF exposure. Similarly, low doses of SNP (0.1 μg/snail) which did not alter opioid-induced analgesia, enhanced the attenuating effects of the fields when combined with ELF MF. These results [Kavaliers *et al.*, 1998] suggest that the inhibitory effects of ELF magnetic fields on opioid analgesia involve alteration in NO and NOS activity. In other experiments, we found that a brief exposure to a 60 Hz field

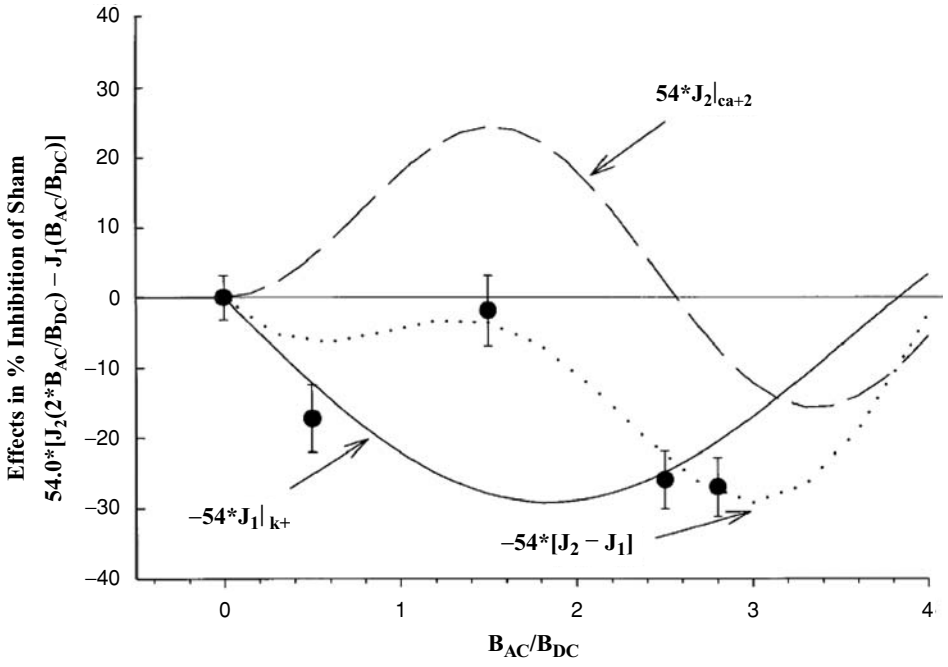

Figure 9. The data is shown as percent inhibition of sham (see Fig 6). Least squares fit of the data to a $[J_2(2B_{AC}/B_{DC})\text{-}J_1(B_{AC}/B_{DC})]$ resulted in a = 54.0 ($R^2 = 0.88$) and is shown as the dotted curve. For reference, the individual curve of $54.0J_2(2B_{AC}/B_{DC})$ is shown as a solid line and that of $54.0J_1(B_{AC}/B_{DC})$ is shown as the line with the long dashes.

Taken with permission from: Prato FS, Kavaliers M, Thomas AW: Extremely low frequency magnetic fields can either increase or decrease analgaesia in the land snail depending on field and light conditions. *Bioelectromagnetics* 2000; 21:287–301.

potentiated, in a light-dependent manner, the inhibitory effects of the NO precursor L-arginine on the level of subsequent opioid-induced analgesia in the land snail *Cepaea nemoralis*. This [Kavaliers and Prato, 1999] again suggests a general light dependency and the involvement of NO in the mediation of the effects of magnetic fields. Since the neuronal form of nitric oxide synthase (cNOS) is active only when bound to the calcium calmodulin complex and since this reversible binding is Ca^{2+}-dependent, one interpretation of these results is that the cellular site of action is the Ca^{2+}-calmodulin protein. This possibility is depicted in Figure 10. In some way, ELF magnetic fields and light stimulate Ca^{2+}-calmodulin and its effect on cNOS. It is interesting that the detection mechanism of Lednev [1993; 1994; 1996a], which best supports our results [Prato *et al.*, 1995; 1996b; 1997; 2000], also predicts that the Ca^{2+}-calmodulin protein is the cellular site of action for ELF magnetic fields tuned to Ca^{2+}.

In recent experiments we found that we could get greater induction of analgesia by using a pulsed magnetic field (see Fig 3) as compared to the application of a continuous sinusoidal field (compare Fig 4 and 5 with Fig 8). Why is this the case? One possibility is that the pulsed field, with its refractory and latency periods, entrains with the underlying neurophysiology of the whole organism. In effect, a protein-ion complex detects the magnetic field, but for

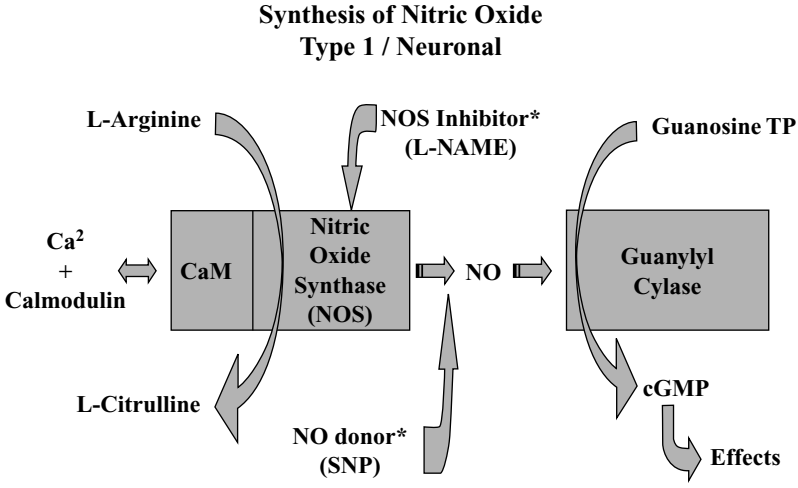

Figure 10. Experiments undertaken by Kavaliers and Prato [1999] and Kavaliers et al. [1998] suggest that ELF MF may drive the Ca^{2+}-calmodulin equation to the right i.e. promote the formation of the calcium-calmodulin complex. This then would upregulate the neuronal form of nitric oxide synthase which can result in the attentuation of opioid induced analgesia. Experiments demonstrated that a similar effect was achieved by increasing L-aginine substrate or an NO donor (SNP). Also, a brief exposure to a 60 Hz field potentiated in a light-dependent manner the inhibitory effects of the nitric oxide precursor, L-arginine, on the level of subsequent opioid-induced analgesia. It is of interest that Lednev [1996a] suggested that it was the calcium-calmodulin complex that could be the ELF MF detector.

that detection to result in a physiological effect, such as induction of analgesia, the application must be "turned" to the underlying neurophysiology associated with analgesia. Hence the pulsed magnetic field is both detected by the magnetic field sensor and then couples to the underlying physiology. The nature of this coupling determines the kind of physiological effect produced. So modifying the latency and refractory periods along with the increase or decrease in pulse waveform presentation would allow a different behaviour/physiological response to be targeted. A tremendous amount of research will be needed to support such a hypothesis. However we have already demonstrated that such a pulsed field can affect a human neurophysiological behaviour i.e., standing balance (see Figure 11) [Thomas *et al.*, 2001a, b] as well as the brain's electrical activity as measured by EEG [Cook *et al.*, in review]. In order to verify the entrainment hypothesis, we believe a number of experiments will be required. One study would utilize an invasive animal model, such as using implanted deep electrodes to record electrical activity within the brain. Electrodes placed within structures hypothesized to be involved in the entrainment process (e.g. intralaminar thalamic nuclei) could then be measured during a real-time pulsed magnetic field exposure to verify or refute the hypothesis. To buttress the more invasive animal model, additional study of human brain dynamics should also be undertaken to investigate possible entrainment. Ideal candidates for this would involve combined electroencephalography (EEG) and magnetoencephalography (MEG). This combined human brain mapping of the brain's electric and magnetic fields would also provide crucial evidence to support or refute the entrainment hypothesis.

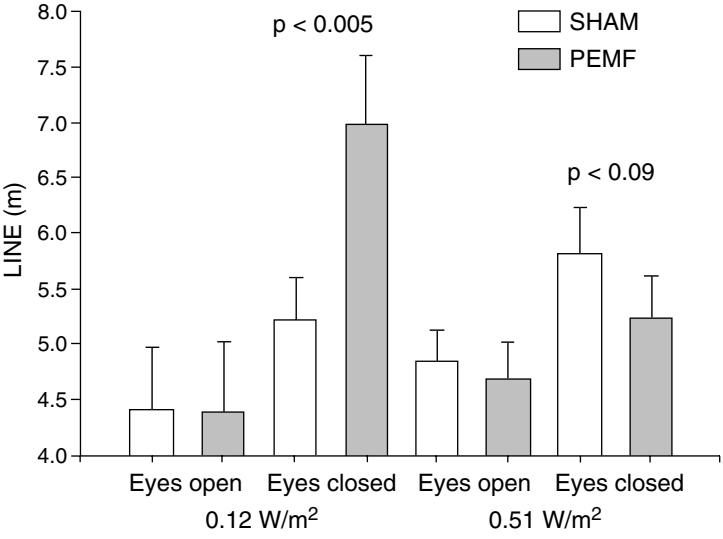

Figure 11. Pattern of sway, as quantitated using line (sum of line segment lengths), for subjects under two different light intensities, with eyes open and eyes closed, and sham exposed or PEMF exposed. Sway is increased with eyes closed and PEMF ($p < 0.005$) under low light intensity (0.12 W/m^2) and decreased (approaching significance, $p < 0.009$) under high intensity light (0.51 W/m^2).

Taken with permission from: Prato FS, Thomas AW, Cook CM: Human standing balance is affected by exposure to pulsed ELF magnetic fields: light intensity-dependent effects. *Neuroreport* 2001; 12:1–5.

Further, consistent with our work using simple sinusoidal magnetic fields, we have demonstrated that this effect is light sensitive. Now that effects can be objectively measured in humans we need to determine if these effects also follow a light sensitive ion-protein complex like mechanism. To do this properly we need to compare results to theory and hence what is needed now are a more complete theory which allows pulsed fields as well as sinusoidal ones and allows the static and time-varying components to be in arbitrary directions. We encourage bioelectromagnetic theoreticians to work towards this goal.

7. FUTURE WORK NEEDED

There have been a number of recent articles in the field of developmental science, that have espoused the concept of multilevel integrative analysis for the study of psychopathology [see Kagan *et al.*, 2002, Cicchetti and Dawson, 2002]. This forward thinking approach essentially dictates that if one is to understand the root cause of a disorder such as schizophrenia, one will not find answers looking just at the neurotransmitter dopamine. One must consider multilevel analysis to fully understand such a complex disorder, considering the temporal periods from prenatal exposures to toxins to the social standing of the person at adult onset. When disciplines function in isolation, they will run the risk of generating incorrect hypotheses because vital information is ignored or not known [Kagan, 2003].

Bioelectromagnetics research is a multidisciplinary field, but tends not to be interdisciplinary. There is often little cross-pollination across the research areas. There has been the long sought after 'smoking gun' to explain the mechanism of interaction, endowing a primacy to a single theory or framework that seems to answer all questions. This viewpoint seriously limits the tools available and approaches needed to study what is already a very complex problem. One direction that we hope will assist us in achieving a greater understanding of the variables that lead to a biological effect of magnetic fields is through multiple levels of analysis. By considering the biological system as what it is, a system of interconnecting variables that interact upon each other across various levels, we should be focusing upon multiple measures to elucidate the answers we seek, in this case, how extremely low frequency magnetic fields interact and affect biological systems. This is particularly important if as we are considering human behaviour, most notably the pain system. Human studies of pain are notoriously difficult to conduct, mostly due to the subjective nature of the pain experience and the subsequent reliance on self-reporting.

One question is that when we select a group for study in our magnetic field-pain experiments, how can we determine whether we will see an effect? We must determine the sources of variance that contribute to the magnetic field effects which we see. When we test in animal models, our subjects, whether they be mice or snails, are a relatively homogeneous population and we still explain only approximately 30–40% of the variance associated with our magnetic field treatment. When we move upwards and test in our human population, we make the same default assumption, that our population is homogeneous. We neglect the critical concept of individual differences, and for us to ferret out the sources of variance responsible for driving our effect, we must use multiple levels of analysis. This includes:

1) Personality—Are there resting baseline differences in our population before we have even administered an experimental treatment? Although it is a difficult concept to quantify, personality is often defined as a characteristic or baseline cognitive or behavioural state of a human [Sugiura *et al*., 2000]. In fact, personality may be one of the largest contributions to extraneous variance in human studies, which makes controlling its effect in bioelectromagnetics experiments all the more important. The control of personality effects in trials for medical and pharmacological research is considered a necessary covariate to allow experimenters to investigate 'true' drug side effects from those that may arise due to personality factors such as negative affectivity. The control of personality factors within a study is therefore necessary to increase the power to detect a treatment effect [Swartzman and Burkell, 1998]. Certain personalities or temperaments are likely to rate pain differently and may also be more likely to respond to magnetic field effects as well. Can we partial out pre-exposure differences that may be important in explaining our effects?
2) Autonomic activity—Closely related to the personality concept, we have to use multiple analysis techniques to assess sympathetic activity or arousal. Kagan [2003] warns against using a single dependent measure to understand 'fear' in an animal model, and this similarly applies to human assessment of pain and magnetic field effects. If we exposure a human subject to a ELF MF and find that systolic blood pressure increases for a brief period post exposure, what does this tell us? Subjects

are experiencing a brief indicator of arousal or stress, but as a single measure, it is not very informative. Does the increase in blood pressure relate further to the pain effect? Pain sensitivity is negatively correlated with blood pressure [Guasti *et al.*, 1999]. The importance of arousal on the accuracy of pain self-report cannot be overstated [Nakamura and Chapman, 2002].

3) Imaging—Image guided electromagnetic pain therapy will significantly alter the management of both acute and chronic pain. Today we know that whole animal exposure to pulsed extremely low frequency magnetic fields can both a) augment opioid induced analgesia and induce analgesia and b) attenuate opioid induced analgesia. However, before such therapy can be effective for the masses we must discover the mechanism and specifically the target tissue. Recently there has been considerable interest in imaging pain centers in the brain using magnetic resonance imaging (MRI) and positron emission tomography (PET) [Talbot *et al.*, 1991; Treede *et al.*, 1999; Casey, 1999]. New knowledge regarding the mechanism of action of analgesic drugs is accumulating and we are actually starting to understand more about the placebo effect with imaging studies allowing us to differentiate between areas of the brain activated by placebo compared to those from analgesics [Zubieta *et al.*, 2001; Petrovic *et al.*, 2002]. For electromagnetic pain therapy we need to discover a) the mechanism with respect to detection and the cascade of events leading to the analgesic effect, b) the anatomical targets, and c) the optimal pulsed magnetic field waveform. It is only through sophisticated imaging methods that we can gather this information. First, we need to establish, using imaging, how pulsed magnetic field therapy affects pain centers in the brain. For example, we can ask whether or not such therapy affects the somatosensory detection of pain or the higher brain functions associated with cognitive process including the placebo effect [Jones, *et al.*, 1991; Bromm, 2001]. This can be done using fMRI and PET in acute pain studies or PET, SPECT (single photon emission computed tomography) or MRI (brain blood flow) to determine basal conditions in patients treated for chronic pain. Imaging studies can tell us how patients treated for chronic pain respond to acute pain. Besides such uses of active imaging methods, it is postulated that, passive imaging in the form of brain mapping (EEG and MEG) could be used to determine how a) treatment to one brain site is electrically connected to other sites and b) how the exposing pulsed magnetic field can be optimized for the individual patient. Monitoring brain electromagnetic activity during pulsed magnetic field therapy and after therapy may allow tuning of the pulse sequence for individual patients. Note that, we, as well as others, have already shown that brain central activity can be altered after exposure to extremely low frequency magnetic fields [Cook *et al.*, 2002; Cook *et al.*, in review]. At this time we do not know how specific the effect is however it demonstrates the proof of concept that brain mapping will play a roll in the future development of treating human pain with ELF magnetic fields. Hence imaging will guide all aspects of electromagnetic pain therapy including the pulsed magnetic field temporal design and the preferred spatial localization. It will even be possible to use imaging to target pulsed magnetic field therapy to areas of the brain associated with negative drug side effects with the purpose of reducing those side effects.

8. SUMMARY

The effects of extremely low frequency magnetic fields (ELFMF) on opioid related behaviours is besides the effect of static fields in animal orientation, the most reliable and largest result yet reported. If the field of bioelectromagnetics is to prosper in the area of therapeutics beyond bone healing then, given these opioid related findings, the area of pain therapy should be vigorously pursued. This will not be easy given the need: 1) to demonstrate proof of principal in humans; 2) to discover the initial biophysical transduction mechanism; 3) to discover the cascade of events from initial transduction to the whole organism physiological/behavioural response and; 4) to do this with today's skepticism and resulting paucity of research funding.

We believe, however, that mainstream medical research has recently given us the tools that are needed to achieve our goals: molecular biology, neuroimaging and brain mapping. Molecular biology now provides us with the tools to study, in animals, the cascade of events just after the initial ELFMF detection to the final behavioural/physiological response. Neuroimaging and brain mapping will allow us to objectively evaluate neurophysiological response in humans to ELFMF exposures. This has already started in the study of transcranial magnetic field stimulation in the understanding of mechanism and its use in therapies [Ueno *et al.* 1990; Ueno 1998; Ueno, 1999; Paus *et al.* 1997; Wassermann, 1998]. Also these imaging methods have been applied to understand the neurocircuits involved in pain, its treatment with exogenous and endogenous opioids and the role of placebo in pain therapy. The time has now come to turn these human imaging and brain mapping tools to the study of ELFMF effects on opioid related behaviours. Initially we can expect progress by studying groups of patients but the ultimate goal will be to use those methods to guide ELFMF pain therapy on an individual basis.

In the future patients in acute post trauma pain and those suffering from chronic debilitating pain will be initially assessed with brain imaging and mapping. Pain areas of the brain abnormally active at rest and those responding to acute experimental pain will be imaged and mapped. Then the patients' response to ELFMF therapy will be imaged and mapped. Individual differences will be accommodated as the target areas of the brain will be individualized and the ELFMF temporal pulse sequence will be optimized to get the greatest therapeutic benefit for the individual patient.

Acknowledgments. This study was funded by Canadian Institutes of Health Research (CIHR) St. Joseph's Health Care (SJHC-London) Foundation; Lawson Health Research Institute; the Department of Nuclear Medicine & MR, SJHC; Natural Sciences and Engineering Research Council of Canada (NSERC); Canadian Institutes of Health Research (CIHR); and National Research Council (NRC); Canada Foundation for Innovation (CFI); and the Ontario Innovation Trust (OIT).

REFERENCES

Adair, R.K., 1994, Constraints of thermal noise on the effects of weak 60 Hz magnetic fields on biological magnetite, *Proc Natl Acad Sci USA* 91:2925–2929.

Basford, J.R., 2001, A historical perspective of the popular use of electric and magnetic therapy, *Arch Phys Med Rehabil* 82:1261–1269.

Betancur, C., Dell'Omo, G., and Allera, E., 1994, Magnetic field effects on stress induced analgesia in mice: Modulation of light, *Neurosci Lett* 182:147–150.

Blakemore, R.P., 1975, Magnetotactic bacteria, *Science* 190:377–379.

Blanchard, J.P., and Blackman, C.F., 1994, Clarification and application of an ion parametric resonance model for magnetic field interaction with biological systems, *Bioelectromagnetics* 15:217–238.

Brody H. In Harrington, A. (ed). The placebo effect: An interdisciplinary exploration 1997 Harvard University Press.

Bromm, B., 2001, Brain images of pain, *News Physiol Soc* 16:244–249.

Canfield, J.M., Belford, R.L., and Debrunner, P.G., 1996, Calculation of earth-strength steady and oscillating magnetic field effects in coenzyme B_{12} radical pair systems, *Molecular Physics* 89:889–930.

Carson, J.J.L., Maxim, P.G., and Walleczek, J., 1999, Real-time evidence for magnetic field-induced modulation and state transitions in the oscillatory peroxidase-oxidase system, *21st Annual Meeting of the Bioelectromagnetics Society 1999, Long Beach (CA) USA, June 20–24, 1999* p72–73.

Casey, K.L., 1999, Forebrain mechanisms of nociception and pain: Analysis through imaging, *Proc Natl Acac Sci* 96:7668–7674.

Chapman, C.R., and Nakamura, Y., 1999, A passion of the soul: an introduction to pain for consciousness researchers, *Conscious Cogn* 8:391–422.

Cicchetti, D. and Dawson, G., 2002, Multiple levels of analysis, *Dev Psychopathol*. 14:417–420.

Choleris, E., Del Seppia, C., Thomas, A.W., Luschi, P., Ghione, G., Moran, G.R., and Prato, F.S., 2002, Shielding, but not zeroing of the ambient magnetic field reduces stress-induced analgesia in mice, *Proc R Soc Lond B Biol Sci* 269:193–201.

Cook, C.M., Thomas, A.W., and Prato, F.S., 2002, Human electrophysiological and cognitive effects of exposure to ELF magnetic and ELF modulated RF and microwave fields: A review of recent studies, *Bioelectromagnetics* 23:144–57.

Crain, S.M., and Shen, K-F., 1990, Opioids can evoke direct receptor-mediated excitatory effects on sensory neurons, *Trends Pharmacol Sci* 11:76–81.

Del Seppia, C., Ghione, S., Luschi, P., and Papi, F., 1995, Exposure to oscillating magnetic fields influences sensitivity to electrical stimuli. I. Experiments on pigeons, *Bioelectromagnetics* 16:290–294.

Del Seppia, C., Luschi, P., Ghione, S., Crosio, E., Choleris, E., and Papi, F., 2000, Exposure to a hypogeomagnetic field or to oscillating magnetic fields similarly reduce stress-induced analgesia in C57 male mice, *Life Sci* 66:1299–1306.

Desjardins, D., Thomas, A.W., Cook, C.M., and Prato, F.S., 2002, Repeated magnetic field shielding induces analgesia in mice, 23rd *Bioelectromagnetics Society Annual Meeting, June 23–27, 2002. Quebec City, Quebec, Canada.* p112–133.

Deutschlander, M.E., Phillips, J.B., and Borland, S.C., 1999, The case for light-dependent magnetic orientation in animals, *J Exp Biol* 202:891–908.

Devinsky, O., Morrell, M.J., and Vogt, B.A., 1995, Contributions of anterior cingulate cortex to behavior, *Brain* 118:279–306.

Drolet, G., Dumont, E.C., Gosselin, I., Kinkead, R., Laforest, S., and Trottier, J.F., 2001, Role of endogenous opioid system in the regulation of the stress response, *Prog Neuropsychopharmacol Biol Psychiatry* 25:729–741.

Dunn, J.R., Fuller, M., Zoeger, J., Dobson, J., Heller, F., Hammann, J., Caine, E., and Moskowitz, B.M., 1995, Magnetic material in the human hippocampus, *Brain Res Bull* 36:149–153.

Edmonds, D.T., 1996, A sensitive optically detected magnetic compass for animals, *Proc R Soc Lond B Biol Sci* 263:295–298.

Eichwald, C., and Walleczek, J., 1998, Magnetic field perturbations as a tool for controlling enzyme-regulated and oscillatory biochemical reactions, *Biophys Chem* 74: 209–224.

Engstrom, S., 1996, Dynamic properties of Lednev's parametric resonance mechanism, *Bioelectromagnetics* 17:58–70.

Engstrom, S., 1997, What is the time scale of magnetic field interaction in biological systems?, *Bioelectromagnetics* 18:244–249.

Frankenstein, U.N., Richter, W., McIntyre, M.C., and Remy, F., 2001, Distraction modulates anterior cingulate gyrus activations during the cold pressor test, *Neuroimage* 14:827–36.

Grissom, C.B., 1995, Magnetic Field Effects in Biology: A Survey of Possible Mechanisms with Emphasis on Radical-Pair Recombination, *Chem. Rev* 95:3–24.

Guasti, L., Gaudio, G., Zanotta, D., Grimoldi, P., Petrozzino, M.R., Tanzi, F., Bertolini, A., Grandi, A.M., and Venco, A., 1999, Relationship between a genetic predisposition to hypertension, blood pressure levels and pain sensitivity, Pain 82:311–317.

Harkins, T.T., and Grissom, C.B., 1994, Magnetic field effects on B_{12} ethanolamine ammonialyase: Evidence for a radical mechanism, *Science* 263: 958–960.

Hofbauer, R.K., Rainville, P., Duncan, G.H., and Bushnell, M.C., 2001, Cortical representation of the sensory dimension of pain, *J Neurophysiol* 86:402–411.

Holcomb, R.R., Worthington, W.B., McCullough, B.A., and McLean, M.J., 2000, Static magnetic field therapy for pain in the abdomen and genitals, *Pediatr Neurol* 23:261–264.

Hsieh, J.C., Stahle-Backdahl, M., Hagermark, O., Stone-Elander, S., Rosenquist, G., and Ingvar, M., 1996, Traumatic nociceptive pain activates the hypothalamus and the periaqueductal gray: a positron emission tomography study, *Pain* 64:303–314.

Huang, L-Y.M., 1995, Cellular mechanisms of excitatory and inhibitory actions of opioids. In *The Pharmacology of Opioid Peptides*. Tseng, L.F., ed. Harwood Academic Publishers, Germany, pp.131–149.

Ioale, P., and Guidarini, D., 1985, Methods for producing disturbances in pigeon homing behavior by oscillating magnetic fields, *J Exp Biol* 116:440–443.

Jeong, J.H., Choi, K.B., Yi, B.C., Chun, C.H., Sung, K.Y., Sung, J.Y., Gimm, Y.M., Huh, I.H., and Sohn, U.D., 2000, Effects of extremely low frequency magnetic fields on pain thresholds in mice: roles of melatonin and opioids, *J Auton Pharmacol* 20:259–264.

Jones, A.K., Liyi, Q., Cunningham, V.V., Brown, D.W., Ha-Kawa, S., Fujiwara, T., Friston, K.F., Silva, S., Luthra, S.K. and Jones, T., 1991, Endogenous opiate response to pain in rheumatoid arthritis and cortical and subcortical response to pain in normal volunteers using positron emission tomography, *Int J Clin Pharamacol Res* 11:261–266.

Jones, R.B., and Wall, J.P., 1989, General practitioners' referrals, *BMJ*. 299:857–858.

Kagan, J., Snidman, N., McManis, M., Woodward, S. and Hardway, C., 2002, One measure, one meaning: multiple measures, clearer meaning, *Dev Psychopathol* 14:463–75.

Kagan, J., 2003, Biology, context, and developmental inquiry, *Annu Rev Psychol* 54:1–23.

Kavaliers, M., and Ossenkopp, K-P., 1985a, Tolerance to morphine-induced analgesia in mice: magnetic fields function as environmental specific cues and reduce tolerance development, *Life Sci* 37:1125–1135.

Kavaliers, M., and Ossenkopp, K-P. 1985b, Magnetic fields as environmental specific cues for morphine-induced analgesia: interactions with tolerance development, *Prog Neuropsychopharmacol Biol Psychiatry* 9:713–716.

Kavaliers, M., and Ossenkopp, K-P., 1985c, Exposure to rotating magnetic fields alters morphine-induced behavioral responses in two strains of mice, *Neuropharmacology* 24:337–340.

Kavaliers, M., and Ossenkopp, K-P., 1986a, Stress-induced opioid analgesia and activity in mice: inhibitory influences of exposure to magnetic fields, *Psychopharmacology (Berl)* 89:440–443.

Kavaliers, M., and Ossenkopp, K-P., 1986b, Magnetic fields differentially inhibit mu, delta, kappa and sigma opiate-induced analgesia in mice, *Peptides* 7:449–453.

Kavaliers, M., and Ossenkopp, K-P., 1986c, Magnetic field inhibition of morphine-induced analgesia and behavioral activity in mice: evidence for involvement of calcium ions, *Brain Res* 379:30–38.

Kavaliers, M., and Ossenkopp, K-P., 1987, Magnetic fields and stress: day-night differences, *Prog Neuropsychopharmacol Biol Psychiatry* 11:279–286.

Kavaliers, M., and Ossenkopp, K-P., 1988, Magnetic fields inhibit opioid-mediated 'analgesic' behaviors of the terrestrial snail, *Cepaea nemoralis*, *J Comp Physiol [A]* 162:551–558.

Kavaliers, M., and Ossenkopp, K-P., 1993, Repeated naloxone treatments and exposures to weak 60-Hz magnetic fields have 'analgesic' effects in snails. *Brain Res* 620:159–162.

Kavaliers, M., Ossenkopp, K-P., and Hirst, M., 1984, Magnetic fields abolish the enhanced nocturnal analgesic response to morphine in mice, *Physiol Behav* 32:261–264.

Kavaliers, M., Ossenkopp, K-P., and Tysdale, D.M., 1991, Evidence for the involvement of protein kinase C in the modulation of morphine-induced 'analgesia' and the inhibitory effects of exposure to 60-Hz magnetic fields in the snail, *Cepaea nemoralis*, *Brain Res* 554:65–71.

Kavaliers, M., Choleris, E., Prato, F.S., and Ossenkopp, K-P., 1998, Evidence for the involvement of nitric oxide and nitric oxide synthase in the modulation of opioid-induced antinociception and the inhibitory effects of exposure to 60-Hz magnetic fields in the land snail, *Brain Res* 809:50–57.

Kavaliers, M., and Prato, F.S., 1999, Light-dependent effects of magnetic fields on nitric oxide activation in the land snail, *Neuroreport* 10:1863–1867.

Kobayashi, A.K., Kirschvink, J.L., and Nesson, M.H., 1995, Ferromagnetism and EMFs, *Nature* 374:123.

Kirschvink, J.L., Kobayashi-Kirschvink A., Diaz-Ricci J.C., and Kirschvink S.L., 1992, Magnetite in human tissues: a mechanism for the biological effects of weak ELF magnetic fields *Bioelectromagnetics* Suppl, 1:1–101.

Kopanev, V.I., Efimenko, G.D., and Shakula, A.V., 1979, Biological effect of a hypogeomagnetic environment on an organism, *Biol Bull Acad Sci USSR* 6:289–298.

Leask, M.J.M., 1977, A physicochemical mechanism for magnetic field detection by migratory birds and homing pigeons, *Nature* 269:144–145.

Lednev, V.V., 1991, Possible mechanism for the influence of weak magnetic fields on biological systems, *Bioelectromagnetics* 12:71–75.

Lednev, V.V., 1996a, Bioeffects of weak combined static and alternating magnetic field, *Biofizika* 41:224–232.

Lednev, V.V., Srebnitskaya, L.K., Il'yasova, Y.N., Rozhdestvenskaya, Z.Y., Klimov, A.A., Belova, N.A., and Tiras, K.P., 1996b, Magnetic paramagnetic resonance in biosystems: Experimental verfication of the predictions of a theory using regenerating planarians *Dugesia Tigrina* as a test system, *Biophysics* 41: 825–835.

Liboff, A.R., Rozek, R.J., Sherman, M.L., McLeod, B.R., and Smith, S.D., 1987, Ca^{45} cyclotron resonance in human lymphocytes, *J Bioelec* 6:13–22.

Mao, J., 1999, NMDA and opioid receptors: Their interactions in antinociception, tolerance and neuroplasticity, *Brain Res Brain Res Rev* 30:289–304.

Melzack, R. and Casey, K.L., 1968, Sensory motivational and central control determinants of pain: A new conceptual model. In D. Kenshalo, ed., *The Skin Senses*, Springfield: Thomas, pp. 423–443.

McGrath, P.J., and Rice, A.S.C., 1999, *Pain: Basic Science* OPAL Open Programs for Associative Learning SA 1994–1999.

McLean, M.J., Holcomb, R.R., and Engstrom, S., 2001, Static magnetic fields for the treatment of pain, *Epilepsy and Behavior* 2:S74–S80.

McLean, M.J., Engstrom, S., and Holcomb, R.R., 2001, Magnetic field therapy for epilepsy, *Epilepsy and Behavior* 2:S81–S87.

Millan, M.J., 1999, The induction of pain: an integrative review., *Prog Neurobiol* 57:1–164.

Nakamura, Y., and Chapman, C.R., 2002, Measuring pain: An introspective look at introspection, *Conscious Cogn*. 11:582–592.

Ossenkopp, K-P., Kavaliers, M., Prato, F.S., Teskey, G.C., Sestini, E., and Hirst, M., 1985, Exposure to nuclear magnetic resonance imaging procedure attenuates morphine-induced analgesia in mice, *Life Sci* 37:1507–1514.

Papi, F., Ghione, S., Rosa, C., Del Seppia, C., and Luschi, P., 1995, Exposure to oscillating magnetic fields influences sensitivity to electrical stimuli. II. Experiments on humans. *Bioelectromagnetics* 16:295–300.

Parris, W.C.V., Janicki, P.K., Johnson, B.W. Jr., and Mathews, L., 1994, The behavioral and biochemical effect of pulsating magnetic field treatment (PMFT) on chronic pain produced by chronic constriction injury of sciatic nerve in rat, *Analgesia* 1:57–64.

Paus, T., Jech, R., Thompson, C.J., Comeau, R., Peters, T., and Evans, A.C., 1997, Transcranial magnetic stimulation during positron emission tomography: A new method of studying connectivity of the human cerebral cortex., *J Neurosci* 17:3178–3184.

Persinger, M.A., 1988, The Modern Magnetotherapies. In A.A. Marino, ed., *Handbook of Bioelectricity*, New York: Marcel-Dekker, pp. 589–627.

Petrovic, P., and Ingvar, M., 2002, Imaging cognitive modulation of pain processing, *Pain* 95:1–5.

Petrovic, P., Kalso, E., Petersson, K.M., and Ingvar, M., 2002, Placebo and opioid analgesia – imaging a shared neuronal network, *Science* 295:1737–1740.

Phillips, J.B., and Borland, S.C., 1992, Behavioral evidence for the use of a light-dependent magnetoreception mechanism by a vertebrate, *Nature* 359:142–144.

Phillips, J.B., and Sayeed, D., 1993, Wavelength-dependent effects of light on magnetic compass orientation in *Drosophila melanogaster*. *J Comp Physiol A*, 172:303–308.

Phillips J.B., Borland S.C., Freake M.J., Brassart J., and Kirschvink J.L., 2002, 'Fixed-axis' magnetic orientation by an amphibian: non-shoreward-directed compass orientation, misdirected homing or positioning a magnetite-based map detector in a consistent alignment relative to the magnetic field?, *J Exp Biol* 205:3903–3914.

Polk, C., 1992, Dosimetry of extremely low frequency magnetic fields. *Bioelectromagnetics* Suppl 1:209–235.

Polk, C., 1994, Effects of extremely low frequency magnetic fields on biological magnetite: Comments., *Bioelectromagnetics* 15:261–270.

Prato, F.S., Carson, J.J.L., Ossenkopp, K-P, and Kavaliers, M., 1995, Possible mechanisms by which extremely low frequency magnetic fields affect opioid function, *FASEB J* 9:807–814.

Prato, F.S., Kavaliers, M., and Carson, J.J.L., 1996a, Behavioral responses to magnetic fields by land snails are dependent on both magnetic field direction and light, *Proc R Soc Lond B Biol Sci*, 263:1437–1442.

Prato, F.S., Kavaliers, M., and Carson, J.J.L., 1996b, Behavioral evidence that magnetic field effects in the land snail, *Cepaea nemoralis*, may not depend on magnetite or induced electric currents, *Bioelectromagnetics* 17:123–130.

Prato, F.S., Kavaliers, M., Cullen, A.P., and Thomas, A.W., 1997, Light-dependent and -independent behavioral effects of extremely low frequency (ELF) magnetic fields in a land smail are consistent with a parametric resonance mechanism (PRM), *Bioelectromagnetics* 18:284–291.

Prato, F.S., Kavaliers, M., and Thomas, A.W., 2000, Extremely low frequency magnetic fields can either increase or decrease "analgesia" in the land snail dependent on field and light conditions, *Bioelectromagnetics* 21:287–301.

Prato, F.S., Kavaliers, M., Thomas, A.W., and Ossenkopp, K-P., 1998a, Modulatory actions of light on the behavioral responses to magnetic fields by land snails probably occur at the magnetic field detection stage, *Proc R Soc Lond B Biol Sci* 265:367–373.

Price, D.D., 2000, Psychological and neural mechanisms of the affective dimension of pain, *Science* 288:1769–1772.

Price, D.D., and Barrell, J.J. 2000, Mechanisms of analgesia produced by hypnosis and placebo suggestions, *Prog Brain Res* 122:255–71.

Price, D.D., Mayer, D.J., Mao, J., and Caruso, F.S., 2000, NMDA-receptor antagonists and opioid receptor interactions as related to analgesia and tolerance, *J Pain Symptom Manage* 1 Suppl:S7–11.

Rainville, P., 2002, Brain mechanisms of pain affect and pain modulation, *Curr Opin Neurobiol* 12:195–204.

Ritz, T., Adem, S., and Schulten, K., 2000, A model for photoreceptor-based magnetoreception in birds, *Biophys J* 78:707–18.

Ritz, T., Dommer, D.H., Phillips, J.B., 2002, Shedding light on vertebrate magnetoreception., *Neuron* 34:503–6.

Scaiano, J.C., Cozens, F.L., and McLean, J., 1994, Model for the rationalization of magnetic field effects in vivo. Application of the radical-pair mechanism to biological systems, *Photochem Photobiol* 59:585–589.

Schulten, K., 1982, Magnetic field effects in chemistry and biology. *Festkörperprobleme* 22:61–83.

Segal, N.A., Toda, Y., Huston, J., Saeki, Y., Shimizu, M., Fuchs, H., Shimaoka, Y., Holcomb, R., and McLean, M.J., 2001, Two configurations of static magnetic fields for treating rheumatoid arthritis of the knee: a double-blind clinical trial, *Arch Phys Med Rehabil* 82:1453–1460.

Sewards, T.V., and Sewards, M.A., 2002, The medial pain system: Neural representations of the motivational aspect of pain, *Brain Res Bull* 59:163–180.

Smith, S.D., McLeod, B.R., Liboff, A.R., and Cooksey, K., 1987, Calcium cyclotron resonance and diatom mobility, *Bioelectromagnetics* 8:215–227.

Smith, S.D., McLeod, B.R., and Liboff, A.R., 1995, Testing the ion cyclotron resonance theory of electromagnetic field interaction with odd and even harmonic tuning for cations, *Bioelectro Bioenerg* 38:161–167.

Sobotka, S.S., Davidson, R.J., Senulis, J.A., 1992, Anterior brain electrical asymmetries in response to reward and punishment, *Electroencephalogr Clin Neurophysiol* 83:236–47.

Spiegel, H., 1997, Nocebo: the power of suggestibility, *Prev Med* 26:616–621.

Talbot, J.D., Marrett, S., Evans, A.C., Meyer, E., Bushnell, M.C., Duncan, G.H., 1991, Multiple representations of pain in human cerebral cortex, *Science* 251:1355–1353.

Thomas, A.W., Kavaliers, M., Prato, F.S., and Ossenkopp, K-P., 1997a, Antinociceptive effects of a pulsed magnetic field in the land snail, Cepaea nemoralis, *Neurosci Lett* 222:107–110.

Thomas, A.W., Kavaliers, M., Prato, F.S. and Ossenkopp, K-P., 1997b, Pulsed magnetic field induced "analgesia" in the land snail, Cepaea nemoralis, and the effects of mu, delta, and kappa opioid receptor agonists/antagonists, *Peptides* 18:703–709.

Thomas, A.W., Kavaliers, M., Prato, F.S., and Ossenkopp, K-P., 1998a, Analgesic effects of a specific pulsed magnetic field in the land snail, *Cepaea nemoralis*: Consequences of repeated exposures, relations to tolerance and cross-tolerance with DPDPE, *Peptides* 19:333–342.

Thomas, A.W., Choleris, E., Cross, S., and Prato, F.S., 1998b, Analgesic and behavioral effects of a 100μT specific pulsed magnetic field on control and morphine treated CF-1 mice, 19th*Bioelectromagnetics Society Annual Meeting. June 7–11, 1998, St Pete's Beach, Florida, USA*. p80–81.

Thomas, A.W., Prato, F.S., Kavaliers, M., and Persinger, M.A., 1999, Low Frequency Magnetic Field Designed Pulses for Therapeutic Use. U.S. Patent #6, 234, 953 and International PCT/CA97/00388 1996, 1997, 1998, 1999.

Thomas, A.W., Drost, D.J. and Prato, F.S., 2001a, Human subjects exposed to a specific pulsed (200 microT) magnetic field: effects on normal standing balance, *Neurosci Lett*. 297:121–4.

Thomas, A.W., White, K.P., Drost, D.J., Cook, C.M. and Prato, F.S., 2001b, A comparison of rheumatoid arthritis and fibromyalgia patients and healthy controls exposed to a pulsed (200 microT) magnetic field: Effects on normal standing balance, *Neurosci Lett*. 309:17–20.

Till, U., Timmel, C.R., Brocklehurst, B., and Hore, P.J., 1998, The influence of very small magnetic fields on radical recombination reactions in the limit of slow recombination, *Chemical Physics Letters* 298:7–14.

Timmel, C.R., Till, U., Brocklehurst, B., McClaughlan, K.A., and Hore, P.J., 1998, Effects of weak magnetic fields on free radical recombination reactions, *Molecular Physics* 95:71–89.

Tracey, I., Ploghaus, A., Gati, J.S., Clare, S., Smith, S., Menon, R.S., Matthews, P.M., 2002, Imaging attentional modulation of pain in the periaqueductal gray in humans, *J Neurosci* 22:2748–2752.

Treede, R.D., Kenshalo, D.R., Gracely, R.H., and Jones, A.K., 1999, The cortical representation of pain, *Pain* 79:105–111.

Ueno, S., Matsuda, T., and Fujiki, M., 1990, Vectorial and focal magnetic stimulation of the brain for the understanding of the functional organization of the brain, *IEEE Trans Magn* 26:1539–1544.

Ueno, S., 1998, Impedence magnetic resonance imaging: A method for imaging of impedance distributions based on magnetic resonance imaging, *J Appl Physics* 83:6450–6452.

Ueno, S., 1999, Biomagnetic approaches to studying the brain, *IEEE Eng Med Biol Mag* 18:108–120.

Vaccarino, A.L., Olson, G.A., Olson, R.D., and Kastin, A.J. 1999, Endogenous opiates: 1998. *Peptides* 20:1527–1574.

Vallbona, C., Hazlewood, C.F., Jurida, G., 1997, Response of pain to static magnetic fields in postpolio patients: a double-blind pilot study, *Arch Phys Med Rehabil* 78:1200–1203.

Vallbona, C., and Richards, T., 1999, Evolution of magnetic therapy from alternative to traditional medicine, *Phys Med Rehabil Clin N Am* 10:729–754.

Villemure, C., and Bushnell, M.C., 2002, Cognitive modulation of pain: how do attention and emotion influence pain processing?, *Pain* 95:195–199.

Wall, P.D., and Melzack, R., 2000, *Textbook of Pain*. Churchill Livingstone, Inc. New York, NY.

Walleczek, J., 1995, Magnetokinetic effects on radical pairs: A paradigm for magnetic field interactions with biological systems at lower than thermal energy, In Blank M., ed., *Electromagnetic fields: Biological interactions and mechanisms*. ACS Advances in Chemistry Series No. 250. p395–420.

Wassermann, E.M., 1998, Risk and safety of repetitive transcranial magnetic stimulation: report and suggested guidelines from the International Workshop on the Safety of Repetitive Transcranial Magnetic Stimulation, *Electroencephalogr Clin Neurophysiol* 108:1–16.

Weaver, J.S., and Astumian, R.D., 1990, The response of living cells to very weak electric fields: The thermal noise limit, *Science* 247:459–462.

Wiltschko, W., Munro, U., Ford, H., and, Wiltschko, R., 1993, Red light disrupts magnetic orientation of migratory birds, *Nature* 364: 525–527.

Wiltschko, W., Munro, U., Wiltschko, R., and Kirschvink, J.L., 2002a, Magnetite-based magnetoreception in birds: the effect of a biasing field and a pulse on migratory behavior, *J Exp Biol* 205:3031–3037.

Wiltschko, W., Traudt, J., Gunturkun, O., Prior, H., and Wiltschko, R., 2002b Lateralization of magnetic compass orientation in a migratory bird, *Nature* 419:467–470.

Zubieta, J.K., Smith, Y.R., Bueller, J.A., Xu, Y., Kilbourn, M.R., Jewett, D.M., Meyer, C.R., Koeppe, R.A., and Stohler, C.S., 2001, Regional mu opioid receptor regulation of sensory and affective dimensions of pain, *Science* 293:311–315.

Chapter 6

The Charge-to-Mass ICR Signature in Weak ELF Bioelectromagnetic Effects

Abraham R. Liboff

ABSTRACT

There is good experimental evidence for a specific biological interaction with ELF magnetic fields that is functionally dependent on ion cyclotron resonance (ICR) frequencies as derived from ionic charge-to-mass ratios. This evidence is gleaned from studies on an extraordinarily wide variety of biological systems. However, no reasonable underlying theoretical construct has surfaced to explain these results at the microscopic level, and thus the nature of this q/m interaction remains empirical at best. The main difficulty with the various theoretical models that have been advanced is that sustaining ion cyclotron resonance in a biological milieu is highly improbable considering the relatively large damping suffered by ions. Further, in cases where the damping problem may be ameliorated, as for example, in the interior pore of ion channels, there is a large discrepancy between expected cyclotron resonance-mediated ion transit times and observed times, which are faster by a factor of 10^7. Some, notably Lednev, Blanchard, Binhi, and Zhadin, have attempted to explain the unique charge-to-mass signature using models that do not explicitly involve the classical ICR mechanism, but nevertheless still result in functional dependences on the ion cyclotron resonance frequency. Most recently, del Giudice has suggested replacing Maxwellian statistics when studying bio-electromagnetic interactions at the cellular level with quantum electro-dynamics, claiming that the experimental results support the view that highly ordered coherent domains are involved. Two additional sets of experimental results, both involving

Abraham R. Liboff Department of Physics, Oakland University, Rochester, MI 48309.

Advances in Electromagnetic Fields in Living Systems, Volume 4, edited by James C. Lin, Springer Science+Business Media, New York, 2005.

conductivity measurements in cell-free systems, have now been reported, first, the discovery by Zhadin that polar amino acids in solution are sensitive to ICR magnetic field exposures, and the second, by Mohri, that a 1 μT ICR magnetic signal applied to ultra-pure (18.2 MΩ-cm) water for as little as one minute will result in increased conductivity lasting for days. These findings may shed light on the persistent and controversial reports claiming that the physical properties of water can be altered by relatively weak magnetic field exposures.

INTRODUCTION

The author reported in 1985 [Liboff, 1985] that the results embodied in the so-called electromagnetic Ca^{2+} efflux effect [Bawin et al. 1975, Blackman et al. 1982] were in striking agreement with predictions based on the resonance characteristics of certain biological ions subject to the Lorentz force. In particular it was shown that the shape of the non-linear frequency dependence of calcium binding to chick brain tissue was very close to what would be expected for a particle with the charge to mass ratio of the potassium ion moving in a combined parallel sinusoidal and DC magnetic field whose AC frequency and DC intensity corresponded to the ion cyclotron resonance (ICR) condition for K^+. This correlation followed earlier indications [Liboff et al. 1984, Takahashi et al. 1986] in cell culture that weak ELF magnetic fields enhanced DNA synthesis in a manner that was clearly not related to Faraday induction, since the additional DNA synthesis did not scale with either frequency or intensity. Furthermore, in light of the very small magnetic intensities involved, well below 0.1 mT, both the Ca^{2+} and the cell culture results were rather unexpected. These observations implied that effects related to cyclotron resonance may play a role in enhancing the sensitivity of biological systems to magnetic fields.

There are a number of reasons why the ICR hypothesis is an attractive concept. Not only are the ions involved (Ca^{2+}, Mg^{2+}, K^+) common to many physiological reactions but the predicted frequencies are in the low ELF range, providing a potential connection to many low-frequency physiological phenomena. Most important, the DC magnetic field intensities corresponding to the ionic charge-to-mass ratios are close to geomagnetic field levels, suggesting that the interaction revealed by the Ca^{2+} experiments may be the result of an heretofore unknown biological function connected to the earth's magnetic field.

Charged particles experiencing the Lorentz force enjoy a well-defined resonance frequency almost always referred to as the cyclotron resonance frequency [Tipler, 1982]. However the conditions under which this frequency is observed are radically different from those encountered in biological systems. As a rule, cyclotron resonance is observed in systems where particles experience little damping or are moving at very high velocities, e.g. in metals at high frequencies, in high energy plasmas, in nuclear interactions, and in the near-vacuum conditions of outer space. In short any cyclotron resonance observation in biological systems is definitely counter-intuitive [Liboff, 1985], since it happens at low frequencies in an environment that one ordinarily thinks of as having considerable damping.

There is a well-defined characteristic ICR frequency that is independent of frictional forces, the energy of the ion, and even the radius of curvature of the particle as it is deflected in the magnetic field. The ICR angular frequency ω_c is solely a function of the charge-to-mass

ratio (q/m) and the magnetostatic field intensity B:

$$\omega_c = (q/m)B \quad (1)$$

Some experimental ICR results have been incorrectly referred to as "combined magnetic field", or CMF, results [Fitzsimmons et al., 1995]. This is very misleading. One can combine AC and DC magnetic fields in a multitude of ways, both in magnitude and relative direction. However, the combination of fields that have been successfully employed in biological systems is very specific, involving very particular ratios of frequency and magnetostatic intensities. Further, it is not merely the frequencies and intensities that result in biological interactiveness, but one must also have a finite component of the AC field vector directed parallel to the DC field. There is much more involved in achieving conditions of resonance than merely combining AC and DC magnetic fields.

On the other hand, it is reasonable to think that at least some of the earlier reports claiming changes in biological response following exposures to weak ELF magnetic fields were actually the result of ICR effects in which the local magnetostatic field was involved but not taken into account by the observer. Because local magnetic fields are not necessarily the same in different laboratories, the appropriate combination of AC and DC magnetic fields required may not have been exactly matched during attempts at replication, leading to the possibility of poor reproducibility between laboratories..

EXPERIMENTAL EVIDENCE

Taken as a whole, the body of experimental evidence [Liboff, 2003] constitutes very strong evidence that weak ELF magnetic fields interact with biological systems through an ICR coupling mechanism the details of which are as yet poorly understood. Because this effect occurs specifically at the cyclotron resonance frequency and because the charge-to-mass ratios of certain ions are specifically implicated, one can arguably refer to these observations as ICR interactions. Nevertheless because of the lack of a reasonable explanation at the molecular level it is still important to recognize that this designation is strictly empirical in nature. However, simply because there is no reasonable theoretical explanation for the observed results does not make them less believable.

The many different types of experimental evidence for ICR bioeffects can be conveniently assembled into distinct categories of model system: bone, rat behavior, diatom motility, cell culture, neural cell culture, complex biological systems, plants, and cell-free systems. These are listed in Tables 1–8.

The work on bone [Diebert et al. 1994] (Table 1) resulted in the development of FDA-approved ICR devices for treating certain bone disorders. Note that the resonance application to bone therapy is complementary to a distinctly different earlier magnetic device that made use of Faraday induction to treat the same problem [Bassett et al. 1974]. The use of ICR sinusoidal magnetic fields as opposed to the earlier use of pulsed magnetic signals, however, reduces the level of magnetic intensity by more than 50-fold.

Although each of the other categories is interesting in its own right, the most impressive among these, in the author's opinion, is the research dealing with the effects of ICR magnetic fields on rat behavior (Table 2). This body of work involves complementary contributions from four separate laboratories [Thomas et al. 1986, Lovely et al.

1993, Lyskov et al. 1996, Zhadin et al. 1999]. Although each used a different experimental design, the results when viewed collectively are highly consistent. A separate, follow-up study by Creim et al. [2002], demonstrated that the rats were not simply sensitive to simple magnetic field exposures, but required exposure to the appropriate combinations of AC and DC fields. This fact was independently shown in the studies by Thomas et al. [1986] and Zhadin et al. [1999], both of whom found negative results when

Table 1. ICR Effects in Bone (in vitro and in vivo)

Freq (Hz)	B_o (μT)	Tuning	Ratio B/B_o	Comments	Reference
100	130	Ca^{2+}	1.0	Enhanced cell (fibroblast) proliferation; B varied between 50 and 500 μT	Ross [1990]
75	98	Ca^{2+}	1.0	Enhanced proliferation	Ross [1990]
16	42	Ca^{2+}	1.0	Enhanced proliferation	Ross [1990]
16	20.9	Ca^{2+}	1.0	Increases in rudiment length and mid-shaft diameter in embryonic chick femur	Smith et al. [1991]
16	12.7	Mg^{2+}	1.0	Similar results to Ca^{2+} tuning	Smith et al. [1991]
16	40.9	K^{+}	1.0	Results opposite to Ca^{2+} and Mg^{2+} cases: bone growth inhibited	Smith et al. [1991]
80	20	Ca^{2+}/ Mg^{2+}	1.0	Added 5^{th} Ca^{2+} to 3^{rd} Mg^{2+} harmonics; enhanced collar thickness and length	Smith et al. [1991]
72.6–80.6	20	Ca^{2+}	1.0	Resonance in IGF-II concentration at 76.6 Hz in osteosarcoma cell line	Fitzsimmons et al. [1993]
76.6	20	Ca^{2+}	1.0	5^{th} harmonic: Enhanced proliferation in osteosarcoma and human bone cells	Fitzsimmons et al. [1993]
15.3	20	Ca^{2+}	1.0	Reduction in TGF β-1 inhibition in chondrocytes	Ryaby et al. [1993a]
25.4	20	Mg^{2+}	1.0	Reduction in TGF β-1 inhibition in chondrocytes	Ryaby et al. [1993a]
76.6	20	Ca^{2+}/ Mg^{2+}	1.0	Reduction in TGF β-1 inhibition in chondrocytes	Ryaby et al. [1993a]
15.3	20	Ca^{2+}	1.0	Enhanced protoglycans synthesis in bovine cartilage	Ryaby et al. [1993a]
76.6	20	Ca^{2+}/ Mg^{2+}	1.0	Mixed 3^{rd} and 5^{th} harmonics reduce bone loss related to castration in rats	Ryaby et al. [1993b]
14.3–18.3	20		1.0	Increase in $_{45}Ca$ maximized at 16.3 Hz in osteosarcoma cell line	Fitzsimmons et al. [1994]
14.3–18.3	20		1.0	Increase in $_{45}Ca$ maximized at 15.3 Hz in a different osteosarcoma cell line	Fitzsimmons et al. [1994]

Table 1. ***Continued***

Freq (Hz)	B_o (μT)	Tuning	Ratio B/B_o	Comments	Reference
15.3	20	Ca^{2+}	1.0	370% increase in stiffness in ostectomized rabbit fibula after 24 hour/28 day exposure	Deibert et al. [1994]
25.4	20	Mg^{2+}	1.0	137% increase in stiffness in ostectomized rabbit fibula after 24 hour/28 day exposure	Deibert et al. [1994]
15.3	20	Ca^{2+}	1.0	Enhanced DNA synthesis and IGF-II levels in osteosarcoma cell line	Fitzsimmons et al. [1995a]
13.3–17.3	20		1.0	Resonance maximum in IGF-II receptors at 15.3 Hz	Fitzsimmons et al. [1995b]
16	20.9	Ca^{2+}	1.0	Enhanced chick femoral diameter and GAGS (glycosaminoglycans)	Regling et al. [2002]
16	12.7	Mg^{2+}	1.0	Large GAGS enhancement (90%)	Regling et al. [2002]
16	40.7	K^{+}	1.0	Opposite effects from Ca^{2+} and Mg^{2+} tuning, confirming Smith et al. [1991]	Regling et al. [2002]

Table 2. ICR Effects on Rat Behavior

Freq (Hz)	B_o (μT)	Tuning	Ratio B/B_o	Comments	Reference
60	26	Ca^{2+}	1.9	3^{rd} harmonic: loss of short-term (temporal) memory	Thomas et al. [1986]
60	26	Ca^{2+}	1.9	3^{rd} harmonic: AC threshold observed (27 μT) for above results	Liboff et al. [1989]
60	27	Ca^{2+}	1.9	3^{rd} harmonic: learning inhibited relative to controls	Lovely et al. [1993]
60	48	Mg^{2+}	1.0	Learning enhanced relative to controls	Lovely et al. [1993]
60	26	Ca^{2+}	1.9	3^{rd} harmonic: no effect	Stern et al. [1996]
50	65	Ca^{2+}		Reduced short-term memory and aggressiveness	Lyskov et al. [1996]
630	500	Mg^{2+}	0.5	Enhanced exploratory activity	Derjugina et al. [1996]
380	500	Ca^{2+}	0.5	Reduced exploratory activity	Derjugina et al. [1996]
63	50	Mg^{2+}	0.7	Enhanced locomotor and exploratory activity	Zhadin et al. [1999]
38	50	Ca^{2+}	0.7	Reduced locomotor and exploratory activity	Zhadin et al. [1999]
630	500	Mg^{2+}	0.7	Enhanced locomotor and exploratory activity	Zhadin et al. [1999]
380	500	Ca^{2+}	0.7	Reduced locomotor and exploratory activity	Zhadin et al. [1999]

Table 3. ICR Effects on Diatom Motility

Freq (Hz)	B_o (μT)	Tuning	Ratio B/B_o	Comments	Reference
5–32	20.9		1.0	Maximum motility occurs at 16 Hz when Ca^{2+} concentration is 0.25 nM. No effect when fields are at 90°.	Smith et al. [1987]
16	20.9	Ca^{2+}	0.0–3.0	Motility maximized when B/B_o ratio is one.	Smith et al. [1987]
16	20.9	Ca^{2+}	0.7	Enhanced motility	McLeod et al. [1987a]
32	20.9	Ca^{2+}	0.7	Even harmonic: no effect	McLeod et al. [1987a]
48	20.9	Ca^{2+}	0.7	3rd harmonic: enhanced motility	McLeod et al. [1987a]
64	20.9	Ca^{2+}	0.7	Even harmonic: no effect	McLeod et al. [1987a]
8	10.45	Ca^{2+}	1.4	Enhanced motility	McLeod et al. [1987b]
12–64	15.7–83.6	Ca^{2+}		Additional ICR frequenciesl 12, 16, 23, 31, 32, 46, 64 Hz also enhance motility	McLeod et al. [1987b]
24,40,120	10.45	Ca^{2+}	1.4	Three ICR harmonics for 10.45 μT (n = 3,5,15) enhance motility	McLeod et al. [1987b]
16-136	10.45	Ca^{2+}	1.40.73	Thirteen other frequencies (n = 2,4,6,7,8,9,10,11,12,13,14,16,17) fail to show effect	McLeod et al. [1987b]
8	20.45	K^+	0.73	Motility inhibited	McLeod et al. [1987b]
16	41	K^+	0.37	Motility inhibited	McLeod et al. [1987b]
24,40,120	20.45	K^+	0.37	Three ICR harmonic frequencies for $B_o = 20.45$ μT (n = 3,5,15) also inhibit motility	McLeod et al. [1987b]
16–136	20.45	K^+	0.37	Thirteen other frequencies (n = 2,4, 6,7,8,9,10,11,12,13,14,16,17) fail to show effect	McLeod et al. [1987b]
16	21	Ca^{2+}	1.0	Enhanced motility	Reese et al. [1991]
16	20.9	Ca^{2+}	1.0	No effect on motility	Parkinson and Sulik [1992]
30	39.2	Ca^{2+}	1.0	No effect on motility	Parkinson and Sulik [1992]
60	78.4	Ca^{2+}	1.0	No effect on motility	Parkinson and Sulik [1992]
16	20.9	Ca^{2+}	1.0	No effect on motility	Saalmen et al. [1992]
16	21	Ca^{2+}	1.0	No effect on motility	Prasad et al. [1994]
16	20.9	Ca^{2+}	1.0	No effect on motility as viewed with real time video szystem	Clarkson et al. [1999]

the rats were exposed to either AC fields alone or DC fields alone. Zhadin et al. [1999] explained the earlier puzzling conclusion by Thomas et al. [1986] claiming that the effect was the result of a Li^+ resonance, showing instead that this earlier data can be readily explained in terms of a higher harmonic of Ca^{2+}. The net conclusion from these studies is that rats exposed to ICR magnetic field combinations that are tuned to Mg^{2+} are significantly enhanced in learning and exploratory behavior, whereas fields tuned to Ca^{2+} act oppositely. It is possible that these results reflect stimulatory binding to NMDA (N-methyl d-aspartate), the glutamate receptor implicated in learning and memory, whose regulatory properties act oppositely to binding Ca^{2+} and Mg^{2+}.

Table 4. ICR Effects on Cell Culture

Freq (Hz)	B_o (μT)	Tuning	Ratio B/B_o	Comments	Reference
14.3	21	$_{45}Ca^{2+}$	1.0	3-fold incorporation of $_{45}$Ca into human lymphocytes	Liboff et al. [1987]
14.3	21	$_{45}Ca^{2+}$		Effect on human lymphocytes disappears at larger AC intensity	Liboff et al. [1987]
14.3	20.9	$_{45}Ca^{2+}$	1.0	2.3-fold uptake in $_{45}$Ca disappears with addition of calcium blocker nifidepene	Rozek et al. [1987]
38.15	50	Ca^{2+}	1.0	No effect on Ca^{2+} in four different cell lines as observed using fura-2	Parkinson and Hanks [1989]
16	20.9	Ca^{2+}	1.0	Enhanced proliferation (46%) for fibroblast culture	Rochev et al. [1990]
??	20.9	K^+	1.0	Reduced proliferation (18%) for Raji cells exposed to K^+ ICR. Frequency not provided.	Rochev et al. [1990]
13.6	16.5	$_{45}Ca^{2+}$	1.2	ICR frequency off by 3.5 Hz. Enhanced $_{45}Ca^{2+}$ levels (75–126%) in 3 cell lines.	Lyle et al. [1991]
60	20	$_{45}Ca^{2+}$	1.0	5^{th} harmonic for $_{45}Ca^{2+}$: Uptake is enhanced 37%.	Lyle et al. [1991]
16	23.4	$?Ca^{2+}$	1.8	Decreased Ca^{2+} influx in mitogen-activated lymphocytes but no effect on resting cells.	Yost and Liburdy [1992]
16	51.1	K^+	1.0	3^{rd} harmonic: Enhanced proliferation of human lymphoma; narrow FWHM.	Liboff et al. [1993]
16	40.9	K^+	1.0	Enhanced proliferation of human lymphoma cells.	Liboff et al. [1993]
16	23.4	Ca^{2+}	3.8, 5.3	No change in Ca^{2+} influx at AC/DC ratio of 3.8; influx at ratio of 5.3 is enhanced	Liburdy and Yost[1993]
16	20.9	Ca^{2+}	1.4	No effect on mouse lymphocytes as observed using Ca fluorochrome	Coulton and Barker [1993]
50	65.3	Ca^{2+}	1.4	No effect on mouse lymphocytes, with and w/o mitogenic stimulation.	Coulton and Barker [1993]
5–100	50–60	$?Ca^{2+}$	2.3–3.0	Saw calcium oscillations over broad frequency range, maximized at 50 Hz.	Lindstrom et al. [1995]
32	42	Ca^{2+}	2.5, 5.0	Increased micronuclei formation in human lymphocytes at Ca^{2+} tuning.	Tofani et al. [1995]
32,50	0			No change in micronuclei formation when DC field is 0	Tofani et al. [1995]
15.3	20	Ca^{2+}	1.0	ICR effect on fura-2 calcium activity is observed only with added serum in cell medium.	Reinbold and Pollack [1997]
76.6	20	Ca^{2+}	1.0	5^{th} harmonic also successful	Reinbold and Pollack [1997]
100	130	Ca^{2+}	1.9	Another ICR fundamental is successful.	Reinbold and Pollack [1997]
100	130	Ca^{2+}	2.8	Repeating ICR application to primary bone cell culture at higher AC intensity	Reinbold and Pollack [1997]

Table 5. ICR Effects on Neural Cell Culture

Freq (Hz)	B_o (μT)	Tuning	Ratio B/B_o	Comments	Reference
16	15–40.8	? Co^{2+} or Fe^{2+}?	0.5–1.3	Enhanced proliferation over controls (60%) in neuroblastoma cell culture	Smith et al. [1992]
16	15–40.8		0.5–1.3	Decreased neurite outgrowth for ?Co^{2+}/Fe^{2+} ICR stimulation; possible Na^+ ICR effect?	Smith et al. [1992]
15.3	20	Ca^{2+}	1.0	Ca^{2+} tuning increases rate of neuronal differentiation in PC-12 cells	Horton et al. [1993]
45	36.6	Mg^{2+}	0.03–1.81	Changes in neurite outgrowth for Mg^{2+}ICR at different AC intensities in PC-12 cells.	Blackman et al. [1994]
25	20.3	Mg^{2+}	0.54–1.26	Similar Mg^{2+} ICR effect on PC-12 neurite outgrowth at another frequency.	Blackman et al. [1994]
45	2.96	H^+	0.14–2.0	H^+ ICR alters PC-12 neurite outgrowth	Trillo et al. [1996]
30	1.97	H^+	0.57–1.4	Similar effects at different ICR combinations	Trillo et al. [1996]
45	59	Ca^{2+}	0.26–1.49	PC-12 cells at Ca^{2+} ICR exhibit changes in neurite outgrowth at different AC intensities	Blanchard et al. [1997]
42.5–47.5	2.97	H^+	0.56–1.5	Bandwidth for PC-12 neurite outgrowth due to H^+ ICR is $\pm$10%.	Blackman et al. [1999]
40, 50	2.97		0.56–1.5	No effect	Blackman et al. [1999]

CLASSICAL APPROACH TO ICR BIOLOGICAL INTERACTION

The well-established phenomenon of cyclotron resonance arises from the fact that any charged particle moving in a magnetic field will be accelerated at a rate proportional to its charge-to-mass ratio. This type of force, also known as the Lorentz Force, is written as

$$\mathbf{F} = \mathrm{q}(\mathbf{E} + \mathbf{v} \times \mathbf{B}), \tag{2}$$

where q is the charge on the particle and **v** its velocity. **E** and **B** are the respective electric and magnetic field intensities experienced by the charged particle. Note that the magnetic component of the Lorentz Force is directed normally to both **v** and **B**. We can rewrite Equation (2) in terms of the mass of the ion, m and its acceleration **a**:

$$\mathbf{a} = (\mathrm{q/m})\,(\mathbf{E} + \mathbf{v} \times \mathbf{B}) \tag{3}$$

Table 6. ICR Effects on Complex Biological Systems

Freq (Hz)	B_o (μT)	Tuning	Ratio B/B_o	Comments	Reference
3–770	10-220		.0064–2.8	No effect on turtle colon transepithelial current as measured in Ussing chamber	Liboff et al. [1991]
33.7	44	Ca^{2+}	1.41	Synthesis and release of rat pineal melatonin is reduced by Ca^{2+} tuning	Lerchl et al. [1991]
15	21	Ca^{2+}	6.7	Fluctuations in heart rate in Daphnia is maximized	Chemeris et al. [1993]
60	78.4	Ca^{2+}	0.13	Cephalic regeneration in planaria delayed 48 hrs.	Jenrow et al. [1995]
60	51.1	K^+	1.0	Regeneration rate unchanged when K^+ tuning is used instead of Ca^{2+} tuning	Jenrow et al. [1995]
60	78.4	Ca^{2+}	0.51	Regeneration anomalies occur at Ca^{2+} tuning for larger AC intensity	Jenrow et al. [1996)
16	20.9	Ca^{2+}	1.8	Enhanced rate of blastema growth during cephalic regeneration in planaria.	Tiras et al. [1996]
16	20.9	Ca^{2+}	0.24–9.6	Evidence that ICR effect on planaria regeneration has an intensity window.	Tiras et al. [1996]
30	39.1	Ca^{2+}	1.8	Evidence corroborating PRM prediction: Max effects on snail analgesia at AC/DC ratio of 1.8.	Prato et al. [1997]
60	78.1	Ca^{2+}	1.8	Effect of light on ICR modulation of snail opioid analgesia is independent of frequency	Prato et al. [1997]
120	156.2	Ca^{2+}	3.6	Effect due to light appears to scale with DC intensity	Prato et al. [1997]
60	78	Ca^{2+}	0–5.3	Ca^{2+} ICR variations with AC intensity support Lednev[1991]model.	Prato et al. [2000]
30	76	K^+	0–2.8	K^+ ICR effects on snail opioid analgesia are reversed with K^+ channel blocker	Prato et al. [2000]
35	45	Ca^{2+}	1.8	Maximum influence on bioluminscence of dinoflagellate Gonylaux in agreement with PRM model.	Berden et al. [2001]
35	45	Ca^{2+}	5.3	Influence reversed, again in agreement with PRM	Berden et al. [2001]
35	45	Ca^{2+}	3.8	No effect at ratio of 3.8, again in PRM agreement	Berden et al. [2001]

Table 7. ICR Effects on Plants

Freq (Hz)	B_o (μT)	Tuning	Ratio B/B_o	Comments	Reference
60	78.3	Ca^{2+}	0.26	Ca^{2+} ICR field stimulates radish growth after delaying germination	Smith et al. [1993]
60	153.3	K^+	0.13	K^+ ICR field enhances germination, reducing growth	Smith et al. [1993]
60	0			No effect	Smith et al. [1993]
60	78.4	Ca^{2+}	0.26	Ca^{2+} stimulates growth, slows germination	Smith et al. [1995]
60	39.2	Ca^{2+}	0.51	Ca^{2+} 2cd harmonic: no effect	Smith et al. [1995]
60	26.1	Ca^{2+}	0.77	Ca^{2+} 3rd harmonic: same as Ca^{2+} fundamental.	Smith et al. [1995]
60	153.3	K^+	0.13	K^+ fundamental results opposite to those of Ca^{2+}: growth inhibited, germination enhanced	Smith et al. [1995]
60	76.6	K^+	0.26	K^+ 2cd harmonic results weakly opposite to fundamental and 3^{rd} harmonics	Smith et al. [1995]
60	51.1	K^+	0.39	K^+ 3^{rd} harmonic: effect same as K^+ fundamental	Smith et al. [1995]
60	47.5	Mg^{2+}	0.42	Mg^{2+} fundamental stimulates growth	Smith et al. [1995]
60	9.5	Mg^{2+}	2.11	Mg^{2+} 5^{th} harmonic stimulates growth	Smith et al. [1995]
60	0			AC only: no effect	Smith et al. [1995]
60	78.3	Ca^{2+}	0.26	Replication of Smith[1993] work	Davies [1996]
60	78.3	Ca^{2+}	0.26	No effect on mustard plant; possible effect on barley plant	Davies [1996]
50	65.3	Ca^{2+}	0.61	Replication of Smith [1993] work on radish, for the 50 Hz Ca^{2+} ICR condition	Tohtz [1996]
50	39.6	Mg^{2+}	0.60	Replication of Smith [1993] for 50 Hz Mg^{2+} condition.	Tohtz [1996]
60	76.3	Ca^{2+}	0.26	Germination weakly enhanced following Ca^{2+} ICR exposure of dry radish seeds	Smith et al. [2000]
60	153.5	Mg^{2+}	0.13	No effect on germination	Smith et al. [2000]
60	47.6	K^+	0.42	Significantly greater (earlier) germination of dry seeds following K^+ ICR exposure.	Smith et al. [2000]
35.8	46.5	Ca^{2+}	1.84	Gravitropic response in millet, flax and clover seedlings enhanced by Ca^{2+} ICR.	Belova et al. [2000a]
58.7	46.5	Mg^{2+}	1.84	Gravitropic response unaffected by Mg^{2+} tuning	Belova et al. [2000a]
54.7	46.5	K^+	1.84	Gravitropic response inhibited by K^+ICR	Belova et al. [2000a]
33.8–37.8	46.5	Ca^{2+}	1.84	Frequency dependent gravitropic response exhibits Ca^{2+} peak, FWHM = 1.6 Hz.	Belova et al. [2000b]

Table 8. ICR Effects on Cell-Free Systems

Freq (Hz)	B_o (μT)	Tuning	Ratio B/B_o	Comments	Reference
8–20	20.9		1.0	Three frequencies (13.0, 14.0, 16.0) affect calmodulin-dependent phosphorylation	Shuvalova et al. [1991]
100	0–260		>0.45	No Ca^{2+} ICR effect on conductance in bilipd layer	Durney et al. [1992]
50–120	0–299		>0.31	No effect on binding of Ca^{2+} to calmodulin using Ca^{2+} ICR	Bruckner-Lea et al. [1992]
20	50	K^+	1.4	No changes due to ICR tuning in gram A channel conductance in lipid bilayer	Galt et al. [1993]
760	50	H^+	15.2	No changes due to ICR tuning in gram A channel	Galt et al. [1993]
0.1–40	25	Asn^+	0.002	Enhanced aqueous conductivity in asparagine solution at 2.9 Hz.	Novikoff and Zhadin [1994]
0.1–40	25	Arg^{2+}	0.002	Enhanced aqueous conductivity in arginine solution at 4.4 Hz.	Novikoff and Zhadin [1994]
0.1–40	25	Glu^+	0.002	Enhanced aqueous conductivity in glutamic acid solution at 2.5 Hz.	Novikoff and Zhadin [1994]
0.1–40	25	Tyr^+	0.002	Enhanced aqueous conductivity in glutamic acid solution at 1.9 Hz	Novikoff and Zhadin [1994]
0.1–40	25		0.2	ICR effect disappears at higher AC/ DC ratio	Novikoff and Zhadin [1994]
0.1–40	0		0.002	ICR effect disappears for very small DC fields	Novikoff and Zhadin [1994]
0.1–40	25		0.002	ICR effects disappear when AC & DC fields at 90°	Novikoff and Zhadin [1994]
12–60	20.9		1.0	No change in Ca^{2+} transport through patch-clamped cell membrane	Hojevic et al. [1995]
10–22	20.9		1.0	No change in Ca^{2+} transport through patch-clamped system, measured over loner times.	Hojevic et al. [1995]
1–10	20–40	Glu^+	.625-1.25 (x .001)	Changes in glutamic acid conductivity in solution. Good agreement with glu^+ ICR q/m prediction	Zhadin et al. [1998]
1–10	40		.25–2.0 (x .001)	Confirmation of earlier work; amino acid response at AC levels of .02-.04 μT.	Zhadin et al. [1998]

Table 8. ***Continued***

Freq (Hz)	B_o (μT)	Tuning	Ratio B/B_o	Comments	Reference
0–10	40	Arg^{2+}	0.001	Sharp change in conductivity observed at 7. 1 Hz, the ICR tuning point for Arg^{2+}.	Del Giudice et al. [2002]
20.6	48?	$H_3O^+(H_2O)$	.02	ICR fields applied to ultra-pure (18.2 MΩ-cm) water for one minute triggers long-term increases in conductivity.	Mohri and Fukushima [2002]
40.1	48?	H_3O^+	.02	Data in agreement with ICR effect in hydronium ion	Mohri and Fukushima [2002]
530	35?	H^+	.03	Data in agreement with ICR effect in proton	Mohri and Fukushima [2002]
16	20.9	Ca^{2+}	1.0	Binding of Ca^{2+} to calmodulin not enhanced using Ca^{2+} ICR fields	Liboff et al. [2003]

However, this equation applies only to a charged particle in free space and does not take account of possible damping forces. In a denser medium, one usually adds a damping term proportional to the velocity, resulting in

$$\mathbf{a} = (\mathrm{q/m})\,(\mathbf{E} + \mathbf{v} \times \mathbf{B}) - \mathbf{v}/\tau \tag{4}$$

where τ is the mean time interval between collisions.

In attempting to apply this approach to weak field biointeractions, the author [Liboff, 1985] argued that the membrane bound ion channel should be considered as the likely interaction site. Ion channels function as ion-selective bypass shunts across the electrically insulating lipid membrane of the cell. In so doing they exhibit remarkably large conductivities. The effective resistivity is many orders of magnitude less for ion channels than it is for the bilipid membrane [Kuyucak et al. 2001]. Since resistivity is one indication of collision rate, this in turn suggests that, if an ICR interaction occurs within an ion channel it may be reasonable to ignore the damping term in Equation (4).

As an example, consider the maxi-K^+ channel, which has a conductance of the order of 200 pS. This value is surprisingly large, considering that it results from a charge flow through an orifice approximately 1.5 Å in radius [Aidley and Stanfield, 1996], and about 40 Å in length. Simple calculation yields an effective resistivity for this channel of approximately 0.10 ohm-m. One can infer that the movement of ions through channels is hardly subject to the normal damping forces usually encountered in the biological milieu.

For the case where the damping term $\mathbf{v}/\tau$ can be ignored, and where the electric field **E** is zero, one can readily show that a unique frequency is attached to the ion. If the particle is initially directed at a 90° angle to **B**, the Lorentz Force causes the ion to move in a circular path of radius ρ, such that the centripetal force mv^2/ρ is equal to the Lorentz Force qvB. The radius of this circle is therefore

$$\rho = (\mathrm{m/q})\,\mathrm{v/B} \tag{5}$$

Moving at constant speed in this circle, the frequency of rotation for the particle will be determined by the period of motion T, equal to $2\pi\rho/v$, or, substituting from Equation. (5), $2\pi m/(qB)$. The frequency of rotation that results is therefore the same as shown in **Eq. (1)**, and, given the relation between angular frequency ω and linear frequency f_c, namely $\omega_c = 2\pi f_c$., we find

$$f_c = (1/2\pi)\, qB/m. \tag{6}$$

Note, as we have stated above, that this frequency is completely independent of the particle's energy as well as the radius of its path.

This frequency remains the same even when the electric field is finite. However, in this case the trajectory is not circular but helical, the axis of the helix determined by the direction of the electric field. This is interesting since the wrap-around protein configuration of the walls of the ion channel also describes a helix [Li-Smerin et al. 2000]. This in turn implies a helically shaped potential within the channel, and the possibility that the ionic path intrinsically exhibits some degree of helical motion as it traverses the channel. Note that for an ion with a non-uniform charge distribution, this helical path need not be that traversed by the atomic mass per se. Since the structure of the channel lumen gives rise to a helical potential along its length, one might expect an enhanced ionic transport if the temporal rotation of excess charge about the center of mass occurred in phase with this spatial helical potential.

One can then argue that resonance effects might occur with the application of an additional external electromagnetic field having this frequency. In a biological milieu one can consider that, under the assumption of little or no damping, the frequency f_c is an intrinsic frequency, independent of the radius of curvature ρ and consequently, of the ion's kinetic energy. In other words, whether the radius of the path is 1 meter or 1 Å, the value of f_c depends only on B and q/m. Further, if one considers the charge to mass ratios of some key biological ions (e.g., Ca^{2+}, K^+, Mg^{2+}, ...) their cyclotron resonance frequencies, as determined in the earth's magnetic field are found to be in the ELF range.

A number of cations have been highlighted as possible ICR candidates. Table 9 shows the relevant characteristics for ten such ions. Note that the sodium ion is not included in Table 9. Although Na^+ certainly carries considerable physiological importance, there have

Table 9. Cation Candidates for in vivo ICR Response

Ion	q/m (Coul/Kg) $\times 10^{-6}$	f_c/B (Hz/μT)
H^+	95.76	15.241
Li^+	13.90	2.212
Mg^{2+}	7.937	1.263
Ca^{2+}	4.814	0.766
Zn^{2+}	2.951	0.470
K^+	2.467	0.393
Arg^{2+}	0.554	0.176
Asn$^+$	0.730	0.116
Glu$^+$	0.656	0.104
Tyr$^+$	0.532	0.085

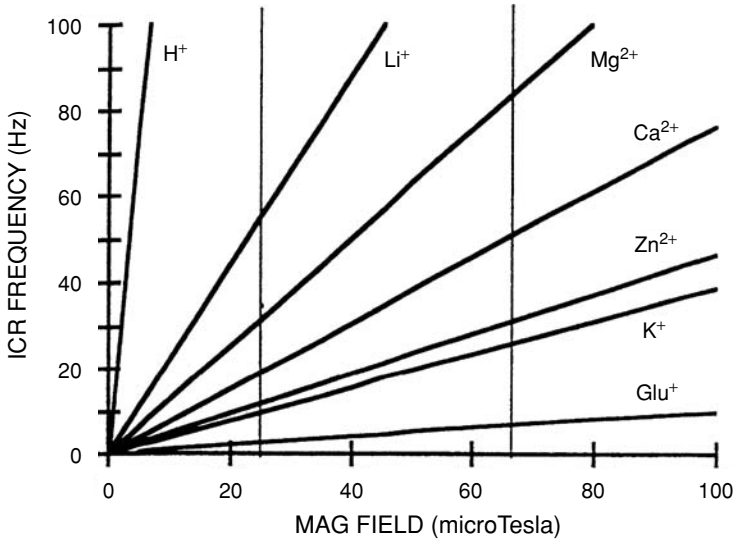

Figure 1. ICR frequencies for seven cations as a function of the magnetostatic field. The two vertical lines represent the limits of the geomagnetic field.

been no observations to support the suggestion that it can be stimulated by means of ICR combined fields.

The fundamental frequencies for seven of the ions listed in Table 9 are plotted in Fig. 1 for magnetostatic fields ranging from 0 to 100 μT, The two vertical lines represent the lower and upper limits of the (total) GMF at the earth's surface. It is seen that at the two frequency extremes, heavier ions such as polar amino acids have lower ICR frequencies, whereas protons require much higher frequencies. Also note that the biologically interesting ions Ca^{2+}, Mg^{2+}, and K^{+} enjoy resonances within the limits of the GMF in the range 10–80 Hz, a frequency range of some relevance to electric and power generation and transmission.

The underlying basis for cyclotron resonance also allows for higher harmonic frequencies. Consistent with this, effects have been reported at higher multiples of the frequency given in Eq. (6). [McLeod et al. 1987, Smith et al.1995]. Also consistent with the underlying physics is the fact that these additional harmonic frequencies are limited to odd multiples of the fundamental frequency.

$$f_n = (2n + 1)(1/2\pi)(qB/m) = (2n + 1)f_c. \tag{7}$$

The appearance of harmonics leads to a rich and surprising set of interactive possibilities. Consider Table 10, which shows the fundamental, 3rd, and 5th harmonic frequency for four ions. Some of the values listed in Table 10 are numerically close to one another. The 5th harmonic of Ca^{2+} is slightly more than 1% greater than the 3rd harmonic for Mg^{2+}. In effect this means that the same combination of AC and DC fields can be used to stimulate two different ions. This approach was used to advantage in the FDA-approved design of two widely used devices in bone repair (OrthoLogic, Inc, Tempe, AZ) where simultaneous stimulation of both ions is preferable to either Ca^{2+} or Mg^{2+} stimulation alone.

Table 10. First Three ICR Harmonics for Four Biologically Relevant Ions

Ion	Fundamental f_c/B: (Hz/□T)	3rd Harmonic f_1/B: Hz/□T)	5th Harmonic f_2/B: (Hz/□T)
$\mathbf{Mg}^{2+}$	1.26	3.79	6.31
$\mathbf{Ca}^{2+}$	0.77	2.30	3.83
$\mathbf{Zn}^{2+}$	0.47	1.41	2.35
$\mathbf{K}^{+}$	0.39	1.18	1.97

OBJECTIONS TO THE CLASSICAL APPROACH

There are some strong theoretical arguments [Liboff, 1985] against the likelihood of weak-field ICR effects in biological systems. One of these has already been mentioned, namely the difficulty in maintaining cyclotronic motion in a highly damped milieu. The relatively high conductivity within ion channels tends to counter this argument. Another problem is that the charge-to-mass ratio for free biological ions is almost always poorly defined, because of the waters of hydration that inevitably surround ions in solution. Ionic motions, in solution, never really involve the ion by itself, but rather a complex of the ion plus a group of water molecules moving as a single entity. This implies that the ionic charge-to-mass level is not determined by the "naked" ionic mass. The ratio of q to m is consequently lowered, resulting in lower and generally unpredictable values for the ICR frequency.

However, this argument fails to hold for the *interior* of membrane ion channels, where it is well established [Hille, 1984] that in many cases ions are transported alone, devoid of their hydration layers. This is made possible because these waters are replaced upon entering the channel by an equivalent structural lining that is fixed on the wall of the channel lumen (Fig. 2).

Although these questions of damping and hydration can be dealt with in a reasonable way, there is a more serious problem that probably constitutes the strongest argument against ICR magnetic fields directly stimulating the transport of ions within the channel. The transit time for ions within channels can be as short as 10^{-9} seconds. By contrast, a number of successful ICR experiments have been carried out at a frequency of 16 Hz, implying a transit time of the order of 10^{-2} s. Nonetheless, it is very tempting to think that the membrane ion channel is somehow closely involved in the question of ICR interactions. For example, it is conceivable instead that the gating mechanism for ion channel transport, a much slower process, may be stimulated by such magnetic fields.

This would require that the portion of the channel protein that acts as the gate: (1) accepts the same ionic species as in the main pore, (2) also has a helical structure, and (3) acts slowly in accord with the time constraints imposed by Eq. (1).

There is also the more general objection to the likelihood of weak field biological interactions, often termed the kT effect. This follows from the limitations on information transfer due to thermal noise. Weaver and Astumian [1990] suggested that in order for an electrical signal to initiate a biological effect, the signal strength must be at least equal to the thermal noise voltage δV as derived from the expression for its mean square fluctuation:

$$(\delta \mathrm{V})^2 = 4\mathrm{RkT}\ \delta\nu \tag{8}$$

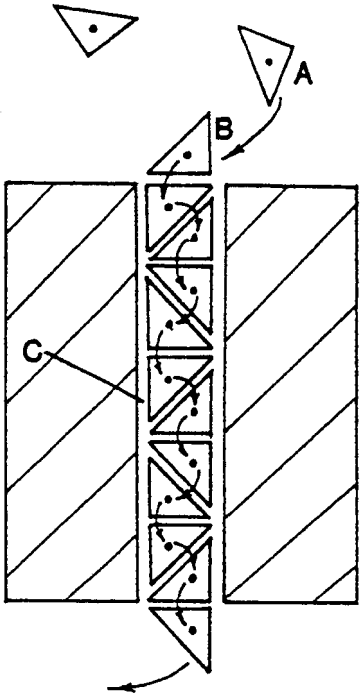

Figure 2. Non-hydrated transport of ions through membrane ion channel. Hydrated layers attached to ion when it is away from mouth of channel, A, are released at mouth B, where ion exchanges its water layers for an equivalent structure that lines the lumen (C). The exchange at B occurs with little or no energy expenditure.

where k is Boltzmann's universal constant, T the absolute temperature, R the resistance of the entity involved, and $\delta\nu$ the frequency bandwidth of the thermal noise spectrum. However, even apart from the resonance nature of the q/m effects, there are some serious questions [Liboff and Jenrow, 2000a] concerning the manner in which this expression has been applied to bioelectromagnetic sensitivity. Most critically, it is not proper to use the electrical properties of membrane lipids, properties more suitable for making calculations for electroporation threshold voltages, when studying weak field ELF bioeffects. Wherever the site of such interactions happens to be, it is highly unlikely that it occurs directly in the cell membrane, arguably that component of the cell having the greatest specific resistance. It is more reasonable to consider those proteins lodged within or attached to the membrane that have effective resistances that are many orders of magnitude lower than the membrane itself. Furthermore, when dealing with resonant phenomena, the bandwidth term in Eq. (8) becomes a critical factor, no less important than the resistance.

By and large, one must recognize that the limitations on weak field effects and, especially those effects that appear to be the result of q/m resonances, have to be imposed by the body of experimental work itself, and not by inappropriate theoretical constructs.

As a very good example of the futility at present in attempting to relate fluctuation expectations to observation, it has recently been reported [Mohri and Fukushima, 2002] that short applications (60 seconds) of ICR-tuned fields act to trigger large, reproducible

Table 11. Candidates for ICR Effects in Water

Ion	q/m (Coul/Kg) $\times 10^{-6}$	f_c/B (Hz/μT)
OH^-	5.667	0.902
H_3O^+	5.066	0.807
$H_3O^+(H_2O)$	2.603	0.414
$H_3O^+(H_2O)_2$	1.751	0.278
$H_3O^+(H_2O)_3$	1.320	0.210
$H_3O^+(H_2O)_4$	1.059	0.168
$H_3O^+(H_2O)_5$	0.884	0.140
$H_3O^+(H_2O)_5 \cdot OH$	0.765	0.121

decreases in the resistivity of highly purified water. The frequencies used in this experiment were in the ELF range and the AC intensity used was extremely small, only 1 μT. Outside of diamagnetic effects in intense magnetic fields [Ueno and Iwasaka, 1994] and molecular responses at microwave frequencies [Frolich, 1980], there is no known interaction that can explain such results. Nonetheless, this work is highly provocative because of the correlation of the ICR triggering frequencies that were used with the number of water clusters attached to the H_3O^+ ion. Table 11 gives the relevant characteristics for those cationic clusters that were found to be most effective in reducing resistivity. (Compare with Table 9).

One interpretation of the observed continuing drop-off in resistivity following the short initial stimulation is that the ICR magnetic field somehow results in a self-sustaining polymerization that is reflected in the resistance. This work represents a possible consolidation of many previous studies [Ayrapetyan et al. 1994, Rai et al. 1995] that have reported difficult-to-understand effects of magnetic fields on the physical properties of water.

RESONANCE FUNCTION

Experimentally, one can explore the biological response as the magnetic field frequency is varied through the expected resonance frequency given in Equation (6). This is particularly useful since there is a good theoretical description of how any physical system enjoying cyclotron resonance effects is expected to vary as a function of frequency.

We rewrite Equation (4)

$$m(d\mathbf{v}/dt + v/\tau) = q(\mathbf{E} + \mathbf{v}\times\mathbf{B}) \tag{9}$$

and assume that **B** is constant and directed along the z-axis, and that **E** is directed along the x-axis and varies sinusoidally in time, as

$$E = \mathbf{E}_o e^{i\omega t} \tag{10}$$

The configuration where **E**(t) and the static **B** field are at 90° is closely equivalent [Liboff, 1997] to the experimental conditions mentioned in the Introduction, where resonance occurs when constant and time varying magnetic fields are applied in parallel directions. Indeed, mathematically there is little difference between the way parallel AC and DC magnetic act on a moving charged particle, compared to the way that perpendicular AC electric and DC magnetic fields act. Note that Eq. (9) is the most general expression possible for the case

of a charged particle moving in combined electric and magnetic fields. The electric field **E**, as given in Eq. (10), is assumed to be induced by a sinusoidal **B**-field. It does not include local electric field components that are independent of those induced by **B**. In addition, the magnetic field is not constant, but can vary, in the simplest case, as:

$$\mathbf{B} = \mathbf{B}_o(1 + \cos \omega t) \tag{11}$$

Apart from the induced electric field given in Eq. (10), the time-varying magnetic field component will, in effect, add a perturbation to the resonance frequency. However, if **B** is linearly polarized, the cross-product $\mathbf{v} \times \mathbf{B}$ term in Eq. (9) does not change direction, even if **B** is time-varying. This more general solution for Eq. (9), including the effects of the time-varying magnetic field, has been examined in detail [Durney et al., 1988], and does not alter any of the basic conclusions arrived at by assuming that **B** is merely constant. In effect the perturbation of the resonance frequency does not change its mean value from that given in Eq. (6).

In this way, starting with Eq. (9), it can be shown [Liboff and McLeod, 1988] that σ_x/σ_o, the relative conductivity of charge carriers in the x-direction, with and without the resonance combination of fields, is given by the following expression

$$\sigma_x/\sigma_o = (1 + (\omega_c + \omega)^2\tau^2)/\{1 + [\left(\omega_c^2 - \omega^2\right)g\tau^2]^2 + 4\omega^2\tau^2\} \tag{12}$$

Fig. 3 explores the variation in σ_x/σ_o as a function of both the frequency ratio ω/ω_c and the time interval between collisions τ. The resonance frequency ω_c in this plot is arbitrarily set equal to 100 radians per second, corresponding approximately to 16 Hz. This in turn establishes the minimum cutoff value. For values of the collision time shorter than $1/f_c$, in this case 0.01 s, one cannot expect any cyclotron resonance effect As Fig. 3 indicates, the resonance at $\omega = \omega_c$ is well delineated for larger values of τ.

The question of the damping of ionic motion in biological systems is very interesting. [Durney et al. 1988] concluded that such ion cyclotron resonance effects were very unlikely because of the extremely high collision rates for ions in solution. However this possibility was already discounted, when in the author's original suggestion [Liboff, 1985], it was pointed out that there was a good likelihood of greatly reduced damping in ion channel proteins.

RELEVANT EXPERIMENTAL RESONANCES

One of the successes of the ICR hypothesis was the use of Equation (12) to explain the shape of the nonlinear response observed in the so-called calcium-efflux experiments [Bawin et al. 1975, Blackman et al. 1982]. It was shown [Liboff and McLeod, 1988] that the original data points can be closely fitted (Fig. 4) to this equation, providing that the experiment was conducted in a DC magnetic field of 35.0 μT, with a collision time τ equal to 0.026 seconds. Although both values are reasonable considering the geomagnetic field at the laboratory where the calcium efflux studies were done, as well as the cutoff collision time mentioned above, the third conclusion from this data fit, namely the value of the q/m ratio, was unexpected.

The q/m value required for the best fit corresponded to the K^+ ion, a surprising result considering that the experimental procedure was focused on the calcium ion. However, a

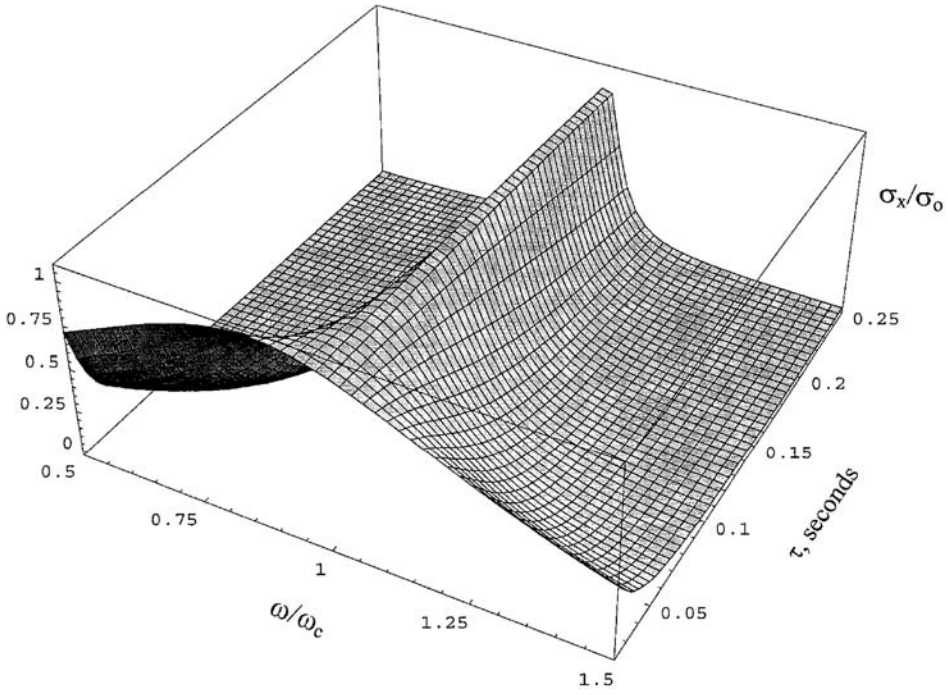

Figure 3. Conductivity of a charged particle moving in combined AC and DC magnetic fields as a function of frequency and the time interval between collisions.

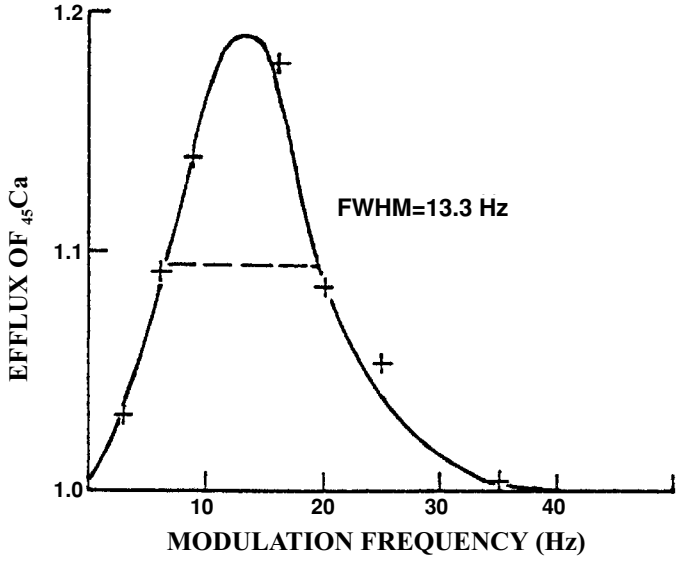

Figure 4. Fitting the calcium-efflux results [Bawin et al. 1975] to equation (12). The crosses are the original data points, and the solid line represents the theoretical result. The assumptions used to obtain the theoretical curve include a DC magnetic field of 35.0 μT, a collision time of 0.026 seconds, and a charge-to-mass ratio corresponding to the potassium ion.

subsequent report [Blackman et al.1985], also examining calcium efflux from brain tissue in a model system similar to the original calcium-efflux model system, found that three ratios of frequency to DC field produced cyclotron resonances, namely 0.39. 0.39, and 1.18 Hz/μT. Examining Table 10, it is clear that these values correspond closely to the cyclotron resonance conditions associated with the potassium ion, thereby adding considerable weight to the conclusion that this ion is intimately connected to the electromagnetic effects resulting in altered calcium efflux.

This question of why a potassium resonance leads to a change in calcium ion concentration has yet to be explained. Presumably, it is related to charge balance within the cell, perhaps indicating that an increase in K^+ channel transport tends to enhance calcium ion pump activity.

In addition to using Eq. (12) to retrospectively examine data from the calcium-efflux experiment, a number of other experiments have been carried out, specifically designed to look for resonances. Two such examples are the resonances discovered in diatom motility [Smith et al. 1987] and in insulin-like growth factor–II (IGF-II) receptor concentration in bone cell culture [Fitzsimmons at al. 1995]. In contrast to the earlier K^+ resonances observed [Bawin et al.1975, Blackman et al.1982] the maxima observed in both cases clearly corresponds to the Ca^{2+} charge-to-mass ratio, 0.765 Hz/μT.

A good measure of comparison for these various model systems is found in the Full-Width Half-Maximum (FWHM) that can be assigned to each resonance curve. Strictly speaking the FWHM applies to oscillating systems that are simpler than that described by Equation (9). Nevertheless this approach provides an easy way to compare resonance effects, in particular the extent of damping.

Thus, if one considers the relative energy $I(\omega)$ radiated by a molecular oscillator having a resonance frequency ω_r [Jackson, 1967].

$$I(\omega) = I_o\{\Omega^2/((\omega - \omega_r)^2 + \Omega^2)\}, \tag{13}$$

the FWHM is defined as $2\Omega = 1/\tau$.

Remarkably, for the two very disparate model systems, diatom motility and IGF-II receptor concentration, both systems exhibit resonances with approximate FWHM values that are approximately the same, 12 Hz, corresponding to a collision time of 0.08 seconds. On the other hand, the results of Bawin et al. [1975] on calcium ion efflux from brain tissue, which we have indicated as apparently connected to a potassium resonance, exhibit a FWHM of 13.3 Hz, or an effective collision time of 0.075 seconds.

ION PARAMETRIC RESONANCE

One obvious problem in pursuing the question of ICR using Eq. (8) as a starting point is that this fails to involve the AC magnetic intensity. The Lorentz Force by itself does not yield any information to help explain the the resonance varies as a function of magnetic intensity. It is reasonable to think that some threshold intensity level is necessary before magnetic interaction effects can occur. Indeed, a clear threshold effect was observed in studies on ICR effects on rat behavior [Liboff et al. 1989].

Lednev [1991] has used a novel approach, termed parametric resonance after a phenomenon found in atomic spectroscopy, to achieve a functional dependence of the

charge-to-mass signature effect on magnetic intensity. When the calcium ion is bound to a calcium-binding protein such as calmodulin, the excited energy levels for this new ion-protein complex will be split by the application of a magnetostatic field B_o, such that the difference in frequencies corresponding to the two new levels is equal to the cyclotron resonance frequency:

$$\omega_c = \omega_1 - \omega_2. \tag{14}$$

In the additional presence of a collinear AC magnetic field, these sublevels ω_1 and ω_2 are modulated in frequency leading to a net probability of transition to the ground state that is calculable in terms of the ratio of the AC magnetic intensity to the DC magnetic intensity, B/B_o. In this way, the possible dependence of the ICR effect on AC magnetic intensity is explicitly available in terms of the probability p(B) of Ca^{2+} transitions to the ground state. The field dependent part of this probability is

$$p(B) = (-1)^n K J_n(nB/B_o) \tag{15}$$

where K is a constant and J_n is the nth order Bessel function having the argument (nB/B_o). In Fig. 5, we plot the first three values of the Bessel function $J_n(nB/B_o)$.

Although there is no additional information relating to the question of intensity threshold in Eq. (15), there is a very specific prediction regarding the form of the response as the intensity varies. Since the first extremum of $J_1(B/B_o)$ occurs at an AC/DC intensity ratio of 1.84, this allows one to design experiments for which the response of the model system is obtained as a function of the argument (B/B_o), to see whether the maximum response does indeed occur when the AC intensity is 1.84 times larger than the DC intensity. There is some question as to whether this predicted response has actually been observed. On the one hand, Prato et al [1995] has presented data tending to confirm the prediction implicit in Equation (15). However, experiments by Smith et al [Smith et al. 1987, 1991, 1993] appear to indicate that the maximum ICR response occurs when the ratio B/B_o is equal to unity. Further complicating this picture, possibly, is Faraday's Law of Induction. Increasing the intensity of B will always cause larger induced currents, possibly leading to extra biological responses that are independent of those that are q/m-related [Jenrow et al. 1996].

It must also be noted that many of the positive results listed in Tables 1–8 employed AC/DC intensity ratios well below 1. For example, this ratio in Zhadin's work on amino acids [Novikoff and Zhadin, 1994] was .002. This is hard to explain using the PRM model, since the Bessell function J_n (nB/B_o) appearing in Eq (15) tends towards zero for vanishingly small values of the ratio B/B_o.

An alternative formulation, very similar to that of parametric resonance, but not necessarily involving calcium-binding proteins, has been suggested by Blanchard and Blackman [1994]. If the ratio B/Bo in Equation (15) is given by r, then the Blanchard/Blackman expression for the expected probability p(B) has the functional dependence $J_n(n2r)$. Thus if $J_1(r)$ has its first maximum at $r = 1.84$, Blanchard/Blackman predicts this maximum will be shifted to $r = 0.92$. This is much closer to the empirical Smith criterion, but still cannot account for those reported effects when $r \ll 1$. An extensive set of data have been advanced [Blackman et al.1994] in support of this model (termed IPR), relating observed changes in neurite outgrowth to the predicted dependence of these changes as a function of the ratio B/B_o. One problem with this work is the stipulation that five separate ionic species (Mg^{2+}, H^+, Mn^{2+}, Li^+, and V^{4+}) are jointly stimulated, in spite of the fact that the combinations

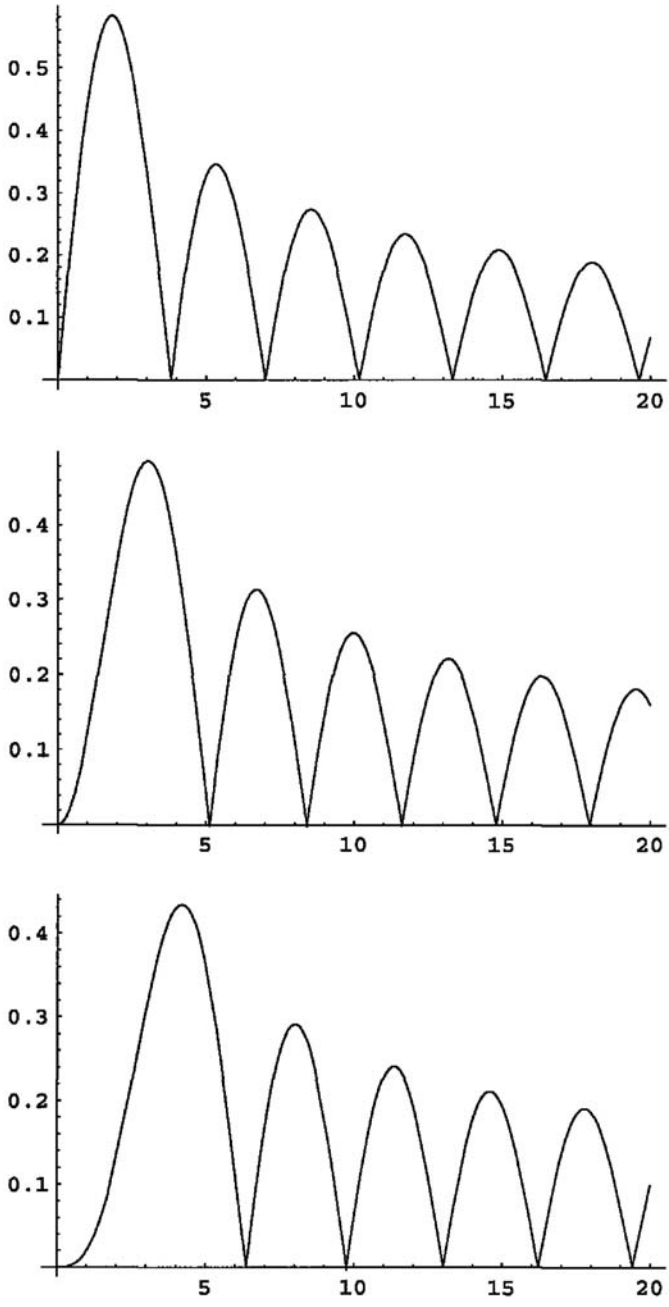

Figure 5. Absolute Bessell function $|J_n(nr)|$ for n = 1, 2, and 3 ($|J_3(3r)|$ at bottom), plotted for ratios of AC to DC intensity up to $(B/B_o) = 20/n$.

of fields that were employed in support of this multi-ion concept are all, without exception, closely equivalent to the ICR condition for the magnesium ion alone. For a second group of field combinations the claim that four new separate ions (Ca^{2+}, Co^{3+}, Ni^{3+}, and Fe^{3+}) were stimulated is also subject to the simpler interpretation that there is only one ion involved, namely Ca^{2+}. Nevertheless, despite the fact that the foundations of the IPR model may be imperfect, the underlying data set is rather impressive.

Adair [1992, 1998] has criticized the various parametric resonance approaches, for some of the same reasons he and others [Weaver and Astumian, 1990, Adair, 1991] have raised against the likelihood of any weak ELF magnetic field effect on biological systems. The transition energy in Eq. (14) at 40 Hz is only 10^{-11} of the thermal energy kT, which would tend to greatly suppress any Zeeman splitting. Further as mentioned above, there is a severe theoretical constraint on any process involving a cyclotron frequency, namely the ultra-short collision times τ that will prevent an ICR response $2\pi/\omega_c$, that is, by definition, much longer, from occurring. For these and other reasons, Adair concludes that magnetic frequencies at ω_c cannot affect the Ca^{2+} transition rate to the ground state.

A totally different approach to the question of ion binding has been taken by Binhi [2000] who has studied possible interaction mechanisms at the protein binding site, asking whether the magnetic field can affect the dissociation probability. Starting with Schrodinger's equation, he has shown that ICR magnetic field combinations can redistribute the ionic probability density when one takes into account interference effects between quantum states, with the wave function shrinking sufficiently to allow the ion to escape. However, the actual size of the ion makes such quantum interference effects rather unlikely.

ROTATION OF ION OSCILLATION/PRECESSIONAL EFFECTS

Another possible explanation for the ICR experimental results takes note of magnetically-induced changes in the thermal energy distribution, with specific reference to Larmor precessional effects [Edmonds, 1993, Zhadin, 1998]. Unlike other models which find the problem of thermal noise difficult to overcome, thermal fluctuations in this case are used to advantage, since limited components of this motion may actually be enhanced under the ICR condition. Changes in biological response would therefore not be associated with dissociative processes between ion and protein, as in the previous cases, but rather with transfers of energy to the protein by the ion. Zhadin [1998] has estimated that changes up to 10% in the initial thermal energy of the ion might occur, and these would be sufficient to trigger important changes in the conformational state of the macromolecule.

ELECTROMAGNETIC COHERENCE DOMAINS

The most recent approach to the q/m question has been advanced by del Giudice et al. [2002] who has framed the problem in terms of quantum electrodynamics. It is hypothesized that the behavior of ions in solution can not be explained by means of electrostatic interactions of the type that are described using classical Maxwell/Boltzmann statistics and the consequent limits corresponding to kT constraints. Instead of an ensemble of loosely coupled gas-like particles, del Giudice argues that at microscopic distances, one should

consider coherent highly ordered configurations, or coherent domains, whose size is the wavelength of the resonating electromagnetic field.

This approach has been used to provide an explanation for the provocative earlier experimental results by Zhadin et al. [1998] (Table 8) in a non-biological system, where the conductivity of glutamic acid in aqueous solution appeared to be sharply altered at the corresponding ICR magnetic field combination. Del Giudice et al. [2002] have successfully repeated this experiment, using, however, polar arginine in solution instead of glutamic acid (See Table 9). One difference remains, in that the observation by Zhadin et al. [1998] found differences in conductivity resulting from different pH levels that corresponded to valence changes in the amino acid and thus to different values of q/m resonances, an effect that was not observed by the Italian group.

DISCUSSION

The results summarized in Tables 1–7 provide strong evidence in favor of a weak ELF magnetic interaction in biological systems carrying a charge-to-mass signature that corresponds to a number of key biological ions.

This interaction is quite similar to what might be expected from an ion cyclotron resonance effect, mainly because the interaction signature clearly involves the ICR, or cyclotronic frequency. However, it has not been possible to formulate a reasonable theoretical basis for such an effect. The weight of experimental evidence has muted the sometimes strident criticisms [Halle 1988, Sandweiss 1990, Bennett 1994] insisting that resonance effects are impossible because of energetic difficulties connected to damping losses. If nothing else, the findings connected to the ICR studies has made it very evident that one cannot depend completely on the macroscopic descriptions of ions in solution when studying the dynamics of ion binding at the protein level.

Without doubt, the most important aspect of all the experimental and theoretical work connected to charge-to-mass signature effects is the refreshingly rational discourse now surrounding the question of weak field ELF bioelectromagnetic interactions. Much of the earlier research was constrained by an approach that insisted that since electromagnetic interactions had to be framed in terms of Joule heating, experimental reports claiming weak-field effects were highly unlikely. There is now little dispute that such effects do indeed occur. The engineering approaches of the past have been replaced with inquiries that are more freely scientific in tone, searching for better theoretical constructs to explain the growing base of experimental observations.

Nowhere is this sea change better illustrated than in the original discussions surrounding the calcium-efflux experiments [Bawin et al. 1975, Blackman et al. 1982]. The fact that different observers found changes that were sometimes in opposite directions, a calcium influx occurring in some laboratories and an efflux at other places, led some to dismiss this entire body of work. The ICR experimental record [Liboff, 2002] has since made it clear that relatively small shifts in the local magnetic field or, equivalently according to Eq. (1) in the frequency, can result in opposite physiological outcomes. This is dramatically illustrated in Table 12, which lists six such reports.

This type of opposite response in the data represents an important clue in trying to comprehend the action of the ICR effect at the molecular level. It is difficult in this context to

Table 12. Opposite Responses Resulting from Shifts in Frequency or Field

Model System	Reference	Freq, Hz	B_o, μT	ION	Response
Diatom motility	[Smith et al. 1987]	16	20.9	Ca^{2+}	Motility incr
		16	41.0	K^+	Motility decr
Embryonic bone	[Smith et al. 1991]	16	20.9	Ca^{2+}	Growth incr
	[Regling, 2002]	16	40.7	K^+	Growth decr
Plant growth	[Smith et al. 1993]	60	78.3	Ca^{2+}	Growth incr
		60	153.3	K^+	Growth decr
Rat behavior	[Zhadin et al. 1999]	63	50	Mg^{2+}	Activity incr
		38	50	Ca^{2+}	Activity decr
Gravitropic response	[Belova & Lednev, 2000]	35.8	46.5	Ca^{2+}	Response incr
		54.7	46.5	K^+	Response decr

argue that a precessional mechanism [Zhadin, 1998] can give rise to such behavior. On the other hand, one can expect just such responses when looking at the effects of competitive ion concentrations on cell metabolism and signaling. A good example is to compare the relative effects of binding Ca^{2+} and Mg^{2+} to NMDA. The concentration of Ca^{2+} in the cytoplasm, itself an implicit function of other ionic concentrations, is carefully regulated through the use of calcium pumps, because the production of key enzymes such as cAMP is enhanced or inhibited depending on the cytoplasmic calcium ion concentration. Because of this it is hard to dismiss the notion that the action of ICR fields must have its origin in membrane-bound cell channels or in those close-by proteins involved in the cell-signaling process.

One of the most interesting results that appears to have escaped general attention is the remarkable similarity between two very distinct and completely independent model experiments, the one examining diatom motility and the other IGF-II receptor concentration. Both indicate a clearly defined peak when the magnetic frequency is varied, this peak very close to the predicted charge-to-mass ratio for Ca^{2+}. Further, the FWHM for both tuning curves is the same, corresponding approximately to a collision time of 0.08 s. Although this is many orders of magnitude longer than observed ionic transit times in membrane ion channels, one must realize that there are other physiological relaxation times that are as long if not longer than 10 ms. In particular it is worth noting that such times are associated with voltage gating mechanisms in ion channels [Kuyucak et al. 2001]. To initiate the opening of an ion channel, the voltage gating process can involve the slow passage of just a few ions at a time. In other words, it may be worth considering that the site for the ICR interaction occurs within those components of the channel protein that control the opening and closing of the channel pore. This site would still be specific to the ion type, and also involve times that are consistent with the lengthy ICR periods. This might also explain the fact that Na^+ resonance stimulation is never observed, since the gating mechanisms associated with the Na^+ channel are much faster than for Ca^{2+} and K^+.

Because there exist a variety of time-varying electric fields in the body (intracellular oscillations, EEG, peristaltic and cardiac signals) the author [Liboff, 1997] hypothesized that ICR conditions may very well occur naturally in living systems. This possibility stems from the ubiquitous exposure of all living things to the earth's magnetic field (GMF). In this case the resonance follows from the perpendicular orientation of the time-varying electric

field with the local GMF. Even though the vectors have to be at 90° for E-field ICR to maximally occur, the resonance frequency in Eq. (6) still applies, the only difference being that one uses the frequency of the electric field instead of the magnetic field. Thus, E-field ICR represents a potential means whereby the GMF can interact naturally with living things. If this is indeed true, then it is reasonable to think that ICR mechanisms may have been incorporated into living things during the long-term processes of evolution [Liboff and Jenrow, 2000b].

Finally, it is difficult, at first glance, to reconcile the experimental ICR results involving the charge-to-mass ratios of biological ions with q/m ratios of water complexed with the hydronium ion. One can speculate that both types of observations can perhaps be reduced to the way in which ions move in magnetic fields. In the one case, it has been argued that the Lorentz force causes ions such as Ca^{2+}, K^{+}, and Mg^{2+} to execute their helical paths within a membrane bound protein. In the second case, it is possible that this same force causes the complex ion H_3O^{+} $(H_2O)_n$ to move in its helical path within the overall constraints of the local water structure. In any case, it is provocative to realize that two such radically different types of observations have surfaced, that they seem to be connected, and that both are in principle, strongly forbidden from occurring because of well-established theories governing thermal fluctuations.

REFERENCES

Adair, R.K., 1991, Constraints on biological effects of weak extremely-low-frequency electromagnetic fields. *Physical Review A* 43: 1039–1048.

Adair, R.K., 1992, Criticism of Lednev's mechanism for the influence of weak magnetic field on biological systems. *Bioelectromagnetics* 13: 231–235.

Adair, R.K., 1998, A physical analysis of the ion parametric resonance model. *Bioelectromagnetics* 19: 181–191.

Aidley, D.J., and Stanfield, P.B., 1996, *Ion Channels*. Cambridge University Press, Cambridge, p. 146.

Ayrapetyan, S.N., Grigorian, K.V., Avansion, A.S., and Stanbltsian, K.V., 1994, Magnetic fields alter electrical properties of solutions and their physiological effects. *Bioelectromagnetics* 18: 133–142.

Bassett, C.A.L., Pawluk, R.J., and Pilla, A.A., 1974, Acceleration of fracture repair by electromagnetic fields: A surgically non-invasive method. In: Liboff A.R., and Rinaldi, R.A., Editors, *Electrically Mediated Growth Mechanisms in Living Systems*. Ann. N.Y. Acad. Sci. 238: 242–262.

Bawin, S.M., Kazmarek, K.L., and Adey, W.R., 1975, Effects of modulated VHF fields on the central nervous system. *Ann. NY Acad. Sci*. 247: 74–81.

Belova, N.A., and Lednev, VV., 2000a, Activation and inhibition of gravitropic response in plants by weak combined magnetic fields. *Biophysics* 45: 1069–1074.

Belova N.A., and Lednev V.V., 2000b, Dependence of gravitropic rersponse in the segments of flax stems on the frequency and amplitude of weak combined magnetic fields. *Biophysics* 45: 1075–1078.

Bennett, W. R., Jr., 1994, *Low-frequency Electromagnetic Fields and Health*. Yale Univ. Press, New Haven.

Berden, M, Zrimec, and Jerman, I., 2001, New biological detection system for weak ELF magnetic fields and testing of the parametric resonance model. *Electro- and MagnetoBiology* 20: 27–41.

Binhi V.N., 2000, Amplitude and frequency dissociation spectra of ion-protein complexes rotating in magnetic fields. *Bioelectromagnetics* 21: 34–45.

Blackman, C.F., Benane, S.G., Kinney, L.S., Joines, W.T., and House, D.E., 1982, Effects of ELF fields on calcium-ion efflux from brain tissue in vivo. *Rad. Res.* 92: 510–520.

Blackman C.F., Benane, S.G., Rabinowitz, J.R., House D.E., and Joines W.T., 1985, A role for the magnetic field in the radiation-induced efflux of calcium ions from brain tissue in vitro. *Bioelectromagnetics* 6; 327–337.

Blackman C.F., Blanchard, J.P., Benane S.G., and House, D.E., 1994, Empirical test of an ion parametric resonance model for magnetic field interactions with PC-12 cells. *Bioelectromagnetics* 15: 239–250.

Blackman, C.F., Blanchard, J.P., Benane, S.G., and House, D.E. 1999, Experimental determination of hydrogen bandwidth fore the Ion Parametric Resonance model. *Bioelectromagnetics* 20: 5–12.

Blanchard, J.P., Blackman, C.F., Benane, S.G., and House, D.E. 1997, IPR response of PC-12 cells exposed to magnetic fields tuned for calcium ions. *The Annual Review of Research on Biological Effects of Electric and Magnetic Fields from the Generation, Delivery and use of Electricity*. Paper A-5, p. 4, San Diego, CA W/L Associates, Ltd. Frederick, MD.

Bruckner-Lea, C., Durney, C.H., Janata, J., Rappaport, C., and Kaminski, M. 1992, Calcium binding to metallochromic dyes and calmodulin in the presence of combined AC-DC magnetic fields. *Bioelectromagnetics* 13: 147–162.

Chemeris, N.K., and Safranova, V.G., 1993, Weak low-frequency magnetic field initiates frequency-dependent fluctuations of period of Daphnia magna's heart beatings. *Biophysics* 38: 511–519.

Clarkson, .H., Davies, M.S., and Dixey, R., 1999, Diatom motilty and low-frequency electromagnetic fields: a new technique in the search for independent replication of results. *Bioelectromagnetics* 20: 94–100.

Coulton, L.A., and Barker, A.T., 1993, Magnetic fields and intracellular calcium: effects on lymphocytes exposed to conditions for "cyclotron resonance". *Phys Med Biol* 38: 347–360.

Creim, J.A., Lovely, R.H., Miller, D.L., and Anderson, L.E., 2002, Rats can discriminate illuminance, but not magnetic fields, as a stimulus for learning a two-choice discrimination. *Bioelectromagnetics* 23: 545–549.

Davies, M.S.,1996, Effects of 60 Hz electromagnetic fields on early growth in three plant species and a replication of previous results. *Bioelectromagnetics* 17: 154–161.

Del Giudice, E., Fleischmann, M., Preperata, G., and Talpo, G., 2002, On the "unreasonable" effects of ELF magnetic fields upon a system of ions. *Bioelectromagnetics* 23: 522–530.

Derjugina, O.N., Pisachenko, T.M., and Zhadin, M.N.,1996, Combined action of alternating and static magnetic fields on behavior of rats in the "Open-field" test. *Biophysics* 41: 762–764.

Diebert, M.C., McLeod, B.R., Smith, S.D., and Liboff, A.R.,1994, Ion resonance electromagnetic field stimulation of fracture healing in rabbits with a fibular ostectomy. *J. of Orthopedic Res.* 12: 878–885.

Durney, C.H., Rushforth C.K., and Anderson A.A., 1988, Resonant AC-DC magnetic fields: Calculated response. *Bioelectromagnetics* 9: 315–336.

Durney, C.H., Kaminski, M., Anderson, A.A., Bruckner-Lea, C., and Rappaport, C.,1992, Investigation of AC-DC magnetic field effects in planar phospholipid layers. *Bioelectromagnetics* 13: 19–33.

Edmonds D.T., 1993, Larmor precession as a mechanism for the detection of static and alternating magnetic fields. *Bioelectrochemistry and Bioenergetics* 30: 3–12.

Fitzsimmons, R.J., Baylink, D.J., Ryaby, J.T., and Magee, F., 1993, EMF-stimulated bone-cell proliferation. in Blank, M., Ed., *Electricity and Magnetism in Biology and Medicine*. San Francisco Press, SanFrancisco.

Ftzsimmons, R.J., Ryaby, J.T., Magee, F.P., and Baylink, D.J., 1994, Combined magnetic fields increased net calcium flux in bone cells. *Calcified Tissue International* 55: 376–380.

Fitzsimmons, R.J., Ryaby, J.T., Magee, F.P., and Baylink, D.J., 1995a, Combined magnetic fields increase insulin-like growth factor-II in TE-85 human osteosarcoma bone cell cultures. *Endocrinology* 136: 3100–3106.

Fitzsimmons, R.J., Ryaby, J.T., Magee, F.P., and Baylink, D.J., 1995b, IGF-II receptor number is increased in TE-85 human osteosarcoma cells by combined magnetic fields. J. *of Bone and Mineral Research* 10: 812–819.

Frohlich, H., 1980, The biological effects of microwaves and related questions. *Adv. Electronics Electron Physics* 53: 85–152.

Galt, S., Sandblom, A., Hamnerius, Y., Hojevic, P., Saalman, E., and Norden, B. 1993, Experimental search for combined AC and DC magnetic field effects on ion channels. *Bioelectromagnetics* 14: 315–327.

Halle, B., 1988, On the cyclotron resonance mechanism for magnetic fields on transmembrane ion conductivity. *Bioelectromagnetics* 14: 381–385.

Hille, B., 1984, *Ionic Channels of Excitable Membranes*. Sinauer Associates, Sunderland, Mass., p. 183.

Hojevic, P., Sandblom, J., Galt, S., and Hamnerius, Y.1995, Ca^{2+} ion transport through patch-clamped cells exposed to magnetic fields. *Bioelectromagnetics* 16: 33–40.

Horton, P. Ryaby, J.T., Magee, F.P., and Weinstein, A.M 1993, Stimulation of specific neuronal differentiation proteins in PC-12 cells by combined AC/DC magnetic fields. In Blank, M., Ed., *Electricity and Magnetism in Biology and Medicine*. San Francisco Press, San Francisco.

Jackson J.D., 1967, *Classical Electrodynamics*. John Wiley & Sons, New York, p. 436.

Jenrow, K.A., Smith, C.H., and Liboff, A.R.,1995, Weak extremely-low-frequency magnetic fields and regeneration in the planarian Dugesia tigrina. *Bioelectromagnetics* 16: 106–112.

Jenrow, K.A., Smith C.H., and Liboff A.R., 1996, weak, extremely-low-frequency magnetic field-induced regeneration anomalies in the planarian Dugesia tigrina. *Bioelectromagnetics* 17: 467–474.

Kuyucak, S., Andersen, O.S., and Chung, S.-H., 2001, Models of permeation in ion channels. *Rep. Prog. Physics* 64: 1427–1472.

Lednev, V.V., 1991, Possible mechanism for the influence of weak magnetic fields on biological systems. *Bioelectromagnetics* 12: 71–75.

Liboff, A.R., Williams, Jr. T., Strong, D.M., and Wistar Jr, R., 1984, Time-varying magnetic fields: Effect on DNA synthesis. *Science* 223: 818–820.

Liboff, A.R., 1985, Geomagnetic cyclotron resonance in living cells, *J. Biol. Physics* 13: 99–102.

Liboff, A.R., Rozek, R.J., Sherman, M.L., McLeod, B.R., and Smith, S.D.,1987, $_{45}Ca^{2+}$ resonance in human lymphocytes. *J. of Bioelectricity* 6: 99–102.

Liboff, A.R. and McLeod, B.R., 1988, Kinetics of channelized membrane ions in magnetic fields. *Bioelectromagnetics* 9: 39–51.

Liboff, A.R., Thomas, J.R., and Schrot, J., 1989, Intensity threshold for 60-Hz magnetically induced behavioral changes in rats. *Bioelectromagnetics* 10:111–113.

Liboff, A.R., and Parkinson, W.C., 1991, Search for ion-cyclotron resonance in an Na^+ transport system. *Bioelectromagnetics* 12: 77–83.

Liboff, A.R., Jenrow, K.A., and McLeod, B.R.,1993, ELF-induced proliferation at 511mG in HSB-2 cell culture as a function of 60 Hz field intensity, in Blank, M., Ed., *Electricity and Magnetism in Biology and Medicine*. San Francisco Press, San Francisco.

Liboff, A.R., 1997, Electric-field ion cyclotron resonance. *Bioelectromagnetics* 18: 85–87.

Liboff, A.R., and Jenrow, K.A., 2000a, Cell sensitivity to magnetic fields. *Electro-MagnetoBiology* 19: 223–236.

Liboff, A.R., and Jenrow, K.A., 2000b, New model for the avian magnetic compass. *Bioelectromagnetics* 21: 555–565.

Liboff, A.R., 2002, Comment on "Extremely low frequency magnetic fields can either increase or decrease analgesia in the Land Snail depending on field and light conditions". *Bioelectromagnetics* 23:406–407.

Liboff, A.R., 2003, in: Sravroulakis P., Editor, *Biological Effect of Electromagnetic Fields*, Springer, Berlin, pp. 76–113.

Liburdy, R.P., and Yost, M.G., 1993, Time-varying and static magnetic fields act in combination to alter calcium signal transduction in the lymphocyte. In Blank, M., Ed., *Electricity and Magnetism in Biology and Medicine*. San Francisco Press, San Francisco.

Lindstrom, E., Lindstrom, P., Berglund, A., Lundgren, E. and Mild, K.H. 1995, Intracellular calcium oscillations in a T-cell line after exposure to extremely-low-frequency magnetic fields with variable frequencies and flux densities. *Bioelectromagnetics* 16: 41–47.

Li-Smerin, Y., Hackos, D.H., and Swartz, K.J., 2000, α-Helical structural elements within the voltage-sensing domain of a K^+ channel. *J. General Physiology* 115: 33–49.

Lovely, R.H., Creim, J.A., Miller, D.L., and Anderson, L.E., 1993, Behavior of rats in a radial arm maze during exposure to magnetic fields: Evidence for effects of magnesium ion resonance. 15th annual meeting *Bioelectromagnetics Society*, Abstract EI-6, Los Angeles.

Lyle, D.B., Wang, X., Ayotte, R.D., Sheppard, A.R., and Adey, W.R.1991, Calcium uptake by leukemic and normal T-lymphocytes exposed to low frequency magnetic fields. *Bioelectromagnetics* 12: 145–156.

Lyskov, Y.B., Chernysev, M.V., Michailov, V.O., Kozlov, A.P., Makarova, T.M., Vasilyeva, Y.V., Druzin, M.Y., Sokolov, G.V., and Vishnevski, A.M., 1996, The effect of a magnetic field with the frequency of 50 Hz on behavior in rats depends on the value of the constant magnetic field. *Biophysics* 41: 881–886.

McLeod, B.R., Smith, S.D., Cooksey, K.E., and Liboff, A.R.1987a, Ion cyclotron resonance frequencies enhance Ca^{2+}-dependent motility in diatoms. *J. of Bioelectricity* 6: 1–12.

McLeod, B.R. , Smith, S.D., and Liboff, A.R. 1987b, Calcium and potassium cyclotron resonance curves and harmonics in diatoms. *J. of Bioelectricity* 6: 153–168.

Mohri, K., and Fukushima, M., 2002, Gradual decreasing characteristics and temperature stability of electric resistivity in water triggered with milligauss AC field. *IEEE Trans. On Magnetics* 38: 3353–3355.

Novikoff, V.V., and Zhadin, M.N., 1994, Combined action of weak constant and variable low-frequency magnetic fields on ionic currents in aqueous solutions of amino acids. *Biophysics* 39: 41–45.

Parkinson, W.C., and Hanks, C.T. 1989, Search for cyclotron resonance in cells in vitro. *Bioelectromagnetics* 10: 129–145.

Parkinson, W.C., and Sulik, G.L.,1992, Diatom response to extremely low frequency magnetic fields. *Radiation Research* 130: 319–330.

Prasad, A.V., Miller, M. W., Cox, C., Carstensen, E.L., Hops, H., and Brayman, A.A., 1994, A test of the influence of cyclotron resonance exposures on diatom motilty. *Health Physics* 66: 305–312.

Prato F.S., Carson J.L., Ossenkopp K.P., and Kavaliers M., 1995, Possible mechanism by which extremely low frequency magnetic fields affect opioid function. *FASEB J.* 9: 807–814.

Prato, F.S., Kavaliers, M., Cullen, A.P., and Thomas, A.W., 1997, Light-dependent and -independent behavioral effects of extremely low frequency magnetic fields. *Bioelectromagnetics* 18: 284–291.

Prato, F.S., Kavaliers, M., and Thomas, A.W., 2000, Extremely low frequency magnetic fields can either increase or decrease analgesia in the land snail depernding on field and light conditions. *Bioelectromagnetics* 21: 287–301.

Rai, S., Singh U.P., and Singh A.K., 1995, X-ray determination of magnetically treated liquid water structure. *Electro-MagnetoBiology* 14: 25–30.

Reese, J.A, Frazier, M.E., Morris, J.E., Buschbom, R.L., and Miller, D.L.1991, Evaluation of changes in diatom motility after exposure to 16-Hz electromagnetic fields. *Bioelectromagnetics* 12: 21–25.

Regling C., Brueckner, C., Liboff A.R., and Kimura J.H., 2002, Evidence for ICR magnetic field effects on cartilage and bone development in embryonic chick bone explants (abstract). *Orthopedic Research Society*, 48th annual meeting, Dallas.

Reinbold, K.A., and Pollack, S.R. 1997, Serum plays a critical role in modulating $[Ca^{2+}]_c$ of primary cell culture bone cells exposed to weak ion-resonance magnetic fields. *Bioelectromagnetics* 18: 203–214.

Rochev, Y.A., Narimanov, A.A., Sosunov, E.A., Kozlov, A.N., and Lednev,V.V.1990, effects of weak magnetic field on the rate of cell proliferation in cell culture. *Studia Biophysica* 135: 93–98.

Ross, S.M.1990, Combined DC and ELF magnetic fields can alter cell proliferation. *Bioelectromagnetics* 11: 27–36.

Rozek, R.J., Sherman, M.L., Liboff, A.R., McLeod, B.R., and Smith, S.D.,1987, Nifedipene is an antagonist to cyclotron resonance enhancement of 45Ca incorporation in human lymphocytes. *Cell Calcium* 8: 413–427.

Ryaby, J.T., Grande, D.A., Magee, F.P., and Weinstein, A.M 1993a, The effects of combined AC/DC magnetic fields on resting articular cartilage metabolism. In Blank, M., Ed., *Electricity and Magnetism in Biology and Medicine*, San Francisco Press, San Francisco.

Ryaby, J.T., Magee, F.P., Weinstein, A.M., Fitzsimmons, R.J., and Baylink, D.J., 1993b, Prevention of experimental osteopenia by use of combined magnetic fields. In Blank, M., Ed., *Electricity and Magnetism in Biology and Medicine*, San Francisco Press, San Francisco.

Saalman, E., Galt, S., Hamnerius, Y., and Norden, B.1992, Diatom motility: Replication study in search of cyclotron resonance effects. In Norden, B., and Ramel, C., Eds. *Interaction Mechanisms of Low-Level Electromagnetic Fields in Living Systems*, Oxford University Press, Oxford, pp. 280–292.

Sandweiss, J., 1990, On the cyclotron resonance model of ion transport. *Bioelectromagnetics* 11: 203–205.

Shuvalova, L.A., Ostrovskaja, M.V., Sosunov, E.A., and Lednev, V.V., 1991, Effect of weak magnetic field in the parametric resonance mode on the rate of calmodulin-dependent phosphorylation of myosin in the solution. *Doklady Akademii Nauk SSSR* (Reports of the Academy of Science of the USSR; in Russian) 317: 227–230.

Smith S.D., McLeod B.R., Liboff A.R., and Cooksey K., 1987, Calcium cyclotron resonance and diatom motility. *Bioelectromagnetics* 8: 215–227.

Smith S.D., Liboff A.R., and McLeod, B.R., 1991, Effects of resonant magnetic fields on chick femoral development in vitro. *J. Bioelectricity* 10: 81–99.

Smith, S.D., Liboff A.R., McLeod, B.R.., and Barr, E.J. 1992, Effects of ion resonance tuned magnetic fields on N-18 neuroblastoma cells. In Allen, M.J., Cleary, A.F., Sowers, A.E., and Shillady, D.D., Eds *Charge and Field Effects in Biosystems-3*, Birkhauser, Boston, pp. 263–271.

Smith S.D., McLeod B.R., and Liboff A.R., 1993, Effects of CR-tuned 60 Hz *magnetic fields on sprouting and early development of Raphanus sativus. Bioelectricity and Bioenergetics* 32: 67–76.

Smith, S.D., McLeod, B.R., and Liboff, A.R., 1995, Testing the ion cyclotron resonance theory of electromagnetic field interaction with odd and even harmonic tuning for cations. *Bioelectrochemistry and Boenergetics* 38: 161–167.

Smith, S.D., Liboff, A.R., and McLeod, B.R., 2000, Potassium ion cyclotron resonance magnetic fields stimulate germination. *Proceedings of the Millennium International Workshop on Biological Effects of Electromagnetic Fields*. Heraclion, Crete, Greece. pp. 347–351.

Stern, S., Laties, V.G., Nguyen, Q.A., and Cox, C.,1996, Exposure to combined static and 60Hz magnetic fields: Failure to replicate a reported behavioral effect. *Bioelectromagnetics* 17: 279–292.

Takahashi, K., Keneko, I., Date, M., and Fukada, E., 1986, Effect of pulsing electromagnetic fields on DNA synthesis in mammalian cells in culture *Experentia*. 42: 185–186.

Tiras, K.P., Srebnitskaya, L.K., Il'jasova, A.A., and Lednev, V.V.,1996, The influence of weak combined magnetic fields on the rate of regeneration in planarian Dugesia tigrina. *Biophysics* 42: 826–831.

Tofani, S., Ferrara, A., Anglesio, L., and Gilli, G.,1995, Evidence for genotoxic effects of resonant ELF magnetic fields. *Bioelectrochemistry and Bioenergetics* 36: 9–13.

Thomas, J.R., Schrot, J., and Liboff, A.R., 1986, Low-intensity magnetic fields alter operant behavior in rats. *Bioelectromagnetics* 7: 349–357.

Tipler, P., 1982, *Physics*, 2cd edition, volume 2, Worth Publishers, p. 729.

Tohtz, S.W.,1996, The influence of ultra weak magnetic fields on growth and differentiation using the ICR hypothesis: an experimental study on radish seedlings and a theoretical discussion on relevant aspects of cartilage, bone, and other connective tissues. Ph.D. Dissertation, Medical Faculty of Humboldt University, Berlin (in German).

Trillo, M.A., Ubeda,. A., Blanchard, J.P., House, D.E., and Blackman, C.F., 1996, Magnetic fields at resonant conditions for the hydrogen atom can affect neurite outgrowth in PC-12 cells. *Bioelectromagnetics* 17: 10–20.

Ueno S. and Iwasake M., 1994, Properties of diamagnetic fluid in high gradient magnetic fields. *J. Applied Physics* 75: 7177–7179.

Weaver, J.C., and Astumian, R.D., 1990, The response of living cells to very weak magnetic fields: The thermal noise limit. *Science* 247: 459–462.

Yost, M.G., and Liburdy, R.P., 1992, Time-varying and static magnetic fields act in combination to alter calcium signal transduction in the lymphocyte. *FEBS Letts* 296: 117–122.

Zhadin M.N., Novikoff V.V., Barnes F.S., and Pergola, M.F., 1998, Combined action of static and alternating magnetic fields on ionic current in aqueous glutamic acid solution. *Bioelectromagnetic*s 19: 41–45.

Zhadin M.N., 1998, Combined action of static and alternating magnetic fields on ion motion in a macromolecule: Theoretical aspects. *Bioelectromagnetics* 19: 279–292.

Zhadin M.N., Deryugina O.N., and Pisachenko T.M., 1999, Influence of combined DC and AC magnetic fields on rat behavior. *Bioelectromagnetics* 20: 378–386.

Contributors

Charles M. Cook
Lawson Health Research Institute
268 Grosvenor Street
London, ON N6A 4V2, Canada

Jenni Heino
Laboratory of Biomedical Engineering
Helsinki University of Technology
P.O. Box 2200
02015 HUT, Finland

Timo Kajava
Laboratory of Biomedical Engineering
Helsinki University of Technology
P.O. Box 2200
02015 HUT, Finland

Toivo Katila
Laboratory of Biomedical Engineering
Helsinki University of Technology
P.O. Box 2200
02015 HUT, Finland

Abraham R. Liboff
Department of Physics
Oakland University
Rochester, MI 48309 USA

James C. Lin
Department of Electrical and Computer Engineering,
and Department of Bioengineering
University of Illinois at Chicago
851 S. Morgan Street, MC 154
Chicago, IL 60607-7053 USA

Ilkka Nissilä
Laboratory of Biomedical Engineering
Helsinki University of Technology
P.O. Box 2200
02015 HUT, Finland

Tommi Noponen
Laboratory of Biomedical Engineering
Helsinki University of Technology
P.O. Box 2200
02015 HUT, Finland

Maria J. Peters
Faculty of Science and Engineering
University of Twente
7500 AE Enschede
The Netherlands

Frank S. Prato
Lawson Health Research Institute
268 Grosvenor Street
London, ON N6A 4V2, Canada

Koichi Shimizu
Graduate School of Engineering, Hokkaido University
N13, W8, Sapporo, 060-8628, Japan

Narayanan Srivasan
Biomedical Engineering Research Centre
Nanyang Technological University
639 798 Singapore

Jeroen G. Stinstra
Faculty of Science and Engineering
University of Twente
7500 AE Enschede
The Netherlands

Alex W. Thomas
Lawson Health Research Institute
268 Grosvenor Street
London, ON N6A 4V2, Canada

Siarhei Uzunbajakau
Faculty of Science and Engineering
University of Twente
7500 AE Enschede
The Netherlands

Index